

# Directional sensing and chemotaxis in eukaryotic cells – a quantitative study

Dissertation  
zur Erlangung des mathematisch-naturwissenschaftlichen Doktorgrades  
„Doctor rerum naturalium”  
der Georg-August-Universität Göttingen

vorgelegt von  
Gabriel AMSELEM  
aus Paris, Frankreich

Göttingen, 2010

Referent: Prof. Dr. Eberhard BODENSCHATZ  
Korreferent: Prof. Dr. Reiner KREE  
Tag der mündlichen Prüfung:

# Contents

<b>Abstract</b>	<b>i</b>
<b>Introduction</b>	<b>1</b>
<b>1 Biological background</b>	<b>5</b>
1.1 General view of eukaryotic chemotaxis . . . . .	5
1.2 The receptors to cAMP . . . . .	7
1.3 G proteins . . . . .	8
1.4 Ras proteins . . . . .	8
1.5 The PI3K/PTEN pathway . . . . .	10
1.5.1 PI3K/PTEN . . . . .	10
1.5.2 PH-domain proteins . . . . .	11
1.5.3 PLC . . . . .	12
1.6 Parallel pathways . . . . .	12
1.6.1 PLA2 . . . . .	13
1.6.2 sGC . . . . .	13
1.7 Cytoskeleton regulation . . . . .	13
<b>2 A bistable model for directional sensing</b>	<b>15</b>
2.1 Models of directional sensing . . . . .	15
2.1.1 Bistable systems in a nutshell . . . . .	18
2.1.2 Bistable dynamics in directional sensing - general idea . . . . .	20
2.1.3 Model overview . . . . .	21
2.1.4 Turing instability in directional sensing [73] . . . . .	21
2.1.5 A model based on the phosphoinositide cycle [77, 112] . . . . .	24
2.1.6 Wave-pinning in a bistable system . . . . .	26
2.1.7 Directional sensing viewed as a phase separation [39] . . . . .	26
2.1.8 The diffusion-translocation model [85] . . . . .	28
2.1.9 The first-hit model . . . . .	30
2.1.10 Local excitation, global inhibition (LEGI) [67, 70] . . . . .	32
2.1.11 The balanced inactivation model . . . . .	34
2.2 A bistable mechanism triggered by internal noise . . . . .	35
2.2.1 Motivation for a our model . . . . .	35
2.2.2 The model . . . . .	35
2.2.3 Simulations . . . . .	38
2.2.4 Results of the model . . . . .	39

2.2.5	Predictions . . . . .	40
2.2.6	Exploration of the parameter space . . . . .	42
2.3	Summary . . . . .	44
	Article: A bistable mechanism for directional sensing, <i>New Journal of Physics</i> (2008)	45
<b>3</b>	<b>Directional sensing of <i>D. discoideum</i></b>	<b>65</b>
3.1	Overview of the chemotaxis pathway . . . . .	65
3.1.1	The cAMP receptors . . . . .	67
3.1.2	Downstream pathway in a very small nutshell (see figure 3.2) . . . . .	67
3.1.3	Cytoskeleton regulation . . . . .	67
3.1.4	Feedback loops . . . . .	69
3.1.5	More details on the PI3K/PTEN pathway and plan of attack . . . . .	69
3.2	Experiment . . . . .	71
3.2.1	Caged cAMP . . . . .	72
3.2.2	Microfluidics . . . . .	74
3.2.3	Gradient of cAMP . . . . .	75
3.2.4	Cell culture . . . . .	81
3.2.5	Microscopy parameters and protocol . . . . .	82
3.3	Image processing . . . . .	83
3.3.1	Finding the cell . . . . .	83
3.3.2	Quantifying the fluorescence intensity . . . . .	83
3.4	Results . . . . .	84
3.4.1	Defining a response . . . . .	84
3.4.2	Cytosolic response . . . . .	85
3.4.3	Membrane response . . . . .	85
3.4.4	Fraction of responding cells . . . . .	91
3.5	Discussion . . . . .	91
3.6	Conclusion . . . . .	93
<b>4</b>	<b>Chemotaxis of <i>Dictyostelium discoideum</i> and description by a Langevin equation</b>	<b>96</b>
4.1	Background . . . . .	97
4.2	Experimental setup . . . . .	97
4.2.1	Cells . . . . .	99
4.2.2	Microfluidics . . . . .	99
4.2.3	Experiment . . . . .	100
4.3	Image processing . . . . .	100
4.3.1	Finding the cells . . . . .	100
4.3.2	Cell tracking . . . . .	101
4.4	What gradient does the cell see? . . . . .	103
4.4.1	Flow effects . . . . .	103
4.4.2	Receptor occupancy . . . . .	104
4.5	Preprocessing: excluding cell tracks . . . . .	106
4.5.1	Excluding cell tracks based on their length . . . . .	106
4.5.2	Excluding pre-polarized cells coming from the top of the channel . . . . .	107
4.5.3	Excluding immobile cells and choice of the time step . . . . .	107
4.6	Chemotactic behavior in different gradients . . . . .	108



4.6.1	Stationarity of the velocity histograms with time . . . . .	109
4.6.2	Cellular velocity as a function of the gradient . . . . .	110
4.6.3	Difference in receptor occupancy . . . . .	110
4.6.4	Signal to noise ratio . . . . .	114
4.6.5	Fraction of long tracks . . . . .	119
4.6.6	Angle histogram, speed as a function of the angle . . . . .	119
4.7	Chemotaxis of SCAR/PIR null mutants . . . . .	119
4.7.1	Chemotactic index, speed . . . . .	119
4.7.2	Fraction of long tracks . . . . .	122
4.8	Summary . . . . .	123
4.9	The Langevin equation . . . . .	124
4.9.1	The early times of a theory of Brownian motion . . . . .	125
4.9.2	Introducing correlations in Brownian motion . . . . .	125
4.9.3	Recent applications of a Langevin equation to cell motion . . . . .	126
4.10	Langevin analysis of the cell tracks . . . . .	129
4.10.1	Principle . . . . .	129
4.10.2	Chapman-Kolmogorov . . . . .	130
4.10.3	Conditional averaging - deterministic terms . . . . .	131
4.10.4	Conditional averaging - stochastic terms . . . . .	134
4.10.5	Evolution of the parameters of the Langevin equation . . . . .	137
4.11	Simulating the data . . . . .	139
4.12	Langevin analysis of four subpopulations . . . . .	141
4.13	Langevin analysis of the SCAR/PIR mutants . . . . .	144
4.14	Summary of the stochastic modeling . . . . .	150
<b>Conclusions and outlook</b>		<b>157</b>
<b>A Stochastic chemical kinetics equation and signal to noise ratio</b>		<b>159</b>
A.1	The number of bound receptors follows a Poisson distribution . . . . .	159
A.2	Perturbation of the steady state . . . . .	160
A.3	Signal to noise ratio in a reaction cascade . . . . .	161
<b>Acknowledgements</b>		<b>174</b>
<b>Curriculum Vitae</b>		<b>176</b>

# List of Figures

1	Developmental cycle of <i>D. discoideum</i> . . . . .	2
1.1	Directional sensing of unpolarized and polarized <i>D. discoideum</i> . . . . .	6
1.2	Expression of cAR1 and cAR3 . . . . .	8
1.3	Dissociation of the G protein in response to a uniform or gradient of stimulus . . . . .	9
1.4	Activation of RasG and PI3K translocation . . . . .	10
1.5	PLC regulation of the PI3K/PTEN pathway . . . . .	12
2.1	Asymmetric CRAC-GFP translocation in response to a gradient of cAMP . . . . .	16
2.2	Chemotaxis efficiency in different gradients of cAMP . . . . .	17
2.3	Steady-state profile of a diffusing species inside the cytosol, depending on its diffusion coefficient . . . . .	18
2.4	Potential for a bistable system . . . . .	19
2.5	Example of nullclines for a bistable system . . . . .	21
2.6	The model of Mori et al. [75] . . . . .	27
2.7	Diffusion-translocation model for directional sensing . . . . .	29
2.8	First-hit model . . . . .	31
2.9	CRAC translocation in response to two opposite stimuli . . . . .	31
2.10	The second version of the LEGI model . . . . .	33
2.11	Response of the bistable model to a gradient and to a uniform stimulus . . . . .	40
2.12	The size of the translocation goes up with the gradient . . . . .	41
2.13	Characteristic time of response as a function of the relative gradient . . . . .	42
2.14	Characteristic time of response as a function of the average waiting time between two perturbations . . . . .	43
3.1	Eukaryotic chemotaxis at a glance . . . . .	66
3.2	Biological pathway from cAMP binding to CRAC translocation . . . . .	68
3.3	Visualization of CRAC in cells treated with latrunculin . . . . .	69
3.4	Biphasic translocation of $\text{PH}_{\text{CRAC}} - \text{GFP}$ . . . . .	70
3.5	Evolution of the gradient of cAMP with time . . . . .	72
3.6	Caged cAMP . . . . .	73
3.7	Absorption spectrum of DMNB caged cAMP . . . . .	73
3.8	Microfluidic channels used for the directional sensing experiments . . . . .	74
3.9	Concentration profile of fluorescein . . . . .	76
3.10	Taylor dispersion . . . . .	77
3.11	Concentration profile of fluorescein - analytic calculation . . . . .	79
3.12	Fluorescence of fluorescein . . . . .	80

3.13	Calibration of the amount of uncaged fluorescein . . . . .	81
3.14	Gradient as a function of the laser power used . . . . .	82
3.15	Cell found using the Isodata algorithm . . . . .	83
3.16	Patches of fluorescence on the membrane . . . . .	84
3.17	Noise in the cytosolic fluorescence . . . . .	85
3.18	Cytosolic response as a function of the cAMP gradient . . . . .	86
3.19	Angular range of the PIP3 patches . . . . .	87
3.20	Average fluorescence of the PIP3 patches . . . . .	87
3.21	Fluorescence and angular range at time $t_{br}$ . . . . .	88
3.22	Times at which the translocation or the fluorescence is maximal . . . . .	89
3.23	Asymmetry as a function of the gradient . . . . .	90
3.24	Asymmetry as a function of the cytosolic response . . . . .	90
3.25	Fraction of responding cells at a given cAMP gradient . . . . .	92
3.26	Cytosolic response as a function of the cAMP gradient . . . . .	94
3.27	Cytosolic response for gradient and line stimulus . . . . .	95
4.1	Chemotaxis under different conditions . . . . .	98
4.2	Microfluidic gradient mixer . . . . .	99
4.3	Image of cells in the gradient mixer using DIC microscopy . . . . .	101
4.4	Image processing . . . . .	102
4.5	Errors in the image processing . . . . .	103
4.6	Flow effects in 2D . . . . .	104
4.7	Histogram of the length of the cell tracks . . . . .	107
4.8	Example of cells at the limit of the gradient . . . . .	108
4.9	Track length . . . . .	109
4.10	Typical evolution of the velocities histograms with time . . . . .	111
4.11	Evolution of the velocities $v_x$ , $v_y$ and $v$ with the gradient for all cells . . . . .	112
4.12	Difference in receptor occupancy as a function of the gradient, and chemotactic index as a function of $\Delta R$ . . . . .	113
4.13	Chemotactic index as a function of the SNR at the receptor level . . . . .	116
4.14	Chemotactic index as a function of the SNR in the chemotactic pathway . . . . .	118
4.15	Collapsing the data from different experiments . . . . .	119
4.16	Collapsing the data from all groups together . . . . .	120
4.17	Fraction of long tracks . . . . .	121
4.18	Angle histogram, speed as a function of angle . . . . .	121
4.19	Evolution of the velocities $v_x$ , $v_y$ and $v$ with the gradient for SCAR/PIR mutants . . . . .	122
4.20	Comparison of the WT cells with the SCAR/PIR mutants . . . . .	123
4.21	Fraction of tracks longer than $30 \mu\text{m}$ for SCAR/PIR mutants . . . . .	124
4.22	Schienbein and Gruler's model . . . . .	127
4.23	Figures from the article of Shenderov and Sheetz (1997) . . . . .	128
4.24	Definition of the axis for Langevin analysis . . . . .	130
4.25	Checking the Chapman-Kolmogorov condition . . . . .	131
4.26	Deterministic term $F_{\perp}(v, \theta)$ . . . . .	133
4.27	Evolution of $F_{\perp}(\theta)$ with $\theta$ . . . . .	134
4.28	Deterministic term $F_{\parallel}(v, \theta)$ . . . . .	135
4.29	Evolution of the fitting parameters $\alpha$ and $\gamma$ with $\theta$ . . . . .	136
4.30	Autocorrelation and cross-correlation of the acceleration . . . . .	137

4.31	Deterministic term $F_{\parallel}(v, \theta)$ . . . . .	138
4.32	Evolution of the fitting parameters $\alpha$ and $\gamma$ with $\theta$ . . . . .	139
4.33	Deterministic term $F_{\parallel}(v, \theta)$ . . . . .	140
4.34	Evolution of the fitting parameters $\alpha$ and $\gamma$ with $\theta$ . . . . .	141
4.35	Parallel and perpendicular noise without binning on $\theta$ . . . . .	142
4.36	Friction coefficient from the Langevin equation . . . . .	143
4.37	Propelling force of the Langevin equation . . . . .	143
4.38	Directional force of the Langevin equation . . . . .	144
4.39	Offset of the noise of the Langevin equation . . . . .	145
4.40	Slope of the noise of the Langevin equation . . . . .	146
4.41	Simulated histograms and autocorrelations . . . . .	147
4.42	Variety of experimental cellular behaviors not captured by the simulations . . .	148
4.43	Deterministic parameters depending for each subpopulation . . . . .	148
4.44	Stochastic parameters for each subpopulation . . . . .	149
4.45	Variety of experimental cellular behaviors not captured by the simulations - subpopulations . . . . .	150
4.46	Evolution of the deterministic parameters of the Langevin equation for the SCAR/PIR mutants . . . . .	151
4.47	Stochastic parameters for the SCAR/PIR mutants - slope . . . . .	152
4.48	Stochastic parameters for the SCAR/PIR mutants - offset . . . . .	153
4.49	Comparison of the deterministic part of the Langevin equation between WT cells and SCAR/PIR mutants . . . . .	154
4.50	Comparison of the stochastic part of the Langevin equation between WT cells and SCAR/PIR mutants . . . . .	155

# List of Tables

2.1	Comparison of bistable models of directional sensing . . . . .	22
2.2	Comparison of non bistable models of directional sensing . . . . .	23
2.3	Parameter values used for the bistable model . . . . .	39

# Abstract

Chemotaxis, the directed motion of cells in a chemical gradient, plays a central role in the life of both prokaryotes and eukaryotes. It is crucial for various processes like wound healing, cancer metastasis or embryogenesis. One of the most widely studied model organisms for eukaryotic chemotaxis is the amoeba *Dictyostelium discoideum*, which shares many of its biochemical pathways with mammalian cells. When starved for about 6 hours, *D. discoideum* becomes chemotactic to the chemoattractant cAMP, and shows directional motion in gradient profiles whose magnitudes range over 4 decades. It has been shown that a difference of as few as 100 occupied receptors between the two ends of a cell could lead to chemotaxis [Song et al., *Eur. J. Cell Biol.*, **85**(9-10), 2006]. The mechanisms that translate external gradients into a directed motion of eukaryotic cells remain unclear – the biochemical pathways are not entirely unraveled, and the interactions between the various intracellular components have not been fully understood.

It is common to divide eukaryotic chemotaxis into three stages: directional sensing, polarization, and motility. Directional sensing refers to the first stage of chemotaxis, where intracellular components rearrange as a response to the gradient. In particular, an intracellular symmetry breaking occurs. Some signaling components accumulate at the part of the membrane experiencing the highest concentration of chemoattractant, while others move toward the side of lowest concentration. In recent years, several phenomenological models have been proposed to account for this initial breaking of symmetry. The difficulty in modeling directional sensing is three-fold. First, *D. discoideum* as well as mammalian neutrophils are extremely sensitive to minute gradients of cAMP. Second, a cellular response is observed for gradients ranging over 4 orders of magnitude. Third, the cells are able to adapt their response to a change in the gradient direction. To reproduce these experimental facts, existing models all assume a basic signaling system with at least one local and one diffusive species, whose interaction leads to the localization of a reporter. In this thesis, we show how coupling bistable kinetics to this basic system allowed for a noise-driven symmetry breaking inside the cell (see chapter 2).

The various models for directional sensing reproduce the experimentally observed asymmetry to a qualitative extent. Quantitatively however, their predictions differ. To experimentally test such models, we used a combination of microfluidics and photouncaging to expose individual *D. discoideum* to gradients as well as uniform concentrations of cAMP (see chapter 3). Under these conditions, we monitored the intracellular dynamics of PH<sub>CRAC</sub> – GFP, a GFP-tagged marker of directional sensing. Our results strongly suggest that, during the first 30 seconds of stimulation with cAMP, the amount of translocated PH<sub>CRAC</sub> – GFP to the cell membrane depends on the total number of occupied receptors, regardless of the stimulus. Locally on the cell membrane, the amount of PH<sub>CRAC</sub> – GFP is independent of the stimulation amplitude, but the area of the membrane where PH<sub>CRAC</sub> – GFP translocates increases as the

---

receptor occupancy goes up.

The second and third stages of chemotaxis are polarization and motility, respectively. Polarization refers to the tendency of a cell to assume an elongated shape, with a stable leading edge from which pseudopodia are extended. Motility corresponds to the last stage of chemotaxis, where the cell actually moves. We quantitatively measured the chemotactic motility of *D. discoideum* in linear gradients of chemoattractant (see chapter 4). Previously it was hypothesized that the accuracy of chemotactic motion was limited by the signal to noise ratio, which compares the amplitudes of the stochastic fluctuations to that of the ideal signal in the intracellular chemotactic pathway [Ueda and Shibata, *Biophys. J.*, **93**(1), 2007]. Based on the signal to noise ratio, a universal data scaling can be found. We were able to rescale our data as well as earlier data from the literature onto one curve. To further describe chemotactic cell motion, the cell tracks were analyzed using a generalized Langevin equation, which separated the deterministic component of motion from stochastic contributions. The evolution of the parameters of the Langevin equation with the gradient is reported for wild-type cells and for a cytoskeletal mutant. We found that, in a gradient, the deterministic part of the Langevin equation was similar for both cell types, while the stochastic part differed.

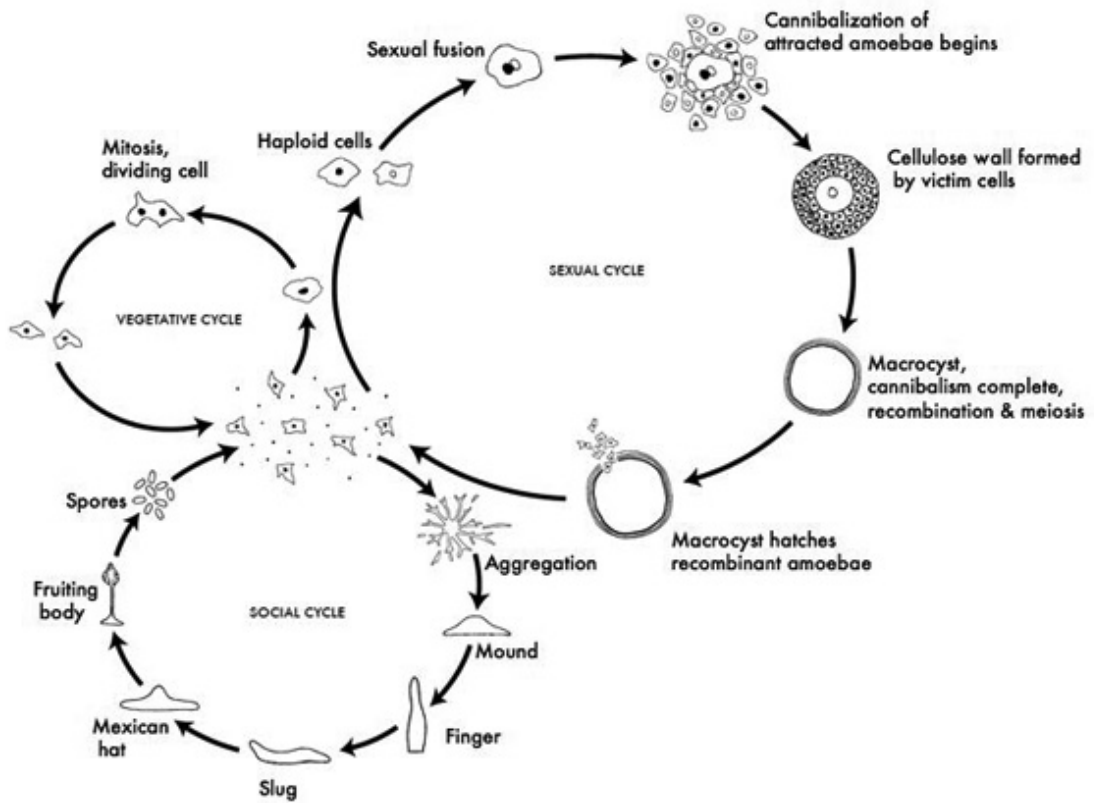
# Introduction

Chemotaxis, the directed motion of cells in a chemical gradient, plays a central role in the life of both prokaryotes and eukaryotes. The intracellular biochemical pathways of bacterial chemotaxis have been thoroughly investigated, and detailed models of prokaryotic chemotaxis are available [128]. In the case of eukaryotic chemotaxis however, the signaling pathways are less well known. Eukaryotic chemotaxis is crucial for various processes like embryogenesis [71], cancer metastasis [21], or wound healing [102]. One of the model organisms for eukaryotic chemotaxis is *Dictyostelium discoideum*. This amoeba, easy to genetically manipulate and to grow in a laboratory, has chemotactic pathways that were highly conserved during evolution. These pathways can be found almost identically in mammalian neutrophils, even though the two species are separated by millions of years in the phylogeny [79].

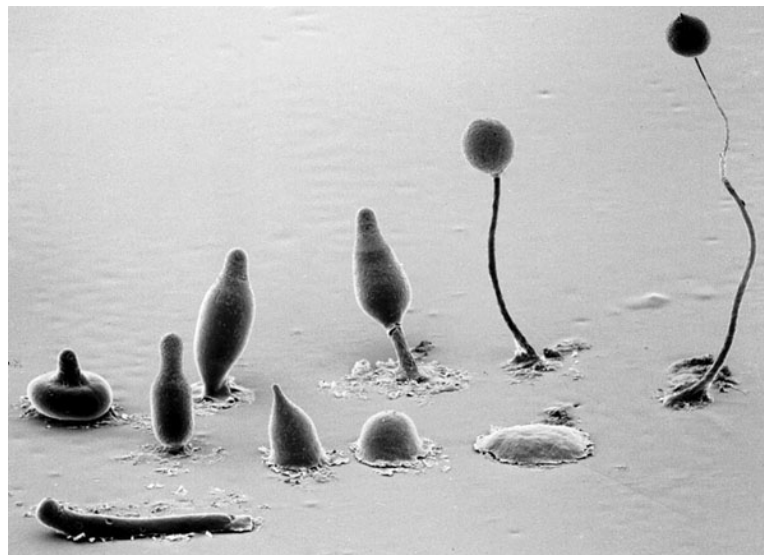
*Dictyostelium discoideum* is an amoeba of roughly 10  $\mu\text{m}$  in size that lives in the soil, where it feeds on bacteria [58]. First discovered in 1935 by Kenneth Raper in a forest of North Carolina, it belongs to the group of social amoebae, also called the cellular slime molds. As long as life conditions are favorable, *i.e.* as long as food supplies are sufficient, they are in a vegetative state and multiply by mitosis while living isolated from each other. This is called the growth phase of their life cycle. Once there is no more nutrient available however, the amoebae start aggregating, forming a multicellular organism whose shape evolves in time as can be seen on figure 1, showing the life cycle of *D. discoideum*. After 24 hours of starvation, the aggregate forms a structure consisting of a stalk and a fruiting body. One of the most striking events following aggregation is the differentiation of the originally identical cells into two kinds, stalk cells that are essentially dead, and spores that are in the fruiting body. If the spores are blown off by the wind and fall on a soil area containing nutrient, the cells become vegetative again, thus completing the life cycle. Note that, instead of the social cycle, a sexual cycle can also be observed under well-defined external conditions [58].

Starved *D. discoideum* can detect gradients of the chemical cyclic AMP (cAMP). After roughly 6 hours of starvation, about 50000 receptors to cAMP are uniformly expressed on the cell membrane [109]. It has been shown that a difference of as few as 100 occupied receptors between the front and back of the cell was sufficient to trigger a chemotactic motion in the direction of the gradient of cAMP [109]. The cells are able to detect gradients with midpoint concentrations spanning 4 orders of magnitude [30, 109]. The same type of sensitivity has been found in mammalian neutrophils [135, 43]. How is a cell able to sense this molecular gradient and translate it into a motion in the direction of the chemoattractant source? This question can be answered on different levels. On the biochemical level, it is important to know all the players of the intracellular chemotactic pathway. The knowledge of the biochemical components is however not the final answer. It is also necessary to know how the different players interact with one another. With computing power increasing, it has become easier to build descriptive models of the cell, which incorporate all of these components [72]. But





(a)



(b)

Figure 1: (a) Sketch of the life cycle of *D. discoideum*, by D. Brown and J.E. Strassmann. (b) Corresponding picture. Scale not given by the authors, but the mound (lower right corner) is roughly 3 mm wide. Image ©M.J. Grimson and R.L. Blanton, Biological Sciences Electron Microscopy Laboratory, Texas Tech University. Both images can be found on <http://www.dictybase.org>.

because the different networks inside a cell can be quite complex, and because all components are not yet known, it is also useful to build simple models that can capture the essential experimental features. In these types of models, the identification of the biological actors with the model variables is mostly conjecture. When a cell detects a gradient of cAMP, and before starting to move, intracellular components rearrange themselves within the cell. In particular, an intracellular symmetry breaking occurs. Some signaling components accumulate at the side of the membrane experiencing the highest concentration of chemoattractant, while others move toward the side of lowest concentration. This stage of chemotaxis, which happens within the first 30 seconds of exposure to a gradient of chemoattractant, is known as directional sensing. Most of the models of directional sensing share a general feature. They are based on at least two species, one of which diffuses in the cytosol, and the other which is on the cell membrane (for more details, see the review of models in chapter 2). In most models, the diffusing species plays the role of an inhibitor, while the local species plays the role of an activator. The inhibitor is supposed to diffuse quickly enough so that its intracellular concentration profile is uniform. The diffusive species therefore reflects the average external concentration of chemoattractant. The profile of the activator on the cell membrane reflects the profile the external gradient of chemoattractant. The interaction between these two species leads to the asymmetric localization of a reporter on the cell membrane. The differences between the existing models come from the details of the interaction between the inhibitor and the activator. In chapter 2, we show how coupling bistable kinetics to the basic system of activator/inhibitor allowed for a noise-driven symmetry breaking inside the cell.

All models of directional sensing qualitatively reproduce the observed symmetry breaking within the cell. Quantitatively, however, the predictions of these models differ. Up to now, and with the notable exception of work presented in [132, 72], no quantitative experiments were performed on directional sensing, which could help to discriminate between the existing models. We performed systematic experiments using a strain of *D. discoideum* expressing  $\text{PH}_{\text{CRAC}} - \text{GFP}$ , an intracellular marker of directional sensing [80]. When stimulated with a gradient of cAMP,  $\text{PH}_{\text{CRAC}} - \text{GFP}$  shows a biphasic translocation to the membrane [132]. We focused on the first phase of translocation. Using flow photolysis, a combination of microfluidics and photouncaging [10], we stimulated individual cells with different well-defined, stable gradients of cAMP and monitored the intracellular dynamics of  $\text{PH}_{\text{CRAC}} - \text{GFP}$  in response to these stimuli. The quantitative evolution of the intracellular response with the gradient is reported in chapter 3. It was hypothesized that the first  $\text{PH}_{\text{CRAC}} - \text{GFP}$  translocation was a local response, not a response depending on the difference of intracellular components between the two ends of the cell. For the first time, we tested this hypothesis quantitatively by comparing the first phase of  $\text{PH}_{\text{CRAC}} - \text{GFP}$  translocation in response to gradients and to uniform stimuli.

The chemotactic motion of *D. discoideum* in various gradients of cAMP has been studied extensively over the past decades. In chapter 4, we used microfluidic devices to produce the stable, linear gradients that the cells were subjected to [109]. It has been recently shown that the accuracy of chemotaxis of *D. discoideum* depends on both the midpoint concentration of cAMP and the absolute gradient experienced by the cell [34]. Because chemical reactions are stochastic processes, Ueda and Shibata hypothesized that the accuracy of chemotactic motion is limited by the amount of stochastic fluctuations propagating through the intracellular chemotactic pathway [119]. They defined a signal to noise ratio (SNR), which was found to be correlated with the experimental results on chemotactic efficiency of Fisher et al. [30]. Estimating the SNR at each point of the microfluidic device, we showed that all data, from

---

our experiments as well as from earlier sources from the literature, could be collapsed onto one curve if the chemotactic efficiency of the cells were plotted as a function of the SNR. Finally, we used a Langevin equation to describe the chemotactic motion of cells in the different gradients used, enabling us to observe the influence of the gradient on both the stochastic and deterministic components of motion. This analysis was reproduced both for wild-type cells and for mutants lacking SCAR/PIR121, a key regulator of the actin cytoskeleton, allowing us to quantify the difference in motion of both cell types.

# Chapter 1

## Biological background

Chemotaxis is the directional migration of cells in a chemical gradient. If the cell migrates up the gradient of chemical, the chemical is called a chemoattractant. In the opposite case, it is termed a chemorepellent. Both prokaryotes and eukaryotes can respond chemotactically to chemical signals. In the case of several bacteria (the most famous one being *E. coli*) all the steps of the chemotactic pathway are known [128]. This doesn't mean that bacterial chemotaxis is completely understood: for example, it is known that *E. coli* can sense temporal gradients of chemoattractant, but there are still debates on whether it can also sense spatial gradients [116]. Still, knowing all the biochemical players was definitely an important step in unraveling the mechanisms of bacterial chemotaxis. In the case of eukaryotic chemotaxis however, parts of the signaling pathway are still being uncovered, and the relationships between the different biochemical components are not as clear [113]. Eukaryotic chemotaxis is crucial in as various processes as embryogenesis [71], cancer metastasis [21], or wound healing [102]. One of the model organisms for eukaryotic chemotaxis is the social amoeba *Dictyostelium discoideum*. When starved, these amoebae can respond chemotactically to cAMP, and forms aggregates of about one million cells [14], This aggregation is only the first part of a survival mechanism that will see 20% of the cells die and form a stalk, on the top of which the 80% remaining cells will form a fruiting body and turn into spores. Interestingly, the chemotactic pathways of *D. discoideum* were highly conserved during evolution and can be found almost identically in mammalian neutrophils, even though the two species are separated by millions of years in the phylogeny [79]. In this chapter, I will give an introductory overview of the current knowledge of the chemotactic pathway of *D. discoideum*, concentrating mostly on the pathway used in chapter 3 of this thesis. The most crucial informations will be shortly summarized in the remaining chapters when needed.

### 1.1 General view of eukaryotic chemotaxis

It has become common to divide eukaryotic chemotaxis into three processes: directional sensing, polarization and motility (see for example the review articles [24, 32, 90, 113]).

**Directional sensing** refers to the first stage of chemotaxis, occurring in *D. discoideum* within the first 10 seconds after the application of an external gradient of chemoattractant. During this stage, the cells reads the external gradient and responds by spatially rearranging several of its intracellular biochemical components. In particular, signaling

## 1.1. General view of eukaryotic chemotaxis

---

components accumulate to the part of the membrane experiencing the highest concentration of chemoattractant. This accumulation can be visualized in fluorescence microscopy using proteins bound to the green fluorescent protein (GFP) [80, 52]. An example of such a marker of directional sensing is shown on figure 1.1a.

**Polarization** refers to the tendency of a cell to assume an elongated shape along an anterior-posterior axis, with a stable leading edge (defining the front of the cell) from which pseudopodia are extended, and a retracting uropod (defining the back of the cell). A *D. discoideum* cell can polarize as a response to a gradient, typically within one minute after the gradient has been applied. However, spontaneous polarization in the absence of asymmetric external cues is also observed [108].

**Motility** is the last stage of chemotaxis and corresponds to the actual motion of the cell. There can also be motility in the absence of an external stimulus.

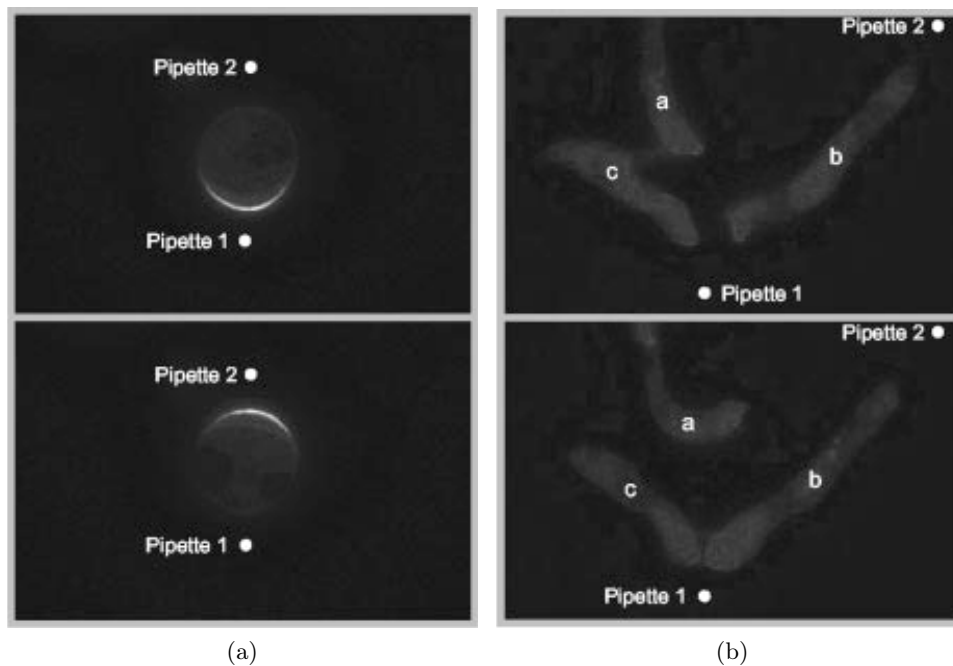


Figure 1.1: (a) Directional sensing: translocation of  $\text{PH}_{\text{CRAC}} - \text{GFP}$  (a marker of directional sensing, see section 1.5) in a cell treated with Latrunculin A (a drug inhibiting actin polymerization). First, the cell is exposed to a gradient of cAMP coming from pipette 1. Then, pipette 1 is turned off and pipette 2 is turned on. Within 60 seconds, the translocation changes side. (b) Effect of polarization on chemotaxis. First, polarized cells migrate towards pipette 1. When additionally, pipette 2 is turned on, cell *a* turns around but cells *b* and *c* continue in their original direction. Both figures taken from [24]. No scale is given in the article from which these pictures are taken, but a Latrunculin-treated cell has probably a diameter  $\sim 10 \mu\text{m}$ , and the polarized cells should be roughly 15-20 microns long.

Directional sensing has been shown to be separable of both motility and polarization. Indeed, when cells are treated with Latrunculin A, an inhibitor of actin polymerization (and

therefore an inhibitor of polarization and of cell motion), intracellular proteins can still translocate in a response to a gradient, and accumulate at the part of the cell experiencing the highest extracellular concentration of cAMP [80]. The response can also adapt to a change in the gradient direction: if the direction of the gradient is switched, so is the intracellular translocation (see figure 1.1a) [80].

In polarized and motile cells, the existence of feedback loops between actin and signaling molecules from the leading edge has been established [96]. It is also known that, when the direction of chemoattractant gradient is changed, a polarized cell can either rearrange its front and back, or keep the same front and turn towards the new gradient direction, showing an influence of polarization on directional sensing (see figure 1.1b) [24, 130].

In chapter 3, we will probe the sensitivity of directional sensing using different gradients of chemoattractant. It has been established that there are at least four parallel pathways that regulate different aspects of chemotaxis [113]. In this chapter, we are focusing mainly on the components of the PI3K/PTEN pathway and their interactions. The PI3K/PTEN pathway will be essential for the experiments reported in chapter 3.

## 1.2 The receptors to cAMP

In *D. discoideum* four receptors to cAMP have been identified, named cAR1 to cAR4, that are expressed at different stages of the life cycle. When the cells are vegetative, there is no receptor to cAMP. The gene coding for cAR1 (cAMP Receptor 1), is the first to be expressed after initiation of starvation, and its expression peaks 6 hours after the onset of starvation [55] (see figure 1.2). At this point in time, there are roughly 70,000 receptors uniformly distributed around the cell membrane. It is interesting to note that the expression of cAR1 depends on the presence of cAMP pulses during early development [81]. Moreover, it is known that the stimulation of a *D. discoideum* cell with cAMP induces the production and release of cAMP by the cell [101]. There is therefore a feedback loop between the production of cAMP and the expression of cAR1.

Within 6 to 9 hours of starvation, the gene coding for cAR1 is down-regulated while the gene encoding cAR3 starts to be expressed. As seen on figure 1.2, the maximal number of cAR3 around the cell is an order of magnitude lower (5,000 sites around the cell) than the maximum number of cAR1. The two other cAMP receptors, cAR2 and cAR4 are expressed later in development. In our work, we will be interested in events occurring between 6 and 8 hours of starvation. The most important receptor for us is therefore cAR1.

When cAR1 is bound to cAMP, it undergoes phosphorylation with a half-time of about 45 s. The fraction of phosphorylated receptors rises with the applied concentration of cAMP [125]. Phosphorylated receptors have a roughly four times lower affinity for cAMP than non-phosphorylated receptors [18]. This means that, at a given concentration of cAMP, the number of phosphorylated receptors bound to cAMP is four times smaller than what the number of bound non-phosphorylated receptors would be. This phenomenon is termed loss of ligand binding. When the chemoattractant is removed, dephosphorylation of cAR1 occurs with a half-time of 2.5 minutes [125].

The dissociation kinetics between cAMP and cAR1 is multiphasic, with time constants of the order of seconds [118]. When a cell is subjected to a gradient of cAMP, binding and unbinding are faster at its leading edge than at its back [118].

In *D. discoideum*, the cAMP receptors are uniformly distributed around the membrane

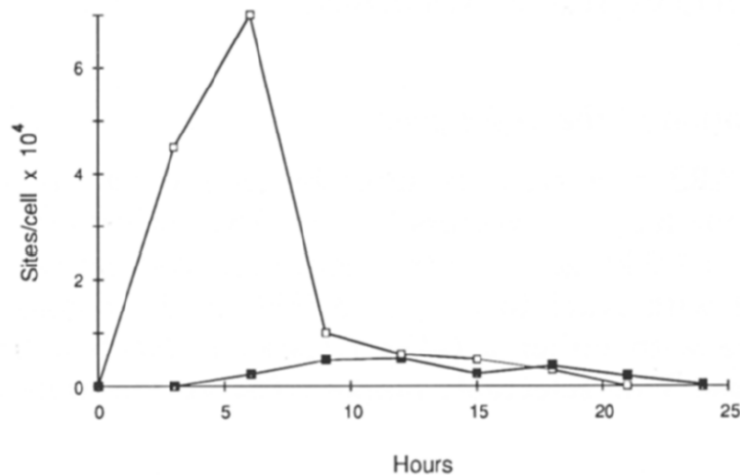


Figure 1.2: Expression of cAR1 (empty squares) and cAR3 (filled squares) as a function of starvation time. Figure taken from [55].

and stay uniformly distributed even when the cell is polarized in a gradient of chemoattractant [131].

### 1.3 G proteins

The different cAMP receptors are transmembrane proteins linked to G2, a heterotrimeric G-protein, *i.e.* a G-protein consisting of three subunits<sup>1</sup>. These subunits are called  $\alpha_2$ ,  $\beta$  and  $\gamma$ . When cAMP binds to a receptor, the G-protein gets activated: the GDP on the  $G\alpha_2$  subunit is exchanged for a GTP, which promotes the dissociation of G2 into the  $G\alpha_2$  monomer and a  $G\beta\gamma$  complex [51]. During continuous stimulation, the G-protein stays dissociated, whether the external stimulus is a uniform concentration of cAMP [51] or a gradient of cAMP [132]. The activation of the G-protein reaches a steady-state level that depends on the local external concentration of chemoattractant, with higher concentrations of cAMP leading to more activation (see figure 1.3). In the case of a gradient stimulus, the extent of activation is bigger at the front of the cell, where there is a higher receptor occupancy, than at the back of the cell. When the stimulus is removed, the G-protein heterotrimer reassociates. Evidence suggests that the  $G\beta\gamma$  is the complex transducing the response from the receptors to the downstream chemotactic pathway, while the  $G\alpha$  subunit binds G2 to cAR [113].

### 1.4 Ras proteins

Dissociation of the G-protein leads to the activation of guanine nucleotide exchange factors (GEFs), which catalyse the exchange of GDP for GTP in proteins of the Ras family, thereby activating them. Proteins of the Ras family are small GTPases that regulate as various cellular processes as mitosis, motility, chemotaxis, endocytosis. *D. discoideum* has five Ras

<sup>1</sup>G-protein is the abbreviation for guanine nucleotide-binding protein.

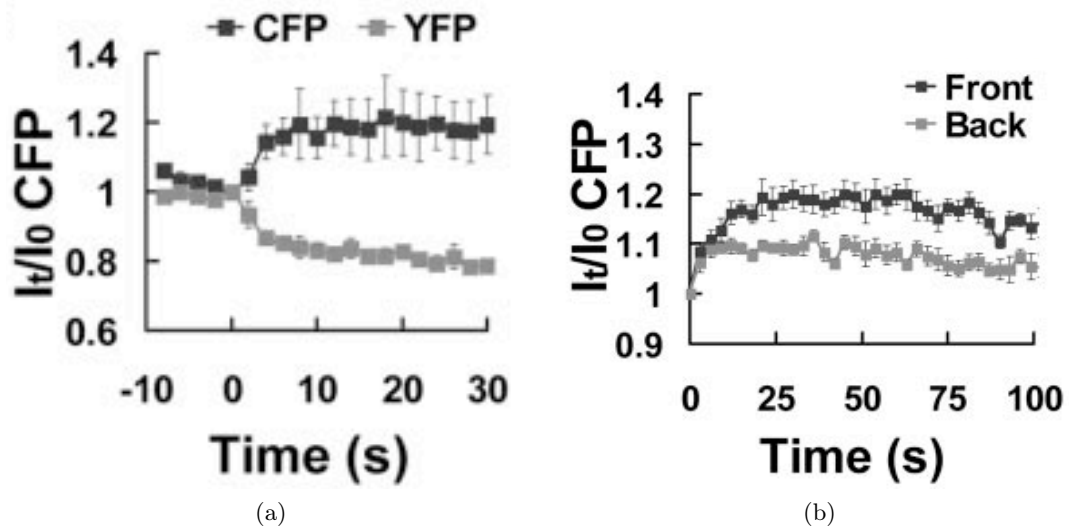


Figure 1.3: Xu et al. [132] monitored the dissociation of the G protein using fluorescence resonance energy transfer (FRET) microscopy (for the principle, see the original paper by Förster [31], and for the biological application, see *e.g.* [99, 53]).  $G\alpha_2$  was tagged with CFP and  $G\beta\gamma$  with YFP. Upon dissociation of the G protein, a loss of YFP fluorescence is observed, concomitant to an increase of the CFP fluorescence. (a) Intensity levels of CFP and YFP upon uniform stimulation of the cell, averaged around the membrane, and normalized by the intensity before stimulation. A uniform stimulus of cAMP leads to a uniform dissociation level of the G protein around the cell. (b) Intensity level of CFP upon gradient stimulation, averaged over the front of the cell (black) and the back of the cell (gray). A gradient stimulus leads to a higher level of dissociated G protein at the front of the cell than at the back. Both figures taken from [132].



proteins that have both unique and overlapping functions [65]. RasG activates PI3K, one of the key enzymes in the chemotactic pathway investigated in this thesis. It has been shown that RasG is uniformly distributed around the cell membrane, in the absence or presence of chemoattractant [95]. In a gradient of cAMP, activation of Ras proteins happens only in the half of the cell experiencing the highest concentration of chemoattractant. The directional activation of Ras is independent of the presence of F-actin, as cells treated with Latrunculin A, an inhibitor of actin polymerization, also show asymmetric activation (see figure 1.4a). Ras activation also does not require PI3K activity, as seen in cells treated with LY294002, a drug inhibiting the activation of PI3K [95]. The directional activation of Ras is – as of now – the first known amplified asymmetric response of *D. discoideum* in a gradient of chemoattractant. This activation is also the first known response that *adapts* when *D. discoideum* is stimulated by a uniform concentration of cAMP: whereas cAR1 is always bound by cAMP and the G protein stays dissociated, the level of activated Ras peaks roughly 10 seconds after the stimulus has been applied, and decreases to its pre-stimulus level within a minute [95].

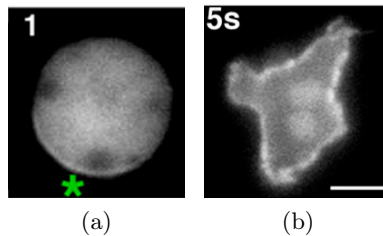


Figure 1.4: (a) A Ras-binding domain is tagged with GFP to monitor the activation of RasG. As a response to a gradient, RasG is activated asymmetrically. Green asterisk: position of the pipette emitting cAMP. The cell is treated with Latrunculin A. (b) PI3K translocation in response to a uniform stimulus of cAMP.

## 1.5 The PI3K/PTEN pathway

### 1.5.1 PI3K/PTEN

GTP-bound Ras proteins activate phosphatidylinositol 3-kinases (PI3K), enzymes which catalyze the formation of the membrane bound phospholipid phosphatidylinositol (3,4,5)-triphosphate (PI(3,4,5)P<sub>3</sub> or PIP<sub>3</sub>) from the membrane bound phosphatidylinositol (4,5)-biphosphate (PI(4,5)P<sub>2</sub> or PIP<sub>2</sub>) [113]. In *D. discoideum* 6 different PI3 kinases have been identified, that all have a Ras-binding domain (RBD). In a stimulated cell, PI3K translocates from the cytosol to the cell membrane (see figure 1.4b), even when PI3K activity is repressed by treatment with LY294002. In a uniform concentration of cAMP, the translocation of PI3K to the membrane is transient. In a gradient of chemoattractant, PI3K localizes to the leading edge of the cell. In cells treated with Latrunculin A and stimulated with cAMP, PI3K does not translocate to the membrane, suggesting that actin might be important for PI3K localization [95]. In non-developed cells, a G protein-independent Ras/PI3K/F-actin feedback loop was identified [96].

The enzyme catalyzing the degradation of PI(3,4,5)P<sub>3</sub> to PI(4,5)P<sub>2</sub> is the phosphatase

and tensin homolog deleted on chromosome 10 (PTEN). In resting cells, a fraction of PTEN is uniformly distributed on the cell membrane. Upon stimulation with a uniform concentration of cAMP, PTEN dissociates from the membrane and diffuses into the cytosol within the first 10 seconds of stimulation. This response is however transient, and PTEN reassociates with the cell membrane within a minute. In a gradient of cAMP, PTEN accumulates at the rear of the cell [35, 48]. Contrarily to PI3K, whose translocation on the membrane depend on the presence of actin, dissociation of PTEN from the membrane also occurs in Latrunculin treated cells [49].

In a gradient of cAMP, PI3K and PTEN therefore show reciprocal localization, which results in the creation of a strong internal gradient of phospholipids, with accumulation of PI(3, 4, 5)P<sub>3</sub> at the leading edge of the cell and of PI(4, 5)P<sub>2</sub> at the rear of the cell. It has been shown that the localization of PI3K is independent of the intracellular level of PI(3, 4, 5)P<sub>3</sub>, and is independent of PTEN. The localization of PTEN is also not regulated by PI(3, 4, 5)P<sub>3</sub>. PTEN has a PI(4, 5)P<sub>2</sub> binding domain which is important both for its localization on the membrane and for its phosphatase activity [49]. This means that PI(4, 5)P<sub>2</sub> is both the product of PTEN and a binding site for PTEN.

### 1.5.2 PH-domain proteins

Proteins containing a pleckstrin-homology domain (PH domain) can bind to PI(4, 5)P<sub>2</sub> and preferentially to PI(3, 4, 5)P<sub>3</sub> [46]. In *D. discoideum*, PH domain proteins include CRAC (cytosolic regulator of adenylyl cyclase), PhdA (PH domain containing protein A) and Akt/PKB (protein kinase B). Upon uniform stimulation, PH domain proteins translocate uniformly to the membrane and it has been established that the translocation profile of PH<sub>CRAC</sub> (the PH domain of CRAC) matches the increase in the level of PI(3, 4, 5)P<sub>3</sub> [46]. PH domain proteins are therefore widely used as a proxy for PI(3, 4, 5)P<sub>3</sub> production (see for example [113] and references therein).

It is interesting to note that, in cells treated with Latrunculin A and stimulated with cAMP, PH domain proteins translocate to the membrane (see figure 1.1a) even though PI3K does not. This suggests the existence of a low basal level of PI3K associated to the membrane before stimulation, which is activated by Ras upon stimulation [95].

Uniform exposure of *D. discoideum* to cAMP triggers two phases of CRAC translocation [86] correlated with two phases of actin polymerization [20]. The first phase consists in a rapid and transient CRAC translocation/actin polymerization within the first 10 seconds of stimulation. The second phase starts after 40 seconds of exposure to cAMP and consists in the apparition of patches of CRAC on the membrane [86], which are associated with the formation of pseudopodia, and in a second phase of actin polymerization, lasting over several minutes [20]. The second peak of PI(3, 4, 5)P<sub>3</sub> formation/actin polymerization can be inhibited by incubating the cells in the PI3K inhibitor LY294002. However, the first phase of the response is surprisingly insensitive to LY294002 treatment. This is also the case in *pten*<sup>-</sup> cells treated with LY294002, indicating that the transient loss of PTEN from the plasma membrane is not the reason of the first PI(3, 4, 5)P<sub>3</sub> peak. This could suggest that very few PI(3, 4, 5)P<sub>3</sub> molecules can trigger actin polymerization during the first phase of the response, and that the second phase of the response requires an amplification of the phospholipid signaling, rendered impossible in cells treated with LY294002 or in *pi3k1*<sup>-</sup>/*2*<sup>-</sup> cells. Or this could also suggest the existence of a parallel pathway controlling the first peak of a actin polymerization. The first phase of the response exists only if the cells are developed for less than roughly 7 hours.

## 1.6. Parallel pathways

After 7 hours of development, cells spontaneously assume a polarized shape along an anterior-posterior axis. When this is the case, the initial phase of actin polymerization does not exist and the cells turn around to adapt to a change in gradient direction, keeping the same front. In 5-hour starved cells, however, new pseudopods can be extended and a new front can be created in response to a change in gradient direction [20, 130].

### 1.5.3 PLC

Phospholipase C (PLC) hydrolyzes  $\text{PI}(4,5)\text{P}_2$  into two cytosolic second messengers, diacylglycerol (DAG) and inositol (1,4,5)-triphosphate ( $\text{I}(1,4,5)\text{P}_3$ ). It is moreover known that PLC is activated by  $\text{G}\alpha_2$  upon stimulation by cAMP [57]. Work from the Van Haastert group [57, 64] showed that PLC regulates the localization of PTEN on the membrane: in  $\text{plc}^-$  cells, there is no dissociation of PTEN from the membrane upon stimulation with a uniform concentration of cAMP. Similarly, PTEN does not localize at the rear and side of  $\text{plc}^-$  cells, as it does in wild-type cells. The mechanism for PTEN regulation by PLC was proposed in [64] (see also figure 1.5). First, activation of  $\text{G}\alpha_2$  upon stimulation by a gradient of cAMP leads to a local degradation of  $\text{PI}(4,5)\text{P}_2$  depending on the external local concentration of cAMP. Upgradient, more PLC is activated, leading to a  $\text{PI}(4,5)\text{P}_2$  gradient inside the cell in the opposite direction of the external cAMP gradient. PTEN colocalizes with  $\text{PI}(4,5)\text{P}_2$ , leading to a gradient of  $\text{PI}(3,4,5)\text{P}_3$  in the direction of the cAMP gradient. The  $\text{PI}(3,4,5)\text{P}_3$  at the leading edge of the cell leads to actin polarization which in turn will enable the activation of PI3K at the leading edge. At the rear of the cell, presence of  $\text{PI}(4,5)\text{P}_2$  allows for binding of PTEN. The gradients of localized PTEN and PI3K are thus stabilized. This mutual spatial exclusion of PI3K and PTEN leads to symmetry breaking.

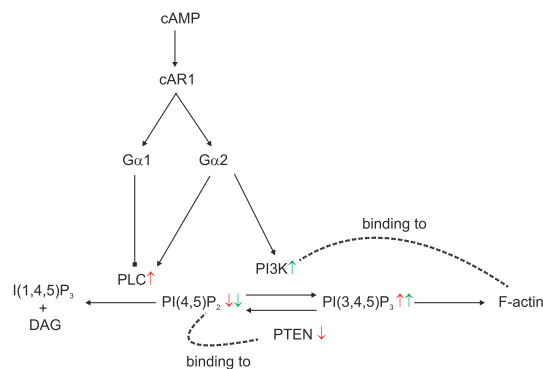


Figure 1.5: Proposed mechanism for the regulation of the PI3K/PTEN pathway by PLC. In red:  $\text{PI}(4,5)\text{P}_2$ /PTEN loop. In green:  $\text{PI}(3,4,5)\text{P}_3$ /F-actin loop. Up and down arrows show activation and inhibition, respectively, by the two pathways. Figure taken from [64].

## 1.6 Parallel pathways

Whereas phospholipid signaling and the PI3K/PTEN pathway described above are relevant for chemotaxis, it has been shown that cells lacking their 5 PI3Ks and PTEN were still able to perform chemotaxis [44], showing that intracellular  $\text{PI}(3,4,5)\text{P}_3$  gradients were not necessary

for chemotactic motion. This suggests the existence of parallel pathways mediating chemotactic signaling. In this section, we briefly discuss the other known pathways of chemotaxis.

### 1.6.1 PLA2

Van Haastert et al. [121] and Chen et al. [19] showed the existence of a pathway involving the phospholipase A<sub>2</sub> (PLA2) in chemotaxis. When either PLA2 or PI3K are inhibited, chemotaxis in shallow gradients is inhibited. In steep gradients, both of the pathways have to be inhibited to prevent chemotaxis<sup>2</sup>. Chen et al. showed that, upon stimulation, the first phase of actin polymerization could be supported by the PLA2 pathway [19]. It was suggested that Ca<sup>2+</sup> is a regulator of PLA2. The exact roles of PLA2 are still unclear though. PLA2 is cytosolic and stays cytosolic upon stimulation with cAMP [59].

The experiments showing that chemotaxis is inhibited when both PLA2 and PI3K are inhibited were performed on cells starved for about 5 to 7 hours, where the cells are not polarized. When cells are starved for more than 7 hours, they assume a polarized shape and are able to respond to gradient of cAMP even in the absence of both PLA<sub>2</sub> and PI3K [126]. This suggests yet another existing pathway of chemotaxis, that becomes operational only after 7 hours of development.

### 1.6.2 sGC

Veltman et al. showed that, in polarized cells (starved for at least 7 hours), two pathways of chemotaxis are mediated by a soluble guanine cyclase (sGC) [126]. The sGC protein localizes to the existing leading edge of the polarized cells, where it interacts with F-actin. The product of sGC, cyclic guanosine monophosphate (cGMP) inhibits de novo pseudopodia formation at the back of the cell by interacting with myosin II [126, 16]. Because the level of activation of sGC is the same in 5-hour starved unpolarized cells and in 7-hour starved polarized cells, Veltman et al. propose that intrinsic prepolarization is a prerequisite for strong chemotaxis by sGC [126].

## 1.7 Cytoskeleton regulation

A rearrangement of the cytoskeleton, and particularly an actin polymerization at the front and actomyosin formation at the back are necessary for cell motion. How does the pathway mentioned above influence the direction of motion? The answer is not yet clear.

At the front of the cell, actin polymerization is stimulated by the action of the Arp2/3 (actin related proteins 2 and 3) complex, which initiates new barbed ends at the end of an existing actin filament. First, Rac guanine-nucleotide-exchange factors (GEFs), that contain a PH-domain, activate small G proteins called Rac (small G proteins are proteins homologous to the G $\alpha$  unit of the G trimeric protein). Rac effectors of the WASP (Wiskott-Aldrich syndrome protein) and SCAR/WAVE (suppressor of cAMP receptor; also known as WAVE) family activate in their turn the Arp2/3 [6]. One of the proteins in the SCAR/WAVE family is SCAR. It is known that SCAR binds to 4 different proteins to form an inactive complex [11]. One of these proteins is PIR121, which is encoded by the *pirA* gene. When *pirA* is disrupted, mutant cells show large protrusions, a high proportion of filamentous actin (F-actin) compared to the

---

<sup>2</sup>Unfortunately, the exact value of the gradient is not given in the articles.

total cellular actin, and an increased rate of pseudopod formation all over the cell [11]. Overall, the phenotype of *pirA*<sup>-</sup> cells is consistent with an overactivation of SCAR. When a double *scar*<sup>-</sup>/*pirA*<sup>-</sup> mutant is constructed, the F-actin content of the cell returns to its wild-type value. The presence of the SCAR complex is however not required for the chemoattractant-induced actin polymerization, as both in *pirA*<sup>-</sup> and in *scar*<sup>-</sup>/*pirA*<sup>-</sup> mutants, addition of cAMP leads to a rise in the level of F-actin [11]. In the last chapter of this thesis, we will perform quantitative chemotaxis experiments on *scar*<sup>-</sup>/*pir*<sup>-</sup> mutants.

At the back of the cell, myosin II assembly is controlled by the nucleotide cGMP and PAKa. High cGMP levels PAKa is localized at the back of the cell and is phosphorylated by Akt/PKB in a PI3K-dependent fashion. In cells migrating in a gradient of chemoattractant, myosin II filaments are also present at the sides of the cells. This provides the mechanism to suppress lateral pseudopodia in chemotaxing cells, enabling a more directed cell trajectory [120].

## Chapter 2

# A bistable model for directional sensing

Chemotactic *D. discoideum* are able to crawl up gradients of cAMP over a wide range in gradient magnitudes. It has previously been shown that a difference in occupancy of as little as 100 receptors between front and back of the cell was sufficient to trigger a chemotactic motion [109]. A typical cell having about 50 000 receptors<sup>1</sup>, this means that a relative difference in receptor occupancy as low as 0.2% is sufficient to induce a chemotactic response [109]. The mechanism that transduces such a small gradient into a directed motion is still not well known, but its main characteristic is the appearance of a breaking of symmetry within the cell, with some biochemical reactions being confined to the front of the cell, while others are restricted to the back of the cell. One of the first known symmetry-breaking events is the phosphorylation of the phospholipid PIP2 into PIP3 on the membrane, at the front of the cell [36]. At the back of the cell, no such phosphorylation occurs [48]. This phosphorylation can be visualized by fluorescence microscopy using green fluorescent protein (GFP) constructs. Indeed, some proteins contain a domain – called a pleckstrin homology (PH) domain – that binds PIP2 and, more specifically, PIP3 [46]. Tagging PH-domain proteins with GFP, we observe an asymmetric fluorescence around the cell membrane when the cell senses a gradient of cAMP (see figure 2.1), showing the asymmetric production of PIP3. This early stage of chemotaxis is known as directional sensing. In this chapter, we will present a model of directional sensing that we developed [8].

### 2.1 Models of directional sensing

There are several difficulties in modeling directional sensing, *i.e.* the asymmetric recruitment of proteins to the membrane of a cell stimulated by a gradient of chemoattractant. First, the cell should essentially be able to respond to gradients independently of the the average concentration it is being exposed to: as seen in Fisher et al. [30] and Song et al. [109], the gradient response spans over 4 orders of magnitude of midpoint concentrations (see figure 2.2). If we convert the concentration gradient into a difference in receptor occupancy between the front half of the cell (*i.e.* the half facing the gradient source) and its back half (*i.e.* the half opposite the gradient source), we see that *D. discoideum* are extremely sensitive to minute

---

<sup>1</sup>It was shown in [55] that at the peak of the expression, the cells had 70 000 receptors. In this chapter, we adopt the number of 50 000, used in [109].

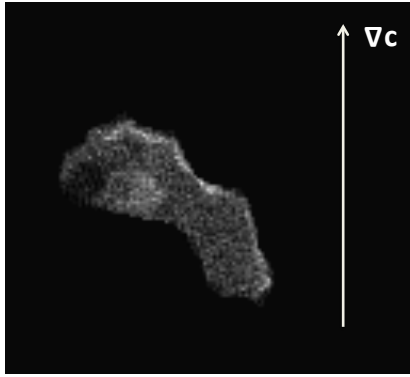


Figure 2.1: A protein containing a PH-domain, CRAC, has been tagged with GFP. On this picture, we see a translocation of CRAC to the front of the cell (where the external concentration of cAMP is maximal) and not to the back. This asymmetric translocation is one of the first occurring responses of *D. discoideum* to a gradient of cAMP.

asymmetries: they are chemotactic as soon as roughly 100 receptors more are occupied at the front than at the back, out of a total of about 50 000 receptors [109]. Second, at the intracellular level, Janetopoulos et al. [52] have shown that the asymmetry of PH-domain proteins is 5 times bigger than the asymmetry of the gradient, thus giving evidence for a strong intracellular amplification of the chemoattractant stimulus. Third, the mechanism should be reversible: if the gradient direction is reversed, so is the motion of the cell and the position of front and back are exchanged [80]<sup>2</sup>. In the case of *D. discoideum* a last requirement is usually coupled to the ones just mentioned. It is known that a uniform concentration of cAMP induces a uniform translocation of PH-domain proteins to the membrane of the cell, indicating the transformation of PIP2 to PIP3 everywhere around the cell [82]. This translocation is transient, as the cell adapts to its new environment [82]. When the models are able to reproduce this last requirement, they can also reproduce another experimental feature: when the cells are stimulated by a gradient, PH-domain proteins first translocate uniformly around the cell membrane, and then only does the asymmetric translocation occur<sup>3</sup>.

Because PH-domain proteins translocate asymmetrically for midpoint concentrations ranging over 4 orders of magnitude, a communication between the front and back of the cell has to be assumed. Biologically, communication implies the existence of a diffusing species in the cytosol of the cell. This diffusing species has yet to be identified experimentally, but is present in all models of directional sensing. Its main characteristic is that its concentration profile should be uniform inside the cell. If we assume that the production of the diffusing species occurs at a constant rate  $k_p$ , that its degradation rate is  $k_{-1}$  and its diffusion coefficient is  $D_m$ , the evolution of the concentration  $c(x, t)$  of the diffusing species is given by [85]:

$$\frac{\partial c(x, t)}{\partial t} = D_m \Delta c(x, t) - k_{-1} c(x, t) + k_p \quad (2.1)$$

<sup>2</sup>At least if the cells have been treated with Latrunculin A, a drug preventing actin polymerization.

<sup>3</sup>The first translocation is not necessarily uniform, as mentioned in [132], and as we saw in our experiments reported in the next chapter. Nevertheless, apart from the very complex model from Meier-Schellersheim et al. [72], no model addresses the possible asymmetry of the first translocation.

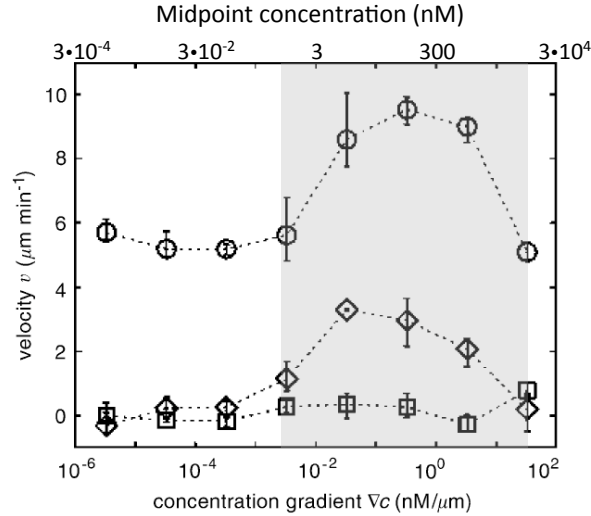


Figure 2.2: Velocity component perpendicular to the gradient direction (squares), in the gradient direction (diamonds) and speed (circles) of starved *D. discoideum* in a gradient of cAMP. The gradient value can be read on the lower x-axis, and the corresponding midpoint concentration on the upper x-axis. In the region where the cells are chemotactic (gray region), there are roughly 100 receptors more occupied at the front of the cell than at the back, out of a total of about 50 000 receptors. Figure and numbers taken from [109].

In steady-state, the characteristic length of the problem is  $\lambda = \sqrt{D_m/k_{-1}}$  [85]. If we approximate the cell by a cylinder, with a production of the diffusing species restricted to one end of the cylinder, about 95% of the molecules are localized within  $3\lambda$  from the source [85]. A typical value for the degradation rate of molecules in the cell is  $k_{-1} = 1 \text{ s}^{-1}$  [85]. Having a uniform profile of concentration then implies to have  $\lambda \sim L$ , where  $L$  is the length of the cell. A cell being roughly  $10 \mu\text{m}$  large, this means that the diffusion coefficient  $D_m$  should be of order  $100 \mu\text{m}^2/\text{s}$ . The steady-state profile of concentration  $c(x)$  is shown on figure 2.3 for different values of the diffusion coefficient  $D_m$ . Depending on the models, putative candidates for the diffusing species are cAMP, cGMP,  $\text{Ca}^{2+}$ , heterotrimeric G-protein subunits, small G-proteins or inositol phosphates, that all have  $D_m \sim 100 \mu\text{m}^2/\text{s}$ .

In the following paragraphs, we will look at different simple models used to explain directional sensing [73, 77, 112, 75, 39, 91, 67, 70, 68]. When summarizing these models, we will follow the classification introduced by Iglesias and Levchenko in [47] to distinguish between two kinds of description: the ones that use bistable dynamics and others. There also exists more realistic and biologically oriented models, that try to incorporate as many known or putative biochemical reactions as possible at the price of an increasing complexity [106, 107, 72]. In particular, Meier-Schellersheim et al. developed in [72] a new software called Simmune (<http://www.simmune.org>), that allows users to enter their own reaction network, and simulates the network for them. This descriptive approach was successful in predicting two unreported patterns of changes in the concentration and location of PI3K and PTEN. Because of its high degree of detail however, and its many assumptions on existence of biochemical components, it is hard to extract the fundamental characteristics of this model, which is why it will not be reviewed here. It would be interesting to reduce the model of Meier-Schellersheim



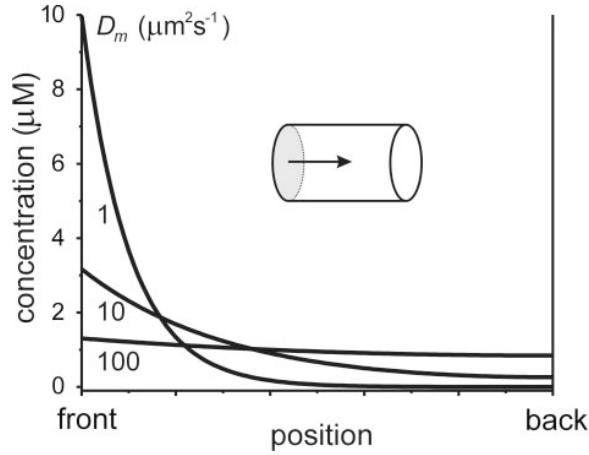


Figure 2.3: A cell is approximated as a cylinder of length  $L = 10 \mu\text{m}$ . Production of the diffusing species occurs on one of the sides of the cylinder (in gray on the figure), with a constant rate  $k_p = 1 \mu\text{Ms}^{-1}$ . Degradation occurs everywhere uniformly with a rate  $k_{-1} = 1 \text{ s}^{-1}$ . The steady-state profile of concentration  $c(x)$  is shown for different values of the diffusion coefficient  $D_m$ . For the concentration profile to be uniform within the cell, we need  $\lambda = \sqrt{D_m/k_{-1}} \sim L$ . Figure and numbers taken from [85].

et al. to a simpler one, or to analyse it using network analysis tools [7].

Before summarizing the simple models mentioned above, and because bistable dynamics play such an important role in many of them (as well as in our model), we will devote a first section to explaining what bistable dynamics are.

### 2.1.1 Bistable systems in a nutshell

We base ourselves on the first chapter of Mikhailov's book, *Foundations of Synergetics, I - Distributed Active Systems* (Springer, 1994) [74]. Consider an extended one-dimensional chemical system, where the concentration  $p(x, t)$  of a species  $P$  is governed by a reaction-diffusion equation:

$$\frac{\partial p}{\partial t} = f(p) + D \frac{\partial^2 p}{\partial x^2} \quad (2.2)$$

In this equation,  $D$  is the diffusion coefficient of the species  $P$  and  $f(p)$  contains the information about the reactions that  $P$  undergoes. Let us now look for a propagating solution to this equation:

$$p(x, t) = p(x - ct) = p(\xi) \quad (2.3)$$

where  $c$  is the velocity of propagation and  $\xi = x - ct$  is our new variable. Then the above reaction-diffusion equation is equivalent to:

$$-c \frac{dp}{d\xi} = f(p) + D \frac{d^2 p}{d\xi^2} \quad (2.4)$$

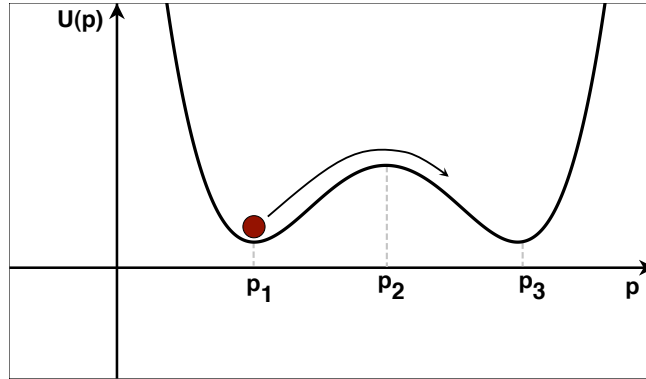


Figure 2.4: Example of a potential  $U(p)$  having two local minima at  $p_1$  and  $p_3$ , and one local maximum at  $p_2$ . If a particle (shown in red) is at  $p_1$  and that a strong enough perturbation is applied to it, it can overcome the potential barrier and go to  $p_3$ .

Let us rewrite this equation as:

$$D \frac{d^2 p}{d\xi^2} = -c \frac{dp}{d\xi} - f(p) \quad (2.5)$$

Forgetting about our initial problem of the evolution of the concentration of a species  $P$  in a reaction-diffusion system, we see that this last equation can be understood as the equation of motion of a particle of mass  $D$ . The position of the particle would be denoted by  $p$ , while time would be called  $\xi$ . The forces acting on the particle would be a friction force with a constant friction coefficient  $c$ , and an external force  $f(p)$ . Now, assume that  $f(p)$  derives from a potential  $U(p)$ , that has two local minima at  $p_1$  and  $p_3$  and one local maximum at  $p_2$  with  $p_1 < p_2 < p_3$ . Such a potential is shown on figure 2.4. At stable equilibrium, the mass will be either in  $p_1$  or in  $p_3$  ( $p_2$  being an unstable equilibrium position). Under the action of an external perturbation on the particle, the system could go from one of these stable positions to the other. For this to happen, the perturbation has to be sufficiently large to overcome both the friction on the particle and the potential barrier.

Let us now go back to our original problem, and still consider a potential  $U(p)$  with two minima. What we have just seen is that the concentration can have two stable values,  $p_1$  and  $p_3$ . A perturbation can drive the concentration  $p$  of the species  $P$  from one stable state to the other. This perturbation spreads as a wave, called a trigger wave, travelling with a velocity  $c$ . What is the velocity  $c$  of this trigger wave? It depends on the function  $f(p)$ . One particular case where an analytical result for  $c$  can be obtained is when  $f(p)$  is a cubic polynomial [74]:

$$f(p) = -p^3 + \alpha p^2 + \beta p + \gamma = -(p - p_1)(p - p_2)(p - p_3) \quad (2.6)$$

It can then be shown that:

$$c = \frac{p_1 + p_3 - 2p_2}{2} \quad (2.7)$$

In other words, if  $(p_1 + p_3) > 2p_2$ , the wave velocity is positive and a sufficiently big perturbation will lead to a transition from  $p_1$  to  $p_3$  (or the perturbation will decay if the system is already in the state  $p_3$ ). In the opposite case, the transition will be from  $p_3$  to  $p_1$  (or will decay if the system is already in the state  $p_1$ ).

In the more general case where nothing is assumed on the particular shape of  $f$  except that it has three zeros at  $p_1 < p_2 < p_3$ , with  $p_1$  and  $p_3$  being the stable equilibrium positions of the system, it can be shown that the trigger wave velocity  $c$  is proportional to the integral  $J$  defined as:

$$J = \int_{p_1}^{p_3} f(p) dp \quad (2.8)$$

and  $c$  is of the same sign as  $J$ , so that if  $J > 0$ , then  $c > 0$  and domains of  $p_3$  will grow, while domains of  $p_1$  will grow if  $J$  is negative.

For more information on bistable systems, the reader is referred to [74].

### 2.1.2 Bistable dynamics in directional sensing - general idea

How can we use the formalism of bistable dynamics to model directional sensing? The general idea is to have a chemical scheme following bistable kinetics, such as [47]:

$$\frac{dx}{dt} = f(x) = -ax + s \frac{x^2 + b}{x^2 + c} \quad (2.9)$$

where  $x$  represents the concentration of a species  $X$ , and where  $s$  is the external stimulus. Degradation of  $X$  occurs at rate  $a$ , the denominator of the fraction allows for saturation of the production of  $X$  and the numerator accounts for autocatalytic production of  $X$  (usually arising through a positive feedback loop). The function  $f(x)$  and the potential  $U(x)$  from which it derives are sketched for different values of the external stimulus  $s$  on figure 2.5a. Depending on the relative values of  $a$ ,  $b$ ,  $c$  and  $s$ , the system can have one or two stable fixed points (where  $f(x) = 0$  and  $f'(x) < 0$ , corresponding to a local minimum of  $U$ ). In theory, it is possible to calculate analytically where these fixed points are. However, this involves solving a cubic equation, whose solution is not straightforwardly interpretable. For this reason, we restrict ourselves to the particular example used by Iglesias and Levchenko in [47],  $a = 2$ ,  $b = 1$  and  $c = 11$ . Then, bistability occurs for  $s = 12$  (green curve). For  $s = 11$  (blue curve), only one fixed point exists, at a low value of  $x$ . On the contrary, for  $s = 13$  (red curve), only the high fixed point exists. If  $s$  varies along the cell such that at the front of the cell only the high fixed point exists, and at the back of the cell only the low fixed point exists, breaking of symmetry can occur. However, if this were the only mechanism, symmetry breaking would happen only in a very narrow range of gradients, for which the midpoint concentration is around  $s = 12$ .

Because directional sensing is efficient over a wide range of midpoint concentrations, a second species  $Y$  is usually assumed, which inhibits the effect of the activator  $X$ . The inhibitor  $Y$  can be either produced from  $X$  or from the stimulus directly. Its diffusion coefficient is big enough for the concentration of  $Y$  to be uniform all over the cell at any moment. When the cell is placed in a gradient, both the concentrations of  $X$  and  $Y$  increase. Because  $Y$  diffuses in the cytosol of the cell though, its concentration is averaged out. At the front of the cell, there is more activator than inhibitor, whereas at the back of the cell, the situation is opposite. As a result, the response is inhibited at the back but remains at the front, leading to an amplified asymmetrical response. The difference between the models essentially comes from the manner in which  $X$  and  $Y$  interact.

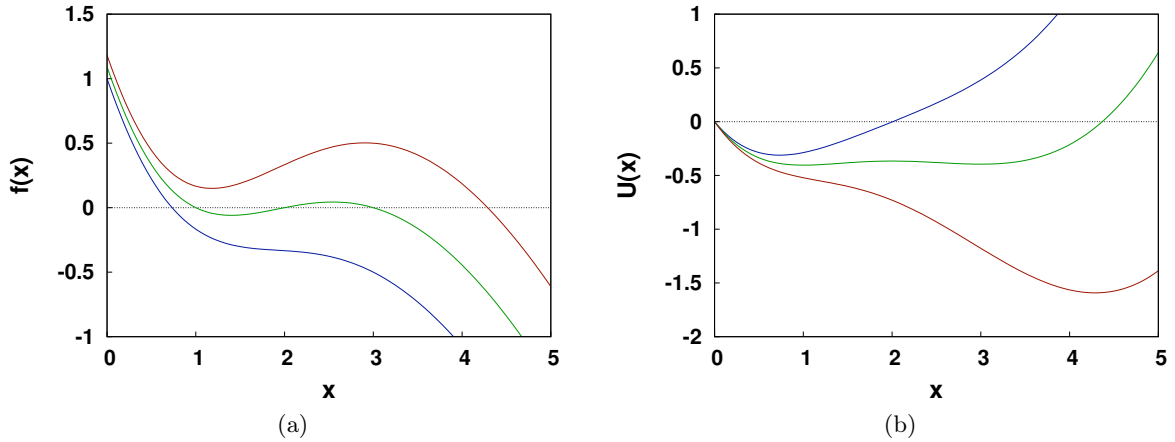


Figure 2.5: Plot of (a)  $f(x)$  and (b) the corresponding potential  $U(x)$  for  $a = 2$ ,  $b = 1$ ,  $c = 11$  and different values of  $s$ . For  $s = 11$  (blue curve), only one steady state exists, at a low value of  $x$ . For  $s = 12$ , the system is bistable (green curve). For  $s = 13$ , the lower steady state is lost (red curve). If  $s$  varies along the cell (as is the case in a gradient), spatial patterning can occur. Figures adapted from [47].

### 2.1.3 Model overview

As a quick overview, the main properties of each model are summarized in table 2.1 for the bistable models and in table 2.2 for the non-bistable ones. We evaluate each model's ability to produce an asymmetric response in response to a shallow ( $\sim 1\%$ ) gradient, and note if the mechanism for directional sensing is reversible. We also mention the ability of the models to reproduce adaptation in a uniform chemoattractant concentration. The biological basis of each model is given, and we comment on the model's performance.

### 2.1.4 Turing instability in directional sensing [73]

One of the first models of chemotaxis was proposed by Meinhardt in 1999 [73]. It was meant to be a very general model, aiming at presenting more a generic (theoretical) scheme that could lead to directional sensing, rather than being a realistic (biological) mechanism. At the core of the model are two species, a local activator  $A$  and a long-range inhibitor  $B$  (of concentration  $a(x, t)$  and  $b(x, t)$  respectively). The activator has autocatalytic dynamics, with a local concentration that depends on the local concentration of the external stimulus. The inhibitor is assumed to be uniformly distributed inside the cell, and takes for value at each time the average concentration of  $a(x, t)$ , that we will write  $\bar{a}(t)$ . This amounts to saying that  $B$  is a rapidly diffusing species produced from  $A$ . "Rapidly diffusing" here means that the diffusion coefficient of  $B$  should be big enough so that at each point in time, the amount of  $B$  inside the cell is uniform. Because of the interaction between  $A$  and  $B$ , the only place where the activator is not inhibited is the front of the cell. The way that the model was implemented by Meinhardt, a cell was able to polarize in response to gradients of 1% across

## 2.1. Models of directional sensing

Model	Asym.	Rev.	Adapt.	Biol.	Comments
Meinhardt [73]	✓	✓	✓	✗	Generic mechanism. Spatial patterns do not remain even if the stimulus keeps being applied, contrarily to experiments.
Narang et al. [77]	✓	✗	✓	PI cycle	The intensity of the response is independent of the stimulus. Adaptation happens at the receptor level in the model, which is not the case in <i>D. discoideum</i> .
Subramanian and Narang [112]	✓	✓	✓	✗	Generic adaptation mechanism coupled to the PI cycle of [77].
Mori et al. [75]	✓	✓	✗	Rho-GTPase	The response is maintained even after the stimulus is removed, which is not the case in <i>D. discoideum</i> .
Gamba et al. [39]	✓	✓	✓	PI3K/PTEN cycle	Noise-driven translocation. In a uniform concentration of chemoattractant, random patches of translocation occur. In a gradient, the first uniform translocation is not seen.
Postma and Van Haastert [85]	✓	✗	✓	✗	The system gets locked.
Beta et al. [8]	✓	✓	✓	✗	Noise-driven bistable system. The intensity of the response is roughly independent of the stimulus.

Table 2.1: Comparison of the bistable models of directional sensing. We review the models’ abilities to produce an asymmetric response in a shallow gradient of chemoattractant (“Asym.”), and note if the mechanism is reversible (“Rev.”). Adaptation in a uniform concentration of chemoattractant is shown in column “Adapt.”. If the authors explicitly base themselves on a biochemical pathway, we mention it in column “Biol.”. Last, we comment on the results of the model and give the main disagreements with experiments, if they exist.

Model	Asym.	Rev.	Adapt.	Biol.	Comments
Postma and Van Haastert [85]	✗	✓	✓	✗	Not enough amplification at shallow gradients.
Rappel et al. [91]	✓	✗	✓	cGMP	Does not allow for two fronts at the same time, disproved in [52].
Levchenko and Iglesias [67]	✓	✓	✓	PI3K/PTEN	The inhibitor was supposed to be PTEN and to be slightly more localized at the front of the cell, disproved in [35].
Ma et al. [70]	✓	✓	✓	PI3K/PTEN	The model assumes that binding sites for PI3K (resp. PTEN) are created (resp. destroyed) when a receptor is locally activated. Experiments later showed that this could actually be the case through a feedback loop PI3K/actin [96] and the hydrolysis of PIP2 (binding site of PTEN) by PLC [64].
Levine et al. [68]	✓	✓	✓	Heterotrimeric G-protein	Assumes the same production rate of activator and inhibitor – quite a strong constraint. Achieved by supposing that the activator is $G_\alpha$ and the inhibitor $G_{\beta\gamma}$ , which are supposed to be unbound at the front, and bound at the back of the cell, disproved in [132].

Table 2.2: Comparison of non bistable models of directional sensing. Columns as in table 2.1.

the cell membrane<sup>4</sup>. One problem encountered though was that the cell would not be able to follow a change in gradient direction. To solve this problem, Meinhardt postulated several possible mechanisms, only one of which could probably be relevant for *D. discoideum*. He hypothesizes the existence of a second inhibitor ( $C$ , of concentration  $c(x, t)$ ), that acts locally and has a longer time constant than the activator. The equations used by Meinhardt are:

$$\frac{\partial a(x, t)}{\partial t} = s(x, t) \frac{a^2(x, t)/b(t) + b_a}{(s_c + c(x, t))(1 + s_a a^2(x, t))} - r_a a(x, t) \quad (2.10)$$

$$\frac{\partial b(t)}{\partial t} = \bar{a}(t) - r_b b(t) \quad (2.11)$$

$$\frac{\partial c(x, t)}{\partial t} = b_c a(x, t) - r_c c(x, t) \quad (2.12)$$

where  $s(x, t)$  is the concentration of the external signal  $S$ , and all small letters with indices are reaction rates. Looking at these equations, we can qualitatively understand why the model would lock into one direction if the third variable  $C$  were not introduced. Indeed,  $A$  exhibits bistable dynamics. Applying a gradient corresponds to applying a perturbation that destabilizes the system. The value of  $A$  goes to one fixed point in the front half of the cell and to the other fixed point in the back half of the cell. Once the system is in this configuration, it is stable, and the cell can only reverse its front and back if a big enough perturbation is applied. If one first applies a gradient of a given value for a time long enough so that the cell can show a polarized distribution of  $A$ , and then reverses the gradient direction (keeping the same absolute value for the gradient), the perturbation is not big enough to reverse the polarization of the cell<sup>5</sup>. This problem is solved when the third variable  $C$  is introduced. However, the polarization of  $A$  then disappears even if the external gradient keeps being applied, in contradiction with experiments on *D. discoideum* [82].

### 2.1.5 A model based on the phosphoinositide cycle [77, 112]

#### A first version [77]

The Meinhardt model represents a generic way to achieve directional sensing, but the putative biological mechanism thought of by Meinhardt ( $\text{Ca}^{2+}$  induced release of  $\text{Ca}^{2+}$ ) was not consistent with experiments. In 2001, Narang et al. [77] proposed a more biological model based on receptor desensitization and on an actual metabolic cycle in *D. discoideum*, the phosphoinositide cycle. The aim of the model was to explain the experimental observation that, apparently, the amount of translocation of PH-domain proteins depended neither on the absolute value of the gradient used [82], nor on the midpoint concentration of chemoattractant [28].

As in Meinhardt's approach, autocatalysis is an essential part of Narang et al.'s model. In the model scheme, three pools of components are described: the membrane phosphoinositides ( $P$ ), the cytosolic inositol and its phosphates ( $I$ ), and phosphoinositides in the endoplasmic reticulum ( $P_s$ ). The total concentration of phosphoinositides ( $P + P_s$  inside the whole cell) is constant. Binding of cAMP to cAR1 leads to the formation of  $P$  and  $I$ , and a positive feedback

---

<sup>4</sup>Here, and everywhere in the remainder of this chapter, we will say that a cell is in a *polarized* state if it shows an asymmetric distribution of a given chemical  $X$ . This is not the usual definition of polarization, as given by Devreotes and Janetopoulos in [24].

<sup>5</sup>Changing the translocation is possible if the gradient direction is switched and at the same time the gradient value is increased though.

loop on  $P$  is assumed, that leads to autocatalytic behavior and the creation of a leading edge. This leading edge would spread by diffusion weren't it for the action of  $I$ , which diffuses in the cytosol and plays the role of an inhibitor. At the back of the cell, the concentration of  $I$  promotes the transfer of membrane phosphoinositides from the plasma membrane to the endoplasmic reticulum, reducing the amount of  $P$  in the membrane, and increasing the amount of  $P_s$  at the back. This model exhibits bistable behavior and both the values of its fixed points, as well as the overall shape of the polarization pattern, do not depend on the gradient used. They rely only on the kinetic parameters and diffusion coefficients of the three variables. This satisfies the aim that the authors wanted to achieve, and the experimental observations from [82, 28] are reproduced. The model also describes adaptation in a uniform concentration of cAMP, although they assume that adaptation happens at the receptor level, which was disproven by Janetopoulos et al. [51]. One issue of the model is that it is not able to describe the change in the polarization direction as the gradient direction is changed. In the same way as Meinhardt's model, the Narang et al. model gets locked in a given configuration. To remedy to this problem and take into account that adaptation occurs downstream of the receptor level, Subramanian and Narang modified this initial model in a subsequent article, published in 2004 [112].

### A second version [112]

In this modification of the original model, Subramanian and Narang took into account the fact that adaptation occurred downstream of the receptor level. They therefore included an adaptation module in their new model. Because the molecular mechanism of adaptation is unknown, Subramanian and Narang postulated a generic form for the adaptation dynamics and coupled the adaptation module to the Narang et al. model. Doing so, the model can reproduce the translocation of phosphoinositides to the leading edge of the cell, as well as adaptation in a uniform concentration of chemoattractant. Contrarily to the first model, the geometry of the phosphoinositide distribution depends on the chemoattractant profile. For a chemoattractant gradient whose midpoint value is small or large, the translocation of phosphoinositides is essentially uniform (only one stable fixed point exists). Intermediate midpoint values lead to a polarized translocation (two stable fixed points exist, the system is bistable), and the size of the translocation goes up with the midpoint value of the chemoattractant. Three other experimental results were reproduced, that were not reproduced by the first model. The first one is the ability of a cell to reverse its polarization (*i.e.* the translocation) when the gradient direction is changed. In other words, the system is not locked anymore in its polarized state. This is made possible by the adaptation module. Subramanian and Narang also reproduced an experimental observation from Devreotes and Janetopoulos in [24]. Devreotes and Janetopoulos showed that, if cells are already chemotaxing towards a gradient source and that a second, competing gradient is turned on, some of the cells turn around toward the new gradient while some others continue their way towards the first gradient. Subramanian and Narang explain this variability in cellular behavior by pointing out that, according to their model, the ability of a cell to be influenced by a second gradient depends on the degree of prepolarization of the cell. The strength of the signal required to create a peak of membrane phosphoinositides ( $P$ ) in the new gradient direction increases as the prepolarization is bigger. The last result that the model can explain is spontaneous polarization. Assuming that the cells are in a uniform concentration of chemoattractant, and considering that this concentration fluctuates (because of thermal noise), the authors show that a noisy ligand concentration is enough to trigger



spontaneous polarization of the cell in their model.

### 2.1.6 Wave-pinning in a bistable system

The model proposed by Mori et al. [75] is interesting by its simplicity. The authors want to model polarization, and assume that it comes from an exchange between a membrane and a cytosolic form of a signaling protein. Their model is based on the conversion between an active membrane form of the protein ( $A$ ) and its inactive cytosolic counterpart ( $B$ ) (see figure 2.6). The total concentration of  $A$  and  $B$  is fixed for a given cell, which reminds of the model of Narang et al. [77]. The conversion of  $A$  into  $B$  is based on bistable dynamics, and the evolution of the concentration  $a$  and  $b$  of species  $A$  and  $B$  is given by:

$$\frac{\partial a}{\partial t} = D_A \frac{\partial^2 a}{\partial x^2} + f(a, b) \quad (2.13)$$

$$\frac{\partial b}{\partial t} = D_B \frac{\partial^2 b}{\partial x^2} - f(a, b) \quad (2.14)$$

where  $f(a, b) = b(k_0 + \frac{\gamma a^2}{K^2 + a^2}) - \delta a$  is the interaction function that leads to bistable kinetics ( $k_0$ ,  $K$ ,  $\delta$  are constants),  $D_A$  is the diffusion coefficient of  $A$  on the membrane and  $D_B$  is the diffusion coefficient of  $B$  in the cytosol ( $D_A \ll D_B$ ). Cytosolic diffusion of  $B$  is fast enough so that the concentration of  $B$  in the cytosol is essentially uniform at all times. The response is characterized by the localization of  $A$  on the membrane. The system, being bistable, needs a perturbation to get from its initial state to its final state. The perturbation is given by the gradient of chemoattractant. As a result, the cell polarizes in the direction of the gradient, *i.e.*  $A$  accumulates at the front of the cell. Polarization occurs through the propagation of a wavefront on the membrane, a typical result of bistable dynamics. The propagation stops once the region of  $A$  reaches a given size, depending only on the total amount of  $A$  and  $B$  inside the cell, not on the external stimulus (which also reminds of [77]). This is what the authors term "wave-pinning". In this model, the cell polarizes in response to a uniform signal subject to noise-induced fluctuations (which reminds of [112]). The system is also able to reverse its polarity if the direction of the gradient is changed. Another prediction is that the polarization remains even if the signal is removed. This is the case for neutrophils, but not for *D. discoideum*. The putative biochemical basis for such a model are molecules of the Rho-GTPase family, that are in their active GTP form on the membrane and in their GDP-inactive form in the cytosol. In *D. discoideum* however, the polarization is already present upstream of the activation of Rho-GTPases.

### 2.1.7 Directional sensing viewed as a phase separation [39]

Gamba et al. [39] used a reaction-diffusion lattice model that describes PI3K and PTEN enzymatic activity, recruitment to the plasma membrane, and diffusion of their phosphoinositide products. The big difference between [39] and other models of directional sensing is that Gamba et al. have performed stochastic simulations of the reaction and diffusion processes, using a tessellation of more than 10,000 sites to represent the cell's membrane. This was made possible at the expense of a considerable computational effort: simulations were performed on a 99 dual-processor nodes Beowulf cluster [2800 MHz Athlon processors with 4 Gbyte of memory each]. The reactions and diffusion processes that were simulated were:

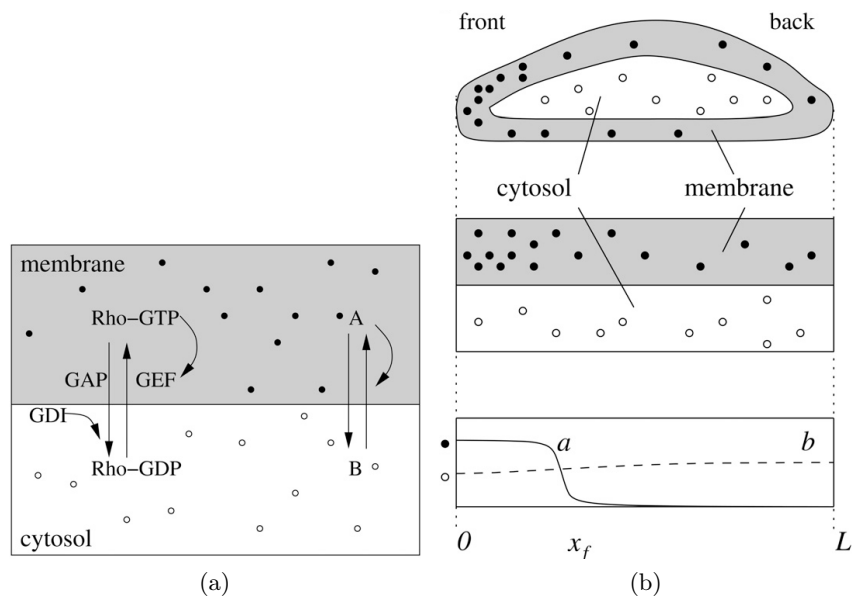
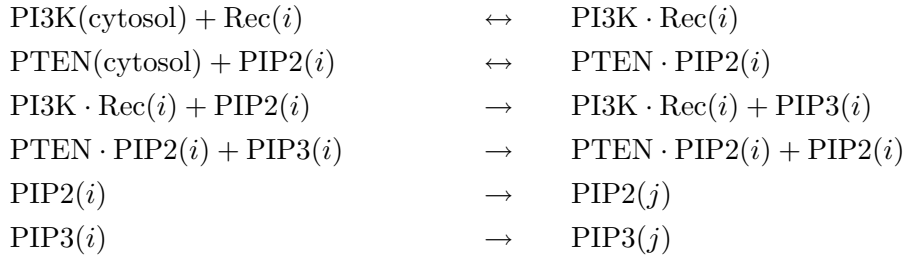


Figure 2.6: The wave-pinning model of Mori et al. [75]. (a) Model of the membrane translocation cycle of a Rho-GTPase by the  $A - B$  reaction diffusion system. (b) Side-view of a cell. Active Rho proteins are shown by the full circles, their inactive version is shown by the empty circles. The system polarizes, with active proteins concentrating on a region of size  $x_f$ . The axis  $0 < x < L$  represents a cell diameter. Figures taken from [75].



The first four equations show reactions, the two last ones describe diffusion. In these equations,  $i$  represents a membrane site and  $j$  is one of its nearest neighbors.  $\text{Rec}(i)$  is the receptor at site ( $i$ ). The probability of performing a reaction on a given site is proportional to the reaction rates and local reactant concentrations. One essential point to bring forward is that the authors are able to reduce their model to a bistable model with molecular noise. In the absence of stimulus, the amount of proteins on the membrane is at equilibrium. This equilibrium point becomes metastable when a gradient is applied, and the transition to the stable state is driven by molecular noise, underlying the importance of the stochastic aspect of the model. At the front of the cell, the stable point is one where PIP3 is high, whereas at the back of the cell, the stable point is such that PIP2 is high. As the gradient is turned on, several patches of PIP3 appear at different locations on the membrane, that either shrink or coalesce, depending on the outer gradient of cAMP and on their positions on the cell membrane. In the end, a phase separation occurs between a region with high concentration of PIP3 and a region with a low concentration of PIP3. This model is very interesting because of its stochastic component, and is conceptually very close to the one that we proposed in [8]. It is able to reproduce polarization in the presence of a gradient, but – because of stochasticity – cells are unable to polarize in a consistent direction when the receptor activation is too low. In other words, there is no directional response under a certain stimulus threshold. Thanks to the constant molecular noise, the system is not frozen in a given state and can adapt to new gradient directions. In the case of a uniform stimulus, the initial uniform state decays to a polarized state, accounting for self-polarization. From their article, it seems that the model of Gamba et al. does not account for the initial uniform translocation seen when a cell is placed in a gradient of chemoattractant.

### 2.1.8 The diffusion-translocation model [85]

Postma and Van Haastert proposed in [85] a model of directional sensing where there is no inhibitor. The model is implemented in the following way (see also figure 2.7):

1. before receptor stimulation, a small number of inactive effector molecules is bound to the membrane;
2. upon receptor stimulation, the membrane-bound effector molecules are activated, leading to the production of phospholipids (that are the second-messenger molecules);
3. because more phospholipids are on the membrane, more effector molecules can translocate from the molecule to the membrane;
4. more effector molecules are therefore available on the membrane and can be activated by the external stimulus, leading to the production of even more phospholipids.

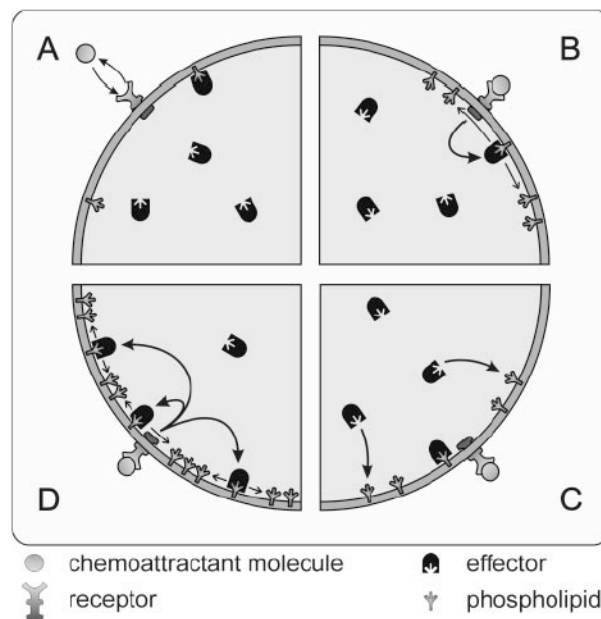


Figure 2.7: The diffusion-translocation model of Postma and Van Haastert [85]. The model relies on a positive feedback loop, whose steps are depicted here. Few inactive effectors are bound to the membrane until (A) a receptor is activated, (B) which activates the membrane bound effector and leads to the production of second-messenger molecules (the phospholipid). (C) Because the phospholipid concentration increases, more effector can translocate from the cytosol to the membrane and (D) this leads to a signal amplification since the receptor can now activate more effectors, leading to more phospholipids produced. Figure taken from [85].

There are therefore two species that can diffuse, an effector that is identified to a PH-domain protein and diffuses in the cytosol, and a phospholipid to which the PH-domain protein can bind, and diffuses on the membrane. The phospholipid promotes its own production by allowing more effector molecules to sit on the membrane, therefore enhancing the number of effector molecules synthesizing phospholipids (autocatalysis). The exact behavior of the model depends on the form assumed for  $P(x)$ , the production rate of the second messenger. At first, the authors assume a linear amplification of the receptor occupancy. The steady-state distribution of the effector molecules on the membrane is then asymmetric. However, the asymmetry is reduced at low average background concentrations. The authors then propose to increase by a factor 5 or 10 the proportionality constant between  $P(x)$  and the receptor occupancy to get a better asymmetry at low background concentrations. However, this deteriorates the response at high background concentrations. To enhance the model's ability to respond to shallow gradients (1% instead of their typical  $\sim 10\%$  example), the authors also point out the possibility to incorporate a nonlinearity in  $P(x)$ . This nonlinearity is however not ideal as it freezes the system: the effector and activator molecules are all at the existing leading edge of the cell, and the cell cannot respond to a change in the gradient direction.

### 2.1.9 The first-hit model

Rappel et al. proposed in [91] what came to be known as the "first-hit" model. The authors argued that what was important for gradient sensing was the temporal component of the gradient. Indeed, it is experimentally impossible to apply a gradient instantaneously, and the cell always sees a temporal gradient before it sees a stable spatial gradient. The model assumes that the membrane receptor of cAMP, cAR1, can be in three different states: quiescent, activated or inhibited. Transitions from quiescent to activated are triggered by the binding of cAMP to the receptor. When the receptors are activated, they trigger the production of an intracellular chemical messenger, hypothesized to be cGMP. The cGMP then diffuses in the cytosol and turns the quiescent receptors to their inhibited state. The inhibited receptors become quiescent at a constant chemical rate. The mechanism of the model is therefore the following: as cAMP diffuses from a micropipette, a gradient establishes, and the part of the cell closest to the pipette (the front) gets activated first, leading to the production of cGMP. There is then a competition between the diffusion of cAMP outside of the cell and the diffusion of cGMP inside the cell. If on the length scales involved, the diffusion of cGMP inside the cell is faster than the diffusion of cAMP outside of the cell, the first chemical to reach the back of the cell will be cGMP. As a result, the quiescent receptors at the back of the cell will be inhibited, and an asymmetry in the active receptors will be created. A schematic of the model can be found on figure 2.8. The drawback of the model is that it can not reproduce the behavior of a cell to which two simultaneous gradients are applied. Indeed, in this model, at most one front of the cell can exist at a time. However, experiments conducted later by Janetopoulos et al. [52] showed that two fronts of PH-domain proteins could exist, if cAMP was diffusing out of two micropipettes located at two diametrically opposed positions (see figure 2.9).

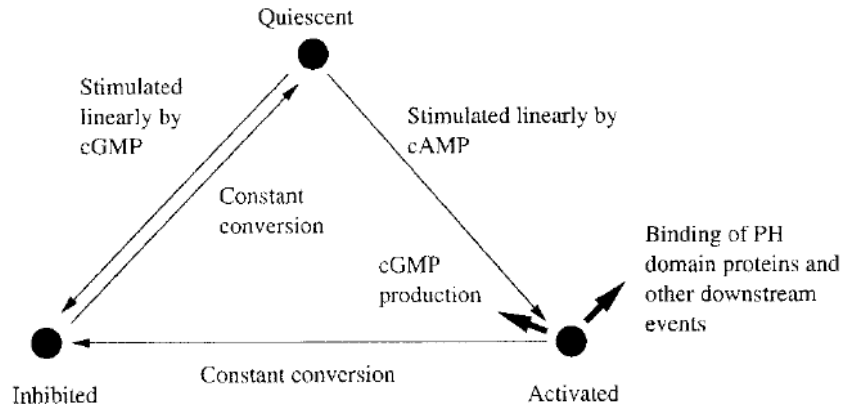


Figure 2.8: The first hit model of Rappel et al. [91]. Before stimulation, the receptors are in a quiescent state. When stimulated with cAMP, the receptors get activated, leading to the production of internal cGMP. Internal cGMP diffuses in the cytosol of the cell and inhibits the quiescent receptors, pre-empting activation in the back of the cell, where the external cAMP arrives more slowly. Figure taken from [91].

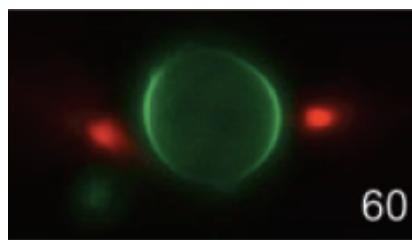


Figure 2.9: Two micropipettes filled with cAMP (in red) are brought close to a cell marked with CRAC-GFP (green). If the gradients of cAMP created on both sides are the same, CRAC translocates to both sides of the cell, disproving the first-hit model prediction. Figure taken from [52].

### 2.1.10 Local excitation, global inhibition (LEGI) [67, 70]

#### A first version [67]

In 2002, Levchenko and Iglesias [67] proposed a mechanism that would account both for the asymmetry and the reversibility of the directional sensing process. Their idea was to have two species, one local activator called  $A$  and one global inhibitor  $I$  that diffuses in the cytosol. The diffusion of  $I$  should be fast enough compared to its production so that the level of  $I$  is uniform in the cytosol. More precisely, calling  $S$  the external concentration of chemoattractant, the equations read:

$$\frac{dA}{dt} = k_a S - k_{-a} A \quad (2.15)$$

$$\frac{\partial I}{\partial t} = k_i S - k_{-i} I + D \nabla^2 I \quad (2.16)$$

where  $k_a$ ,  $k_i$  are the production rates of  $A$  and  $I$ ,  $k_{-a}$ ,  $k_{-i}$  are their degradation rates, and  $D$  is the diffusion coefficient of the inhibitor in the cytosol. In steady-state, the concentration of  $A$  is therefore locally reflecting the external signal  $S$  while the concentration of  $I$  should be uniform inside the cell and reflect the averaged signal concentration. The activator promotes the transition from a quiescent state  $R$  of a protein to its activated state  $R^*$ , while the inhibitor has the opposite effect. The output from the model is the concentration of  $R^*$  on the membrane of the cell, or an effector downstream of  $R^*$ . The aim of the model is to reproduce two experimentally observed behaviors:

- in presence of a spatially uniform signal  $S$ , there is a transient uniform production of  $R^*$  that disappears after a given time (time depending on the rate constants chosen in the model);
- if the external signal is a gradient, there should be an internal gradient of  $R^*$  produced, that amplifies the external gradient.

These two behaviors can be correctly reproduced by the model. If the equation for the production of  $R^*$  was just

$$\frac{dR^*}{dt} = k_1 A R - k_{-1} I R^* \quad (2.17)$$

we would have a steady state where  $R^* = k_1 R_{\text{tot}} \frac{A/I}{k_1 + k_{-1} A/I}$ , assuming that the local concentration  $R_{\text{tot}} = R + R^*$  is conserved. This mechanism does not amplify the external gradient however. To get a better amplification, Levchenko and Iglesias assumed a couple of feedback loops. The way the putative biochemical pathway is implemented, the response still depends on the local ratio of activator to inhibitor. When this ratio is high (typically at the front of the cell), the concentration of  $R^*$  is high, whereas the concentration of  $R^*$  is low when  $A/I$  is low (at the back of the cell). In other words, there is a high translocation of  $R^*$  at the front of the cell and a low (or no) translocation of  $R^*$  at the back of the cell. The amount of amplification of the external signal (*i.e.* what a "high" and "low" concentration of  $R^*$  quantitatively means) is strongly dependent on the rate constants chosen for the simulation. One major advantage of this model over the Meinhardt model is that the translocation can switch direction if the gradient direction is switched. A problem of the LEGI model is the identification of the activator and the inhibitor that the authors made with biological species. Levchenko and Iglesias proposed that the activator was PI3K and the inhibitor PTEN. According to the LEGI, PTEN

should have a roughly uniform concentration inside the cell, with a slight localization at the front of the cell. Unfortunately, Funamoto et al. [35] showed that PTEN localizes at the back of the cell. To reproduce this experimental fact, Ma et al. suggested a new version of LEGI in [70].

### A second version [70]

The second version of the LEGI model contains two independent LEGI modules, one describing the accumulation of PI3K and the other one describing the accumulation of PTEN. In the PI3K module, activation of the receptors leads to more binding sites for PI3K. On the contrary, in the PTEN module, receptor activation destroys binding sites for PTEN. Therefore, a gradient of PI3K appears on the cell membrane, pointing in the same direction as the cAMP gradient. Similarly, a gradient of PTEN develops, pointing in the opposite direction of the gradient of cAMP. PI3K promotes the phosphorylation of PIP2 into PIP3 at the front, while the conversion of PIP3 to PIP2 is increased by PTEN at the back of the cell. This leads to a polarized distribution of PIP3, with an accumulation at the front of the cell. A schematic of the model is shown on figure 2.10

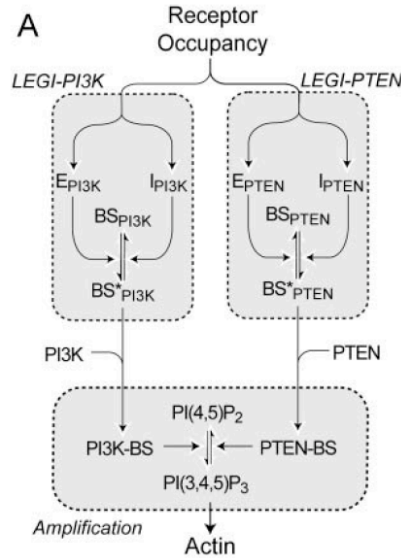


Figure 2.10: Receptor occupancy regulate two LEGI modules. The first LEGI module describes the kinetics of PI3K, the second one describes the kinetics of PTEN.  $E_\alpha$  is the membrane-bound activator of the species  $\alpha$ , while  $I_\alpha$  is the global inhibitor for species  $\alpha$  ( $I_\alpha$  diffuses freely in the cytosol).  $BS_\alpha$  is an inactive binding site for the species  $\alpha$ , and  $BS_\alpha^*$  is its activated version. Receptor activation promotes the production of binding sites for PI3K and the destruction of binding sites for PTEN. This leads to an accumulation of PIP3 at the front of the cell. Figure taken from [70].



### 2.1.11 The balanced inactivation model

Another approach proposed by Levine et al. [68] to model directional sensing is the following. They assume equal production rates for the activator and the inhibitor. The inhibitor can either be in its cytosolic form  $B$  or be bound to the membrane and is then called  $B_m$ . The activator is called  $A$ , and can react with the membrane-bound version of the inhibitor:

$$\frac{dA}{dt} = k_a S - k_{-a} A - k_i A B_m \quad \text{at the membrane} \quad (2.18)$$

$$\frac{\partial B_m}{\partial t} = k_b B - k_{-b} B_m - k_i A B_m \quad \text{at the membrane} \quad (2.19)$$

$$\frac{\partial B}{\partial t} = D \nabla^2 B \quad \text{in the cytosol} \quad (2.20)$$

At the membrane, the boundary condition is:

$$D \frac{\partial B}{\partial n} = k_a S - k_b B \quad (2.21)$$

for the outward pointing normal derivative of the cytosolic inhibitor  $B$ . In this case, the reporter is the activator  $A$ . The assumption of equal production rates for the activator and the inhibitor ensures that  $A$  remains only at the front of the cell; there is a clear spatial asymmetry of  $A$  when the cell is stimulated, and the behavior of the cell is spatially "switch-like". To compare this model with the LEGI model presented in section 2.1.10, we can note that, whereas the standard LEGI acts basically like a division, with a reporter concentration depending on the ratio between the activator and inhibitor concentrations, the balanced inactivation model acts like a subtraction between the activator and inhibitor levels, which explains the absence of activator at the back of the cell. One should note that the assumption of equal production rates of activator and inhibitor is a very strong one, and the authors assume this hypothesis to be met by identifying the activator with the  $G_\alpha$  subunit of the heterotrimeric G protein, while the role of the inhibitor would be played by the  $G_{\beta\gamma}$  subunit of the G protein. Indeed, it is known that the G protein dissociates when *D. discoideum* is stimulated with cAMP. The assumption is therefore that  $G_{\beta\gamma}$  reassociates to  $G_\alpha$  at the back of the cell during a gradient stimulus, whereas the G protein stays dissociated at the front of the cell. Unfortunately, this hypothesis is contradicted by experiments presented by Xu et al. in [132], where the authors use FRET to monitor the dissociation of the G protein as *D. discoideum* were put in a uniform concentration or a gradient of cAMP. In their article, Xu et al. show that the G protein stays in a dissociated state at the front and at the back of the cell when the cell is stimulated by a gradient of cAMP. The direct identification of activator and inhibitor with G protein subunits therefore seems risky. The proposed mechanism is interesting from a theoretical point of view, but finding two biochemical species produced at the exact same rate remains a serious challenge.

## 2.2 A bistable mechanism triggered by internal noise<sup>6</sup>

### 2.2.1 Motivation for a our model

The motivation for our model of directional sensing comes from two experimental facts. The first one is the robustness of chemotactic motion over three orders of magnitude in gradient steepness (between  $10^{-2}$  and  $10$  nM/ $\mu$ m). Within this interval, the chemotactic velocity is only weakly dependent on the gradient. Schematically, one can understand this graph as showing two behaviors: one "off" behavior, where the cell shows its basal motility and one "on" behavior, where the cell moves with a chemotactic velocity that depends very weakly on the gradient steepness. The off and on modes can be thought of as two stable fixed points of a bistable system. Our aim was to propose a bistable mechanism that would respond identically to gradients of different steepnesses. The second fact that we wanted to introduce was that the cell environment is by definition noisy. In our proposed mechanism, the intrinsic cell noise is used to drive the transition between the two stable fixed points of the bistable system. If there were no sources of noise in the cell, this model would not work and the cell would be stuck in one state or the other. It should also be mentioned that the model proposed is just a generic model, and that no particular biochemical constituents were identified. This can be considered as a drawback, but on the other hand, in several of the existing articles presenting a simple model for directional sensing, the identification of biochemical components is a conjecture, when not a guess, and does not bring much to our biological understanding of the cell. However, it is known that biological networks and chain reactions can be reduced to bistable systems, as shown in [2]. Of all the models described in the previous section, the ones that exhibited a constant response for gradients of different steepnesses were either unable to adapt to a change in the gradient direction [77], or the polarization would remain even after the gradient was removed [75], which is inconsistent with experiments. The non bistable models predict a response that gets stronger for increasing gradients. In my opinion, the most interesting model of chemotaxis is the one proposed by Gamba et al. in [39]. In their case, it is also the noise that drives the transition to a polarized state. The only feature that the model doesn't show is the initial transient uniform translocation of PIP3 on the membrane, that occurs when a cell is stimulated with either a gradient or a uniform concentration of cAMP. This is a feature that we would like to reproduce in our model.

### 2.2.2 The model

#### Basic idea

The idea behind the model is to have a reporter,  $P$ , whose concentration  $p$  obeys bistable dynamics and translocates to the front of the cell only when the cell is put in a gradient of cAMP. Here, the front of the cell designates as usual the half of the cell where the external cAMP concentration is maximal. Schematically, the two stable states of  $p$  should have values 1 and 0. When a gradient of cAMP is applied, the front of the cell should go to 1, while the back should stay at 0. The way we chose to implement this asymmetry was by having a trigger wave velocity changing sign at the middle of the cell: perturbations can then lead to the propagation of one state in the upper part of the cell, while they lead to the propagation of the other state in the lower part of the cell. How can we achieve such a behavior? We base

---

<sup>6</sup>This work was published as C. Beta, G. Amselem and E. Bodenschatz, *New Journal of Physics*, **10**, 083015 (2008). The article is reproduced at the end of the chapter.

our model on the well-known scheme of a localized activator and a global inhibitor. Where the ratio between the local activator and inhibitor concentrations is higher than a given threshold, the wave velocity is positive and state 1 propagates. Conversely, state 0 propagates where the ratio between the local activator and inhibitor concentrations is lower than the chosen threshold. To summarize, there are three parts in our model:

- a local activator, global inhibitor scheme;
- an intermediate species, called  $Q$  thereafter, comparing the local concentrations of activator and inhibitor;
- the reporter  $P$  that follows bistable dynamics and whose value depends on the value of  $Q$ .

These three parts are detailed in the following pages.

### Local activator, global inhibitor

We consider a one-dimensional cell (the extension to two dimensions is straightforward and is just computationally more demanding), where the activator  $A$  and the inhibitor  $B$  are produced locally proportionally to the concentration  $s$  of the external chemoattractant  $S$ , the inhibitor  $B$  diffusing in the cytosol while the activator  $A$  stays on the membrane. The equations are:

$$\frac{da}{dt} = k_a s - k_{-a} a + k_{+a} \quad (2.22)$$

$$\frac{\partial b}{\partial t} = k_b s - k_{-b} b + k_{+b} + D \nabla^2 b \quad (2.23)$$

In these equations,  $k_a$  and  $k_b$  are the rate constants for the production of  $A$  and  $B$  from  $S$ ,  $k_{-a}$  and  $k_{-b}$  are the degradation rates of  $A$  and  $B$  and we also account for self-production of  $A$  and  $B$  via the kinetic constants  $k_{+a}$  and  $k_{+b}$ . As the diffusion of  $B$  in the cytosol has the effect of averaging the external signal, a simplified way of writing the kinetic equation for the concentration  $b$  of the species  $B$  is to consider the spatial average  $\bar{s}$  of the concentration  $s$ :

$$\frac{db}{dt} = k_b \bar{s} - k_{-b} b + k_{+b} \quad (2.24)$$

Writing this assumes that the time needed for the homogenization of  $B$  inside the cell is smaller than the time constants related to the production and degradation rates of  $B$ . The stationary concentrations of  $A$  and  $B$  read:

$$a = \frac{k_a s + k_{+a}}{k_{-a}} \quad \text{and} \quad b = \frac{k_b \bar{s} + k_{+b}}{k_{-b}} \quad (2.25)$$

### Local comparison of activator and inhibitor concentrations

We introduce an intermediary species  $Q$  that is created by  $B$  and degraded by  $A$ , so that the evolution of its concentration  $q$  is given by:

$$\frac{dq}{dt} = k_q b - k_{-q} a q \quad (2.26)$$

Assuming that we are at equilibrium, we get for the steady state concentration of  $Q$ :

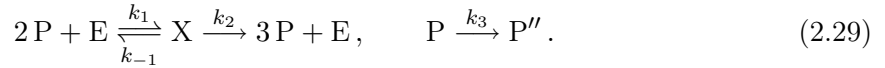
$$q = \frac{k_q}{k_{-q}} \frac{b}{a} \quad (2.27)$$

### Bistable kinetics

We now assume that there exists a species  $P$  that follows bistable kinetics. This can be achieved by postulating the following reaction-diffusion equation for  $p$ :

$$\frac{\partial p}{\partial t} = v \frac{p^2}{p^2 + K} - k_3 p + D_p \nabla^2 p \quad (2.28)$$

The first term on the right-hand side of the equation corresponds to cooperative binding with a Hill coefficient of 2, the second term takes degradation into account and the last one shows the diffusion of  $P$  along the membrane (we do not assume any cytosolic diffusion). The chemical reactions that involve  $P$  are written:



where  $E$  is an enzyme and  $X$  is an enzyme-substrate complex. The Michaelis-Menten constant  $K$  is then equal to:

$$K = \frac{k_{-1} + k_2}{k_1} \quad (2.30)$$

We should now look for the fixed points of the system. They are the solutions of:

$$v \frac{p^2}{p^2 + K} - k_3 p = 0 \quad (2.31)$$

which reduces to:

$$k_3 p \left( p^2 - \frac{v}{k_3} + K \right) = 0 \quad (2.32)$$

and, defining  $e_1 = \frac{v}{k_3}$ , gives three roots:

$$\begin{cases} p_1 = 0 \text{ (stable fixed point)} \\ p_2 = \frac{e_1}{2} \left( 1 - \sqrt{1 - \frac{4K}{e_1^2}} \right) \text{ (unstable fixed point)} \\ p_3 = \frac{e_1}{2} \left( 1 + \sqrt{1 - \frac{4K}{e_1^2}} \right) \text{ (stable fixed point)} \end{cases} \quad (2.33)$$

As mentioned in section 2.1.1, the velocity of the trigger wave is proportional to:

$$J = \int_{p_1}^{p_3} f(p) dp \quad (2.34)$$

$$= \int_0^{p_3} \left( v \frac{p^2}{p^2 + K} - k_3 p \right) dp \quad (2.35)$$

$$= -k_3 \frac{p_3^2}{2} + v p_3 - v \sqrt{K} \arctan \left( \frac{p_3}{\sqrt{K}} \right) \quad (2.36)$$

We want the velocity of the trigger wave to change sign in the middle of the cell, which implies that  $J$  has to change sign. In other words,  $p_3$  or  $K$  (or both) have to vary across the cell in order for the sign change to occur. The stable fixed point  $p_3$  depends itself on  $v$ ,  $k_3$  and  $K$ . One way to implement the change of sign of  $J$  across the cell is to have a varying  $K$ . We require for  $k_{-1}$  to depend on the concentration  $q$ :  $k_{-1} = \tilde{k}_{-1}q$ . As we need  $K$  to vary over the cell, we need to have  $k_{-1}q \gg k_2$ , which amounts to:

$$\tilde{k}_{-1} \frac{k_q}{k_{-q}} \frac{b}{a} \gg k_2 \Leftrightarrow \tilde{k}_{-1} \frac{k_q k_{-a}}{k_{-q} k_{-b}} \frac{(k_b \bar{s} + k_{+b})}{(k_a s + k_{+a})} \gg k_2 \quad (2.37)$$

and leads to  $K \approx \tilde{K}q$  with  $\tilde{K} \approx k_{-1}/k_1$ . The wave-velocity is zero at the middle of the cell, which implies

$$-k_3 \frac{p_3^2}{2} + vp_3 - v\sqrt{K} \arctan\left(\frac{p_3}{\sqrt{K}}\right) = 0 \quad (2.38)$$

at the middle of the cell, and gives a relationship between the different quantities at play. To make the next calculations easier, we now make several simplifying assumptions on the different values of the rate constants, which we will keep throughout the chapter, unless otherwise mentioned. First, we take  $k_q = k_{-q}$ , so that  $q = b/a$ . Then, we take  $k_a = k_{-a} \gg k_{+a}$  and  $k_b = k_{-b} \gg k_{+b}$ , so that

$$q = \frac{b}{a} \approx \frac{\bar{s}}{s} \quad (2.39)$$

Replacing  $p_3$  by its value in equation 2.38, and calling  $\gamma = K/e_1^2$ , we get:

$$\frac{1}{4} \left(1 + \sqrt{1 - 4\gamma}\right) + \frac{\gamma}{2} - \sqrt{\gamma} \arctan\left[\frac{1}{2\sqrt{\gamma}} \left(1 + \sqrt{1 - 4\gamma}\right)\right] = 0 \quad (2.40)$$

which can be numerically solved to yield  $\gamma \approx 0.21$ . In the middle of the cell, and taking into account our simplifying assumptions mentioned in the previous paragraph, we have  $q \approx 1$ , so that the condition for zero wave velocity at the middle of the cell becomes:

$$\tilde{K}/e_1^2 \approx 0.21 \quad (2.41)$$

### 2.2.3 Simulations

We simulated equations 2.22, 2.24 and 2.28 on a one-dimensional domain with periodic boundary conditions, representing an “unfolded” membrane. The length of the membrane is  $L = 10$ , discretized with a grid length  $\Delta x = 0.02$ . In [109], the gradients used were linear across the cell. Because in our case the membrane is unfolded, the stimulus we have to apply is sinusoidal:  $s = \bar{s} + s_{\max} \sin\left(\frac{2\pi}{L}x\right)$ . The equations are integrated using a forward Euler scheme and a nearest-neighbor representation of the Laplacian operator. The time step used is  $\Delta t = 0.1$ . The rate constants and diffusion coefficient used can be found in table 2.3. The transition between the two stable states is triggered by localized random perturbations. These perturbations have a fixed width of  $\Delta \tilde{x} = 0.08$  and their location is randomly chosen from a uniform distribution on the membrane. Their amplitude is taken from a uniform distribution between  $p_1$  and  $p_3$  (which are the two stable fixed points of the system). They occur at random times, with a waiting time between two perturbations taken from a uniform distribution. The minimum waiting time is 0 and the maximum waiting time  $\Delta_{\text{noise}} t_{\max}$ . We call  $\Delta_{\text{noise}} t$  the average waiting time between two perturbations.

Parameter	Value	
$k_a$	50	Production rate of $A$
$k_{-a}$	50	Degradation rate of $A$
$k_{+a}$	0.01	Self-production of $A$
$k_b$	3	Production rate of $B$
$k_{-b}$	3	Degradation rate of $B$
$k_{+b}$	0.01	Self-production of $B$
$k_1$	200	Production of $P$
$\tilde{k}_{-1}$	87	
$k_2$	0.14	
$k_3$	1000	
$\tilde{e}_0$	$k_3/k_2$	
$D_P$	0.1	Diffusion coefficient of the reporter $P$ on the membrane
$\Delta_{\text{noise}}t$	0.05	Average waiting time between two perturbations

Table 2.3: Parameters used in the simulations. The values listed are dimensionless. To convert them to quantities with dimensions, the reader is referred to table A.2 of the article, reprinted at the end of this chapter.

## 2.2.4 Results of the model

### Response to a spatial gradient, response to a uniform concentration

The model was meant to simulate polarization of a cell in a gradient, as well as adaptation in response to a uniform concentration. It is therefore expected to perform well on these two features, which it does, as can be seen on figure 2.11. The spikes seen on the profile of  $p$  are the random perturbations that are applied to the system, and trigger the transition from one stable state to the other. Adaptation imposes a relationship between the rates constants of  $A$  and  $B$ . We want to have an activator  $A$  that rises faster than the inhibitor  $B$ , so that initially the fixed point is  $p_3 = 1$  everywhere around the cell. This implies  $k_a > k_b$ , and leads to an initial uniform translocation. This translocation should decay as the cell adapts, and the fixed point of the system should become  $p_1 = 0$  on the membrane. This means that the final concentration of  $B$  should be higher than the final concentration of  $A$ , for all values of the uniform signal  $\bar{s}$ :

$$\frac{k_a \bar{s} + k_{+a}}{k_{-a}} < \frac{k_b \bar{s} + k_{+b}}{k_{-b}}. \quad (2.42)$$

If there is no signal ( $\bar{s} = 0$ ), there should also be no translocation, so we need to have

$$\frac{k_{+a}}{k_{-a}} < \frac{k_{+b}}{k_{-b}}. \quad (2.43)$$

One very simple way to satisfy the condition in equation 2.42 for all values of  $\bar{s}$  is to have  $k_a = k_{-a}$  and  $k_b = k_{-b}$ . However, this condition can be relaxed. It will just impose an upper bound on the value of  $\bar{s}$  for which there is adaptation: for values  $\bar{s} > \bar{s}_0$  with

$$\bar{s}_0 = \left[ \frac{k_{+b}}{k_{-b}} - \frac{k_{+a}}{k_{-a}} \right] \left[ \frac{k_a}{k_{-a}} - \frac{k_b}{k_{-b}} \right]^{-1} \quad (2.44)$$

there is no adaptation. Note that  $s$  is the extracellular concentration of cAMP. It is more meaningful to talk in terms of receptor occupancy. To convert a concentration into a receptor

occupancy, one usually assumes Michaelis-Menten kinetics at the receptor level. At concentrations much bigger than the Michaelis-Menten constant  $K_d$ , the receptor occupancy saturates. In other words, if  $\bar{s}_0$  is much bigger than  $K_d$ , there will always be adaptation.

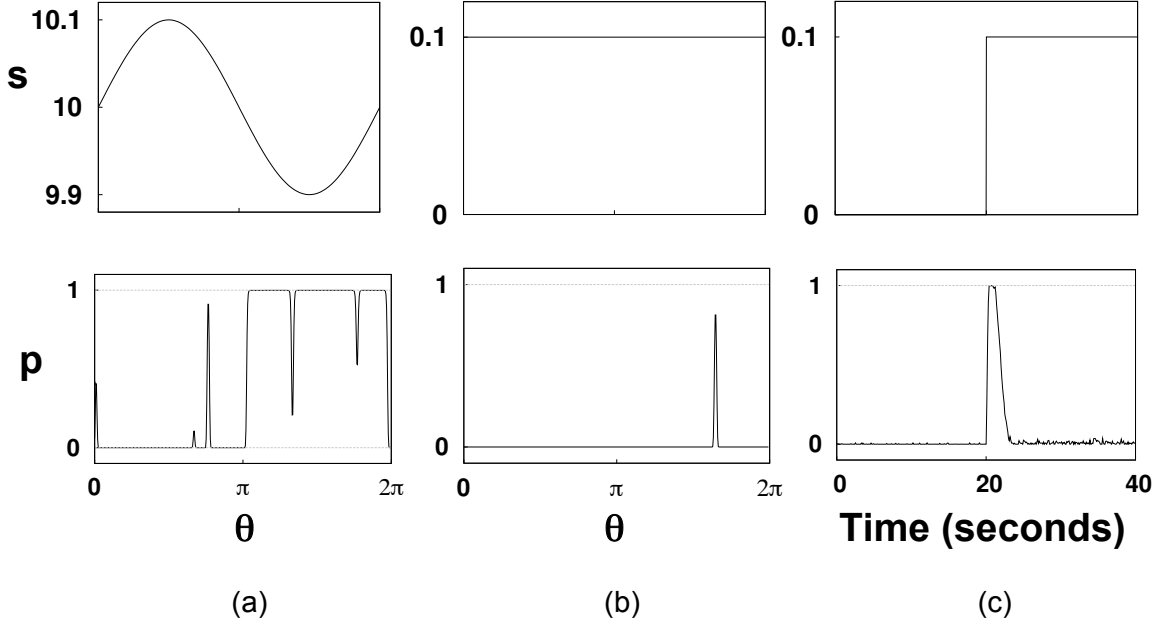


Figure 2.11: Spatial response to (a) a relative gradient of 1% and (b) to a uniform concentration  $s = 0.1$ . The spikes seen on the profile of  $p$  are the random perturbations applied, that trigger the transition from one state to the other. (c) Temporal response to a sudden jump in external concentration  $s$ . At each moment in time, the profile of  $p$  is averaged over the cell membrane. We observe a transient uniform translocation.

### 2.2.5 Predictions

We now turn to the predictions of the model.

#### The region of translocation increases with the gradient

The model predicts a threshold for directional sensing. Indeed, for translocation to occur, one needs to have locally more activator than inhibitor ( $a > b$ ). Having fixed the reaction constants, if we apply a gradient  $s(x) = \bar{s} + s_{\max} \sin(2\pi x/L)$ , there will be no translocation as long as

$$\frac{k_a(\bar{s} + s_{\max}) + k_{+a}}{k_{-a}} < \frac{k_b\bar{s} + k_{+b}}{k_{-b}}. \quad (2.45)$$

If condition 2.45 is not verified, there will be translocation on the part of the cell such that

$$\frac{k_a[\bar{s} + s_{\max} \sin(2\pi x/L)] + k_{+a}}{k_{-a}} < \frac{k_b\bar{s} + k_{+b}}{k_{-b}}. \quad (2.46)$$

which leads to

$$x < \frac{L}{2\pi} \arcsin \left[ \frac{1}{k_a s_{\max}} \left( k_{-a} \frac{k_b \bar{s} + k_{+b}}{k_{-b}} - k_{+a} - \bar{s} k_a \right) \right] \quad (2.47)$$

and a maximal translocation size of  $L/2$  (half of the cell). This behavior is schematically shown on figure 2.12

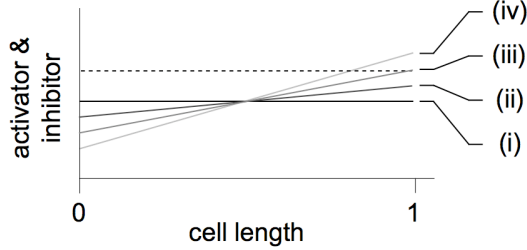


Figure 2.12: The size of the translocation goes up with the gradient. The concentration  $a$  of the activator is shown in bold, the concentration  $b$  of the inhibitor in a dashed line. (i) For a uniform stimulus uniform,  $a < b$  and no translocation occurs. (ii) For a directional stimulus, there is no translocation at shallow gradients. (iv) If the gradient is steep enough, the part of the cell where  $a > b$  will show a translocation. The limiting case is shown in (iii).

### The intensity of the translocation depends weakly on the steepness of the gradient

The intensity of the translocation is given in our model by the value of the stable fixed point  $p_3$ . According to equation 2.33, we have

$$p_3 = \frac{e_1}{2} \left( 1 + \sqrt{1 - \frac{4K}{e_1^2}} \right) \quad (2.48)$$

where  $K \approx \tilde{K} \frac{b}{a}$  and  $\frac{\tilde{K}}{e_1^2} \approx 0.21$ . Considering an external signal  $s(x) = \bar{s}[1 + \alpha \sin(\frac{2\pi}{L}x)]$ , where  $\alpha$  is the strength of the gradient, we find that the maximal variation of  $p_3$  is proportional to  $(1 + \alpha)^{-1/2} \sim 1 - \alpha/2$  for small values of  $\alpha$ . It is independent of the midpoint concentration of the concentration profile.

Note that it would be possible to have an intensity of translocation completely independent of the gradient. If we want to have  $p_3 = 1$  independent of the stimulus, we see from equation 2.32 that we need to introduce the condition  $K + 1 = v/k_3$ , which is what we did in the main text of our article [8].

### The time of response goes up at low gradients

The translocation is established via a trigger wave, whose velocity depend on the ratio of inhibitor to activator, as shown on figure 2.13a. We see that for values of  $q = b/a$  between 0.5 and 2, the wave velocity depends linearly on  $q$ . The shallower the gradient, the smaller the difference between  $a$  and  $b$ , resulting in a slower wave propagation. Therefore, the time to



## 2.2. A bistable mechanism triggered by internal noise

reach steady state increases. To characterize this time, we have defined the deviation of the system state at time  $t$  from the ideal steady-state solution as:

$$\delta(t) = \frac{1}{N} \sum_{i=1}^N \sqrt{(p_i(t) - \tilde{p}_i)^2}, \quad (2.49)$$

where  $N$  is the number of grid points along the cell membrane,  $p_i(t)$  is the value of  $p$  at position  $i$  and time  $t$ , and  $\tilde{p}_i$  is the ideal steady-state solution, which should be 0 for  $a < b$  and  $p_3 \approx 1$  for  $b > a$ . The evolution of  $\delta$  is shown on figure 2.13b for gradients of different slopes (and a fixed midpoint concentration  $\bar{s} = 10$ ). To obtain the characteristic time scale of the response, we fitted an exponential to these curves, of the form  $C e^{-t/\tau^*} + D$ . We plotted the evolution of  $\tau^*$  as a function of the gradient on figure 2.13c. The response time increases at low gradients.

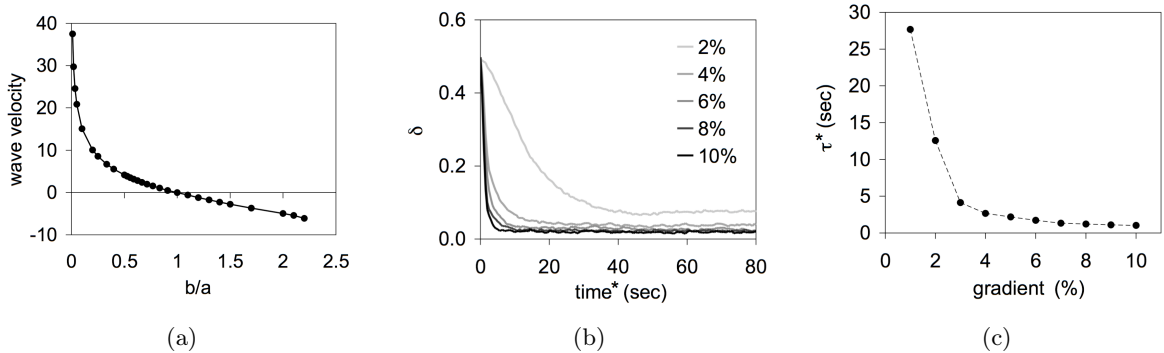


Figure 2.13: (a) Trigger wave velocity as a function of the ratio  $q = b/a$ . As the gradient gets shallower,  $q$  becomes closer to 1 and the trigger wave velocity is small. (b) Evolution of  $\delta(t)$  for different values of the relative gradient. The midpoint concentration is  $\bar{s} = 10$ . These curves were fitted by an exponential of the form  $C e^{-t/\tau^*} + D$ , and the characteristic time  $\tau^*$  is plotted on figure (c) as a function of the gradient.

### 2.2.6 Exploration of the parameter space

#### Time scale of the fluctuations

The transition we observe is triggered by random perturbations, occurring at random times. The average waiting time between two perturbations is an important parameter of the model. If the average waiting is smaller than the time scale of the trigger wave propagation, no pattern will be able to emerge and the system will be dominated by perturbations. If the average waiting time is infinitely long, no perturbations will be triggered. On figure 2.14a, we plotted the evolution of  $\delta(t)$  for different values of the average waiting time  $\Delta_{\text{noise}} t^*$ . This evolution was fitted by an exponential of the form  $C e^{-t/\tau^*} + D$ , and we plotted the characteristic time scale  $\tau^*$  on figure 2.14b. Note that at very small values of  $\Delta_{\text{noise}} t^*$ , the system goes very fast to its steady-state, but this steady-state is one that is dominated by noise (the offset  $D$  from the exponential fit is not such that  $D \ll 1$ ). As  $\Delta_{\text{noise}} t^*$  increases, the system gets more precise

( $D$  decreases) but also slower. The model is therefore good to work with in an intermediate range of  $\Delta_{\text{noise}}t^*$ , where the response is both precise ( $\delta < 0.05$ ) and fast (time of response smaller than 5 seconds, which is the biological time scale for a response [132]). On figure 2.14, we see that this corresponds to  $25 \leq \Delta_{\text{noise}}t^* \leq 750$  ms.

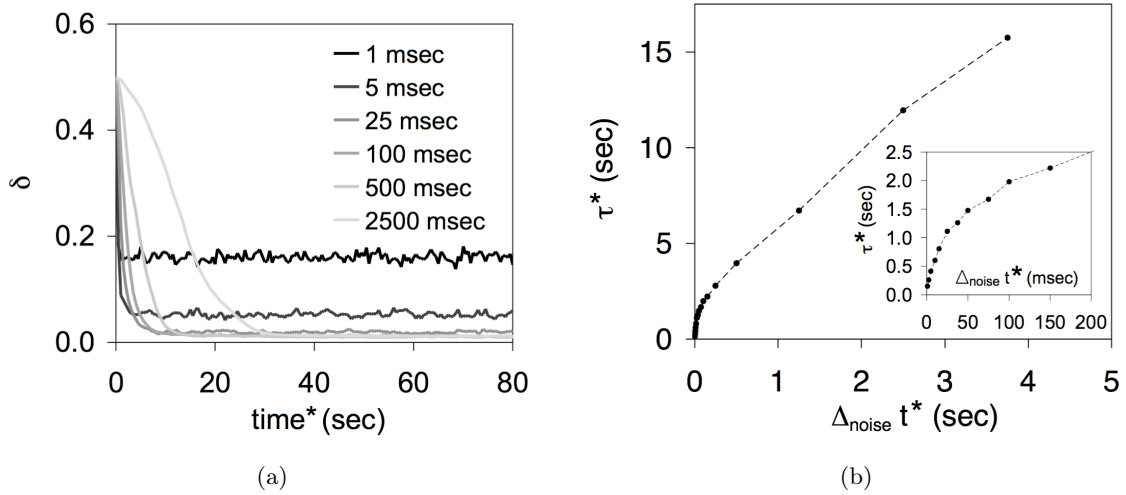


Figure 2.14: (a) Evolution of  $\delta(t)$  for different values of the average waiting time  $\Delta_{\text{noise}}t^*$ . These curves were fitted by an exponential of the form  $C e^{-t/\tau^*} + D$ , and the characteristic time  $\tau^*$  is plotted on figure (b) as a function of  $\Delta_{\text{noise}}t^*$ . At values of  $\Delta_{\text{noise}}t^*$  lower than 25 ms, the system goes to a steady state in less than 500 ms, but this steady state is dominated by the perturbations – no directional translocation is observed. At values of  $\Delta_{\text{noise}}t^*$  bigger than 750 ms, the system takes more than 5 seconds to reach the polarized steady-state, which is more than the biological timescale mentioned in [132].

### Fluctuations in the value of $\tilde{K}$

We have imposed the constraint  $\tilde{K}/e_1^2 = \gamma \approx 0.21$  (equation 2.41) to obtain a trigger wave velocity that changes sign in the middle of the cell. Note however that there will still be a translocation even if this condition is not verified, as long as the trigger wave velocity changes sign at some arbitrary point  $x^*$  on the membrane. We will then have two domains of unequal size. Let us assume that  $\tilde{K}$  fluctuates (the situation where  $e_1$  fluctuates can be treated exactly in the same way). The trigger wave velocity will change sign at a point  $x^*$  where the ratio  $q = b/a$  is not equal to 1, and such that  $\tilde{K}q = \gamma e_1^2$ . We consider a profile of concentration  $s(x) = \bar{s}(1 + \alpha \sin(2\pi x/L))$ , where  $\alpha$  is the strength of the gradient. We can then show that, as long

$$(1 - \alpha)\gamma e_1^2 < \frac{\tilde{k}_{-1} + k_2(1 - \alpha)}{k_1} \quad \text{and} \quad (1 + \alpha)\gamma e_1^2 > \frac{\tilde{k}_{-1} + k_2(1 + \alpha)}{k_1} \quad (2.50)$$

there will be a biphasic response.

## 2.3 Summary

The model we proposed combines the main advantage of the LEGI model, which is the ability to reverse the polarization in response to a change of the gradient direction, with the advantage of a bistable dynamics, which is the amplification of low asymmetries. The model was made to reproduce five experimental properties:

1. there is a translocation over a wide range of gradients, and the translocation remains as long as the gradient is kept on - *this is assured by the LEGI type mechanism,*
2. there is a distinct front and back over the range of gradients where the cell responds - *this is done by the bistable module,*
3. the mechanism should be reversible: *done by the LEGI module,*
4. as much as possible, the translocation should be constant over a wide range of gradients (this would reproduce the two-states-like behavior of the chemotactic velocity): *done by the bistable module,*
5. there is adaptation when the cell is uniformly stimulated (*i.e.* we see a temporary uniform translocation): *implies an inequality relationship between the production constants of  $A$  and  $B$ .*

As a consequence of these five experimental properties, the model makes four predictions:

1. there is a threshold gradient below which the cell does not respond (consequence of the relationship between the production constants of  $A$  and  $B$ , made to reproduce adaptation),
2. the size of the translocation goes up with the gradient and reaches a maximum (consequence of the bistability).
3. the intensity of the translocation is roughly constant over the range of gradients where the cell responds (consequence of the bistability).
4. the time of response goes up when the gradient goes down (consequence of the bistability)

As a final note, the model we proposed is actually very close to Meinhardt's [73]. We were able to get rid of Meinhardt's slow inhibitor (called  $C$  in [73]) because we impose fluctuations in our system, that trigger a transition from one state to the other.

## A bistable mechanism for directional sensing

C Beta<sup>1,2,3</sup>, G Amselem<sup>2</sup> and E Bodenschatz<sup>2</sup>

<sup>1</sup> Institute of Physics and Astronomy, University of Potsdam,  
Karl-Liebknecht-Strasse. 24/25, 14476 Potsdam-Golm, Germany

<sup>2</sup> Max Planck Institute for Dynamics and Self-Organization, Am Fassberg 11,  
37077 Göttingen, Germany

E-mail: [carsten.beta@uni-potsdam.de](mailto:carsten.beta@uni-potsdam.de)

*New Journal of Physics* **10** (2008) 083015 (20pp)

Received 25 November 2007

Published 14 August 2008

Online at <http://www.njp.org/>

doi:10.1088/1367-2630/10/8/083015

**Abstract.** We present a generic mechanism for directional sensing in eukaryotic cells that is based on bistable dynamics. As the key feature of this modeling approach, the velocity of trigger waves in the bistable sensing system changes its sign across cells that are exposed to an external chemoattractant gradient. This is achieved by combining a two-component activator/inhibitor system with a bistable switch that induces an identical symmetry breaking for arbitrary gradient input signals. A simple kinetic example is designed to illustrate the dynamics of a bistable directional sensing mechanism in numerical simulations.

### Contents

<b>1. Introduction</b>	<b>2</b>
<b>2. Bistable model</b>	<b>3</b>
<b>3. Kinetic example and numerical simulations</b>	<b>6</b>
3.1. Model . . . . .	6
3.2. Numerical simulations . . . . .	8
<b>4. Discussion</b>	<b>13</b>
<b>Acknowledgment</b>	<b>15</b>
<b>Appendix A. Dimensionless variables</b>	<b>15</b>
<b>Appendix B. Robustness</b>	<b>16</b>
<b>References</b>	<b>18</b>

<sup>3</sup> Author to whom any correspondence should be addressed.

## 1. Introduction

Chemotaxis is the directed movement of a cell towards a chemical source. It is of fundamental importance for many biomedical processes including wound healing, cancer metastasis and morphogenesis of the nervous system [1]–[3]. Directed locomotion of bacteria has been intensively investigated and detailed models of prokaryotic chemotaxis are available [4]. On the other hand, directional motion of eukaryotic cells is more complex. Here, less is known about the chemotactic signaling pathways that link the membrane receptor input to rearrangements of the cytoskeleton and directed actin polymerization [5]. Eukaryotic cells like neutrophils or the social amoeba *Dictyostelium discoideum* can detect chemoattractant gradients as shallow as a 1% difference in concentration between the front and the back of the cell and exhibit robust directional motion over a large range of different gradient steepnesses [6]–[8].

This response behavior cannot be achieved by simple amplification or any other linear mapping of the external gradient into the cell. Instead, it can be expected that highly nonlinear interactions govern the early stages of chemotaxis, generally referred to as *directional sensing*. During the first 10 s after gradient exposure, an intracellular symmetry breaking occurs that is reflected in asymmetric spatial distributions of numerous proteins across the cell [9]. These subcellular reorganizations have been experimentally observed by fluorescence microscopy imaging of various green fluorescent protein (GFP)-tagged constructs. Among these redistributing components, the small GTPase Ras, pleckstrin homology (PH) domain proteins, and the p21-activated kinase A (PAKa) have been identified, see [10] and references therein. Although a complete picture of the precise role of these individual players is still missing, it is generally assumed that the asymmetric rearrangement of proteins during directional sensing controls the downstream events that lead to actin driven membrane protrusions and, ultimately, cell locomotion [11].

Numerous efforts have been undertaken to develop mathematical descriptions of directional sensing. Since many molecular details of the chemotactic signaling network remain unknown, most models proposed to date consequently focused on abstract, low-dimensional descriptions. The most common approach is based on two-component activator/inhibitor kinetics. Combining slow diffusing, locally acting excitatory components with a rapidly diffusing, global inhibitor (local excitation/global inhibition (LEGI) models) amplification of the external gradient signal is obtained [9, 12, 13]. Other variants have been proposed, like the ‘first hit’ [14] and the ‘intermediate depletion’ model [15]. While the former is unable to adapt to subsequent changes in the direction of the initial gradient stimulus, the latter suffers from a strong dependence on the average chemoattractant concentration that is not observed in experiments. Intracellular symmetry breaking via a Turing instability in response to external gradient stimuli has been considered by Meinhardt [16]. This approach was later refined and adapted to specifically describe the dynamics of asymmetric localization of phosphoinositides such as PIP<sub>3</sub> at the leading edge of migrating cells [17, 18]. As more and more elements of the chemotactic pathway are identified, first attempts were made to capture directional signaling in high-dimensional realistic models [19]. Here, the authors simulate a complex signaling network to describe temporally multiphasic responses in membrane translocation events following gradient stimulation. Current modeling efforts focus on stochastic effects that influence the distribution of occupied receptors across the membrane and become important for directional sensing in shallow gradients [20]–[23].

In [8], we performed a quantitative study of chemotactic motion of the eukaryotic micro-organism *D. discoideum*. Chemotaxis of *Dictyostelium* cells was characterized in well-controlled linear chemoattractant gradients using microfluidic technology. In this study, we observed chemotactic responses for gradient signals that range over three orders of magnitude in gradient steepness (between  $10^{-2}$  and  $10 \text{ nM } \mu\text{m}^{-1}$ ). Within this interval, chemotactic motion was robust and showed only a weak dependence of the chemotactic velocity on the gradient steepness. This has prompted us to look for models that respond with an identical symmetry breaking to gradient stimuli of very different steepness.

The models summarized in the previous paragraph do not meet this condition. Gamba *et al* have designed a model of directional sensing that is based on phase separation of membrane phospholipids into PIP<sub>2</sub>- and PIP<sub>3</sub>-rich domains, mediated by phosphoinositide diffusion and the enzymatic activity of phosphatidylinositol 3-kinase (PI3K) and its counteracting phosphatase PTEN [24, 25]. Their diffusion-limited phase separation model accounts for a strong symmetry breaking even at shallow gradients. But it does not show the initial transient uniform response to both isotropic and gradient stimuli that is observed in experiments on phosphoinositide signaling in chemotactic cells [26]. Recently, Levine *et al* proposed a model that takes the switch-like nature of gradient sensing into account and, at the same time, also reproduces the transient response dynamics correctly [27]. Their ‘balanced inactivation model’ is composed of a two-component activator/inhibitor system. Under gradient stimulation, this model exhibits a clear symmetry breaking into an activated front and a back, where activation is vanishing. Note, however, that activation levels at the front depend on the external signal and scale linearly with the gradient steepness.

Here, we propose a mechanism where the activated and quiescent states at the front and back of a cell are independent of the external gradient signal as long as a critical gradient value is exceeded. We achieve this property by building our model on the simple pattern formation paradigm of bistability: an underlying LEGI-type activator/inhibitor system is combined with an autocatalytic step that results in an identical symmetry breaking event for arbitrary gradient inputs. Note that our model is restricted to the initial symmetry breaking during directional sensing. Down-stream cytoskeletal responses like the protrusion and bifurcation of pseudopods [28] or the dynamics of complex actin structures in the cell cortex [29] are not described by our model. In the following sections, we first introduce the underlying idea of a bistable model for directional sensing and later present numerical simulations of a specific kinetic example.

## 2. Bistable model

We assume that the chemotactic pathway is mediated by a membrane-bound species P. It lives on the cytosolic side of the plasma membrane and is diffusively mobile along the inner membrane surface. The formation of P will depend on extracellular chemoattractant signals that are communicated to the inside of the cell via transmembrane receptors. In the presence of P, downstream events are initiated that influence actin polymerization and rapid reorganization of the cytoskeleton. In this simplified picture, *directional sensing* is defined as the formation of an asymmetric membrane distribution of P in response to an extracellular gradient signal. The asymmetry in P will result in asymmetric stimulation of cytoskeletal activity that controls the formation of membrane protrusions and directional cell movement.

In general, the dynamics of P on the inner side of the plasma membrane follows a reaction–diffusion equation

$$\dot{p} = f(p) + D_p \nabla^2 p, \quad (1)$$

where  $p$  denotes the concentration of P and  $D_p$  the coefficient of diffusion along the membrane. Note that throughout this work, physical quantities are given in dimensionless variables. They have been non-dimensionalized by the reference quantities that can be found in appendix A. Quantities that carry a dimension are marked with an asterisk. The kinetics of P formation and degradation depends on the external chemoattractant signal and is summarized in the interaction function  $f$ . For the model presented here we require that the form of  $f$  leads to bistability in the dynamics of P. This typically implies that the local kinetics  $\dot{p} = f$  has three fixed points,  $p_1 < p_2 < p_3$ , where  $p_1$  and  $p_3$  are linearly stable and  $p_2$  is unstable [30]. Here, we assume that the two stable fixed points  $p_1$  and  $p_3$  are independent of the external chemoattractant signal S, whereas the unstable fixed point  $p_2$  depends on S (see appendix B for the more general case, in which both  $p_2$  and  $p_3$  are depending on S).

Cellular systems are noisy, so that localized transitions from one fixed point to the other can occur. Due to diffusive coupling, such perturbations may induce similar transitions at neighboring locations, so that transitions from one fixed point to the other can spread through the system in the form of a *trigger wave*. Their shape and velocity are uniquely defined. Let  $p = p(\xi)$  with  $\xi = x - ct$  denote a transition from  $p_1$  to  $p_3$ , that spreads with velocity  $c$  through the system, i.e.  $p \rightarrow p_1$  ( $p \rightarrow p_3$ ) for  $\xi \rightarrow \infty$  ( $\xi \rightarrow -\infty$ ). The sign of the trigger wave velocity  $c$  is determined by the sign of the integral [31],

$$A = \int_{p_1}^{p_3} f(p) dp. \quad (2)$$

Depending on the sign of  $c$ , domains of  $p_3$  ( $c > 0$ ) or  $p_1$  ( $c < 0$ ) will grow, so that the system eventually converges to one of the two stable fixed points<sup>4</sup>.

As the central assumption of our model, it is required that the trigger wave velocity changes sign across a cell that is exposed to an external gradient in the chemoattractant S ( $s$  denoting the concentration of species S). In particular, in the front half of the cell, pointing towards higher chemoattractant concentrations, the wave velocity shall be positive, so that  $p$  eventually takes the value of the stable fixed point  $p_3$ . In the back half of the cell,  $c$  is negative and  $p$  converges to  $p_1$ . The interface between the two membrane fractions of high and low P concentration is formed by a frozen trigger wave of zero velocity.

How can such a dependence of the dynamics of P on the external chemoattractant signal arise? We assume that the receptor input is transmitted to the P-signaling system via a two-component activator/inhibitor module that shows similar dynamical behavior as previously proposed LEGI-type models of directional sensing [12]. The system shall have the following properties: (i) both activator and inhibitor are produced locally proportional to the external chemical signal. (ii) The activator A is an immobile, membrane bound species, so that its concentration  $a$  on the membrane reflects the external gradient across the cell. (iii) The inhibitor B is a cytosolic, fast diffusing component. Assuming that diffusive spreading of the inhibitor

<sup>4</sup> Note that there is also a trigger wave solution with  $p \rightarrow p_1$  ( $p \rightarrow p_3$ ) for  $\xi \rightarrow -\infty$  ( $\xi \rightarrow \infty$ ). The propagation velocities of these two solutions always have an identical absolute value and opposite sign. For a more thorough treatment of bistable systems the reader is referred to standard textbooks, see e.g. [31] and references therein.



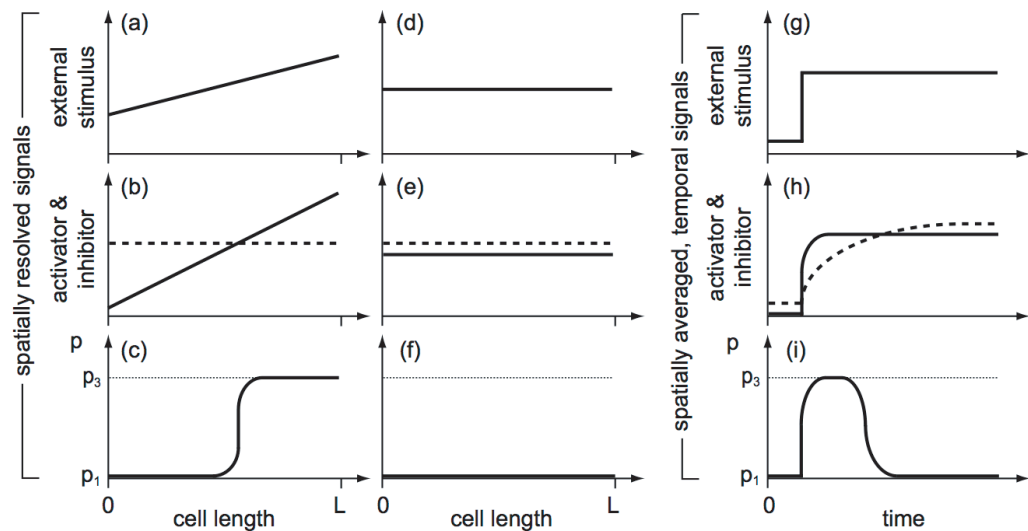


**Figure 1.** General idea of a bistable model for directional sensing. We consider a one-dimensional cell of length  $L$ . Three different stimulation scenarios are schematically displayed. (a), (d) and (g) show the external stimulus  $s$ . (b), (e) and (h) display the concentrations of activator ( $a$ , bold) and inhibitor ( $b$ , dashed). In (c), (f) and (i) the main dynamical variable  $p$  can be seen. On the left, stimulation with a stationary linear gradient is displayed. The middle column exhibits the spatial distribution of  $a$ ,  $b$  and  $p$  across the cell under a stationary, spatially uniform stimulation as shown in (d). On the right-hand side, the temporal evolution in response to a uniform, stepwise increase in the external chemoattractant concentration is shown. Here, (g)–(i) display the time evolution of the mean values of  $s$ ,  $a$ ,  $b$  and  $p$  averaged across the cell.

occurs instantaneously, its concentration  $b$  is proportional to the midpoint concentration of the external gradient everywhere in the cell. This is illustrated in figure 1(b), where the activator and inhibitor concentrations are shown across the one-dimensional projection of a cell exposed to an external gradient stimulus as indicated schematically in figure 1(a). (iv) The sign of the trigger wave velocity depends on the ratio of the activator and inhibitor concentrations  $a$  and  $b$  and has to change across a cell that is exposed to an external gradient. In the example described below, we have,  $c = 0$  for  $a = b$ ,  $c > 0$  for  $a > b$ , and  $c < 0$  for  $a < b$ . Perturbations in  $p$  then induce a convergence to  $p = p_3$  in the front and to  $p = p_1$  in the back of the cell as shown in figure 1(c). (v) Inhibitor levels are slightly higher than the averaged activator concentration in stationary cases. Under this condition, the entire membrane will be eventually driven to  $p = p_1$  for uniform, stationary levels of chemoattractant, since  $c < 0$ . This situation is schematically illustrated in figures 1(d)–(f). (vi) Production and degradation of the inhibitor are slower than the corresponding timescales of the activator dynamics, i.e. upon uniform stimulation, the activator reaches stationary levels earlier than the inhibitor, see figures 1(g) and (h). For intermediate times, the activator may thus exceed the concentration of the inhibitor, so that a transient response of  $p = p_3$  can be observed uniformly across the cell as displayed in figure 1(i). For longer times, perturbations will decay to  $p = p_1$  as required for stationary cases.

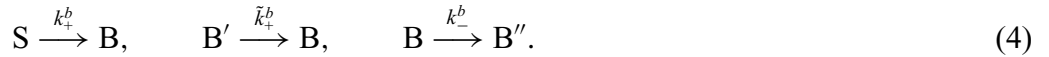
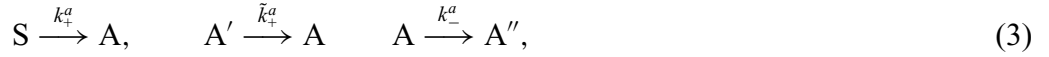


### 3. Kinetic example and numerical simulations

Let us now turn to a simple example that fulfills the general requirements outlined in the previous section. We will first describe the specific model composed of an activator/inhibitor system (LEGI module) that couples to an autocatalytic membrane bound species P (bistable module). We then present a numerical analysis of the one-dimensional model and an example of a two-dimensional simulation.

#### 3.1. Model

**3.1.1. LEGI module.** The external chemoattractant signal S acts on a two-component LEGI-type activator/inhibitor system. According to condition (i), we require that both the activator A and the inhibitor B are produced proportional to the external chemoattractant signal S. Furthermore, A and B are part of other metabolic pathways, so that they are continuously formed and degraded independently of the external signal S,

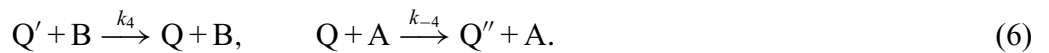


The S-independent production and degradation reactions ensure that both species exhibit a residual background concentration in the absence of S. As required by conditions (ii) and (iii), the activator A is an immobile, membrane bound component, while the inhibitor B spreads in the cytosol by diffusion. If cytosolic diffusion of B occurs quickly, we can approximate the production of B to depend on the averaged concentration of S,  $\bar{s} = \int s dx$ , at each location in the cell. We thus obtain the following kinetics for A and B:

$$\frac{da}{dt} = k_+^a s + \tilde{k}_+^a - k_-^a a, \quad \frac{db}{dt} = k_+^b \bar{s} + \tilde{k}_+^b - k_-^b b. \quad (5)$$

Here, we have assumed that the concentrations of species A' and B' for the endogenous production of A and B are constant (large reservoirs). The numerical values of the rate constants of activator and inhibitor kinetics do not matter as long as conditions (v) and (vi) are fulfilled. The values that were chosen for our numerical simulations can be found in the caption of figure 3.

We assume that the action of the activator/inhibitor system on downstream events in the signaling pathway is determined by the ratio of activator and inhibitor concentrations [12]. Such a dependence can occur via a third species Q that is formed and decomposed depending on the presence of the activator and inhibitor,



Again, we assume a constant substrate concentration Q' (large reservoir), so that the kinetics of Q is

$$\frac{dq}{dt} = k_4 b - k_{-4} a q. \quad (7)$$

If the dynamics of Q is fast compared to the timescales of the LEGI system, the concentration of Q will be determined at all times by the ratio of activator and inhibitor concentrations,

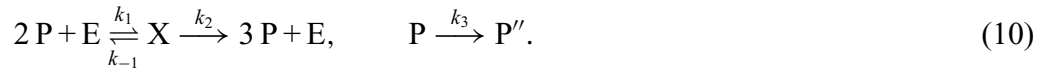
$$q = \frac{k_4}{k_{-4}} \frac{b}{a}. \quad (8)$$

For simplicity, we take  $k_4 = k_{-4}$ , so that  $q = b/a$ . The concentration of Q is the readout quantity of the LEGI module.

*3.1.2. Bistable module.* Following the general outline in section 2, the LEGI module transmits the receptor input signal S to the bistable signaling system of a membrane bound species P. In general, temporal changes in the concentration of P,  $\frac{dp}{dt} = f(p)$ , will be determined by production and degradation terms,

$$f(p) = v^+(p) - v^-(p). \quad (9)$$

For our specific example, we assume an autocatalytic production of P that takes place in an enzymatic reaction following Michaelis–Menten-type kinetics. Degradation of P is taken to be linear, so that



We take cooperative binding effects into account by introducing a Hill coefficient  $\alpha$  (in the present example, we set  $\alpha = 2$ ). Under the assumption of a quasi-steady-state, the concentration of the enzyme–substrate complex X is constant. With the total enzyme concentration  $e_0$  conserved, the well-known Michaelis–Menten rate law can be derived for the production of P. We thus find the following expression for the interaction function  $f$ :

$$\frac{dp}{dt} = \frac{v p^2}{p^2 + K} - k_3 p \equiv f(p). \quad (11)$$

Here,  $v = k_2 e_0$  denotes the maximal reaction velocity and  $K = (k_{-1} + k_2)/k_1$  the Michaelis constant. The shape of the interaction function  $f$  can be seen in figure 2. It has two stable fixed points  $p_1$  and  $p_3$ , and an unstable fixed point  $p_2$ , for which  $p_1 < p_2 < p_3$ . The fixed points are determined by

$$k_3 p \left( p^2 - \frac{v}{k_3} p + K \right) = 0. \quad (12)$$

How is the dynamics of the species P linked to the LEGI module and thus to the external signal S? As a key property, our model has to fulfill condition (iv). The latter requires that the trigger wave velocity, i.e. the integral (2), changes sign across a cell that is exposed to an external gradient in S. This can be achieved if we assume that the unstable fixed point  $p_2$  depends on the concentration of Q, i.e. on the ratio of activator and inhibitor concentrations, while the two stable fixed points are independent of Q. To obtain such a dependence, we require  $K + 1 = v/k_3$ , so that equation (12) reduces to

$$k_3 p(p - p_2)(p - 1) = 0. \quad (13)$$

In this case, the two stable fixed points become  $p_1 = 0$  and  $p_3 = 1$ , and the unstable fixed point is  $p_2 = K$ . The dependence of  $p_2$  on the ratio of the activator and inhibitor concentrations is now implemented by choosing  $K = \tilde{K} q$ . Since  $K = (k_{-1} + k_2)/k_1$ , the  $q$ -dependence of  $K$  implies a  $q$ -dependence of at least one of the rate constants, e.g.  $k_{-1} = \tilde{k}_{-1} q$ , with  $\tilde{k}_{-1} \gg k_2$ . Note that from the condition  $K + 1 = v/k_3$ , it also follows that  $v/k_3 = k_2 e_0/k_3$  has to depend on  $q$ . We achieve this by assuming that the total enzyme concentration is  $e_0 = \tilde{e}_0(\tilde{K} q + 1)$  with  $k_2 \tilde{e}_0/k_3 = 1$ .

The value of  $\tilde{K}$  has to be chosen such that the trigger wave velocity changes sign across a cell that is exposed to a chemoattractant gradient. Under a gradient stimulus, the activator

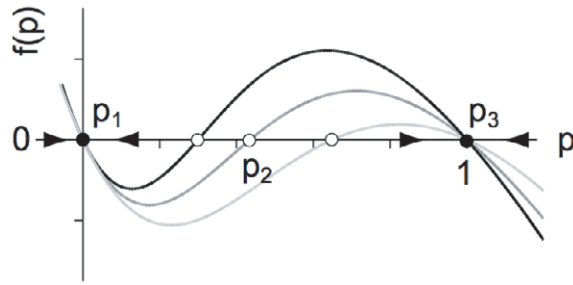


**Figure 2.** The interaction function  $f(p)$  for  $a > b$  (black),  $a = b$  (dark gray), and  $a < b$  (light gray), corresponding to positive, zero and negative trigger wave velocities, respectively. The arrows denote the flow in one-dimensional phase space defined by the sign of the temporal derivative  $\dot{p} = f(p)$ . The roots of  $f$  are fixed points, where  $p_{1,3}$  are stable (bold circles) and  $p_2$  is unstable (open circle).

and inhibitor concentrations change from  $a > b$  to  $a < b$  across the cell, see figure 1(b). We therefore require that the integral (2),

$$A = \int_0^1 \left[ \frac{vp^2}{K+p^2} - k_3p \right] dp$$

$$= v - v\sqrt{K} \arctan \frac{1}{\sqrt{K}} - \frac{k_3}{2} \quad (14)$$

and thus the trigger wave velocity, is zero for  $a = b$ . This ensures an opposite sign of the trigger wave velocity in the parts of the cell where  $a > b$  and  $a < b$ , respectively. In figure 2,  $f(p)$  is shown for  $a > b$  (black)  $b = a$  (dark gray) and  $a < b$  (light gray) to illustrate this. Under the condition that  $A = 0$  for  $a = b$ , equation (14) leads to the relation  $\sqrt{K} \arctan \frac{1}{\sqrt{K}} = 1 - \frac{1}{2(K+1)}$ , which can be solved numerically to yield  $\tilde{K} = 0.4357$ .

In the preceding discussion, several restrictions were imposed on the choice of the model parameters to ensure that  $p_3$  is independent of  $q$  and to enforce a zero trigger wave velocity for  $q = 1$ . In appendix B, we have analyzed the robustness of our model under conditions where these restrictions, in particular the condition  $K + 1 = v/k_3$ , are relaxed.

### 3.2. Numerical simulations

**3.2.1. Equations and parameters.** We have performed numerical simulations of equation (1) for the dynamics of  $p$ , where  $f$  is given by equation (11). The activator and inhibitor dynamics are based on equations (5). The parameter values can be found in the caption of figure 3. Simulations are performed on a one-dimensional domain of length  $L = 10$  that is discretized with a grid length of  $\Delta x = 0.02$ . To mimic a two-dimensional cut through a circular cell, periodic boundary conditions are imposed. A linear gradient stimulus that spans from  $\bar{s} - s_{\max}$  to  $\bar{s} + s_{\max}$  then maps onto the cell perimeter in the form of a sine function,  $s = \bar{s} + s_{\max} \sin(\frac{2\pi}{L}x)$ . The time step is  $\Delta t = 0.001$  and for the diffusion constant of P we choose  $D_P = 0.1$ , a typical value for membrane diffusion. The system of equations is integrated numerically using a forward Euler scheme and a nearest-neighbor representation of the Laplacian operator.

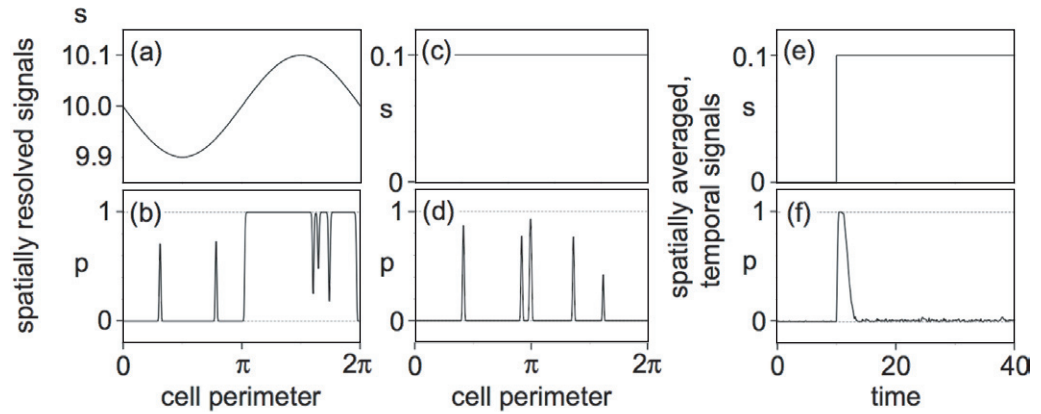


**Figure 3.** Numerical simulations of equations (1) and (5) with  $f$  as given in equation (11). (a) Gradient stimulus of 1%. (b) Directional response of  $p$  for a stationary gradient stimulus as shown in the panel above. (c) Uniform stimulus with a value of  $s = 0.1$ . (d) Quiescent membrane under stationary uniform stimulation with  $s = 0.1$ . (e) Time evolution of a uniform stimulus. At time = 10,  $s$  is uniformly switched from 0 to 0.1. (f) Response in  $p$ , averaged across the cell perimeter, to a uniform increase in  $s$  as shown in the panel above. The parameters are  $k_1 = 200$ ,  $\tilde{k}_{-1} = 87$ ,  $k_2 = 0.14$ ,  $k_3 = 1000$ ,  $\tilde{e}_0 = k_3/k_2$ ,  $k_+^a = k_-^a = 50$ ,  $\tilde{k}_+^a = 0.01$ ,  $k_+^b = k_-^b = 3$ ,  $\tilde{k}_+^b = 0.01$  and  $D_p = 0.1$ . Random perturbations are applied with an average waiting time of  $\Delta_{\text{noise}}t = 0.05$ .

We assume that the cellular system is noisy, so that, on a microscopic level, the quantity  $p$  undergoes random fluctuations. From time to time, fluctuations add up and become sufficiently large to induce a local transition between the two stable fixed points of the system. In our simulations, noise is taken indirectly into account by initiating random localized transitions between the two fixed points. The positions of perturbations are randomly chosen from a uniform distribution across the cell. The perturbations are  $\Delta\tilde{x} = 0.08$  in size and their amplitudes are uniformly distributed between 0 and 1. Also the waiting times between such perturbations is random and drawn from a uniform distribution that extends from zero to some maximal waiting time. Depending on the sign of the trigger wave velocity, perturbations may grow or decay.

**3.2.2. Response to shallow gradients.** Numerical simulations were performed to mimic stimulation with directional and uniform cues. In figure 3(b), a  $p$ -profile is shown that results from exposure to a linear gradient in  $s$  across the cell. The gradient stimulus is shown in figure 3(a) and corresponds to a sine profile along the perimeter of a circular cell. Figure 3(d) displays the concentration of P under exposure to a uniform level of  $s$  that can be seen in figure 3(c). For the same simulation, the temporal evolution of the averaged  $p$ -level along the membrane is displayed in figure 3(f). Here,  $s$  undergoes a uniform, stepwise increase from  $s = 0$  to  $s = 0.1$  at  $t = 10$ , figure 3(e). The presence of random perturbations is reflected by the spiky shape of the  $p$ -profiles in figures 3(b) and (d) and the slight fluctuations in the averaged  $p$ -level displayed in figure 3(f).

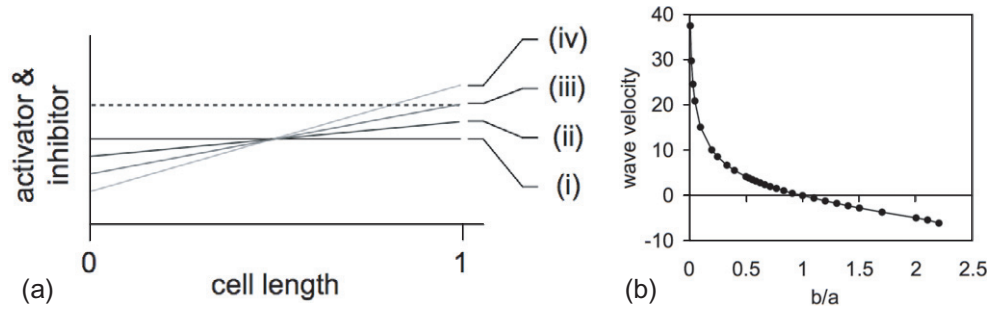


**Figure 4.** (a) Threshold behavior in the activator/inhibitor system. The response to gradients of different slopes and identical midpoint are displayed for the activator (bold) and the inhibitor (dashed). (i) Spatially uniform, (ii) subthreshold, (iii) threshold and (iv) superthreshold gradient stimuli. (b) Dependence of the trigger wave velocity on the ratio of activator and inhibitor concentrations,  $q = b/a$ . For values of  $q = 0.5 \dots 2$ , a linear relation between  $q$  and the trigger velocity is observed.

One of the outstanding characteristics of directional sensing in eukaryotic cells is an extraordinary sensitivity to shallow gradients. Experiments have shown that concentration differences as low as 1% between the front and the back of a cell can be identified [6]–[8]. The bistable mechanism we propose here can account for a reliable performance of directional sensing over a large range of gradient steepnesses. An example for sensing of shallow gradients is shown in figures 3(a) and (b). A gradient in  $S$  that is ranging from  $s = 9.9$  to  $10.1$  across the cell is sufficient to induce a clear symmetry breaking: in the front half of the cell,  $p$  converges to the stable fixed point of  $p_3 = 1$ , in the back it takes the value of the second stable fixed point  $p_1 = 0$ . Although the limit for detection of shallow gradients will be ultimately determined by the noise level of the system, the constant values of the fixed points  $p_{1,3}$  ensure that our model shows an almost identical response over a wide range of gradient stimuli. Only two features of the response dynamics depend on the gradient steepness and are described in the following.

**3.2.3. Threshold for directional responses.** The fraction of the membrane with  $p = 0$  is slightly larger than the  $p = 1$  part. This asymmetry increases for decreasing gradients. It is caused by the inhibitor level that always exceeds the averaged activator concentration as required by condition (v) in section 2. This is schematically shown in figure 4(a). With decreasing gradient, the membrane fraction for which  $a > b$  becomes smaller until it disappears for

$$\frac{k_+^a(\bar{s} + s_{\max}) + \tilde{k}_+^a}{k_-^a} \leq \frac{k_+^b\bar{s} + \tilde{k}_+^b}{k_-^b}. \quad (15)$$

Here,  $\bar{s}$  denotes the average concentration of  $S$  over the cell and  $s_{\max}$  the maximal deviation from the average, i.e. the gradient stimulus spans from  $\bar{s} - s_{\max}$  to  $\bar{s} + s_{\max}$  across the cell.

**3.2.4. Timescale of directional responses.** The time it takes to establish a directional response increases with decreasing gradient. The reason for this is a dependence of the trigger wave velocity on the ratio of activator and inhibitor concentrations,  $q = b/a$ . This dependence is

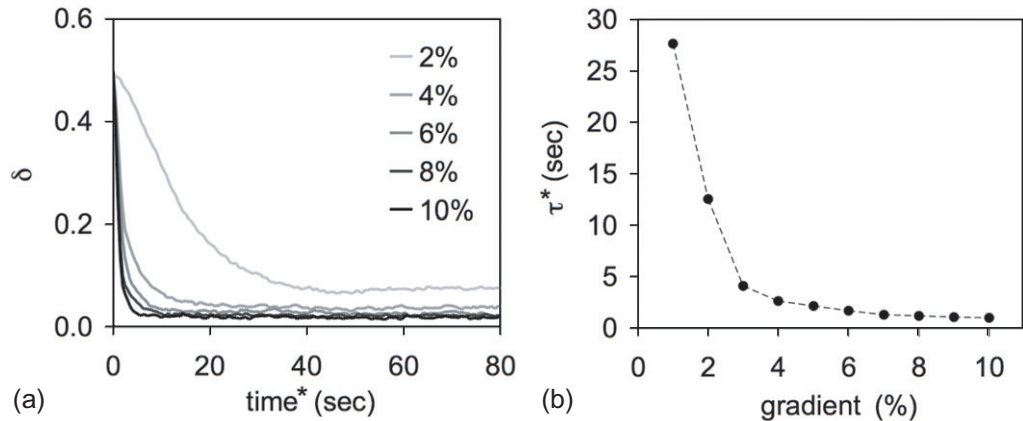


**Figure 5.** Dependence of the response time on the gradient. (a) Temporal evolution of the deviation  $\delta$  of the actual system state from the complete directional response for different  $\tau$  gradients, see main text for a definition of  $\delta$ . (b) Characteristic response time  $\tau^*$  obtained from exponential fits to the curves in panel (a). Asterisks denote quantities that carry a dimension, see appendix A.

displayed in figure 4(b). The shallower the gradient, the smaller the difference between  $a$  and  $b$ , so that the trigger wave velocity is confined to small values around zero. This results in a slower growth of perturbations and thus in longer transient times to establish a directional response. For values of  $q = 0.5, \dots, 2$ , a linear relation between  $q$  and the trigger wave velocity is found. In this regime, which spans up to gradients of about 50%, the model can be operated safely. Situations outside this range are not considered here<sup>5</sup>.

We have characterized the dependence of the response time on the gradient steepness. To this end, we define the deviation of the actual system state from a complete directional response as

$$\delta(t) = \frac{1}{N} \sum_{i=1}^N \sqrt{(p_i(t) - \tilde{p}_i)^2}, \quad (16)$$

where  $N$  is the number of grid points along the cell membrane and  $\tilde{p}_i = 0$  or  $1$  for  $a < b$  or  $a > b$ , respectively<sup>6</sup>. Following exposure to a gradient,  $\delta$  will decay as  $p$  approaches the response state  $\tilde{p}$ . In figure 5(a), the decay of  $\delta$  is shown for a selection of different gradients. We determine the response time by fitting with an exponential of the form  $C e^{-t/\tau} + D$  with the fit parameters  $C$ ,  $D$  and  $\tau$ . The latter is taken as the characteristic timescale of the response. In figure 5(b), the timescale  $\tau$  is shown for gradients ranging from 1 to 10%. At shallow gradients, increased response times are observed. For gradients above 4%,  $\tau$  stabilizes at values below 3 and is only weakly dependent on the gradient steepness.

<sup>5</sup> For smaller  $q$ , a strong nonlinear increase of the velocity is observed. Towards larger  $q$ , a qualitative change in the dynamics of the model takes place, when the two fixed points  $p_2$  and  $p_3$  coincide. In our case, this occurs for  $q = 2.297$ . For  $q > 2.297$ , the  $q$ -independent fixed point at  $p = 1$  becomes unstable while the  $q$ -dependent fixed point turns stable and takes values larger than one.

<sup>6</sup> The idealized response state is time independent. It is determined by the stationary profiles of  $a$  and  $b$  under the respective gradient stimulus.



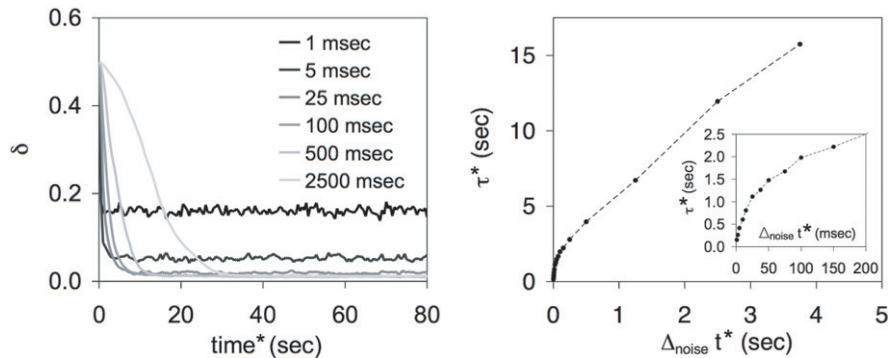


**Figure 6.** Dependence of the response time on the frequency of random perturbations. (a) Temporal evolution of the deviation  $\delta$  of the actual system state from the complete directional response for different average waiting times  $\Delta_{\text{noise}} t^*$  between perturbations, see main text for a definition of  $\delta$ . (b) Characteristic response time  $\tau^*$  obtained from exponential fits to the curves in panel (a). Asterisks denote quantities that carry a dimension, see appendix A.

**3.2.5. Influence of noise.** The presence of noise is an essential prerequisite for our bistable model of directional sensing. Without noise, the  $p$ -signaling system cannot initiate transitions between the two stable fixed points  $p_1$  and  $p_3$  in response to changes in the external signal  $S$ . As explained above, noise is indirectly taken into account by imposing localized perturbations that are randomly distributed in space and time (see the paragraph on equations and parameters at the beginning of this section). How does the response dynamics of the model depend on these random perturbations?

The essential parameter that influences the response dynamics is the waiting time between the application of individual perturbations. The waiting times are random and drawn from a uniform distribution between zero and some maximal waiting time. Two limiting cases can be distinguished. For infinitely long waiting times, no response to external stimuli will occur since no transitions from the quiescent state  $p = 0$  to the fixed point at  $p = 1$  are initiated. In the limit of waiting times that are much shorter than the characteristic timescale of the trigger wave velocity, the system is dominated by perturbations, so that no coherent response profile can form. We have performed a series of numerical simulations, in which we systematically investigated the influence of the average waiting time  $\Delta_{\text{noise}} t$  between perturbations on the response dynamics of the model. Again, we recorded the temporal behavior of the deviation  $\delta$  of  $p$  from the target response state  $\tilde{p}$ ; for a definition of  $\delta$  see equation (16).

In figure 6(a), the time evolution of  $\delta$  is shown for a number of different average waiting times  $\Delta_{\text{noise}} t$ . For small  $\Delta_{\text{noise}} t$ , the high frequency of perturbations prevent a relaxation to the complete response state and  $\delta$  takes a finite value different from zero. As  $\Delta_{\text{noise}} t$  increases,  $\delta$  is converging to values close to zero indicating a clear directional response of the system. However, for large  $\Delta_{\text{noise}} t$ , perturbations become rare and strongly increased decay times of  $\delta$  are observed. To quantify the characteristic decay times, an exponential decay function  $C e^{-t/\tau} + D$  is fitted to the  $\delta(t)$ -profiles. The resulting values of the characteristic response timescale  $\tau$  are displayed in figure 6(b). It shows a steep increase for short average waiting times and levels off to a linear increase for growing  $\Delta_{\text{noise}} t$ .

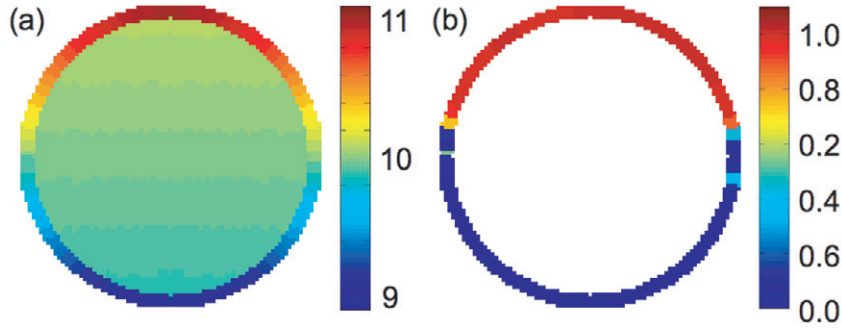


**Figure 7.** Example of a two-dimensional simulation of equations (1) and (5) with  $f$  as given in equation (11) on a circular domain. (a) The activator and inhibitor concentrations  $a$  and  $b$  are shown on the membrane and in the cytosol, respectively, for a 10% gradient across the cell. (b) Directional response of  $p$  on the membrane, corresponding to the activator/inhibitor distributions shown in (a). The parameters are  $k_1 = 200$ ,  $\tilde{k}_{-1} = 87$ ,  $k_2 = 0.14$ ,  $k_3 = 80$ ,  $\tilde{e}_0 = k_3/k_2$ ,  $k_+^a = k_-^a = 50$ ,  $\tilde{k}_+^a = 0.01$ ,  $k_+^b = k_-^b = 3$ ,  $\tilde{k}_+^b = 0.01$ ,  $D_P = 1$  (membrane diffusion of P),  $D_B = 100$  (cytosolic diffusion of B) and  $\Delta_{\text{noise}}t = 0.025$ .

**3.2.6. Two-dimensional example.** We have performed two-dimensional simulations of our model. Contrary to the previous computations, where the cytosolic concentration of the inhibitor B was taken proportional to the average stimulus across the cell  $\bar{s}$ , we now take cytosolic diffusion of B explicitly into account,

$$\frac{db}{dt} = k_+^b s + \tilde{k}_+^b - k_-^b b + D_B \nabla^2 b, \quad (17)$$

with  $D_B$  the corresponding cytosolic diffusion constant. Simulations were performed in polar coordinates on a circular domain of radius  $r = 4$ . Angle and radius were discretized with  $\Delta r = 0.2$  and  $\Delta \theta = 2\pi/80$ , respectively, the time step was  $\Delta t = 10^{-6}$  until  $t = 4$  and  $\Delta t = 10^{-4}$  for larger times.

In figure 7, an example of a simulation is displayed that corresponds to a two-dimensional cut through a circular cell. The cell is exposed to an extracellular gradient in S that points in the upward direction and changes by 10% across the cell. On the left-hand side, figure 7(a), the activator and inhibitor concentrations are shown on the membrane and in the cytosol, respectively. Note that due to the finite diffusion constant of B, a slight gradient in the cytosolic inhibitor concentration can be observed. In figure 7(b), the distribution of P along the membrane is displayed. It can be seen that two domains of  $p = 1$  and  $p = 0$  are formed that are connected by narrow interfaces in the regions where the activator and inhibitor concentrations are equal,  $a = b$ . These interfaces correspond to stationary trigger waves.

#### 4. Discussion

We have proposed a mechanism for directional sensing based on bistable dynamics of a membrane bound autocatalytic component P. Our model is constructed of two modules: the external signal S acts on a two-variable, LEGI-type activator/inhibitor system, which controls



the autocatalytic kinetics of a bistable species P. In section 3, we presented a kinetic example that fulfills the requirements for bistable directional sensing that were explained in section 2.

Let us summarize the predictions of our model. They do not depend on the specific choice of the kinetic equations (5) and (11) as long as the conditions explained in section 2 are fulfilled.

- (1) The response in  $p$  to a spatially uniform increase in  $s$  is uniform in space and transient in time.
- (2) The response to a gradient in  $s$  is asymmetric and bimodal in space, i.e.  $p = p_3$  in the front (towards higher  $s$ ) and  $p = p_1$  at the back of the cell (toward lower  $s$ ). It is stationary in time and can be reversed by reversing the direction of the external gradient stimulus.
- (3) The amplitude of responses in  $p$  to uniform and directional stimuli depends neither on the mean concentration of S nor on the steepness of gradients in S as long as condition (15) is not fulfilled. The reason for this is that the two stable fixed points  $p_1$  and  $p_3$  are independent of the external stimulus S.
- (4) There is a threshold to trigger a response in  $p$ , i.e. uniform stimuli have to exceed a certain minimal increase in  $s$  and directional stimuli have to exceed a minimum gradient steepness, see condition (15). This is due to an inhibitor concentration that exceeds the averaged activator levels as illustrated in figure 4(a) for the gradient case.
- (5) For a directional response, the membrane fraction with  $p = p_3$  decreases in size for decreasing steepness of the extracellular gradient. This can be seen from figure 4(a) as well.
- (6) The time it takes for an asymmetric distribution of  $p$  to establish depends on the gradient steepness, see figure 5. It increases for shallower gradients since the trigger wave velocity depends on the ratio of activator and inhibitor concentrations, see figure 4(b).

The properties (1) and (2) have been experimentally established and form the basis of previous LEGI-type directional sensing models [26]. To assess the validity of our present model, experiments are required that focus on the predictions (3)–(6). In particular, systematic mapping of the intracellular response as a function of the external gradient signal is needed. The one-dimensional simulations can then be compared to two-dimensional confocal cuts through the cell body.

Systematic experiments rely on techniques to produce well-controlled gradient signals with high spatiotemporal resolution. In the recent literature, several experimental efforts are reported to perform quantitative experiments on chemotaxis and on the intracellular rearrangement of proteins related to directional sensing [32, 33]. In particular, advances in microfluidic technology have opened up new perspectives to construct devices for quantitative migration experiments [8, 34, 35] and for well-controlled single cell stimulation, see [36] and references therein. In a recent publication, we have presented a technique for controlled directional stimulation of chemotactic cells based on the photochemical release of signaling substances in a microfluidic chamber [37]. We suggest that this approach may provide the basis to experimentally test the modeling predictions made here.

In earlier modeling work, it has been speculated that autocatalytic steps are involved in membrane phospholipid kinetics [17]. In the more recent literature, the role of phospholipid signaling is controversially discussed in the light of current experimental findings [38, 39]. It has been suggested that PI3K is not essential for directional movement under strong

stimuli but plays an important role for directional sensing in shallow gradients [40]. However, no ultimate consensus has been reached about the role of phosphoinositide signaling in the chemotactic pathway. In the present work, we therefore do not propose any explicitly biochemical assignment to the model components A, B and P. The specific reaction scheme that leads to equation (11) is a simplistic example, intended to illustrate the dynamics of a bistable directional sensing mechanism. It is not supported by direct biochemical evidence. Other kinetic schemes can be found that fulfill the assumptions of section 2 equally well.

We have proposed a generic mechanism of directional sensing that is based on bistable dynamics. In particular, our model combines a LEGI-type activator/inhibitor module with an additional bistable reaction. The activator/inhibitor part of the model does not involve any autocatalytic terms or other nonlinear interactions. Thus it will not generate any self-organized structures on its own. Only in combination with the additional bistable component are the characteristic properties of a pattern forming system introduced. This allows us to combine the advantages of a LEGI model—adaptation after uniform stimuli, independence of the midpoint concentration—with the switching dynamics of a bistable system. To show the desired dynamical behavior, only a number of general conditions have to be fulfilled (listed in section 2). As a result, we obtain a model that shows a clear and almost identical symmetry breaking over a large range of gradient input signals. This is in contrast to earlier models, where a dependence of the directional response on the gradient steepness [27] or the midpoint concentration is observed [15, 16]. In such models, nonlinear behavior is typically introduced directly at the level of the activator/inhibitor system. In comparison, our combined model allows for more flexibility in creating the desired response dynamics.

Similar to previous models of directional sensing, our model is restricted to the initial stages of gradient sensing. Note that this is only a limited part of the entire chemotactic process, which involves complex cytoskeletal mechanics and shape deformations leading to the formation of pseudopods and actual cell movement. An integral model that includes a description of cell polarization and motility remains the ultimate future goal of modeling efforts in this field.

## Acknowledgment

We thank Albert Bae for discussions.

## Appendix A. Dimensionless variables

Throughout this work, physical quantities have been non-dimensionalized by the reference quantities listed in table A.1. For example, the concentration of species X is given as the non-dimensional value

$$x = \frac{x^*}{c^*}, \quad (\text{A.1})$$

where  $x^*$  is the concentration in  $\text{mol l}^{-1}$ . Similarly, length and time parameters are normalized by  $l^*$  and  $t^*$ . Here, we have marked quantities that carry a dimension with an asterisk. The non-dimensionalized model parameters can be found in table A.2.

**Table A.1.** Reference quantities used to non-dimensionalize physical quantities.

Notation	Units	Quantity
$c^*$	$1 \text{ mol l}^{-1}$	Concentration
$t^*$	1 s	Time
$l^*$	$1 \mu\text{m}$	Length

**Table A.2.** Non-dimensionalized model parameters.

Parameter
$k_1 = k_1 * (c^*)^2 t^*$
$k_{-1} = k_{-1} * t^*$
$\tilde{k}_{-1} = \tilde{k}_{-1} c^* t^*$
$k_2 = k_2 * t^*$
$k_3 = k_3 * t^*$
$k_4 = k_4 * t^*$
$k_{-4} = k_{-4} * c * t^*$
$k_+^a = k_+^a t^*$
$\tilde{k}_+^a = \tilde{k}_+^a t^* / c^*$
$k_-^a = k_-^a t^*$
$k_+^b = k_+^b t^*$
$\tilde{k}_+^b = \tilde{k}_+^b t^* / c^*$
$k_-^b = k_-^b t^*$
$K = K * (c^*)^2$
$\tilde{K} = \tilde{K} / c^*$
$v = v * t^* / c^*$
$e_0 = e_0 * / c^*$
$\tilde{e}_0 = \tilde{e}_0^* c^*$
$D_{P,B} = D_{P,B} * t^* / (l^*)^2$

## Appendix B. Robustness

In the main text, several restrictions are imposed on the choice of the model parameters. Here, we will investigate the robustness of our model by relaxing the most severe of these restrictions.

### B.1. Relaxing the condition $K + 1 = \frac{v}{k_3}$

In the main text, we required  $K + 1 = v/k_3$ . This condition ensured that the fixed point  $p_3$  became  $p_3 = 1$ , independent of the external gradient. We will now drop this restriction. The Michaelis constant  $K$  still depends on the external gradient,  $K = (\tilde{k}_{-1}q + k_2)/k_1$ , but no relation with the maximal reaction velocity  $v$  is assumed. The parameter  $v$  may take a constant value, independently of  $K$ . Solving equation (12) gives the general expressions for the two fixed points

$$p_2 = \frac{e_1}{2} \left( 1 - \sqrt{1 - \frac{4K}{e_1^2}} \right), \quad (\text{B.1})$$

$$p_3 = \frac{e_1}{2} \left( 1 + \sqrt{1 - \frac{4K}{e_1^2}} \right), \quad (\text{B.2})$$

where we have introduced the notation  $e_1 = v/k_3$ . As  $K$  depends on the external gradient,  $p_3$  will now also change as a function of the gradient signal.

Optimally, parameters are chosen such that the trigger wave velocity is zero in the middle of the cell. This leads to a clearly defined, equally sized front and back part of the cell under gradient stimuli. The sign of the trigger wave velocity is determined by the integral in equation (2),  $A = \int_{p_1}^{p_3} f(p) dp$ . With  $f(p)$  as given in equation (11), we find

$$A = -k_3 \frac{p_3^2}{2} + vp_3 - v\sqrt{K} \arctan \left( \frac{p_3}{\sqrt{K}} \right) \quad (\text{B.3})$$

as the general form of equation (14) in the case of  $p_3 \neq 1$ . We now substitute the solution (B.2) for  $p_3$  into equation (B.3) and introduce the notation  $\gamma = K/e_1^2$ , where  $K \approx \tilde{K}q$  with  $\tilde{K} = (\tilde{k}_{-1} + k_2)/k_1$ ,  $\tilde{k}_{-1} \gg k_2$ . From equation (B.3) we then obtain

$$\frac{1}{4}(1 + \sqrt{1 - 4\gamma}) + \frac{\gamma}{2} - \sqrt{\gamma} \arctan \left[ \frac{1}{2\sqrt{\gamma}}(1 + \sqrt{1 - 4\gamma}) \right] = 0 \quad (\text{B.4})$$

as the condition for zero wave velocity. This equation can be solved numerically to yield  $\gamma \approx 0.21$ . In the middle of the cell, we have  $q = 1$  and  $K = \tilde{K}$ . Equation (B.4) thus restricts the choice of  $\tilde{K}$  and  $e_1$ , so that  $\tilde{K}/e_1^2 \approx 0.21$  is fulfilled.

### B.2. Dependence of $p_3$ on the external gradient

Relaxing the condition  $K + 1 = v/k_3$  introduces a dependence of  $p_3$  on the external gradient signal  $s = \bar{s}[1 + \alpha \sin(\frac{2\pi}{L}x)]$ , where  $x$  denotes the spacial coordinate running along the cell perimeter. How strong is this dependence? From equation (B.2) we can see that the variation of  $p_3$  with the external gradient is proportional to<sup>7</sup>

$$\sqrt{K} \propto \sqrt{\tilde{K} \frac{b}{a}} \propto \sqrt{\frac{1}{1 + \alpha \sin(\frac{2\pi}{L}x)}}. \quad (\text{B.5})$$

For small gradient steepness  $\alpha$  the maximal variation is proportional to  $\sqrt{1/(1+\alpha)} \approx 1 - \alpha/2$ . It becomes stronger for steeper gradients but does not depend on the midpoint concentration  $\bar{s}$ .

### B.3. Fluctuations in the choice of parameters: robustness

After relaxing the condition  $K + 1 = \frac{v}{k_3}$ , equation (B.4) led to a constraint in the choice of the ratio  $\tilde{K}/e_1^2$ . This constraint arose from the requirement that the trigger wave velocity should be zero in the middle of the cell. However, for a directional response to occur we do not need to fulfill this condition precisely. As long as the trigger wave velocity becomes zero *somewhere* inside the cell, we will observe a biphasic membrane response with one part of the membrane showing  $p = p_1$  and the other part showing  $p = p_3$ , although now the two parts will not be of

<sup>7</sup> We maintain the assumptions that  $\tilde{k}_{-1} \gg k_2$  and  $k_+^i \gg \tilde{k}_+^i$  for  $i = a, b$ .

equal size any more. Thus, we may allow for fluctuations in the parameters  $\tilde{K}$  and  $e_1$  as long as equation (B.4) is satisfied at some position  $x^*$  along the cell membrane, with  $0 < x^* < L$  and  $L$  the length of the cell perimeter.

Let us first assume that  $e_1$  is fixed and  $\tilde{K}$  may fluctuate, so that  $\tilde{K} \neq \gamma e_1^2$ , i.e. the trigger wave velocity will not be zero in the middle of the cell. Away from the cell center, we have  $q \neq 1$ . Here, a zero trigger wave velocity may result if  $\tilde{K}q = \gamma e_1^2$ . Note however that the ratio of activator and inhibitor concentrations  $q = b/a$  is determined by the external gradient  $s = \bar{s}[1 + \alpha \sin(\frac{2\pi}{L}x)]$ . The tolerable range of fluctuations in  $\tilde{K}$  will thus depend on the steepness  $\alpha$  of the external gradient. In particular, we obtain<sup>8</sup>.

$$(1 - \alpha)\gamma e_1^2 < \frac{\tilde{k}_{-1} + k_2(1 - \alpha)}{k_1} \quad (\text{B.6})$$

and

$$(1 + \alpha)\gamma e_1^2 > \frac{\tilde{k}_{-1} + k_2(1 + \alpha)}{k_1}. \quad (\text{B.7})$$

From this estimate we conclude that we will observe a biphasic response as long as fluctuations in  $\tilde{K}$  remain on the order of the gradient steepness. Similar relations are found for fluctuations in  $e_1$ , i.e.  $v$  and/or  $k_3$ , while keeping  $\tilde{K}$  constant.

## References

- [1] Clark R 1996 *The Molecular and Cellular Biology of Wound Repair* (New York: Plenum)
- [2] Condeelis J, Singer R H and Segall J E 2005 The great escape: when cancer cells hijack the genes for chemotaxis and motility *Annu. Rev. Cell Dev. Biol.* **21** 695–718
- [3] Orourke N A, Dailey M E, Smith S J and McConnell S K 1992 Diverse migratory pathways in the developing cerebral-cortex *Science* **258** 299–302
- [4] Berg H C 2003 *E. coli in Motion* (New York: Springer)
- [5] Van Haastert P J M and Devreotes P N 2004 Chemotaxis: signalling the way forward *Nat. Rev. Mol. Cell Biol.* **5** 626–34
- [6] Zigmond S H 1977 Ability of polymorphonuclear leukocytes to orient in gradients of chemotactic factors *J. Cell Biol.* **75** 606–16
- [7] Fisher P R, Merkl R and Gerisch G 1989 Quantitative-analysis of cell motility and chemotaxis in *Dictyostelium discoideum* by using an image-processing system and a novel chemotaxis chamber providing stationary chemical gradients *J. Cell Biol.* **108** 973–84
- [8] Song L, Nadkarni S M, Bödeker H U, Beta C, Bae A, Franck C, Rappel W-J, Loomis W F and Bodenschatz E 2006 *Dictyostelium discoideum* chemotaxis: threshold for directed motion *Eur. J. Cell Biol.* **85** 981–9
- [9] Parent C A and Devreotes P N 1999 A cell's sense of direction *Science* **284** 765–70
- [10] Manahan C L, Iglesias P A, Long Y and Devreotes P N 2004 Chemoattractant signaling in *Dictyostelium discoideum* *Annu. Rev. Cell Dev. Biol.* **20** 223–53
- [11] Charest P G and Firtel R A 2006 Feedback signaling controls leading-edge formation during chemotaxis *Curr. Opin. Genet. Dev.* **16** 339–47
- [12] Levchenko A and Iglesias P A 2002 Models of eukaryotic gradient sensing: application to chemotaxis of amoebae and neutrophils *Biophys. J.* **82** 50–63

<sup>8</sup> For simplicity, we have assumed that  $k_+^i = k_-^i$  for  $i = a, b$  as in the main text.

- [13] Ma L, Janetopoulos C, Yang L, Devreotes P N and Iglesias P A 2004 Two complementary, local excitation, global inhibition mechanisms acting in parallel can explain the chemoattractant-induced regulation of PI(3,4,5)P<sub>3</sub> response in *Dictyostelium* cells *Biophys. J.* **87** 3764–74
- [14] Rappel W J, Thomas P J, Levine H and Loomis W F 2002 Establishing direction during chemotaxis in eukaryotic cells *Biophys. J.* **83** 1361–7
- [15] Postma M and Van Haastert P J M 2001 A diffusion-translocation model for gradient sensing by chemotactic cells *Biophys. J.* **81** 1314–23
- [16] Meinhardt H 1999 Orientation of chemotactic cells and growth cones: models and mechanisms *J. Cell Sci.* **112** 2867–74
- [17] Narang A, Subramanian K K and Lauffenburger D A 2001 A mathematical model for chemoattractant gradient sensing based on receptor-regulated membrane phospholipid signaling dynamics *Ann. Biomed. Eng.* **29** 677–91
- [18] Subramanian K K and Narang A 2004 A mechanistic model for eukaryotic gradient sensing: spontaneous and induced phosphoinositide polarization *J. Theor. Biol.* **231** 49–67
- [19] Meier-Schellersheim M, Xu X H, Angermann B, Kunkel E J, Jin T and Germain R N 2006 Key role of local regulation in chemosensing revealed by a new molecular interaction-based modeling method *PLoS Comput. Biol.* **2** 710–24
- [20] van Haastert P J M and Postma M 2007 Biased random walk by stochastic fluctuations of chemoattractant-receptor interactions at the lower limit of detection *Biophys. J.* **93** 1787–96
- [21] Wang K, Rappel W J, Kerr R and Levine H 2007 Quantifying noise levels of intercellular signals *Phys. Rev. E* **75** 061905
- [22] Kimmel J M, Salter R M and Thomas P J 2006 An information theoretic framework for eukaryotic gradient sensing *Adv. Neural Inform. Process. Syst.* **19** 705–12
- [23] Ueda M and Shibata T 2007 Stochastic signal processing and transduction in chemotactic response of eukaryotic cells *Biophys. J.* **93** 11–20
- [24] Gamba A, de Candia A, Di Talia S, Coniglio A, Bussolino F and Serini G 2005 Diffusion-limited phase separation in eukaryotic chemotaxis *Proc. Natl Acad. Sci. USA* **102** 16927–32
- [25] Gamba A, Kolokolov I, Lebedev V and Ortenzi G 2007 Patch coalescence as a mechanism for eukaryotic directional sensing *Phys. Rev. Lett.* **99** 158101
- [26] Janetopoulos C, Ma L, Devreotes P N and Iglesias P A 2004 Chemoattractant-induced phosphatidylinositol 3,4,5-trisphosphate accumulation is spatially amplified and adapts, independent of the actin cytoskeleton *Proc. Natl Acad. Sci. USA* **101** 8951–6
- [27] Levine H, Kessler D A and Rappel W J 2006 Directional sensing in eukaryotic chemotaxis: a balanced inactivation model *Proc. Natl Acad. Sci. USA* **103** 9761–6
- [28] Andrew N and Insall R H 2007 Chemotaxis in shallow gradients is mediated independently of ptdins 3-kinase by biased choices between random protrusions *Nat. Cell Biol.* **9** 193–1
- [29] Killich T, Plath P J, Hass E C, Xiang W, Bultmann H, Rensing L and Vicker M G 1994 Cell-movement and shape are nonrandom and determined by intracellular, oscillatory rotating waves in *Dictyostelium amebas* *Biosystems* **33** 75–87
- [30] Cross M C and Hohenberg P C 1993 Pattern formation outside of equilibrium *Rev. Mod. Phys.* **65** 851
- [31] Mikhailov A S 1994 *Foundations of Synergetics I* (Berlin: Springer)
- [32] Xu X H, Meier-Schellersheim M, Jiao X M, Nelson L E and Jin T 2005 Quantitative imaging of single live cells reveals spatiotemporal dynamics of multistep signaling events of chemoattractant gradient sensing in *Dictyostelium* *Mol. Biol. Cell* **16** 676–88
- [33] Samadani A, Mettetal J and van Oudenaarden A 2006 Cellular asymmetry and individuality in directional sensing *Proc. Natl Acad. Sci. USA* **103** 11549–54
- [34] Jeon N L, Baskaran H, Dertinger S K W, Whitesides G M, Van de Water L and Toner M 2002 Neutrophil chemotaxis in linear and complex gradients of interleukin-8 formed in a microfabricated device *Nat. Biotechnol.* **20** 826–30

- [35] Herzmark P, Campbell K, Wang F, Wong K, El-Samad H, Groisman A and Bourne H R 2007 Bound attractant at the leading versus the trailing edge determines chemotactic prowess *Proc. Natl Acad. Sci. USA* **104** 13349–54
- [36] Breslauer D N, Lee P J and Lee L P 2006 Microfluidics-based systems biology *Mol. Biosyst.* **2** 97–112
- [37] Beta C, Wyatt D, Rappel W-J and Bodenschatz E 2007 Flow photolysis for spatiotemporal stimulation of single cells *Anal. Chem.* **79** 3940–4
- [38] Loovers H M, Postma M, Keizer-Gunnink I, Huang Y E, Devreotes P N and van Haastert P J M 2006 Distinct roles of PI(3,4,5)P<sub>3</sub> during chemoattractant signaling in dictyostelium: a quantitative *in vivo* analysis by inhibition of PI3-kinase *Mol. Biol. Cell* **17** 1503–13
- [39] Hoeller O and Kay R R 2007 Chemotaxis in the absence of PIP3 gradients *Curr. Biol.* **17** 813–7
- [40] Takeda K, Sasaki A T, Ha H J, Seung H A and Firtel R A 2007 Role of phosphatidylinositol 3-kinases in chemotaxis in *Dictyostelium*. *J. Biol. Chem.* **282** 11874–84

## Chapter 3

# Directional sensing of *D. discoideum*

In the previous chapter, we gave an overview of different models of directional sensing. We now turn to experiments in order to validate or infirm the suggested theoretical mechanisms. We used a combination of microfluidics and caged-component photolysis to apply well-defined gradients of chemoattractant to chemotactic *D. discoideum* cells. One commonly used marker of directional sensing is the Pleckstrin-Homology domain of CRAC, the Cytosolic Regulator of Adenylyl Cyclase (PH<sub>CRAC</sub>). In our work, we used mutants expressing PH<sub>CRAC</sub> – GFP, enabling us to directly observe the intracellular dynamics of PH<sub>CRAC</sub>. When the cell senses a gradient of cAMP, PH<sub>CRAC</sub> – GFP is recruited to the front of the cell, where the concentration of external chemoattractant is maximal. Two successive phases of PH<sub>CRAC</sub> – GFP translocation have been reported [132] (see section 3.1). In our experiments, we quantified the first phase of PH<sub>CRAC</sub> – GFP translocation in different gradients of cAMP, keeping the relative gradient fixed but varying the absolute value of the gradient. We compared the translocation of PH<sub>CRAC</sub> – GFP for cells in gradients with the one for cells stimulated with a uniform concentration of cAMP. It was found that both experiments gave similar results if the total number of occupied receptors were similar, indicating that the first phase of PH<sub>CRAC</sub> – GFP translocation in a gradient is a local effect, not the result of the comparison of the number of occupied receptors between the two ends of the cells.

### 3.1 Overview of the chemotaxis pathway

As already mentioned in the first chapter of this thesis, *D. discoideum* becomes chemotactic to cAMP after about 5 hours of starvation. Over the past years, a large amount of research has been done to understand the chemotaxis mechanism in *D. discoideum*. However, the details of the chemotactic pathway are still not well known, as we miss both a knowledge of part of the players molecular of chemotaxis, and on how these players interact with one another. In this section, we will give a very short overview of the chemotactic pathway relevant to our experiments. For a more complete view, the reader is referred to chapter 1 and references therein. The part of the cell which is closer to the chemoattractant source will be called the front of the cell, while the part of the cell in the region where the chemoattractant concentration is the lowest will be called the back of the cell. When the cell is crawling by extending pseudopods, we call the part of the membrane from which the pseudopod is projected the leading edge. An illustration of the chemotactic pathway taken from a recent review by Bagorda and Parent [6] is shown on figure 3.1.





### 3.1.1 The cAMP receptors

Cells that are chemotactic are able to sense a gradient of chemoattractant concentration. In *D. discoideum*, four different receptors that bind the chemoattractant cAMP were identified, labeled cAR1 to cAR4 [81]. These receptors are expressed sequentially throughout the development of *D. discoideum* and for our matter, the most relevant receptor is cAR1. After 6 hours of starvation, about 70 000 of these receptors are uniformly expressed over the cell membrane, in the presence or absence of a chemoattractant [82]. There is no spatial rearrangement of cAR1 on the membrane during chemotaxis[131].

cAR1 is linked to a guanine nucleotide-binding protein (G-protein). The G-protein is trimeric, and its subunits are called  $\alpha$ ,  $\beta$  and  $\gamma$ . When activated, the  $\alpha$  subunit loses a GDP, which is replaced by a GTP. Moreover, the  $\alpha$  subunit dissociates from  $\beta\gamma$ , that form a dimeric subunit. Thirteen  $\alpha$  subunits have been identified, numbered from  $\alpha_1$  to  $\alpha_{13}$ . In *D. discoideum*, cAR1 is linked to the  $G\alpha_2\beta\gamma$  protein [113]. Like the cAR1 receptors, the G proteins are always uniformly distributed on the cell membrane [82]. They remain dissociated as long as receptors are occupied [51].

### 3.1.2 Downstream pathway in a very small nutshell (see figure 3.2)

After the dissociation of  $G\alpha$  from  $G\beta\gamma$ , the  $\beta\gamma$  subunit acts as the main transducer of chemotactic signals [6], and is probably a subunit that is necessary and sufficient for the transmission of the cAMP signal [111]. The  $G\beta\gamma$  activates Ras at the front of the cell, which in turn activates the phosphoinositide 3-kinase (PI3K). This enzyme converts the membrane-bound phospholipid phosphatidylinositol (4,5)-biphosphate (PIP2) into phosphatidylinositol (3,4,5)-triphosphate (PIP3). At the same time, phosphatase and tensin homolog (PTEN) localizes at the back and side of the cell, most likely under the regulation of a phospholipase called PLC [64]. PTEN degrades PIP3 into PIP2, so that a gradient of PIP3 is formed along the cell membrane, with PIP3 at the front of the cell and not at the back. It is important to underline that the initial symmetry-breaking of the cell (*i.e.* the initial localized activation of Ras) is still not understood.

As stated, an intracellular<sup>1</sup> gradient of PIP3 is formed. Knowing the shape of this gradient was one of the aims of the experimental work presented in this chapter. PIP3 has a binding site for pleckstrin-homology (PH) domain proteins. In *D. discoideum*, these proteins include CRAC (cytosolic regulator of adenylyl cyclase), PhdA (PH-domain-containing protein) and Akt/PKB (protein kinase B). These proteins serve as proxies for the observation of PIP3 on the membrane: when the cells are not stimulated, PH-domain proteins are uniformly distributed in the cytosol, and they translocate to the membrane sites where PIP3 is formed after PI3K activation (see figure 3.2 for a simple sketch of the pathway). In our experiments, we used a GFP construct, PH<sub>CRAC</sub> – GFP, to monitor the localization and amount of PH<sub>CRAC</sub> in the cell.

### 3.1.3 Cytoskeleton regulation

A rearrangement of the cytoskeleton, particularly actin polymerization at the front and actomyosin network formation at the back are necessary for cell motion. How does the pathway

---

<sup>1</sup>Note that “intracellular” does not mean “cytosolic”: PIP3 is bound to the cell membrane, and the gradient of PIP3 is therefore intracellular, along the cell membrane.

### 3.1. Overview of the chemotaxis pathway

---

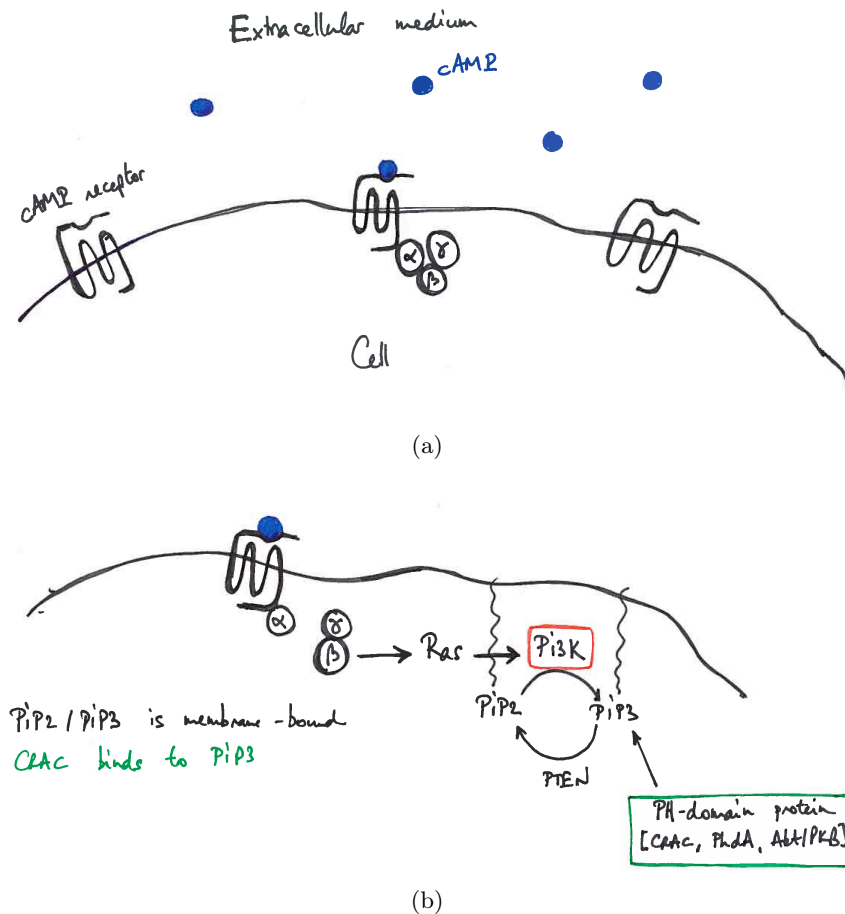


Figure 3.2: (a) cAMP binds to the cAR receptor, which is coupled to a  $G\alpha\beta\gamma$  protein. (b) After binding of cAMP,  $G\beta\gamma$  dissociates from  $G\alpha$  and activates Ras, which activates PI3K, which phosphorylates the membrane-bound phospholipid PIP2 into PIP3. Thereafter, proteins that have a PH-domain, like CRAC, can bind to PIP3.

mentioned above influence the direction of motion? The answer is not yet clear. What we mention here was taken from a review by Bagorda and Parent [6].

At the front of the cell, Rac guanine-nucleotide-exchange factors (GEFs), that contain a PH-domain, activate small G proteins called Rac (small G proteins are proteins homologous to the  $G\alpha$  unit of the G trimeric protein). Rac effectors of the WASP (Wiskott-Aldrich syndrome protein) and SCAR/WAVE (suppressor of cAMP receptor mutation) family activate in their turn the Arp2/3 (actin related proteins 2 and 3) complex. Arp2/3 is a protein stimulating actin polymerization by initiating new barbed ends at the end of an existing actin filament. At the back of the cell, myosin II assembly is controlled by cGMP (cyclic GMP) and PAKa. Experiments suggested that PAKa is itself activated by Akt [63].

### 3.1.4 Feedback loops

Of course, the reactions mentioned above are just part of the known biochemical players and of the way they interact with each other. There is for example an indication that a G protein-independent Ras/PI3K/F-actin circuit regulates the basic cell motility [96]. We do not know if and how this circuit is interrupted during chemotaxis. It is however known that F-actin is not necessary for PI3K signaling in a gradient, as cells that are treated with Latrunculin A (a drug preventing actin polymerization, presumed to bind in a 1:1 way to actin monomers [134]) still show PH-domain localization at their front [80, 82] (see figure 3.3), even though PI3K does not translocate to the front of the cell [95]. This would suggest the existence of a low basal level of PI3K associated to the membrane before stimulation, which is activated by Ras upon stimulation [95].

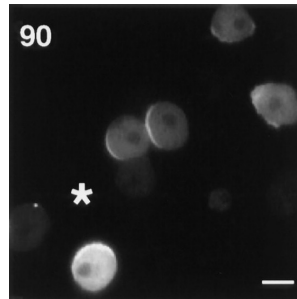


Figure 3.3: Visualization of CRAC in cells treated with Latrunculin A, an inhibitor of actin polymerization. The asterisk indicates the position of the micropipette out of which cAMP diffuses. The cells have been stimulated for 90 seconds. Scale bar: 12  $\mu\text{m}$ . Picture taken from [80].

### 3.1.5 More details on the PI3K/PTEN pathway and plan of attack

By using mutants lacking PI3K, Hoeller and Kay showed in [44] that chemotaxis could occur without intracellular gradients of PIP3. However, the values of the gradients needed to elicit chemotaxis in PI3K-null mutants were not mentioned in [44]. Van Haastert et al. then showed in [121] that the PI3K pathway was crucial to chemotaxis in shallow gradients, and the translocation of  $\text{PH}_{\text{CRAC}} - \text{GFP}$  at shallow gradients was reported by Bosgraaf et al. [15]. However, the term “shallow gradient” is ill-defined: what is reported as a shallow gradient



### 3.1. Overview of the chemotaxis pathway

in [15] is an absolute gradient of  $500 \text{ pM}/\mu\text{m}$  of cAMP. Still, not much is known about the effect of the midpoint concentration of cAMP on directional sensing. Calling  $c_0$  the midpoint concentration of cAMP and  $\Delta c$  the difference of concentration between front and middle of the cell, we define the relative gradient as  $\Delta c/c_0$ . It is unclear if the important quantity to take into account is the relative gradient, or the absolute difference of concentration  $\Delta c$ . It has been argued by Janetopoulos et al. that the relative gradient was the most important factor determining  $\text{PH}_{\text{CRAC}}-\text{GFP}$  translocation [52]. This led to a model based on a local activation, global inhibition mechanism (LEGI, see chapter 2) [52, 70]. On the other hand, Xu et al. argued that at constant relative gradients, the translocation of  $\text{PH}_{\text{CRAC}}-\text{GFP}$  showed different behaviors depending on the midpoint concentration used [132]. A detailed and complex model of the cell's directional sensing pathway was developed by Meier-Schellersheim et al. [72], which accounts for the observations made by Xu et al. This model differs significantly from the LEGI model as one of its key components is a *local* inhibitor, whose biological identity yet has to be found. The existence of such a local inhibitor was however strongly suggested by further experiments of Xu et al., reported in [133]. One of the biological issues with the model of Meier-Schellersheim et al. is that it assumes recruitment of PI3K to the membrane of the cell. However, in the case of cells treated with Latrunculin, no such recruitment has been shown to occur [95]. As Xu et al. used Latrunculin-treated cells, the model published in [72] is likely not the final answer to the directional sensing mechanism, even if it correctly reproduces the experimental results of [132].

Xu et al. reported a biphasic translocation of  $\text{PH}_{\text{CRAC}}-\text{GFP}$  to the cell membrane [132, 72]. The second phase of translocation was always found to be directional. It is the translocation reported by Bosgraaf et al. in [15]. The first phase of translocation was found to be either uniform or directional, depending on the value of the midpoint concentration used (see figure 3.4). At a high midpoint concentration ( $1 \mu\text{M}$ ), the first translocation was uniform, while it was asymmetric at midpoint concentrations smaller than  $100 \text{ nM}$  [72]. In these experiments, the relative gradient  $p$  was kept fixed ( $p = 0.33$ ) and the midpoint concentration  $c_0$  was varied. Calling  $R$  the cell radius ( $R = 5 \mu\text{m}$  [132]), and taking the origin of our coordinate system in the center of the cell, the concentration profile is then written as:  $c(y) = c_0(1 + \frac{p}{R}y)$  for  $-R \leq y \leq R$ .

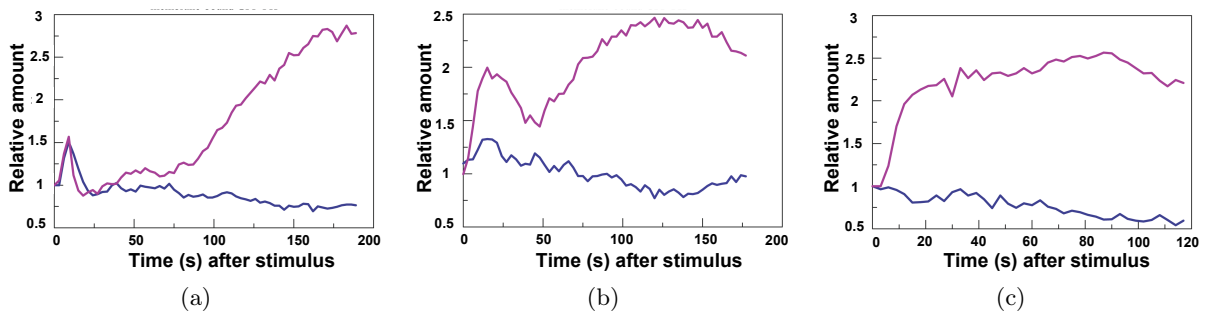


Figure 3.4: Translocation of  $\text{PH}_{\text{CRAC}}-\text{GFP}$  to the cell membrane for different gradients  $c(y) = c_0(1 + p/Ry)$ . The relative gradient was fixed to  $p = 0.33$ . Purple curve: front of the cell. Blue curve: back of the cell. (a)  $c_0 = 1 \mu\text{M}$  (b)  $c_0 = 100 \text{ nM}$ . (c)  $c_0 = 10 \text{ nM}$ . The back of the cell only shows a translocation for  $c_0 = 1 \mu\text{M}$ . Graphs taken from [72].

In [132], the authors used a micropipette to create their gradients. To observe the establishment of the gradient, they mixed the red fluorescent dye Alexa 594 with the cAMP. We retrieved the fluorescence information from one of their published movies showing the evolution of the gradient with time (see figure 3.5). To establish the gradient, a micropipette was first positioned 1 mm away from a cell and then quickly moved within 100  $\mu\text{m}$  of the cell. The evolution of the concentration profile with time at a distance  $d$  from the pipette center can then be expressed with the help of the complementary error function [84]:

$$c(d, t) = \frac{\alpha}{d} \operatorname{erfc} \left( \frac{1}{2} \frac{d - r_0}{\sqrt{Dt}} \right) \quad (3.1)$$

where  $r_0$  is the radius of the pipette,  $\alpha$  depends on the concentration of chemical in the pipette, and  $D$  the diffusion coefficient of the chemical considered. The characteristic time scale for the establishment of the gradient is then given by  $\tau = (d - r_0)^2 / (2D)$ . In the case of Xu et al., we found from their movie that at the back of the cell,  $\tau \sim 1.6$  s, while at the front  $\tau \sim 1.0$  s. This implies that the concentration profile reaches 50% of its steady state value in roughly 11 seconds. Because the first translocation of PH<sub>CRAC</sub> – GFP occurs within the first 10 seconds of stimulation, one may therefore ask what is the influence of this varying concentration profile of cAMP on the response.

In our work, we will combine the use of microfluidics and chemical photolysis to establish stable spatial gradients in a time of the order of 1 second [10, 5]. The main aim of our work is to quantify the first PH<sub>CRAC</sub> – GFP translocation in stable gradients. Xu et al. reported that the spatial extent of the first translocation of PH<sub>CRAC</sub> – GFP depended on the midpoint concentration of cAMP, but used only 3 different midpoint concentrations. We aim at taking more quantitative data and see how the influence of the midpoint concentration is reflected in the PIP3 formation. Moreover, we do not know how the amount of PH<sub>CRAC</sub> – GFP *i.e.* the amount of PIP3 locally produced depends on the gradient used: do gradients eliciting a bigger translocation also lead to more local production of PIP3? Last, all experiments made by Xu et al. and Janetopoulos et al. involve cells treated with Latrunculin. To evaluate the importance of the actin cytoskeleton in the first phase of PH<sub>CRAC</sub> – GFP translocation, we will not use Latrunculin-treated cells in our experiments.

## 3.2 Experiment

As just mentioned, the aim of the experiment is to quantify the early response of *D. discoideum* to given gradients of cAMP. By early response, we here mean the first translocation of PH<sub>CRAC</sub> – GFP to the membrane, which is one of the first tractable intracellular directional events. We needed to apply a temporally stable gradient of cAMP to different cells. Moreover, the establishment of the gradient was meant to be as fast as possible. For this purpose, the use of caged compounds in microfluidics seemed to be an adapted technique: as shown in [10], a stable gradient of cAMP can then be reached in roughly a second, and Bae et al. showed that uncaging a component upstream of a cell was the fastest way to deliver it to the cell [5]. A total of 428 different cells were stimulated. Each cell was stimulated only one time.

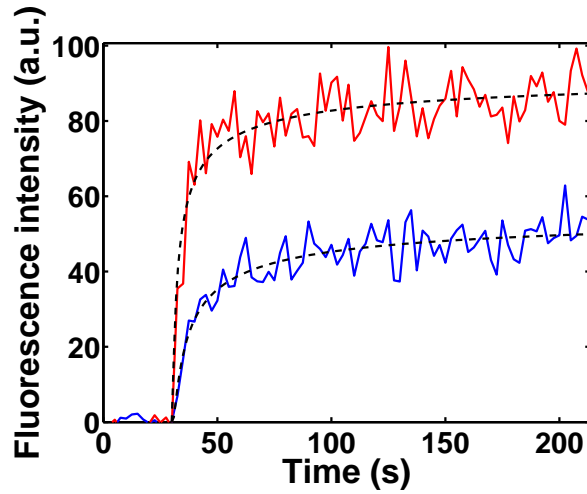


Figure 3.5: Evolution of the concentration of cAMP at the front of the cell (red) and at its back (blue). The pipette is brought within  $100 \mu\text{m}$  of the cell at time  $t = 30 \text{ s}$ . The data were fitted with a complementary error function (dashed lines). The characteristic time scales were found to be  $\tau \sim 1.6 \text{ s}$ , and  $\tau \sim 1.0 \text{ s}$  at the back and front of the cell, respectively. The concentration profile reaches 50% of its steady-state value in roughly 11 seconds. Data extracted from supplementary video 6 in [132].

### 3.2.1 Caged cAMP

#### Principle

A caged compound is a species that remains biologically inert until it is activated by light. The molecule that we aim to activate is bound to a chemical group, the cage, that hinders the natural biological activity of the considered molecule. The bond between the molecule and the cage is photolabile, that is it can be broken when light is flashed on it. Typically, the light is in the UV range, with a wavelength around  $350 \text{ nm}$  [1, 41]. In our case, *D. discoideum* are responsive to cAMP so we will use caged cAMP, with a 4,5-dimethoxy-2-nitrobenzyl (DMNB) caging group (Invitrogen, Carlsbad, CA). cAMP as well as its caged version are shown on figure 3.6.

We used a near-UV laser ( $\lambda = 405 \text{ nm}$ ) to uncage the cAMP. The absorption spectrum of DMNB-caged cAMP is shown on figure 3.7. The absorption at  $405 \text{ nm}$  is approximately 10% only of that at  $350 \text{ nm}$ , where the uncaging efficiency is maximal [78]. An estimation of the amount of released material in our experiments is reported in the next section.

#### Combination with microfluidics

One way to create a gradient would be to put the cells on a Petri dish in a solution of caged cAMP, and uncage cAMP next to them. However, the gradient produced in this way would be varying with time: the profile of concentration builds up as the uncaging takes place, and is then smeared out by diffusion. For this reason, we flowed caged cAMP in a microfluidic channel, and uncaged on a spot. The uncaged cAMP was then advected with the flow, and established a gradient in the direction perpendicular to the flow. The use of microfluidics also

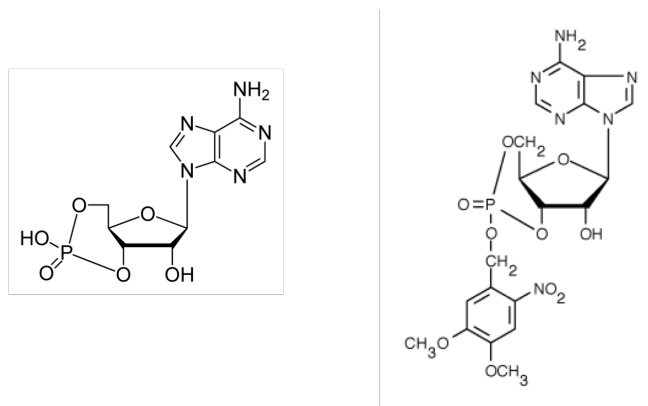


Figure 3.6: cAMP (left) and DMNB caged cAMP (right).

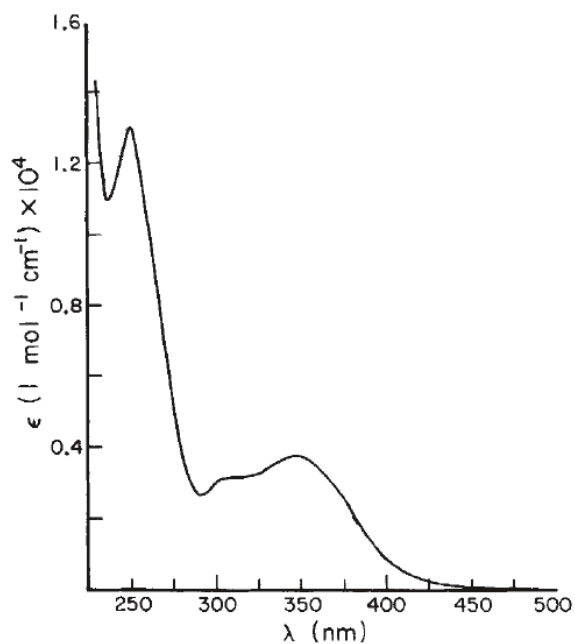


Figure 3.7: Absorption spectrum of DMNB caged cAMP. Irradiation at wavelengths between 280 and 420 nm results in the liberation of free cAMP [78]. We used a near-UV laser at  $\lambda = 405$  nm to uncage the cAMP. At such wavelength, the uncaging efficiency is not maximal and only a fraction of the caged cAMP was uncaged. Figure taken from [78].



## 3.2. Experiment

---

enabled us to stimulate each time previously unstimulated cells: by starting to uncage cAMP next to cells located downstream of the channel and stimulating cells that were always more upstream, we are sure that the cells had been stimulated only once. Moreover, microfluidics prevented intercellular communication and ensured that cellular waste products were washed away.

### 3.2.2 Microfluidics

#### Principle

The microfluidic channels were built using standard soft lithography techniques, see *e.g.* [129] for a review and [76] for our precise protocol. The channels used were simple straight channels, 25  $\mu\text{m}$  high, 500  $\mu\text{m}$  wide and 3 cm long (see figure 3.8). After loading the cells in the channel, a gentle flow of caged cAMP was applied (5  $\mu\text{L/hr}$ , which corresponded to an average velocity of 111  $\mu\text{m/s}$ ).

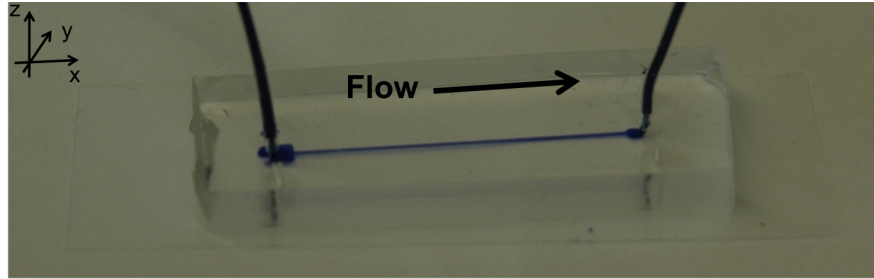


Figure 3.8: Microfluidic channels used for the directional sensing experiments. The cells are loaded in the channel, and caged cAMP is then flown through one of the inlets. The  $x$  axis is in the direction of the flow.

#### Flow profile in the channel

The flow profile can be calculated making several approximations. The Reynolds number, measuring the relative importance of inertia and viscosity, is given by:

$$\text{Re} = \frac{UL}{\nu} \quad (3.2)$$

where  $U$  is the characteristic flow speed,  $L$  a characteristic length scale and  $\nu$  is the kinematic viscosity. In our case,  $U \sim 100 \mu\text{m/s}$ ,  $L = 25 \mu\text{m}$  is the height of the channel and  $\nu = 10^{-6} \text{m}^2/\text{s}$ , so  $\text{Re} \sim 10^{-4} \ll 1$ . The flow is laminar and dominated by viscosity. The equations we have to solve to get the flow profile are therefore:

$$-\nabla p + \mu \Delta \mathbf{u} = 0 \quad (3.3)$$

$$\nabla \cdot \mathbf{u} = 0 \quad (3.4)$$

where  $p$  is the pressure,  $\mu$  is the dynamic viscosity of water, and  $\mathbf{u}$  is the flow velocity. The aspect ratio of the microfluidic device is moreover much bigger than one, as the channel width

is 20 times bigger than its height. In this case, we can make the lubrication approximation, leading to a parabolic flow profile in  $z$ :

$$u(z) = \frac{3}{2}\bar{u} \left[ 1 - 4 \left( \frac{2z}{L} \right)^2 \right] \quad (3.5)$$

where we have taken the origin of the  $z$  axis in the middle of the channel, called  $\bar{u}$  the mean speed of the flow and  $L$  the height of the channel. In the  $y$  direction, the flow profile is essentially plug-like.

### 3.2.3 Gradient of cAMP

In this part, we derive analytically the concentration profile of cAMP around the cell, and estimate the amount of uncaged material.

#### Concentration profile of cAMP

**Experiment** We used a near-UV laser ( $\lambda = 405, \text{nm}$ ) mounted on a confocal microscope (Olympus Fluoview 1000) to perform the uncaging. In the focal plane, the uncaging region was a spot of radius  $1.6 \mu\text{m}$ . The uncaging was monitored using DMNB-caged fluorescein. Fluorescein is, as its name suggests, a fluorescent molecule that has its peak absorption at around  $500 \text{ nm}$  and its peak emission around  $520 \text{ nm}$  (see figure 3.12a). When it is caged however, the fluorescence disappears. DMNB-caged fluorescein was flown at  $111 \mu\text{m/s}$  in an empty microfluidic channel, and the uncaging laser was turned on for 30 seconds. The uncaged fluorescein was both advected with the flow and diffused in the direction perpendicular to the flow. The stationary fluorescein profile thus obtained is shown on figure 3.9. In the region where the cell would typically be, the concentration profile was approximately linear (figure 3.9b). However, fluorescein has a diffusion coefficient  $D_{\text{fluo}} = 364 \mu\text{m}^2/\text{s}$  [4], different from the diffusion coefficient of cAMP  $D_{\text{cAMP}} = 444 \mu\text{m}^2/\text{s}$  [26]. The concentration profile of uncaged cAMP is therefore different from the profile of uncaged fluorescein. We now show how to recover analytically both of these profiles.

**Analytic solution** We described the evolution of the concentration  $c(x, y, t)$  of uncaged material by the following convection-diffusion equation:

$$\frac{\partial c}{\partial t} + u(z) \frac{\partial c}{\partial x} = D \left( \frac{\partial^2 c}{\partial x^2} + \frac{\partial^2 c}{\partial y^2} \right) + a \delta(x) \delta(y) \quad (3.6)$$

where  $u(z)$  is the flow speed (see section 3.2.2),  $a$  is the uncaging rate, and  $D$  is the diffusion coefficient of the chemical considered (fluorescein or cAMP). The uncaging is idealized as a point source positioned at the origin. This equation would be complex to solve, but can be simplified thanks to an elegant argument due to Taylor [115]. Taylor considered a flow in a cylindrical channel of radius  $R$ , and asked how an infinitesimally thin stripe of chemical would evolve in this pipe (figure 3.10). Diffusion was neglected in the direction of the flow, and considered only in the radial direction. As shown on figure 3.10, the stripe will tend to be stretched, following the parabolic flow profile  $u(r) = u_0(1 - r^2/R^2)$ . At the same time however, the chemical will diffuse across the channel and its concentration profile will be smoothed. The characteristic time needed to obtain a homogeneous profile of concentration

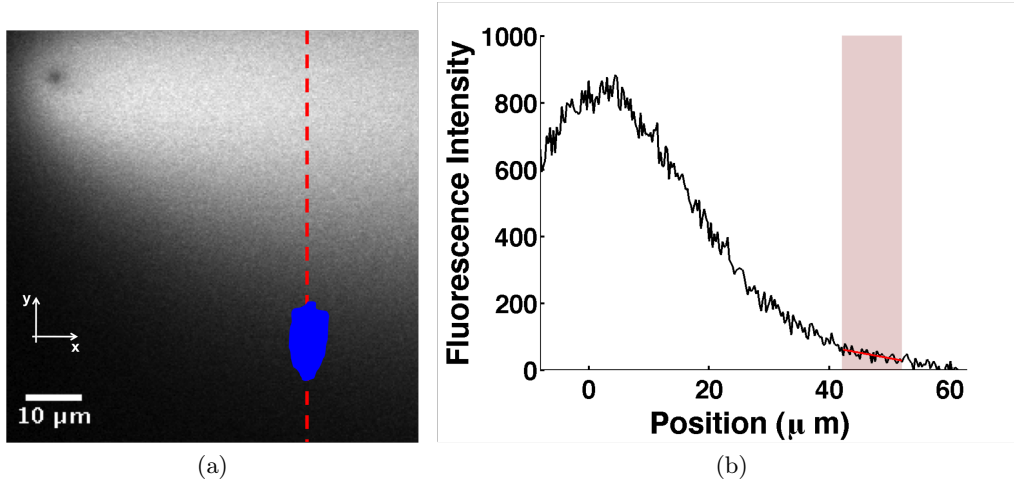


Figure 3.9: (a) Stable fluorescein profile. The uncaging laser was focused in the upper left corner, at the position of the black spot. This black spot is due to the photobleaching of the caged fluorescein under the uncaging laser. A sketch of the cell is shown in blue. (b) Concentration profile of fluorescein along the vertical dashed line shown on figure (a). The cell's approximate position is indicated by grayed area. At the cell's scale, the concentration profile is approximately linear. The red solid line shows the linear approximation of the concentration profile around the cell.

in the radial direction is approximately  $\tau \sim R^2/D$ . The concentration profile is then a plug of width approximately  $W \sim u_0\tau$ , where  $u_0$  is the maximal flow velocity, in the center of the channel. By cutting the plug into many stripes, it is possible to reperform the same analysis: each of these stripes will be stretched by the parabolic flow profile, and then homogenized by diffusion in a time  $\tau$ . After a time  $t = N\tau$ , the initial stripe will have undergone  $N$  diffusive steps of size  $W$ , and the total width of the plug profile will be:

$$W(t = N\tau) \sim \sqrt{N}W \sim \sqrt{\frac{u_0^2 h^2}{D} t} \quad (3.7)$$

so that the effective diffusion coefficient in the direction of the flow is

$$D_x \sim \frac{u_0^2 h^2}{D} \sim \text{Pe}^2 D \quad (3.8)$$

where we have introduced the Péclet number  $\text{Pe} = u_0 R/D$ . This analysis was first done by Taylor in 1953 and the phenomenon has been termed Taylor dispersion. The analysis is only valid on times scales bigger than the diffusive time scale  $\tau$ . Moreover, the exact relationship between  $D_x$  and  $\text{Pe}$  depends on the geometry of the channel. There is however one caveat with this argument: diffusion was neglected in the axial direction. The effective diffusion coefficient is in  $D^{-1}$ , implying that a solute having a very high diffusion coefficient  $D$  should have a very small effective diffusion. This discrepancy was solved in 1956, as Aris complemented Taylor's work [3] to the case of channels of arbitrary cross-section, and to arbitrary diffusion coefficients. In the case of a rectangular channel, Aris proved that the effective diffusion coefficient  $D_x$  was

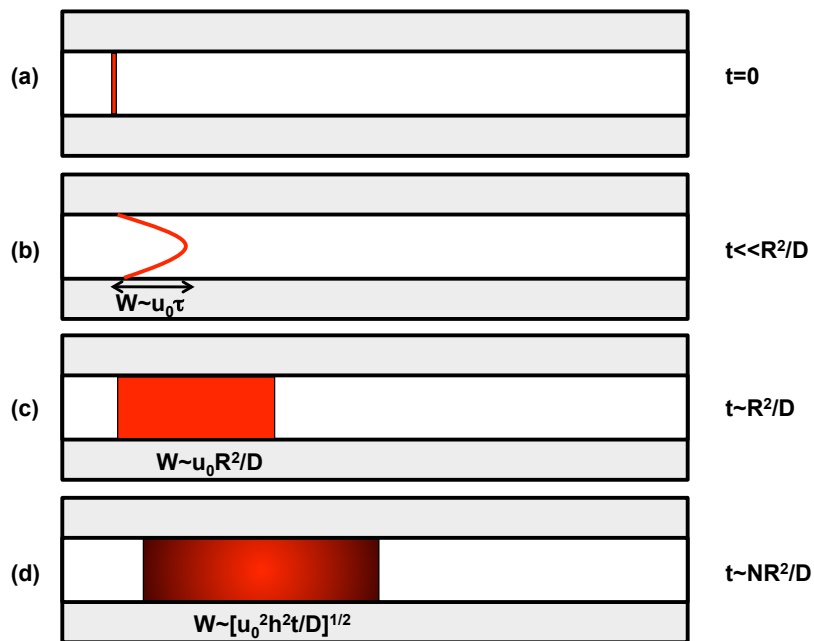


Figure 3.10: Taylor dispersion. (a) An infinitesimally thin stripe of chemical in a circular pipe of radius  $R$ . (b) The parabolic flow in the pipe deforms the stripe ( $u_0$  is the flow speed in the center of the pipe). (c) Because of diffusion across the pipe, the parabolic concentration profile is smoothed into a plug profile. This happens on a characteristic time  $\tau \sim R^2/D$ . (d) The plug can be decomposed into many thin stripes who undergo the same processes (a)-(c). Figure taken from [110].

given by:

$$D_x = D \left( 1 + \frac{\text{Pe}^2}{210} \right) \quad (3.9)$$

where the Péclet number is given by  $\text{Pe} = \bar{u}h/D$ , with  $\bar{u}$  the average speed velocity and  $h$  the height of the channel.

The evolution of the concentration  $c(x, y, t)$  can then be described by the following convection-diffusion equation:

$$\frac{\partial c}{\partial t} + \bar{u} \frac{\partial c}{\partial x} = D_x \frac{\partial^2 c}{\partial x^2} + D_y \frac{\partial^2 c}{\partial y^2} + a\delta(x)\delta(y) \quad (3.10)$$

where  $D_y = D$ . This equation can be solved by first finding its Green function, solution of:

$$\frac{\partial G}{\partial t} + \bar{u} \frac{\partial G}{\partial x} = D_x \frac{\partial^2 G}{\partial x^2} + D_y \frac{\partial^2 G}{\partial y^2} + a\delta(t)\delta(x)\delta(y) \quad (3.11)$$

By Fourier-transforming in  $x$  and  $y$  and Laplace-transforming in time, we get:

$$\tilde{G}(k_x, k_y, s) = \frac{a}{-k_x^2 D_x - k_y^2 D_y - i\bar{u}k_x + s} \quad (3.12)$$

for the transform  $\tilde{G}$  of  $G$ , where  $s$ ,  $k_x$  and  $k_y$  are the conjugate variables of  $t$ ,  $x$  and  $y$  respectively. Reverse-transforming, one gets:

$$G(x, y, t) = \frac{a}{4\sqrt{D_x D_y}t} \exp\left[-\frac{(x-ut)^2}{4D_x t}\right] \exp\left[-\frac{y^2}{4D_y t}\right] \quad (3.13)$$

so the solution of 3.10 is:

$$c(x, y, t) = \int_0^t \frac{a}{4\sqrt{D_x D_y}(t-t')} \exp\left[-\frac{(x-u(t-t'))^2}{4D_x(t-t')}\right] \exp\left[\frac{-y^2}{4D_y(t-t')}\right] dt' \quad (3.14)$$

The profile  $c(x, y)$  calculated in this way for fluorescein, with a diffusion coefficient  $D_{\text{fluor}} = 364\mu\text{m}^2/\text{s}$ , is shown on figure 3.11. As can be seen, there is a good agreement between the analytical solution and the experimental results. The calculated profile of cAMP as a function of time is shown on figure 3.11b. After 1.3 seconds of uncaging, the concentration profile of cAMP is stable (the relative change between two consecutive times is smaller than 1%).

### Estimating the amount of uncaged cAMP

We tested two different methods to estimate the fraction of caged cAMP that was uncaged by the laser. First, in our group, Albert Bae and Christian Westendorf tried quantifying directly the amount of cAMP released after uncaging using High Pressure Liquid Chromatography (HPLC). However, the amounts uncaged were too small to get an estimate of the uncaging efficiency.

We therefore turned to an indirect method to estimate the amount of uncaged cAMP, and used again DMNB-caged fluorescein. Because the caging group used was the same for fluorescein and cAMP, we expected the release dynamics of both compounds to be similar. First, we made a calibration curve by measuring the fluorescence of solutions of different concentrations of fluorescein. To prevent photobleaching, the fluorescein was flown in a microfluidic channel (height: 24  $\mu\text{m}$ , width: 500  $\mu\text{m}$ ) at a rate of 3.8  $\mu\text{L}/\text{hr}$  (mean flow speed: 88  $\mu\text{m}/\text{s}$ ). As could

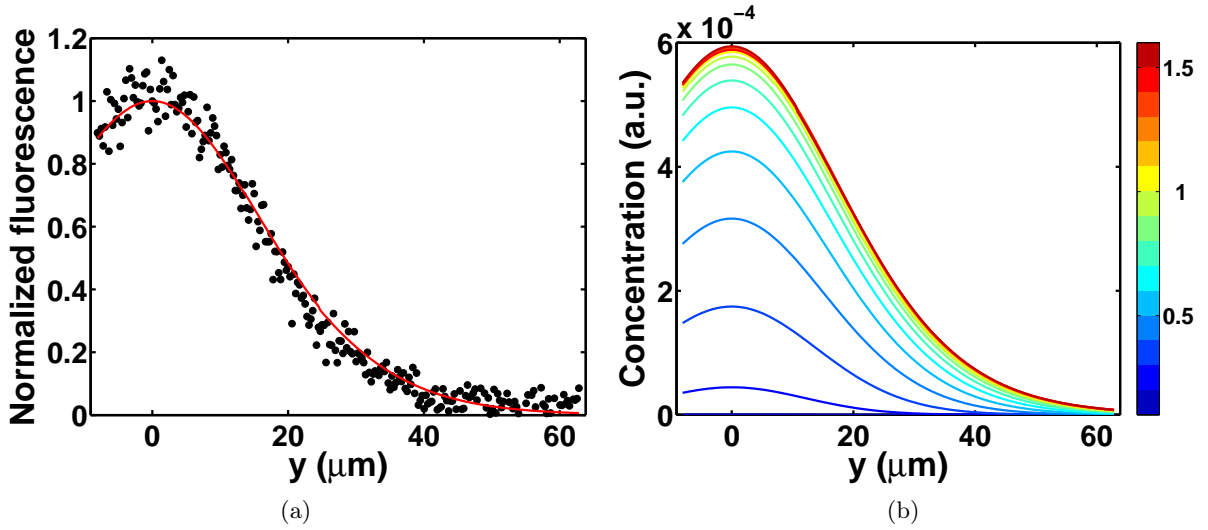


Figure 3.11: (a) Analytically calculated concentration profile of fluorescein at time  $t = 2$  s (red line), compared with the experimental results (black dots). (b) Concentration profile of cAMP at different times, calculated using equation 3.14. The times (in seconds) are shown on the color bar. The concentration profile is stable after  $t = 1.3$  s. Parameters used:  $D_{\text{fluo}} = 364 \mu\text{m}^2/\text{s}$ ,  $D_{\text{cAMP}} = 444 \mu\text{m}^2/\text{s}$ ,  $u = 111 \mu\text{m}/\text{s}$ ,  $x = 42 \mu\text{m}$  (corresponding to the position of the red dashed line in figure 3.9a).

be expected, the intensity of the solution of fluorescein scaled linearly with its concentration (see figure 3.12b). Then, we flowed caged fluorescein in a microchannel. The fluorescence of the caged fluorescein was slightly higher than the background fluorescence. That allowed us to quantify the amount of fluorescein already uncaged in the solution: 0.4% of the caged fluorescein was uncaged. We then uncaged the solution of caged fluorescein on a spot using the uncaging laser, as already mentioned above. This created a gradient of fluorescein in the direction perpendicular to the flow (see figure 3.9a). As can be seen on figure 3.9a, a dark spot appears on the picture at the location of the uncaging. This dark spot is due to the bleaching of the uncaged fluorescein by the uncaging laser. The bleaching in turn implies that the fluorescence values obtained from figure 3.9a can not be directly compared to the calibration curve from figure 3.12b.

To know which fraction of the fluorescein was bleached under the laser spot, we flowed caged fluorescein in a microfluidic channel and stopped the flow. We then uncaged caged fluorescein on a spot, and monitored the evolution of the fluorescence intensity at the location of the uncaging laser spot. By scanning on a single line in the center of the spot, we were able to observe the evolution of the intensity with a time step of the order of the millisecond. The evolution of the intensity with time is shown on figure 3.13a. As the uncaging laser was turned on (at time  $t_{\text{on}}$ ), the fluorescence intensity jumped, indicating the release of the fluorescein molecules. As the uncaging laser was turned off (time  $t_{\text{off}}$ ), the fluorescence intensity jumped again, before eventually decaying. Between  $t_{\text{on}}$  and  $t_{\text{off}}$ , we see the effect of both uncaging and bleaching. The second increase of the fluorescence intensity, at times bigger than  $t_{\text{off}}$ , is due to the uncaging reaction still continuing. The newly uncaged fluorescein molecules

## 3.2. Experiment

are then not subject to bleaching anymore [17]. Diffusive mixing explains the final decay of fluorescence. The ratio of the average fluorescence intensity at times after<sup>2</sup> and before  $t_{off}$  gives us the ratio of bleached fluorescein. Using this ratio, we can compare the intensity of the fluorescence on figure 3.9a to the intensities from the calibration curve on figure 3.12b. The evolution of the amount of uncaged fluorescein as a function of the laser power is summarized on figure 3.13b.

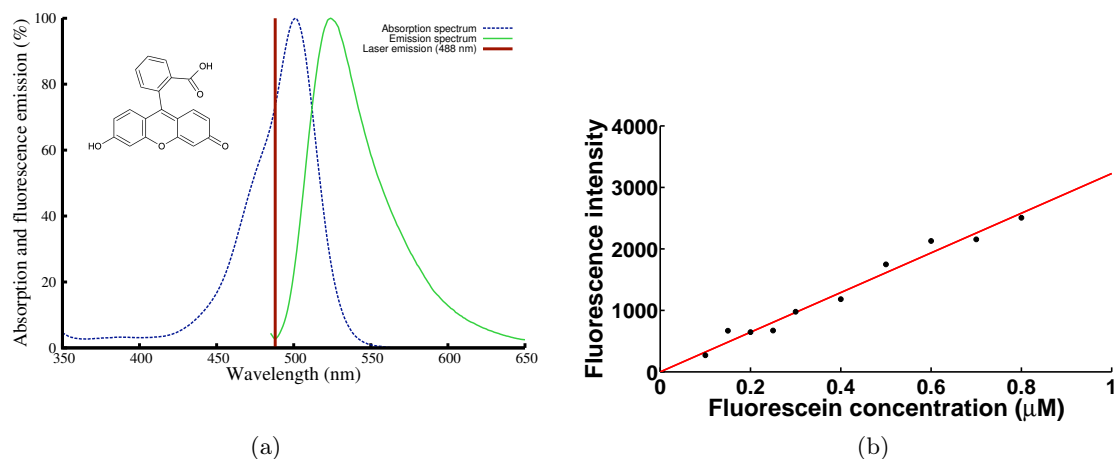


Figure 3.12: (a) Absorption (blue) and emission (green) spectra of fluorescein. Red line: wavelength of the imaging laser. Data taken from <http://www.invitrogen.com>. (b) Fluorescence intensity of different solutions of fluorescein. As could be expected, the intensity of the solution of fluorescein scales linearly with its concentration. Black dots: experimental data, red line: linear fit.

### Varying the cAMP gradient

Varying the cAMP gradient can be achieved in three different ways: by changing the concentration of the solution of caged cAMP, by adjusting the laser power, or by using a different flow speed. Changing the flow speed will have the effect of changing the shape of the concentration profile, whereas the two other methods keep the shape of the profile fixed. The concentration of uncaged material is a linear function of the concentration of the caged solution: if the concentration of the solution of caged cAMP is doubled, with all other parameters fixed, the uncaging will release twice as much cAMP. The effect of changing the laser power on the amount of caged fluorescein released was already shown on figure 3.13b. On figure 3.14a, we plotted the profile of fluorescence along the line shown on figure 3.9a for different powers of the uncaging laser. On figure 3.14b, all these curves are renormalized by their maximum value. For laser powers between 5 and 60%, all curves collapse on one, which shows that the relative gradient is kept constant while we change the laser power. For curves made with a laser power higher than 60%, the bleaching under the laser spot displaces the peak of fluorescence further downstream, which explains why the curves do not superpose. Still, if there

<sup>2</sup>but before diffusion becomes important on our length scale.

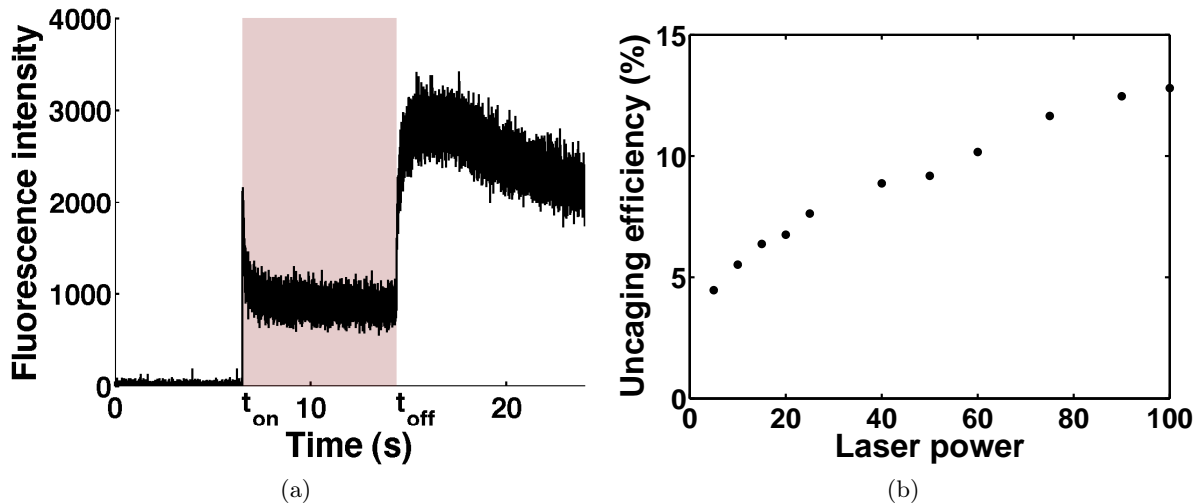


Figure 3.13: (a) Evolution of the average fluorescence under the uncaging spot. The uncaging laser was turned on between  $t_{on}$  and  $t_{off}$  (shaded area). (b) Evolution of the amount of uncaged fluorescein (in percent of the original concentration of caged material flown in the channel), as a function of the laser power (in percent of the maximal power of the laser).

were no bleaching, we would expect all the curves to collapse onto one. The same behavior would be observed if we were to keep the laser power constant but changed the concentration of the caged fluorescein concentration.

Using equation 3.14 to analytically calculate the profile of cAMP, we found that the concentration profile around the cell (assumed to have a radius  $R = 5 \mu\text{m}$ ) could be approximated by a linear one. The relative gradient was  $p = 0.46$ , so that the concentration profile around the cell could be written as:

$$c(y) = c_0(1 + 0.46 * y/R) \quad (3.15)$$

where we have taken the center of our coordinate system at the center of the cell and  $-R \leq y \leq R$ .

### 3.2.4 Cell culture

We used the Wf38 cell line, a generous gift of P.N. Deverotes, Johns Hopkins University. The Wf38 cell line expresses the PH domain of CRAC fused to GFP ( $\text{PH}_{\text{CRAC}} - \text{GFP}$ ) into a wild-type AX3 background. The cells were grown on a dish in the axenic medium HL-5 until they became confluent. They were then resuspended in a shaking phosphate buffer solution (PB, volume: 20 mL). After one hour of starvation, the cells were supplied with  $60 \mu\text{L}$  of cAMP (Sigma) every 6 minutes for five hours. After six hours of starvation, the cells were removed from the shaking culture, centrifuged, and loaded into the microfluidic channel used for the experiment. After having been allowed to settle on the cover glass of the microfluidic channel for about 5 minutes, a flow of caged cAMP was turned on for 20 to 30 minutes before the stimulations began. This allowed for the possible clumps of cells to deaggregate.



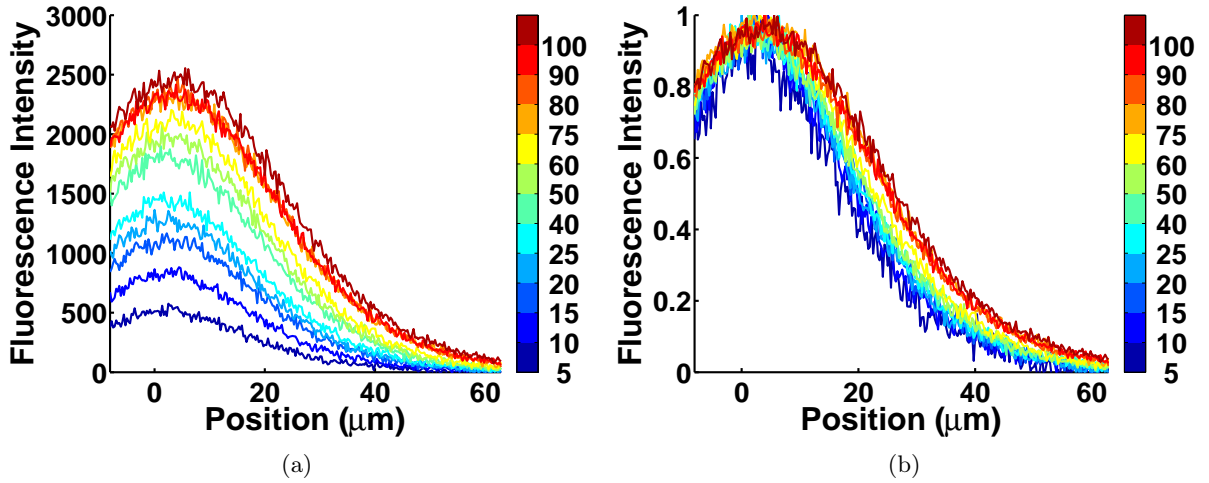


Figure 3.14: (a) Gradient of fluorescein obtained at different laser powers. (b) Curves of figure (a) normalized by their maximal value. All curves made using powers between 5 and 60% collapse onto one, showing that the relative gradient is kept constant while we change the laser power. The curves made at a laser power higher than 60% do not superpose with the other ones because photobleaching under the laser spot displaces the peak of fluorescence further downstream. If there were no bleaching, all curves would superpose. The colorbar shows the laser power used (in %).

### 3.2.5 Microscopy parameters and protocol

We imaged the cells using a confocal microscope (Olympus Fluoview 1000). The Olympus Fluoview 1000 has two lasers, one that we used for imaging ( $\lambda = 488$  nm) and the other one that we used for uncaging ( $\lambda = 405$  nm). To prevent photobleaching, the imaging laser power was set to 8 % of its maximal power. We used a 60X objective (NA=1.4), and an additional digital zoom of 3X. In the end, our image was 256 by 256 pixels wide, where the pixel size was 278 nm. This is above the theoretical resolution limit, given by the diameter of the Airy disk:  $0.51 * \lambda / \text{NA} \approx 180$  nm in our case. The pixel residence time for the imaging was chosen to be the smallest possible on this microscope, which was 2  $\mu\text{s}$ . An image was taken every second. Cells were imaged during 50 to 60 seconds.

The uncaging laser was turned off during the first 10 seconds of the imaging, and then turned on during the remaining time of the experiment. The uncaging laser was put 30 pixels away (8.3  $\mu\text{m}$ ) from the top border of the image as well as 30 pixels away from the left border of the image. The field of view was chosen so that the cell would be positioned in the lower right quadrant of the imaging region. Because different cells have different shape and size, and that cells are randomly moving in the microfluidic channel, it was impossible to control exactly the position of the cell at the beginning of the stimulation, but they were all in the lower right quadrant of the imaging region at the beginning of the uncaging (see figure 3.9a).

### 3.3 Image processing

We monitored the evolution of the fluorescence of PH<sub>CRAC</sub> – GFP in the cytosol and on the membrane of the cells. The image processing was made using customized code in Matlab (The Mathworks).

#### 3.3.1 Finding the cell

The cell was found using a procedure based on the isodata algorithm [93]. The steps were:

1. apply a gaussian blurring;
2. choose a threshold value (in our case, half of the maximal pixel value of the image);
3. calculate the mean value  $m_a$  ( $m_b$ ) of the pixels above (below) this threshold;
4. update the threshold to  $(m_a + m_b)/2$ ;
5. repeat steps 2 and 3 until the threshold has stabilized, or for a maximum of 20 times.

Once the threshold had been found, and because some parts of the cytosol could be slightly darker than what the threshold actually was, the image was filled using the Matlab command `imfill`. The membrane region was then defined as the outer 3 pixel zone ( $0.7 \mu\text{m}$ ), and the rest of the cell defined the cytosol (see figure 3.15).

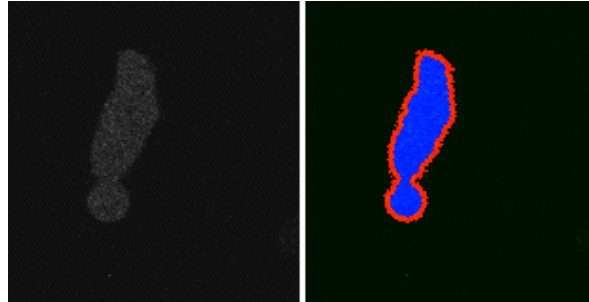


Figure 3.15: Left: original image taken with the microscope. Right: the cell has been automatically found using the Isodata algorithm. Blue: cytosol. Red: membrane.

#### 3.3.2 Quantifying the fluorescence intensity

The average background intensity of each image was subtracted to the whole image. When PH<sub>CRAC</sub> – GFP bound to the newly formed PIP3 on the membrane, the fluorescence intensity raised on the membrane. It will be important in the next part of our work to define where the translocation occurs. To do so, we needed to define a threshold above which the fluorescence is considered sufficiently important for us to say that there has been a translocation. We defined this threshold in the following way: during the first 10 seconds of imaging, when no stimulus was applied, we calculated the ratio  $r_i$  of the fluorescence value  $m_i$  of each membrane pixel  $i$  with the average cytosolic fluorescence value  $\bar{\kappa}$ :

$$r_i = \frac{m_i}{\bar{\kappa}} \text{ for each membrane pixel } i \quad (3.16)$$

We then took the average value  $\bar{r}$  as well as the standard deviation  $\sigma$  of all the  $r_i$  obtained during the first 10 seconds of imaging. We defined our threshold for bright pixels as  $I_t = \bar{r} + 2\sigma$ . Moreover, to get rid of possible noisy bright isolated pixels, and as we know both from the literature (see for example the pictures in [86, 132]) and from our experiments that PH<sub>CRAC</sub> – GFP makes patches on the membrane, we defined a minimal patch size, as well as a minimum patch life below which we considered that the bright pixels seen were the consequence of noise in the imaging system. First, we divided the cell into 40 angular sectors. Patches were defined as 8-connected elements of at least 3 pixels ( $0.3 \mu\text{m}^2$ ). We noted at each time to which angular sector each patch belonged. If an angular sector contained patches for more than 3 consecutive seconds, all patches within this sector and during this time were kept. Otherwise, they were discarded (see figure 3.16).

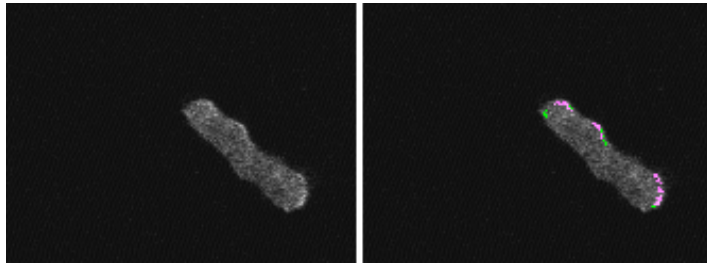


Figure 3.16: Left: original image. Right: the bright pixels have been found automatically on the membrane. Purple: pixels belonging to a patch. Green: bright pixels due to noise (see text for details).

## 3.4 Results

We monitored the evolution of both the cytosolic and the membrane intensity as a function of time.

### 3.4.1 Defining a response

When PH<sub>CRAC</sub> – GFP is recruited to the membrane, the fluorescence intensity in the cytosol drops. A typical time series of the cytosol fluorescence intensity is shown on figure 3.17a. How can we distinguish this drop from the noisy fluorescent signal of non stimulated cells? We took time series of 14 unstimulated *D. discoideum* over one minute, and computed at each time step their (spatial) mean cytosolic intensity. A typical time series for one cell is shown on figure 3.17b. For each of the 14 time series, we calculated the temporal average of the mean cytosolic intensity, as well as its standard deviation. We found that the standard deviation, *i.e.* the amplitude of the fluctuations, was of the order of 5% of the mean. The fluctuations are likely due to intracellular flows and cell movements. To exclude non-responsive cells from our processing, we defined a response as a drop in cytosolic intensity that was at least 8% of the mean initial cytosolic value (this value being calculated over the first 10 seconds of the experiment, when no stimulus was applied). All the time series were moreover evaluated manually. Indeed, if cells get out of the confocal plane, they show a drop of their cytosolic intensity that can be bigger than the threshold, but these cells should not be taken into account

as responsive cells. Furthermore, we excluded from our analysis all prepolarized cells, in the sense that they showed a translocation of CRAC-GFP on their membrane prior to stimulation, and were likely not to respond in the same way as naive, unpolarized cells. We defined the response of a cell as its relative drop in cytosolic fluorescence:

$$\text{response} = \frac{\text{cytosolic drop}}{\text{mean initial cytosolic intensity}} \quad (3.17)$$

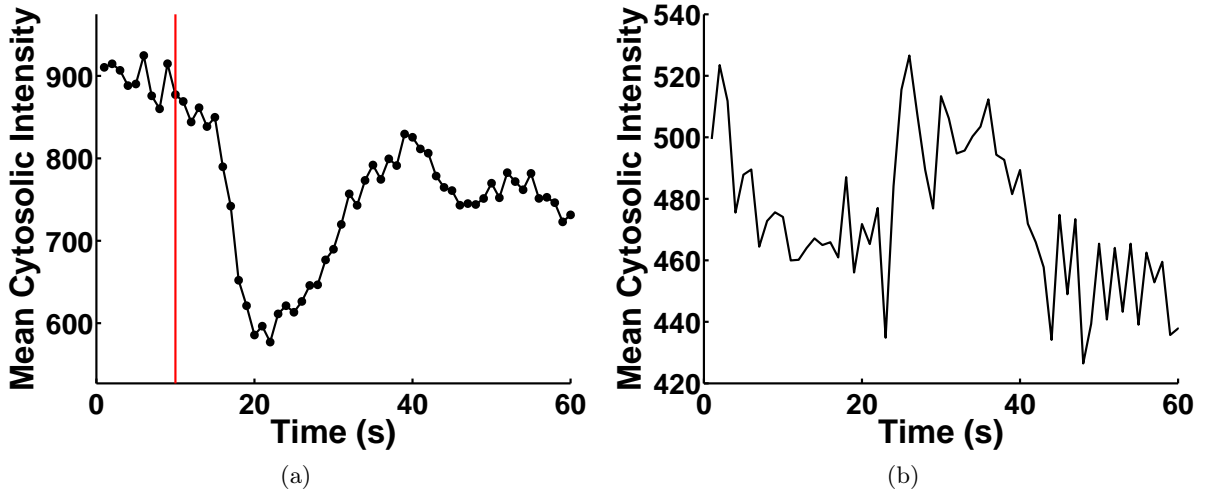


Figure 3.17: (a) Mean cytosolic fluorescence of a stimulated cell. The stimulus is turned on at  $t = 10$ s (red line) and stays on until the end of the experiment. (b) Mean cytosolic fluorescence of an unstimulated cell as a function of time. The fluorescence fluctuates due to cell motion and to intracellular flows.

### 3.4.2 Cytosolic response

The evolution of the cytosolic response as a function of the applied gradient is shown on figure 3.18a. Each point represents the average response for an experiment on a given day. There were at least 2 responsive cells per day (average number of responsive cells per day: 11), and similar experimental conditions were repeated one to five times on different experimental days. The error bar shows the standard error. An overall increase of the cytosolic response with the gradient is observed. This increase is even clearer if the results of experiments made in the same conditions are averaged (figure 3.18b). However, by averaging over different experimental days, we lose information on cell-to-cell variability. In the rest of this part, we will therefore not average our results.

### 3.4.3 Membrane response

#### Angular range of translocation, patch fluorescence

There are two ways that the cytosolic depletion could be reflected on the membrane: either the region of the membrane where  $\text{PH}_{\text{CRAC}} - \text{GFP}$  translocates (*i.e.* the region where PIP3 is

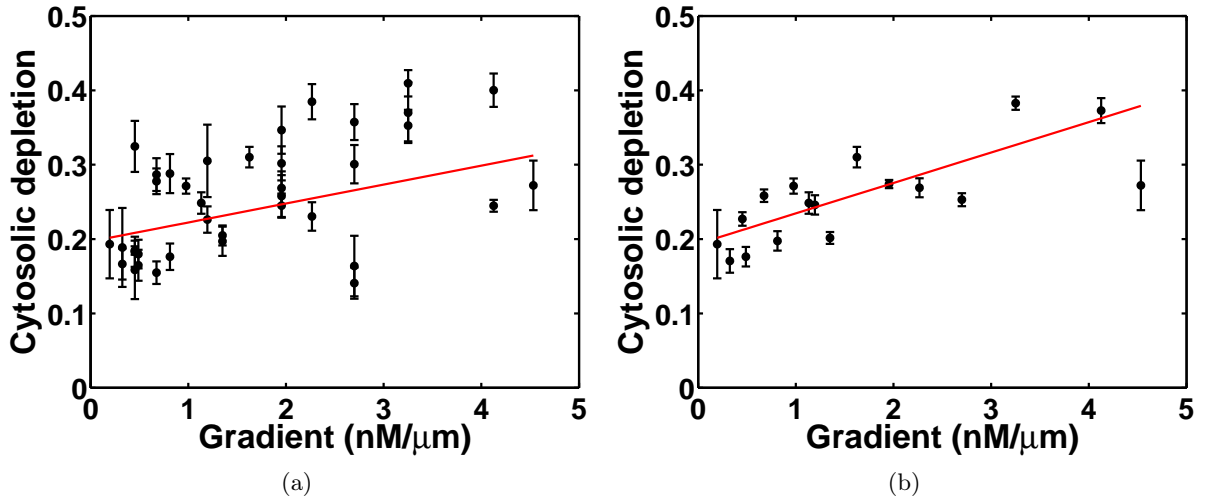


Figure 3.18: (a) Cytosolic response as a function of the cAMP gradient. Each point is the average response for one experimental day. The error bar shows the standard error. The response increases with the gradient (red line: linear fit). (b) Average cytosolic response as a function of the cAMP gradient, when we average similar experiments made on different days.

formed) could increase in size, or the size of the translocation region could stay the same, only with more PIP3 produced locally, which would be reflected by an increase in  $\text{PH}_{\text{CRAC}} - \text{GFP}$  fluorescence. These two possibilities are not mutually exclusive.

At each time, we computed the number of angular sectors in which there were patches of PIP3. At the time  $t_{tr}$  where this number was maximum (time of maximum translocation), we computed the angular range of the PIP3 patches on the membrane (which is just the number of angular sectors multiplied by the angle of each sector, here  $\pi/20$ ). The evolution of this angular range with the gradient is shown on figure 3.19a, showing an increase of the fraction of the membrane where PIP3 production takes place at higher gradients. The angular range is clearly correlated with the cytosolic depletion, as shown on figure 3.19b. As reported in Xu et al. [132] for the case of Latrunculin-treated cells, the translocation does not cover the whole membrane (the angular range is smaller than  $2\pi$ , and even smaller than  $\pi$  in most of our experiments). The average fluorescence of the PIP3 patches at time  $t_{tr}$  is shown on figure 3.20a as a function of the gradient. For each cell, the fluorescence of the PIP3 patches was normalized by the mean cytosolic intensity before stimulation. No correlation between the gradient and the patch fluorescence is observed. As shown on figure 3.20b, there is also no correlation between the average fluorescence intensity at time  $t_{tr}$  and the cytosolic depletion.

Next, we computed the average fluorescence of the PIP3 patches at the time  $t_{br}$  where the fluorescence of the PIP3 patches was maximal. The results are shown on figure 3.21, where we have also plotted the angular range of the translocation at time  $t_{br}$ . The evolutions of the time of maximal translocation  $t_{tr}$ , as well as the time of maximal fluorescence  $t_{br}$  are shown as a function of the gradient and the cytosolic response on figure 3.22. As a first point, the time at which the most PIP3 has been synthesized,  $t_{br}$ , is bigger than the time of maximum translocation  $t_{tr}$ , which indicates that there is a build-up of PIP3 with time (figure 3.22). Second, we observe a decrease of  $t_{tr}$  as the cytosolic depletion increases,

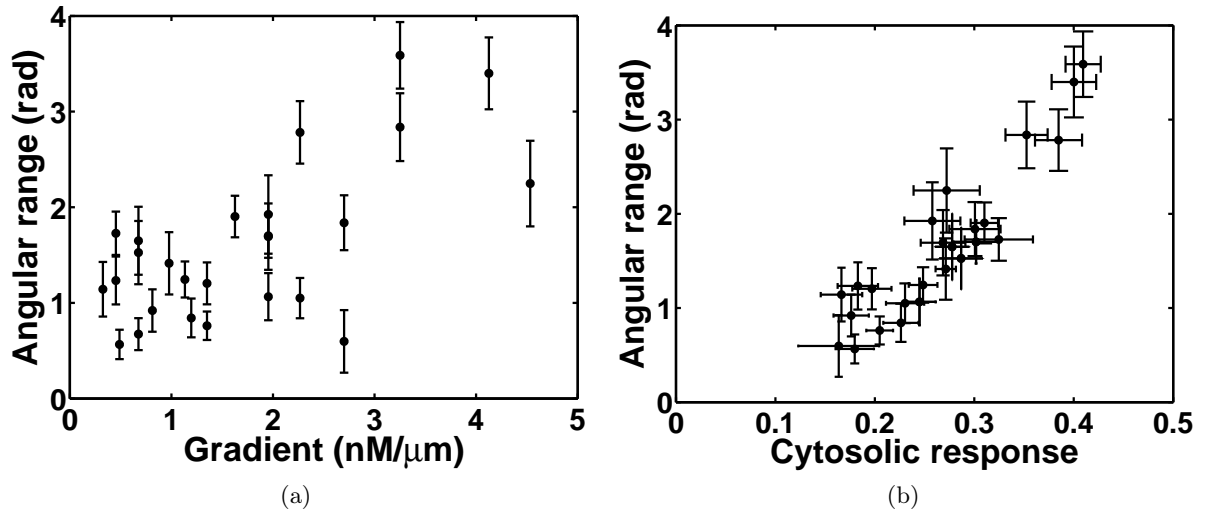


Figure 3.19: Angular range of the PIP3 patches on the cell membrane at the time  $t_{tr}$  where the translocation is maximal, as a function of (a) the gradient and (b) the cytosolic depletion.

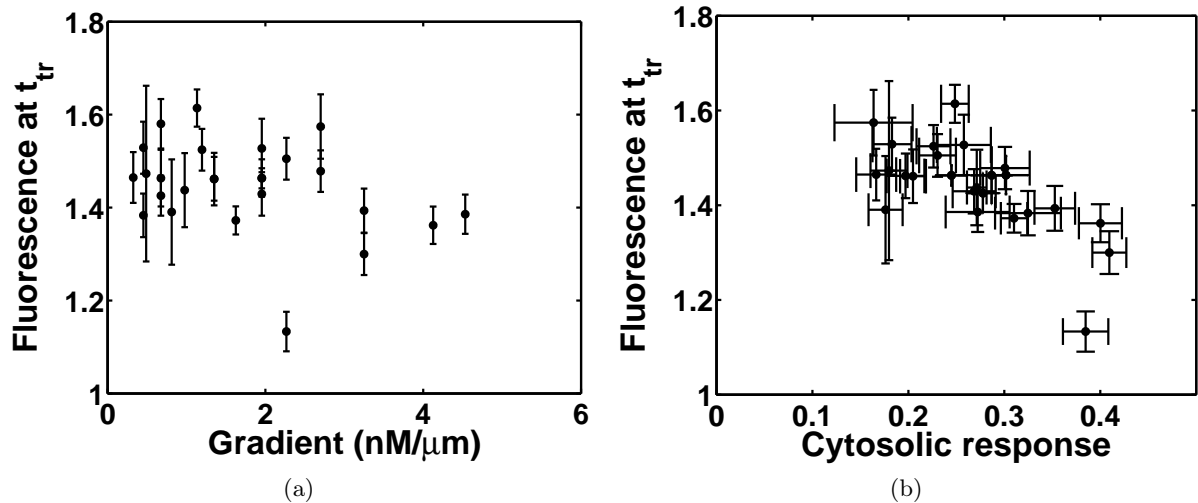


Figure 3.20: Average fluorescence of the PIP3 patches on the cell membrane at the time  $t_{tr}$  where the translocation is maximal, as a function of (a) the gradient and (b) the cytosolic depletion. The fluorescence was normalized by the mean cytosolic intensity before stimulation.

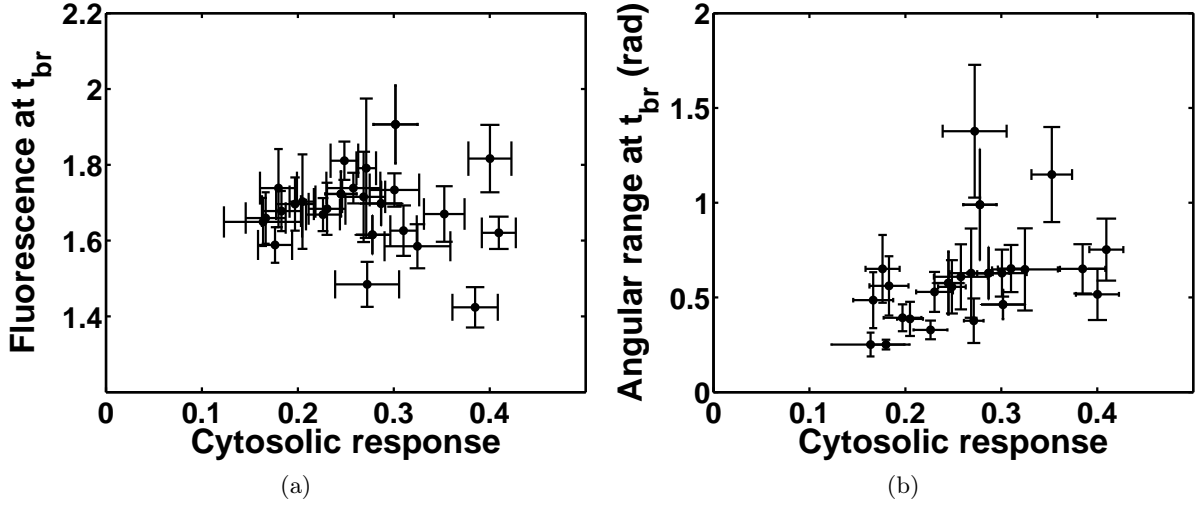


Figure 3.21: (a) Average fluorescence of the patches of PIP3 at time  $t_{br}$ . (b) Angular range of translocation at time  $t_{br}$ .

indicating that a signal leading to a weak response will also lead to a longer response time. Third, the average fluorescence intensity of the PIP3 patches at time  $t_{br}$  does not depend on the cytosolic depletion, possibly indicating a saturation process. Last, the angular range at  $t_{br}$  is independent of the cytosolic response, and is smaller than the angular range at time  $t_{tr}$  by a factor of 1 to 5, indicating that regions where PIP3 builds up are restricted in space.

### Asymmetry

We have reported that the angular range of the translocation did not cover the whole cell circumference. Are the patches of fluorescence at random locations on the membrane, or is there already, in this first stage of directional sensing, a directional response? To answer this question, we divided the cell into two parts, front and back, defined as the angular region in the direction of the gradient and opposite the gradient, respectively. We then defined the asymmetry  $\alpha$ , a function of the number of super-threshold pixels belonging to patches in the front ( $n_{front}$ ) and back ( $n_{back}$ ) of the cell:

$$\alpha = 2 \frac{n_{front}}{n_{front} + n_{back}} - 1. \quad (3.18)$$

If all the patches are localized at the front half of the cell, this ratio is equal to one, while it has a value of 0 if there are as many patches at the front and at the back of the cell. If the patches are localized at the back of the cell,  $\alpha = -1$ . We plotted  $\alpha$  as a function of the gradient at times  $t_{tr}$  and  $t_{br}$  on figure 3.23. It is plotted as a function of the cytosolic depletion on figure 3.24. In all the experiments,  $\alpha$  had a value bigger than 0, indicating that there were always more patches at the front of the cell than at its back. Moreover, the asymmetry at time  $t_{tr}$  goes down with the gradient, which reflects the fact that PIP3 is synthesized on larger portions of the membrane, and not only at the front of the cell.

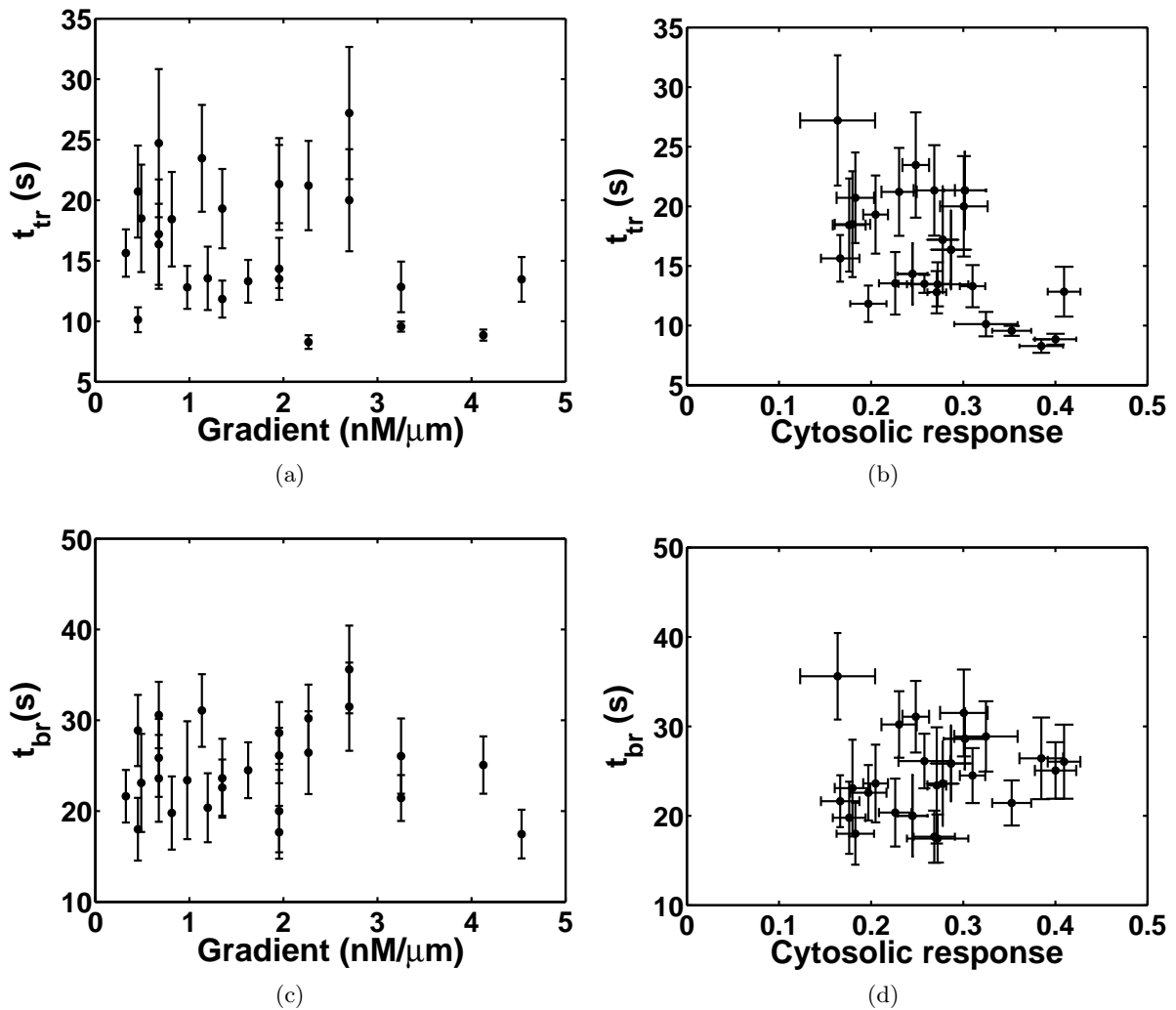


Figure 3.22: (a), (b) Time  $t_{tr}$  at which the angular range of translocation on the membrane is maximal, as a function of the gradient and the cytosol response. (c), (d) Time  $t_{br}$  at which the average patch fluorescence is maximal, as a function of the gradient and the cytosol response.



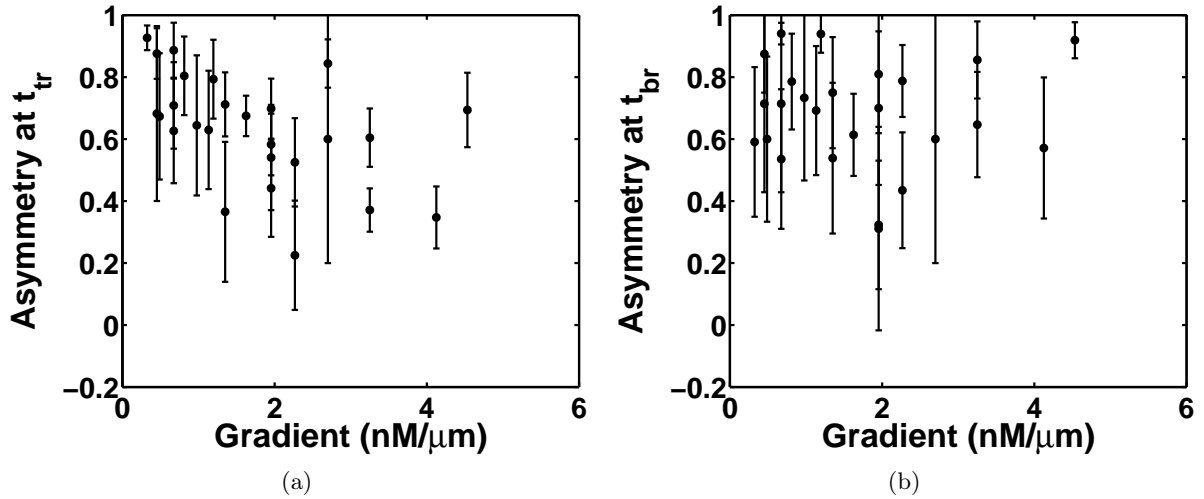


Figure 3.23: Asymmetry as a function of the gradient (a) at the time of maximal translocation  $t_{tr}$ , and (b) at the time  $t_{br}$  where the patch intensity is at its maximum.

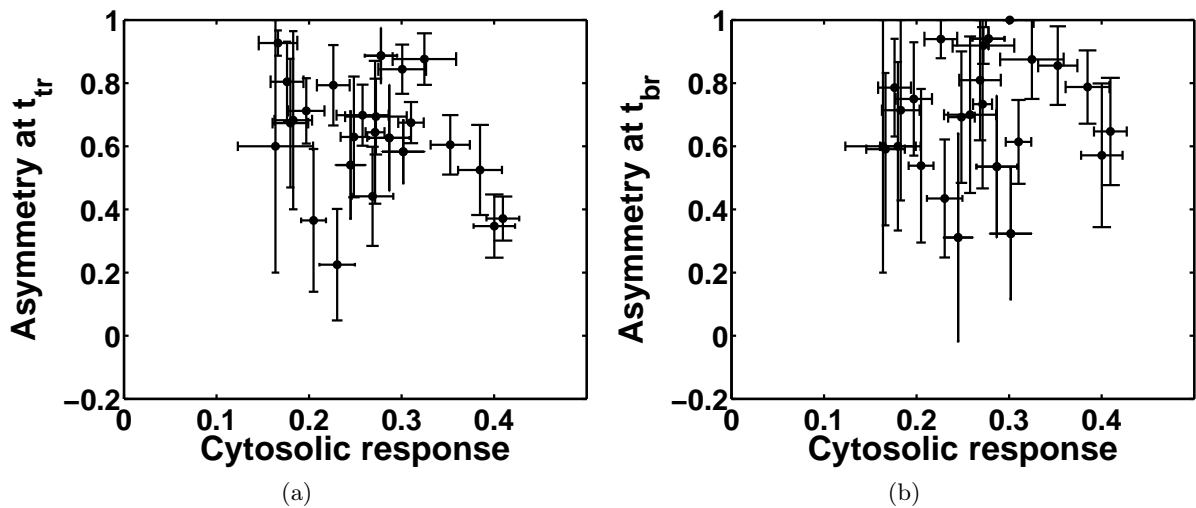


Figure 3.24: Asymmetry as a function of the cytosolic response (a) at the time of maximal translocation  $t_{tr}$ , and (b) at the time where the patch intensity is at its maximum.

### 3.4.4 Fraction of responding cells

At a given gradient, not all cells respond. The fraction of responding cells is shown on figure 3.25a as a function of the gradient of cAMP. The curve shows a sharp increase at low gradients, which could be an indication that we are doing our experiments at the lower limit of the cell's ability to detect a gradient. On figure 3.25a, one point does not fit on the overwhole curve, namely the point at a gradient of 28 nM/ $\mu$ m for which only 40% of the cells respond. For this experiment, the cytosolic depletion is also lower than what would be expected (figure 3.18a). We can only speculate on the causes of this observed behavior: it is possible that the cells did not develop as well on that day as they otherwise did, or that there was a mistake in the dilution of the caged cAMP solution used on this particular day. However, if the fraction of responding cells is plotted as a function of the average cytosolic response of the responding cells, this point fits on the overall curve (figure 3.25b). A likely explanation for the correlation observed on figure 3.25b is that each cell responds differently to the same applied gradient, and that there exists a threshold gradient for PH<sub>CRAC</sub> – GFP translocation. It is likely that this threshold varies from cell to cell and that at a given gradient, some cells will respond whereas others will not. Preliminary experiments were conducted to test this hypothesis. We stimulated three cells at a low gradient without observing any response, and then applied a higher gradient that elicited a translocation. The cells were then stimulated one more time at the original low gradient, and no translocation could be observed. These experiments are not easy to conduct, for two reasons. First, one has to use a gradient that elicits a response in a part of the population, and find a cell that does not respond. Second, one has to track this cell for at least 5 minutes: each stimulus lasts one minute and the waiting time between each stimulation should be of the order of one minute, to allow for the effect of the previous stimulus to decay. During these five minutes, severe photobleaching occurs, which impairs our ability to observe a translocation. It would be worthwhile to conduct such experiments again with another marker of PIP3 than PH<sub>CRAC</sub> – GFP, such as PhdA-GFP, reported to give a better fluorescence signal [36].

## 3.5 Discussion

We have seen that the cytosolic depletion increases with the gradient, a feature that can be reproduced by most of the models presented in chapter 2. However, we also observed an asymmetric first translocation of PH<sub>CRAC</sub>–GFP on the cell membrane in the range of gradients used. This asymmetric translocation can be reproduced only by the model of Gamba et al. [39] or of Meier-Schellersheim et al. [72]. In all other models, which are based on a deterministic local excitation, global inhibition scheme, the first translocation of PH<sub>CRAC</sub> – GFP is predicted to be uniform, while only the second translocation would be asymmetric [8, 70, 68]. In the model of Gamba et al. however, the distribution of PIP3 on the cell membrane is asymmetric over a wide range of gradients, but PIP3 is always produced also at the back of the cell. Because of this, the only remaining model having a chance to be correct is the one of Meier-Schellersheim et al. This model supposes the action of a local inhibitor, which has yet to be identified. It is worth noting that our experiments agree with the ones of Xu et al. [132] even though our cells were not treated with Latrunculin, contrarily to the cells used in [132], showing that the actin cortex plays no crucial role, and does not prevent the establishment of the first asymmetric translocation of PH<sub>CRAC</sub> – GFP. Moreover, we reported that, at a population level, and at a given stimulus, some cells would not respond. This underlines

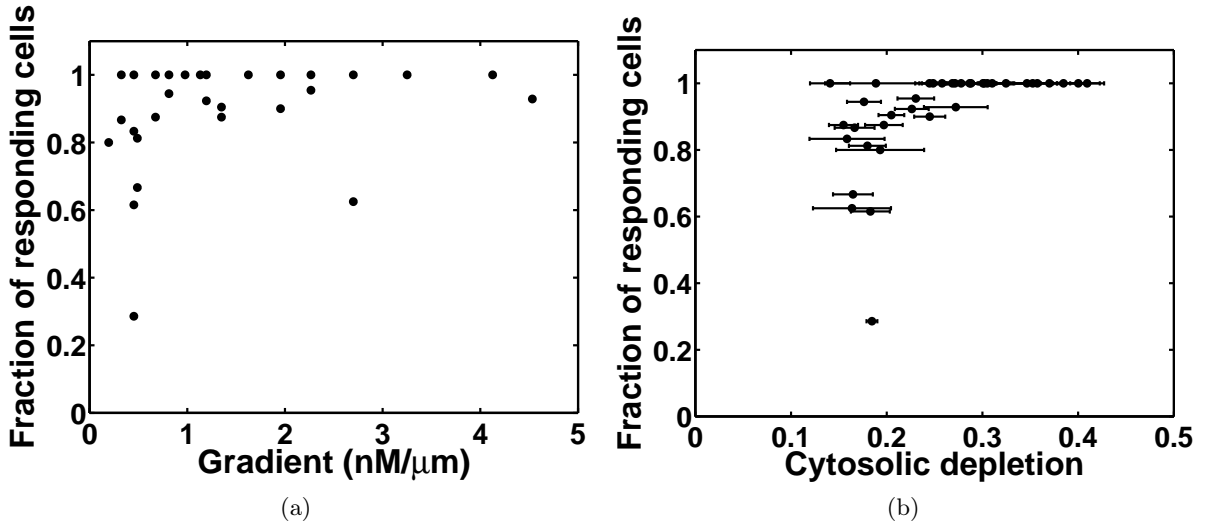


Figure 3.25: (a) Fraction of responding cells as a function of the cAMP gradient. (b) Fraction of responding cells as a function of the mean cytosolic response.

the importance of cellular individuality in directional sensing. A further step in the model of Meier-Schellersheim et al. would be the incorporation of stochasticity in the biochemical networks used, which would then enable to reproduce the individual behaviors experimentally observed.

Can we relate the first  $\text{PH}_{\text{CRAC}} - \text{GFP}$  translocation to cell motion? It has been hypothesized by Ueda and Shibata [119] that a cell's chemotactic efficiency was directly related to the difference in production of a second messenger between front and back of the cell. More precisely, because chemical reactions are stochastic processes, both receptor binding and the signals at the level of the second messenger contribute a certain amount of noise. It is then possible to define a signal to noise ratio (SNR), which was found to be in direct relationship with the cell's chemotactic efficiency. This will be discussed in more details in chapter 4, where we will show that the SNR is indeed a quantity describing accurately cellular chemotaxis for all types of gradients used (section 4.6.4). For the time being, it is sufficient to know that such a SNR can be calculated. Is the SNR also the important quantity in the  $\text{PH}_{\text{CRAC}} - \text{GFP}$  translocation? We plotted the cytosolic depletion as a function of the SNR on figure 3.26c. On this figure and on the following ones, we averaged the results of experiments made in the same conditions, in order to average out the cell-to-cell variability. There is a global increase of the cytosolic depletion with the SNR, but the plot appears to be very noisy. This is a first indication that the first  $\text{PH}_{\text{CRAC}} - \text{GFP}$  translocation and cellular motility are maybe not directly related. We wanted to further test this hypothesis. On figure 3.26a, we plotted the evolution of the cytosolic response as a function of  $\Delta R$ , the difference of receptor occupancy between front and back of the cell, calculated as:

$$\Delta R = \frac{R_{\text{tot}}}{2L} \left[ \int_0^L \frac{c(y)}{c(y) + K_d} dy - \int_{-L}^0 \frac{c(y)}{c(y) + K_d} dy \right] \quad (3.19)$$

where  $L = 5 \mu\text{m}$  is the cell radius,  $R_{\text{tot}} = 80\,000$  [119] is the total number of receptors around the cell membrane, and  $K_d = 180 \text{ nM}$  [119] is the dissociation constant of cAMP with the

receptor cAR1. There is a clear correlation between the cytosolic depletion and  $\Delta R$ . However, note that in our experiment, as the same time as  $\Delta R$  increases, the total number of occupied receptors  $R^*$  also increases. The total number of occupied receptors was estimated using the formula:

$$R^* = \frac{R_{\text{tot}}}{2L} \int_{-L}^L \frac{c(y)}{c(y) + K_d} dy \quad (3.20)$$

It appears on figure 3.26b that  $R^*$  and the cytosolic response are also clearly correlated.

To test the idea that the total number of occupied receptors  $R^*$  was the quantity determining the extent of the first  $\text{PH}_{\text{CRAC}} - \text{GFP}$  translocation, and not  $\Delta R$ , we stimulated the cells with a uniform concentration of cAMP. This can be conveniently done using the same microfluidics setup, but by uncaging on a line (perpendicular to the flow direction, see figure 3.27a) instead of uncaging on a spot [10]. We stimulated 316 individual cells and monitored their cytosolic response. The evolution of the cytosolic response to a uniform stimulus as a function of the number of occupied receptors is shown on figure 3.27b (red dots). The black dots show the cytosolic depletion for the gradient stimulus, also plotted as a function of the total number of bound receptors (same data as in figure 3.26b). Both curves fit well onto each other, strongly indicating that the first  $\text{PH}_{\text{CRAC}} - \text{GFP}$  translocation in a gradient is indeed due to a local mechanism, and that no comparison between front and back is made.

### 3.6 Conclusion

In this chapter, we used a combination of microfluidics and photouncaging to apply stable and well-defined gradients of cAMP to developed *D. discoideum* cells. The gradients were established in roughly one second, which is 10 times faster than what had been previously used [132]. The relative gradient was kept fixed, but the absolute gradient was changed. We saw an increase in the cytosolic depletion of  $\text{PH}_{\text{CRAC}} - \text{GFP}$  as the absolute gradient was increased, corresponding to an increase in the midpoint concentration. This corresponded to an increase of the spatial extent of the translocation of  $\text{PH}_{\text{CRAC}} - \text{GFP}$  on the membrane, indicating a production of PIP3 on more sites at higher gradients. Locally however, the amount of PIP3 was independent of the gradient. We found no correlation between the signal to noise ratio, which compares the amount of second messenger between front and back of the cell, and the cytosolic response. This was a first indication that the observed response was maybe a local mechanism, not an integrated one where front and back of the cell would be compared. There is moreover a close agreement between the response of uniformly stimulated cells and that of cells in a gradient, when the number of occupied receptors around the membrane are similar. This is one more element contributing to the hypothesis that the first  $\text{PH}_{\text{CRAC}} - \text{GFP}$  translocation in cells subject to a gradient is a local response, depending on the total number of occupied receptors and not on the difference of occupied receptors between the two ends of the cell.

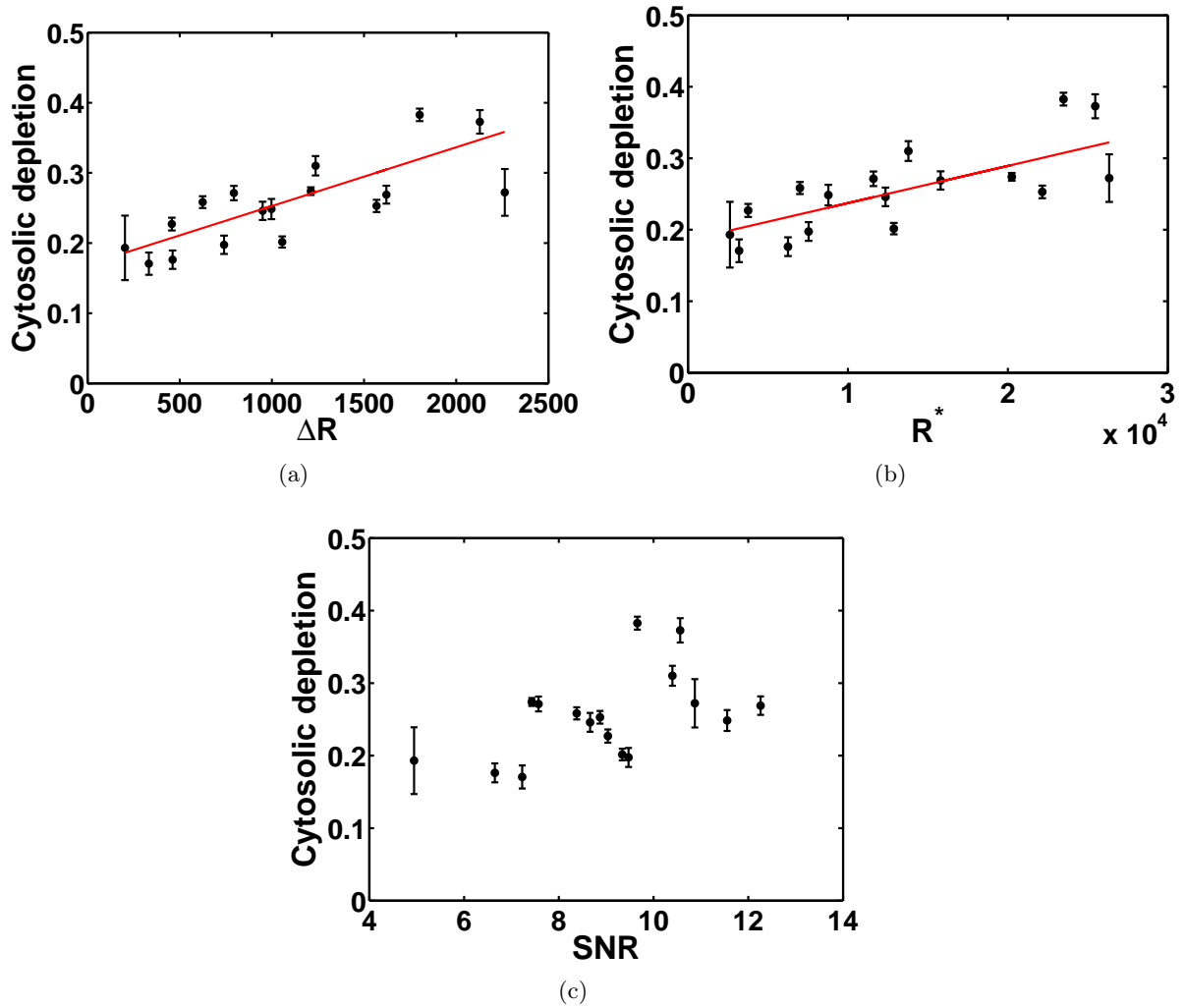


Figure 3.26: (a) Cytosolic response as a function of the difference in receptor occupancy between front and back of the cell  $\Delta R$ . (b) Cytosolic response as a function of the total number of bound receptors  $R^*$  around the cell. (c) Cytosolic response as a function of the signal to noise ratio at the level of the G-protein. The SNR is found to be in direct correlation with the chemotactic motion of the cells (see chapter 4 of this thesis and [119]), but is of little help in predicting the CRAC translocation.

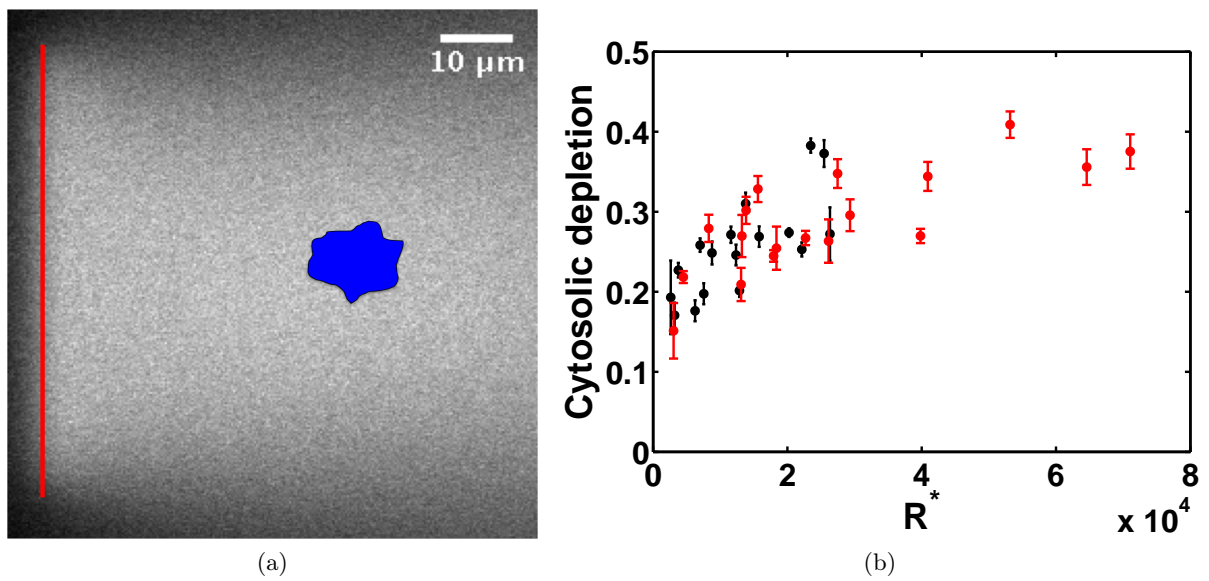


Figure 3.27: (a) Uniform fluorescence profile after uncaging on a line (shown in red). The cell is sketched in blue. (b) Cytosolic response as a function of the total number of occupied receptors for a gradient stimulus (black points) and for a uniform stimulus (red points). As can be seen, all data fall on the top of each other, strongly indicating that the first  $\text{PH}_{\text{CRAC}} - \text{GFP}$  translocation is a local response.

## Chapter 4

# Chemotaxis of *Dictyostelium discoideum* and description by a Langevin equation

In the previous chapter, we quantified the intracellular response of the PH-domain protein CRAC to gradients of cAMP. The gradients were applied for at most 50 seconds, and we focused on an intracellular response occurring within the first 10 seconds of stimulation. We can now ask what happens at larger time and spatial scales: in this chapter, we will quantify the migration of *D. discoideum* over 40 minutes in a stable linear gradient of cAMP<sup>1</sup>. The gradients were produced using microfluidic gradient mixers already described in [109]. Because in our experiments, the difference in receptor occupancy between the front and the back of the cell is of the order of 350 receptors at most, out of around 23 000 occupied receptors, it is necessary to take into account the stochasticity of ligand-binding to fully understand the chemotactic response. In this respect, a signal to noise ratio (SNR) can be defined, based on both the midpoint concentration and the gradient value [119]. We will see that the SNR is in direct relationship with the chemotactic index of the cells. Moreover, the fraction of cells that respond chemotactically depends on the SNR.

In chemotaxis assays, the migration of a whole population is usually monitored, and the average behavior is typically reported. It is however also known (and we saw it ourselves in the last chapter) that each cell might behave differently – there is biological diversity. Moreover, as can be seen on videos of chemotactic cell motion (see movie online at <http://www.lfpn.ds.mpg.de/biophysics/documents/movies/chemotaxis.mov> for a vertical gradient of 1.7 nM/ $\mu\text{m}$ , pointing upwards), cells do not necessarily move straight in the gradient direction, or with a constant speed. By calculating only average quantities (like the average speed of a cell population), one loses the biological variability observed in cell motion. Our aim in the second part of the chapter is to describe chemotactic motion not with averaged quantities, but with histograms: using a method pioneered by Siegert et al. [105], we will model cell motion using a generalized Langevin equation.

The raw data that I will analyze has been taken by Matthias Theves as part of his Diplomarbeit [117].

---

<sup>1</sup>Strictly speaking, the gradient of cAMP is constant and the concentration profile of cAMP is linear. However, it seems that the term “linear gradient” is commonly used in the literature to describe a linear concentration profile of a chemical.

## 4.1 Background

Chemotaxis of *Dictyostelium discoideum* has been an ongoing area of research for the past 60 years, and analysis of the chemotactic motion of the amoebae under a gradient of cAMP has been the subject of numerous articles. The most recent is from Fuller et al. [34], where the authors systematically changed the slope and midpoint concentration of the chemoattractant gradient and monitored cell migration under these conditions. Using tools from information theory, they showed that at low midpoint concentrations, the main source of noise in the gradient sensing process comes from the detection of the chemoattractant at the receptor level, whereas at high midpoint concentrations, the main source of noise comes from the intracellular chemotactic pathway. This was a result already pointed out by Ueda and Shibata in [119], where the authors defined a signal to noise ratio (SNR) for the chemotactic signal and correlated it with the cellular chemotactic behavior.

In [34], the authors used a microfluidic device to generate an exponential concentration profile, where the *relative* gradient seen by a cell is constant in all parts of the channel. The first use of microfluidic devices to monitor *D. discoideum* chemotaxis was done in the lab of Eberhard Bodenschatz [109], where the concentration profiles were linear: the *absolute* gradient was constant across the microfluidic device. Song et al. [109] reported a threshold gradient for chemotactic cell motion, which they correlated to the difference in receptor occupancy between the front and back of the cell. The main result of the paper is shown on figure 4.1a, where the average velocities of cells in a gradient of cAMP are shown. The decrease of the chemotactic velocity at steep gradients is explained by the authors of [109] by the simultaneous rise in the midpoint concentration, which saturates the receptors. In the current chapter, we will use the same device as Song et al. and complement their approach by taking into account the stochasticity of ligand-binding and of chemical reactions to explain when a cell population responds chemotactically [119].

Before the development of microfluidic devices, diffusion chambers were used to monitor chemotactic cell motion. Varnum and Soll reported the evolution of both the chemotactic index (a measure of the accuracy of chemotactic motion), and of the cell speed as a function of the gradient [124]. The result concerning the chemotactic index are consistent with the ones found in [109]. The evolution of the accuracy of chemotaxis (a measure related to the chemotactic index) of *D. discoideum* was also reported by Fisher et al. [30], and here again, the results are consistent with [124, 109]. The evolution of the speed observed in [124] was not reported in later experiments and could not be reproduced in [109].

In this chapter, the experiments of Song et al. were repeated using both wild-type cells and putatively defective chemotaxis mutants, namely SCAR/PIR null mutants (for the role of SCAR, see chapter 1 or section 4.7). Moreover, to investigate the influence of the midpoint concentration on the gradient sensing process, a few experiments were conducted with a similar value of the absolute gradient and a different value of the midpoint concentration. The cells were automatically tracked and analyzed using a Langevin equation.

## 4.2 Experimental setup

The experiments described in this chapter were conducted by Matthias Theves [117]. In his work, Matthias found and tracked the cells over time. In this section, I will summarize his experimental protocol and in particular show the limits of the automated cell segmentation



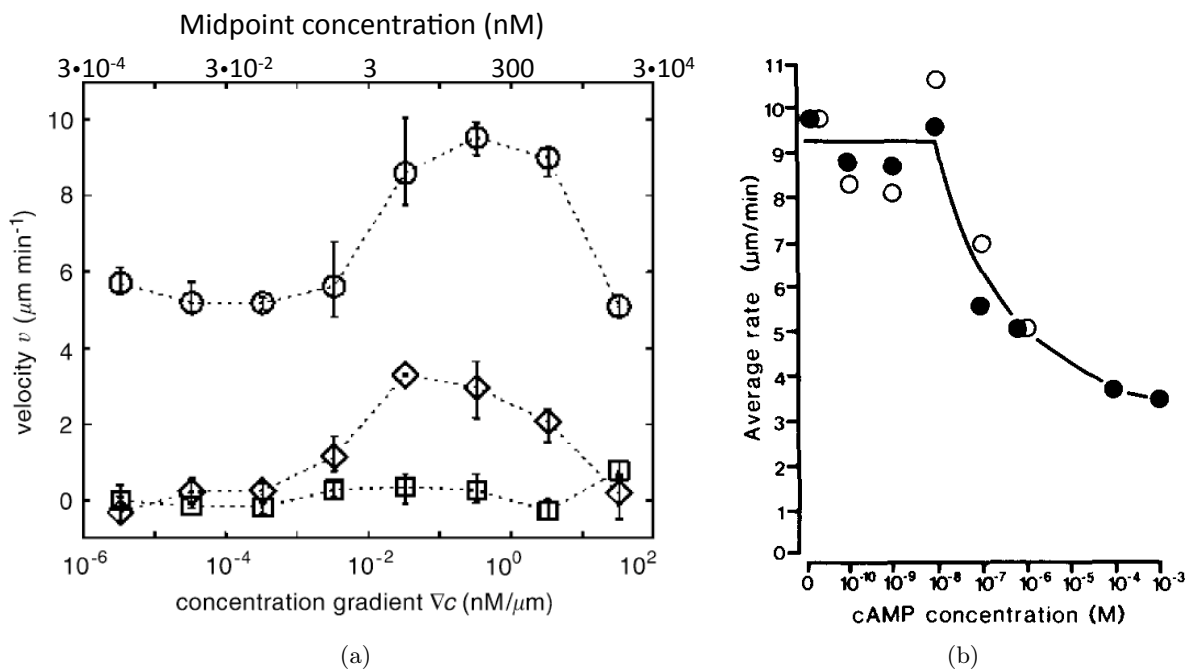


Figure 4.1: (a) Evolution of the velocity perpendicular to the gradient direction  $v_x$  (squares), the chemotactic velocity  $v_y$  in the gradient direction (diamonds) and the speed  $v$  (circles) as a function of the gradient of cAMP. Figure taken from [109]. (b) Evolution of the speed of cells in a uniform background of cAMP (filled circles) or in a gradient whose midpoint is given by the horizontal axis (empty circles). Figure taken from [124].

algorithm he used, which will be of crucial importance for the rest of the chapter.

#### 4.2.1 Cells

Wild-type AX3 cells were grown on Petri dishes in HL5 medium (ForMedium Ltd., 7 g/L yeast extract, 14 g/L peptone, 0.5 g/L  $\text{KH}_2\text{PO}_4$ ,  $\text{Na}_2\text{HPO}_4$ ) until the dish was confluent. The cells were then resuspended in a shaking culture at a concentration of  $2 \cdot 10^6$  cells/mL and starved in phosphate buffer (15 mM  $\text{KH}_2\text{PO}_4$ , 1mM  $\text{Na}_2\text{HPO}_4$ , pH=6.0) for 1 hour before being pulsed with cAMP for 4 hours (60  $\mu\text{L}$  of cAMP every 6 minutes). After these 5 hours of starvation, the cells were removed from the shaking culture, centrifuged, and injected into the microfluidic gradient mixer.

#### 4.2.2 Microfluidics

The gradient mixer used for these experiments is the same as the one described by Song et al. in [109], and is derived from an original design by Jeon et al. [54]. It consists of two inlets that join in a mixing cascade, as shown on figure 4.2a. Cyclic AMP is injected at a concentration  $c_{\min}$  in one of the inlets and at a concentration  $c_{\max}$  in the other inlet. As a result, a linear gradient of cAMP is formed in the main channel of the gradient mixer. In our case, the width of the main channel is 525  $\mu\text{m}$ , while its height is 50  $\mu\text{m}$ . Using an average flow speed of 320  $\mu\text{m/s}$ , the gradient of cAMP is linear over a 320  $\mu\text{m}$  wide central region in the main channel. This is shown on figure 4.2b, where the central region of the microgradient is visualized using fluorescein (Invitrogen, Carlsbad, CA).

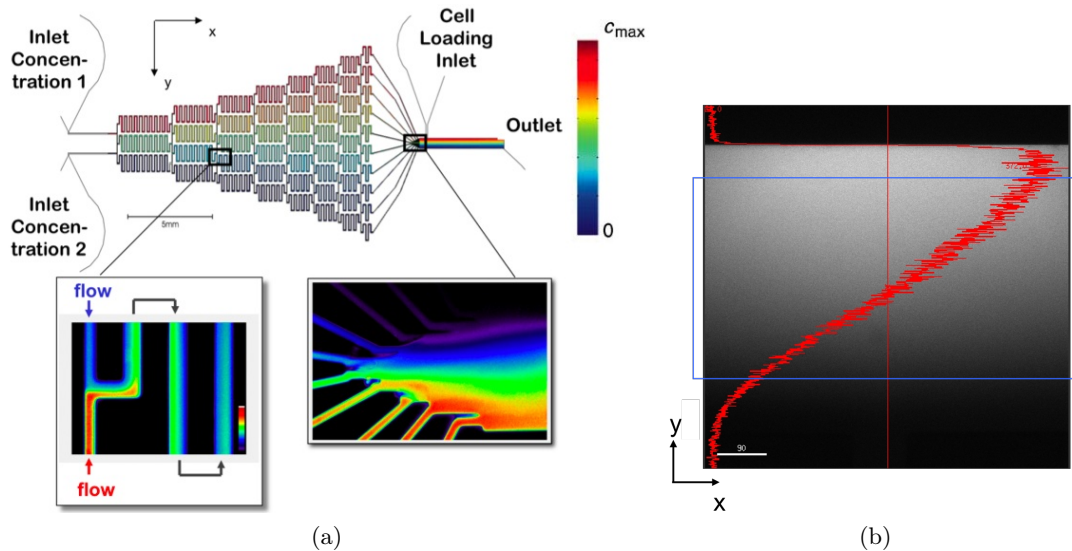


Figure 4.2: (a) The microfluidic gradient mixer used for the chemotaxis experiments. Figure taken from [92]. (b) Profile of the gradient visualized using fluorescein: at our flow rate, the gradient is linear in the central part of the main channel, in a region 320  $\mu\text{m}$  wide (shown by the blue rectangle). The scale bar is 90  $\mu\text{m}$  large. Figure taken from [117].

As can be seen on figure 4.2a, there are two more ports in the gradient mixer apart from the inlets used for chemoattractant or buffer injection. One of them is used to load in the cells,

while the other one is an outlet. Apart from providing a convenient way to produce gradients, the use of microfluidics prevents intercellular communication and washes out cellular waste products.

### 4.2.3 Experiment

Three different areas along the channel were monitored, and pictures were taken at a frame rate of 6/min. A typical snapshot of from the experiment is shown on figure 4.3a. We used a CoolSNAP CCD (Princeton Instruments) to take the pictures, with a resolution of 1024x1024 pixels. The cells were observed with a 10X objective (Olympus plan achromat, NA=0.40), leading to a resolution of 0.6409  $\mu\text{m}$  per pixel. How does this resolution compare with the diffraction limit? Using green light with wavelength  $\lambda = 550 \text{ nm}$ , the smallest details we should be able to observe are of the order of  $r = \lambda/(2NA) \approx 690\text{nm}$ , which is comparable to our pixel size. Images were taken using differential interference contrast (DIC) microscopy. For the principle of DIC microscopy, the reader is referred to a review by Pluta [83].

## 4.3 Image processing

The image processing consisted of two steps. First, the cells were found and then were tracked over time.

### 4.3.1 Finding the cells

#### Principle

DIC microscopy, explained in more detail in [83], enables to see otherwise transparent objects by converting a gradient of optical paths into an intensity gradient. The steeper the gradient, the higher the contrast on the resulting image. Depending on the configuration of the DIC setup, positive gradients of optical path along a reference direction (also called the shear direction) are converted into brighter or darker regions. A typical snapshot of the cells seen under DIC microscopy is shown on figure 4.3.

To find the cells, Matthias convolved the original DIC image with the following kernel [56]:

$$K(x^*, y^*) = \exp\left(-\frac{x^{*2}}{2\sigma_{x^*}^2}\right) \exp\left(-\frac{y^{*2}}{2\sigma_{y^*}^2}\right) \text{sgn}(x^*) \quad (4.1)$$

where  $(x^*, y^*)$  is the coordinate of a point in a reference frame rotated by an angle  $\theta$ , with  $\theta$  the angle of the DIC shear vector. The shape of the convolution kernel is shown on figure 4.4a for  $\phi = 37.5^\circ$ ,  $\sigma_{x^*} = 10$  pixels,  $\sigma_{y^*} = 1$  pixel. The result of the convolution can be seen on figure 4.4b. The cells now have a uniform intensity, distinct from the background, which enables us to use a simple intensity threshold to find them. This threshold was automatically found using the Isodata algorithm adapted from [93] and already described in section 3.3.1.

#### Limitations

As all automated methods of image segmentation, this one is not exempt from errors. To estimate the error, we manually found the outlines of 56 cells in a frame, and computed the position of their centroids. We then compared the position of these manually found centroids

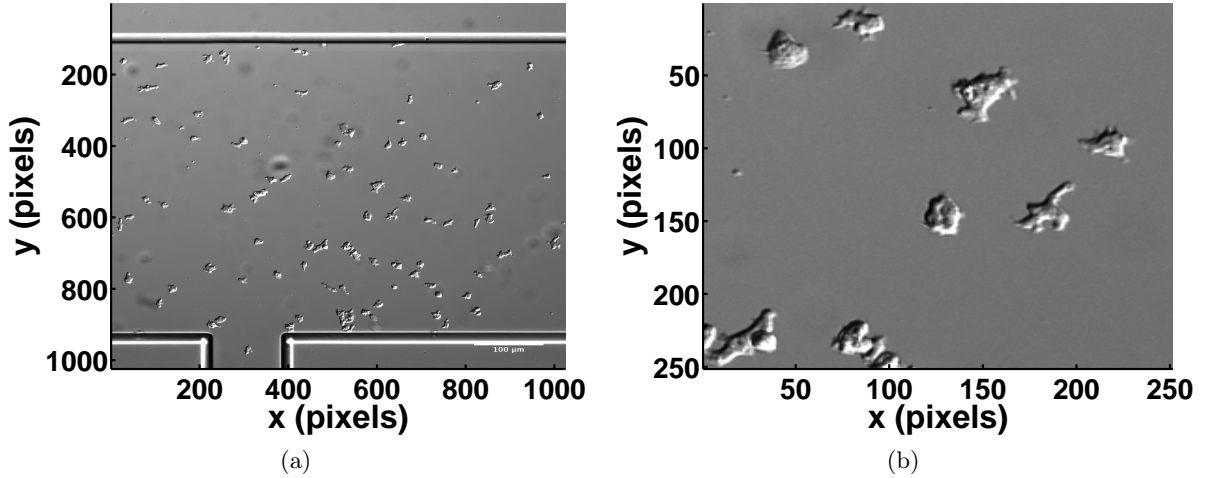


Figure 4.3: (a) Image of cells in the gradient mixer using DIC microscopy. (b) Enlarged regions showing individual cells. The shear direction is the direction of the line separating the dark from the bright region. Scale: 1 pixel corresponds to  $0.6409 \mu\text{m}$ .

with the corresponding positions given by the segmentation algorithm. The precision of the algorithm depends on the three parameters of the gaussian convolution kernel,  $\sigma_{x^*}$ ,  $\sigma_{y^*}$ , and  $\theta$ . First, we fixed the variances  $\sigma_{x^*} = 10$  pixels,  $\sigma_{y^*} = 1$  pixel of the gaussians and varied the angle  $\theta$ . As expected, the minimum error was found for  $\theta$  around the shear direction,  $\theta = 37.5^\circ$  (figure 4.5a). Then, keeping  $\theta = 37.5^\circ$  fixed, we varied  $\sigma_{x^*}$  and  $\sigma_{y^*}$ . The average error on the position of the cells' centroids is shown on figure 4.5b. As can be seen on this figure, different combinations of parameters allow to process the data equally well. We circled with a black line a region of parameters giving a mean error between 1.7 and 1.9 pixels, and a standard deviation of the mean between 0.7 and 0.8 pixels. Matthias chose  $\sigma_{x^*} = 10$  pixels,  $\sigma_{y^*} = 1$  pixel, for which the error is  $1.8 \pm 0.8$  pixels. This result is very important for the rest of the chapter: if we want to be accurate in our estimate of the cells' velocities, the cells should move at least 2.6 pixels in one time step.

### 4.3.2 Cell tracking

The cell tracking algorithm was adapted from an existing algorithm by Crocker and Gier [22], based on log-likelihood maximization. A complete description of the algorithm can be found in [117]. To briefly summarize, the algorithm considers that each cell is a Brownian particle. The probability  $P_i(\delta_i, \Delta t)$  that cell  $i$  makes a step of size  $\delta_i$  in a time  $\Delta t$  can then be analytically expressed. Moreover, because cells are supposed to be independent of each other, the probability that cell 1 makes a step  $\delta_1$ , cell 2 a step  $\delta_2, \dots$ , cell  $N$  a step  $\delta_N$  is given by the product of the individual probabilities:  $P(\delta_1, \dots, \delta_N, \Delta t) = \prod_{i=1}^N P_i(\delta_i, \Delta t)$ . The algorithm performs a maximization of  $P(\delta_1, \dots, \delta_N, \Delta t)$ , which gives the most likely positions of the particles at time  $t + \Delta t$ , knowing their positions at time  $t$ .

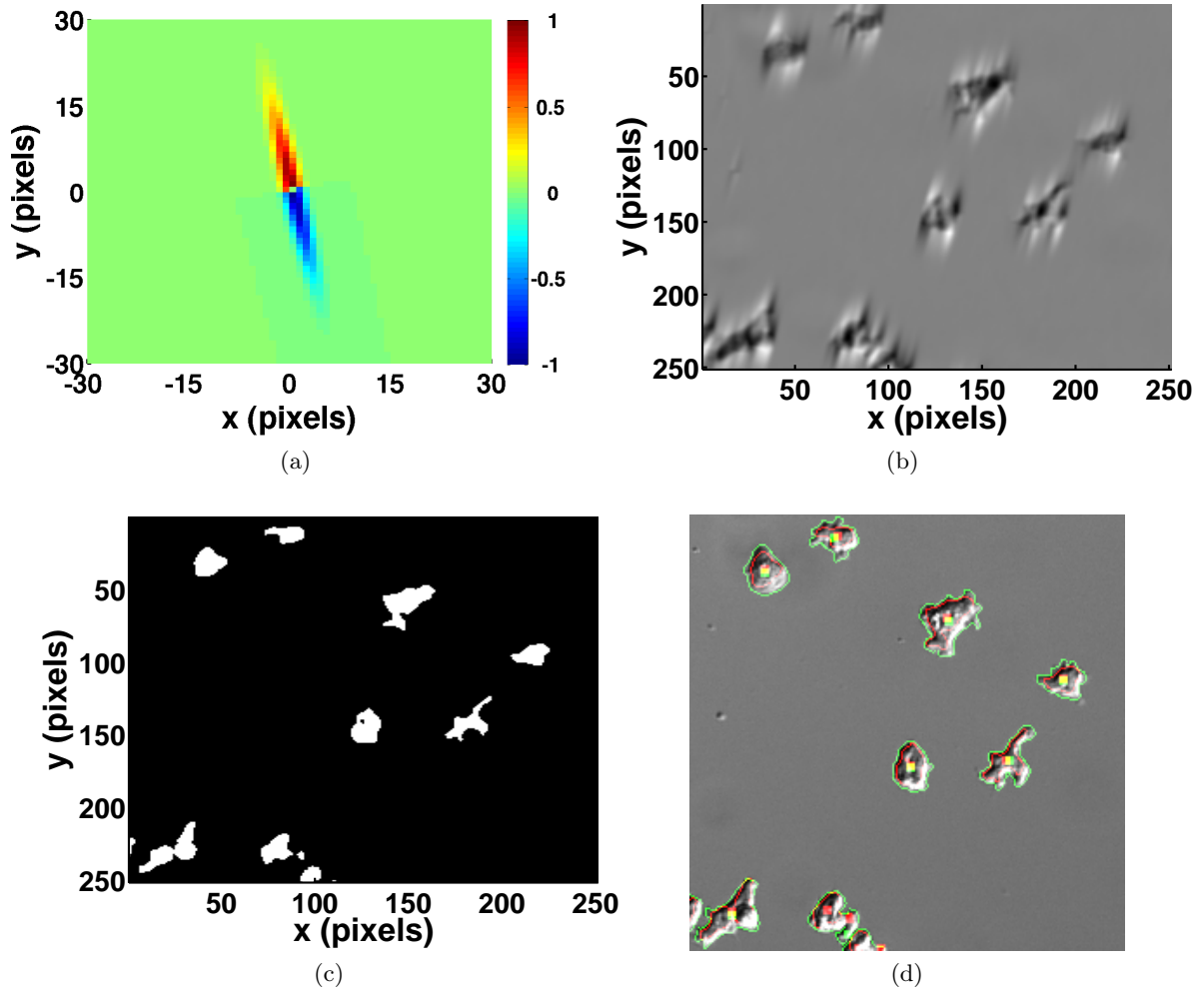


Figure 4.4: .

(a) Convolution kernel used in the algorithm to automatically find the cells. (b) Image resulting from the convolution of the original microscopy image and the 2D gaussian kernel. (c) Result of the isodata algorithm to threshold the convolved image, showing the cells found by the algorithm. (d) Comparison of the manually found edges and centers of mass of the cells (green) with the automated procedure (red). The outlines of the cells are different, but the center of mass is reasonably well found (mean error: 1.8 pixels, see main text).

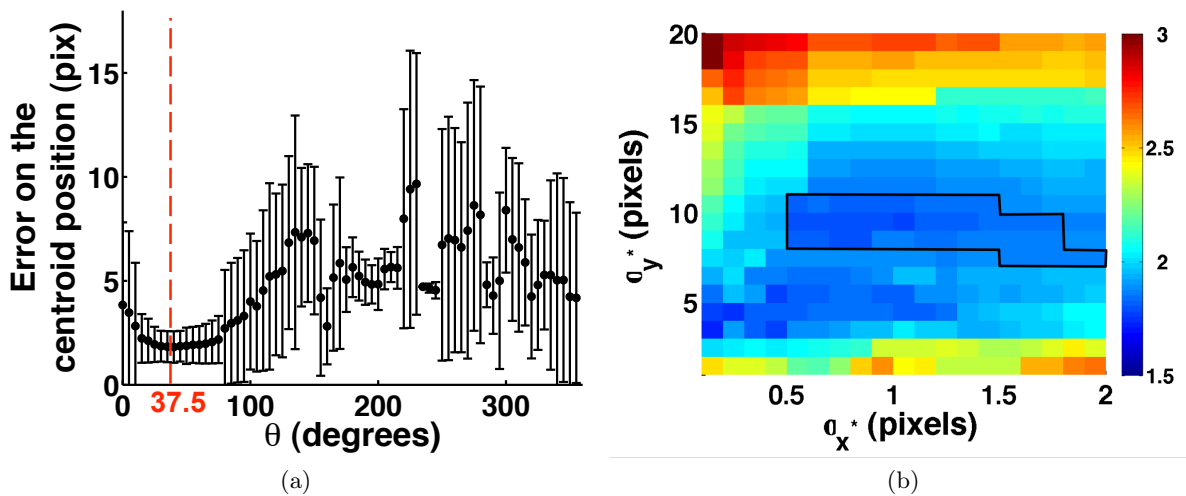


Figure 4.5: (a) Mean error on the position of the centroid found by the automated algorithm, as a function of the angle  $\theta$ . Error bars show the standard deviation. As expected, the error gets minimum around  $\theta = 37.5^\circ$ , which is the direction of the shear of the DIC image. Other parameters:  $\sigma_{x^*} = 10$  pixels,  $\sigma_{y^*} = 1$  pixel. (b) Mean error on the position of the center of mass found by the automated algorithm, as a function of  $\sigma_{x^*}$  and  $\sigma_{y^*}$ , for  $\theta = 37.5^\circ$ . The black line circles adjacent parameters that give similar results: the mean error is then between 1.7 and 1.9 pixels, with a standard deviation between 0.7 and 0.8 pixels.

## 4.4 What gradient does the cell see?

Before looking at the experimental results, let us think about the gradient seen by the cell. First of all, the cell is an obstacle that disturbs the flow, so the gradient around the cell is distorted by the cell's presence [9]. Second, we have to translate a concentration of cAMP into an amount of occupied receptors on the cell's surface.

### 4.4.1 Flow effects

The effect of a flow on the external gradient of cAMP has been studied in Beta et al. [9]. Using Comsol Multiphysics, the authors simulated a three-dimensional flow in a microchannel in which a cell was sitting. Starting from a linear concentration profile upstream of the cell, they computed the concentration profile of cAMP around the cell, changing the flow speed, the relative height of the cell and the channel, and the elongation and orientation of the cell. Two effects counterbalance each other. The first one is what the authors called the *shielding effect*, that causes a cell to be exposed to a concentration gradient lower than the one expected if the cell were not there. For simplicity, consider a 2D flow and a 2D cell (see figure 4.6a). At the cell's midpoint, the concentration of cAMP is  $c_0$ . Because the streamlines divide at the middle of the cell, if the diffusion effects are negligible compared to the convection effects, the cell would experience a uniform concentration of cAMP of  $c_0$ . We can now consider the other extreme case, where diffusion effects are more important than convection effects. In the upper half of the cell ( $y > 0$ ), the concentration in the boundary layer is lower than in

#### 4.4. What gradient does the cell see?

the bulk. Because of this, there will be a diffusive flux towards the boundary layer, that will tend to increase the local concentration of cAMP. Similar reasoning for the lower half of the cell ( $y < 0$ ) shows a decrease of the local concentration of cAMP. In other words, diffusion increases the gradient seen by the cell. To compare the effects of diffusion and convection, the authors introduce the two-dimensional Péclet number:

$$Pe_{2D} = \frac{v\pi r}{D} \quad (4.2)$$

where  $D$  is the diffusion coefficient of cAMP,  $r$  is the radius of the cell and  $v$  is the flow speed. This Péclet number can be extended to 3D, where it is written (see equation (14) in [9]):

$$Pe_{3D} = \frac{L_{cell,x}}{D} h v_0 (3 - 2h) \quad (4.3)$$

where  $L_{cell,x}$  is the length of the cell in the direction of the flow (see figure 4.6b),  $h$  is the ratio of the cell height and the channel height, and  $v_0$  is the average flow velocity at mid-height of the channel. As a rule of thumb, the authors conclude that a Péclet of the order of 1 will assure gradient deviations below 10%. In our case, the channel's height is  $50 \mu\text{m}$ , the cell's height is about  $4 \mu\text{m}$ , the diffusion coefficient of cAMP is  $400 \mu\text{m}^2/\text{s}$ , the length of the cell along the flow is around  $10 \mu\text{m}$ , and the mean flow velocity at mid-height of the channel is  $476 \mu\text{m}/\text{s}$ . This gives a Péclet of 2.45, which ensures that the deviations from the imposed gradient are less than 5% (see [9]).

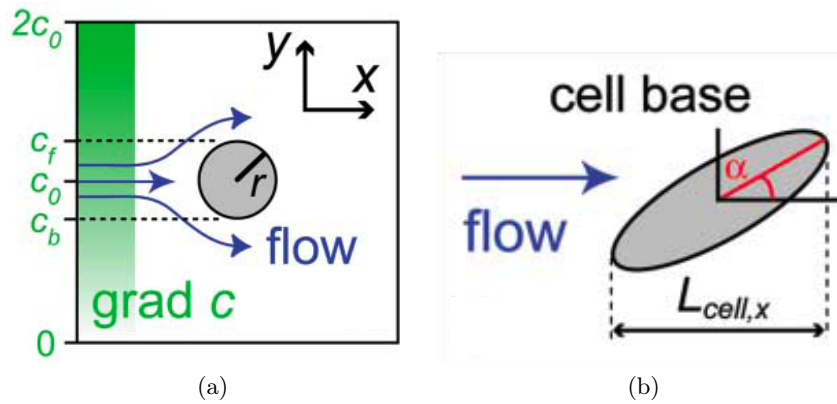


Figure 4.6: (a) A 2D circular cell in a 2D flow of chemoattractant. The chemoattractant profile is a linear gradient upstream of the cell. (b) Definition of  $L_{cell,x}$ , the length of the cell in the direction of the flow. Both figures taken from [9].

#### 4.4.2 Receptor occupancy

How does a gradient of cAMP expressed in  $\text{nM}/\mu\text{m}$  translate in terms of difference in receptor occupancy between front and back of the cell? The reversible binding of cAMP to a receptor can be written:



where  $k_1$  is the binding rate of cAMP to a free receptor Rec,  $k_{-1}$  is its unbinding rate, cAMP·Rec is an activated receptor (bound to cAMP), and the total number of receptors is

$$R_{\text{tot}} = [\text{Rec}] + [\text{cAMP} \cdot \text{Rec}] \quad (4.5)$$

At equilibrium:

$$\frac{d[\text{cAMP} \cdot \text{Rec}]}{dt} = k_1[\text{cAMP}][\text{Rec}] - k_{-1}[\text{cAMP} \cdot \text{Rec}] = 0 \quad (4.6)$$

So that

$$k_1[\text{cAMP}](R_{\text{tot}} - [\text{cAMP} \cdot \text{Rec}]) - k_{-1}[\text{cAMP} \cdot \text{Rec}] = 0 \quad (4.7)$$

$$\Leftrightarrow [\text{cAMP} \cdot \text{Rec}] = R_{\text{tot}} \frac{[\text{cAMP}]}{[\text{cAMP}] + K_d} \quad (4.8)$$

where we have defined  $K_d = k_{-1}/k_1$ . For a concentration of cAMP equal to  $K_d$ , half of the receptors of the cell are occupied. The value of  $K_d$  has been determined to be  $230 \pm 45$  nM by Dormann et al. [25]. The fraction  $\rho$  of occupied receptors is therefore:

$$\rho = \frac{[\text{cAMP}]}{[\text{cAMP}] + K_d} \quad (4.9)$$

Let's now assume that the cell measures the cAMP gradient surrounding it by averaging the number of occupied receptors in its upper half and comparing it to the average number of occupied receptors in its lower half. Consider a 1D cell and call  $y_m$  the coordinate of the middle of the cell,  $y_b$  the coordinate at its bottom and  $y_t$  the coordinate at its top. The cell's length is  $L$ , and the concentration profile of cAMP  $c(y)$  is linear in  $y$ :

$$c(y) = ay \quad (4.10)$$

where  $y = 0$  corresponds to the bottom of the gradient region. In the upper half of the cell, the average number of occupied receptors is:

$$R_{\text{up}} = \frac{R_{\text{tot}}}{L} \int_{y_m}^{y_t} \frac{c(y)}{c(y) + K_d} dy = \frac{R_{\text{tot}}}{L} \int_{y_m}^{y_t} \frac{ay}{ay + K_d} dy \quad (4.11)$$

$$= \frac{R_{\text{tot}}}{L} \left[ \frac{L}{2} - \frac{K_d}{a} \ln \left( \frac{ay_t + K_d}{ay_m + K_d} \right) \right] \quad (4.12)$$

Similarly, in the lower half of the cell, the average number of occupied receptors is:

$$R_{\text{low}} = \frac{R_{\text{tot}}}{L} \left[ \frac{L}{2} - \frac{K_d}{a} \ln \left( \frac{ay_m + K_d}{ay_b + K_d} \right) \right] \quad (4.13)$$

The difference of receptor occupancy between front and back is:

$$\Delta R = R_{\text{up}} - R_{\text{low}} = \frac{R_{\text{tot}} K_d}{aL} \ln \left[ \frac{(ay_m + K_d)^2}{(ay_b + K_d)(ay_t + K_d)} \right] \quad (4.14)$$

$$= - \frac{R_{\text{tot}} K_d}{aL} \ln \left[ 1 - \frac{(aL)^2}{4(ay_m + K_d)^2} \right] \quad (4.15)$$

$$(4.16)$$



A cell is typically 10  $\mu\text{m}$  long, so if we consider a cell in the middle of the gradient region, at a position  $y_m = 160 \mu\text{m}$ , we can safely approximate  $\Delta R$  by:

$$\Delta R \simeq \frac{K_d R_{tot} a L}{4(a y_m + K_d)^2} \quad (4.17)$$

If we want to know what happens for a 2D cell, we have to calculate :

$$\Delta R = \frac{R_{tot}}{2\pi} \left[ \int_0^\pi \frac{a(y_m + L/2 \sin \phi)}{a(y_m + L/2 \sin \phi) + K_d} d\phi - \int_\pi^{2\pi} \frac{a(y_m + L/2 \sin \phi)}{a(y_m + L/2 \sin \phi) + K_d} d\phi \right] \quad (4.18)$$

where  $L$  is now the cell's diameter. The calculations get lengthy, and the result is:

$$\Delta R = \frac{2R_{tot}K_d}{\pi\sqrt{(ay_m + K_d)^2 - (aL/2)^2}} \arctan \left[ \frac{aL/2}{\sqrt{(ay_m + K_d)^2 - (aL/2)^2}} \right] \quad (4.19)$$

Doing the same approximation as in the 1D case, which is that  $L \ll y_m$  in general, we get:

$$\Delta R \simeq \frac{K_d R_{tot} a L}{\pi(a y_m + K_d)^2} \quad (4.20)$$

In both the 1D and the 2D calculation (and this could be extended to 3D), the difference in receptor occupancy is therefore proportional to

$$\frac{a}{(a y_m + K_d)^2} \quad (4.21)$$

which shows the importance of both the slope of the concentration profile  $a$  and of the mid-point concentration  $a y_m$ . The analysis presented here slightly differs from the one shown in Song et al. [109] in that we average the receptor occupancy in each half of the cell. In [109], the authors compared the receptor occupancy at the very top of the cell (where the concentration is maximal,  $c_{\max}$ ) to the receptor occupancy at the very bottom of the cell (where the concentration is minimal  $c_{\min}$ ). This is equivalent to having a concentration profile looking like a step function, with all the receptors of the lower half of the cell sensing a concentration  $c_{\min}$  and all the receptors of the upper half of the cell sensing a concentration  $c_{\max}$ . Using our formula, we will therefore get lower estimates of the difference in receptor occupancy than in [109].

## 4.5 Preprocessing: excluding cell tracks

After these preliminaries, we move on to the data processing. First, we explain why several cell tracks were excluded before performing the analysis.

### 4.5.1 Excluding cell tracks based on their length

The tracking algorithm, described in section 4.3.2, is not always able to find a complete cell trajectory. For example, this is the case when two cells run into each other, and the centroids of these two cells become undistinguishable. It also happens that the position of the cell's centroid jumps too large of a distance between two consecutive frames for the algorithm to be able to connect the dots. For this reason, the cell tracks are sometimes interrupted. The

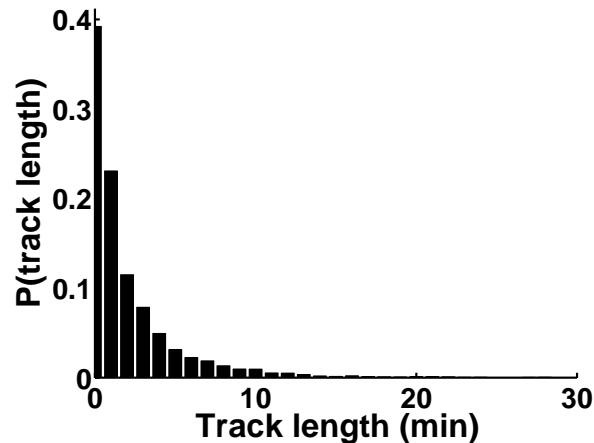


Figure 4.7: Typical histogram of the length of the cell tracks found by the tracking algorithm. As a total, 6342 tracks were identified. More than 60% of them are shorter than one minute.

histogram of length of all cell tracks is shown on figure 4.7, for one typical experiment. As can be seen, more than 60% of the tracks are shorter than one minute.

In our later analysis, we will need to calculate the average velocity along a cell track. The greater the number of points in a track, the more accurate this average velocity will be. It is therefore important that our track be not too short, and we want to discard all tracks that are shorter than a given length. On the other hand, if the threshold length is too high, we will retain too few tracks. We decided arbitrarily to put the threshold at 60 points (keeping tracks longer than 10 minutes). In our particular example shown on figure 4.7, this left us with 247 tracks out of the initial 6342.

#### 4.5.2 Excluding pre-polarized cells coming from the top of the channel

As already mentioned in 4.2.2, the cAMP gradient does not cover the whole width of the gradient mixer. Some cells are near the top of the channel, where there is no gradient. These can be cells that have crawled up the gradient and reached the top, or ones that were already at the top of the channel at the beginning of the experiment. These cells show a random motion and sometimes crawl down into the gradient region. It then takes them some time to sense the gradient and go back to the top of the channel again. Examples of such tracks are shown on figure 4.8. This behavior in itself is very interesting: it tells us how long it takes for a prepolarized, moving cell, to sense a gradient pointing in the direction opposite its motion. It is however a different behavior than the one we would like to quantify, which is the chemotactic motion of non-prepolarized cells. For this reason, we excluded these tracks from the analysis. In the example mentioned above, 6 tracks showed this behavior. This left us with 241 cells to analyze.

#### 4.5.3 Excluding immobile cells and choice of the time step

In a population of cells, there are always a few cells that are not motile (whether the cells are in a gradient or in buffer). In all the articles on chemotactic cell motion [127, 30, 109, 34] it is considered normal to take into account only the moving cells in the analysis of cell motion.

#### 4.6. Chemotactic behavior in different gradients

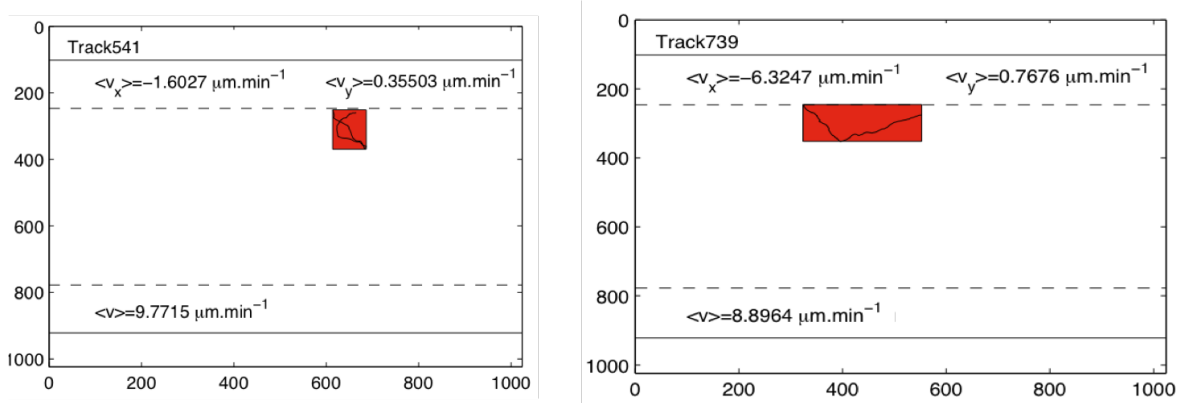


Figure 4.8: Examples of cells starting their motion at the top of the channel, where there is no gradient of cAMP. The cell starts to go down the gradient before realizing that the gradient points up, and crawling up again. This kind of tracks was excluded from the later data processing. Solid line: borders of the gradient mixer. Dashed line: limits of the gradient region. Axis labels: pixel coordinate (pixel size:  $0.6409 \mu\text{m}$ ).

This introduces an arbitrary parameter in the data processing: we have to decide when a cell is immobile and when it is not. In our case, we base our exclusion criterion on the cell's displacement. The time step used to calculate the cell's velocities will be chosen based on our exclusion criterion. We have shown that the error on the position of the cell centroid was on average  $1.8 \pm 0.8$  pixels. Between two consecutive time steps, the cell moves a distance  $d$ . For this distance to be accurately measured, it has to be bigger than the error of the segmentation algorithm, *i.e.*  $d > 1.8 + 0.8 = 2.6$  pixels, equivalent to  $1.7 \mu\text{m}$ .

We excluded cells that were not fulfilling this requirement as follows. First, we enclosed the trajectories in circles and defined the track length by the length of the circle diameter (see figure 4.9a). The distribution of track length is shown on figure 4.9b. We chose to keep all trajectories whose enclosing circle had a diameter larger than  $30 \mu\text{m}$ . Because the cell tracks were at least 10 minutes long, the cells' speeds were on average  $3 \mu\text{m}/\text{min}$ . This ensures that  $1.7 \mu\text{m}$  were covered on average in 40 seconds, which will be the time step used in the rest of this chapter to calculate velocities. The choice of keeping cell tracks that were longer than  $30 \mu\text{m}$  comes from a compromise. The longer the threshold length, the smaller time step we can use, but the more cell tracks we discard. The smaller the threshold length, the more cells we can keep, but the bigger the time step has to be, which reduces the number of points in each track. In the end, out of the 241 tracks that we had above, 221 remained.

#### 4.6 Chemotactic behavior in different gradients

Now that the data have been preprocessed, we come to the analysis of cell motion as a function of the gradient. When cellular chemotaxis is assayed, it is common to report two average quantities: the cells' average speed  $\bar{v}$ , and their average chemotactic index (CI), which is defined differently by different groups. Varnum and Soll [124] defined the chemotactic index for each cell as the length of the path in the gradient direction divided by the total length of the track, *i.e.*  $\text{CI} = \bar{v}_y / \bar{v}$  where  $\bar{v}_y$  is the average velocity in the gradient direction. Note

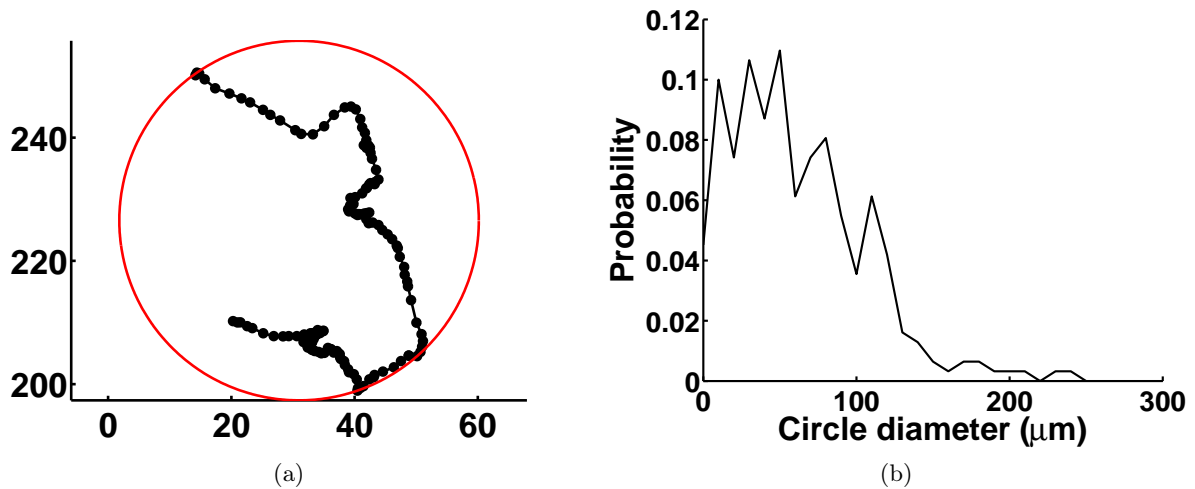


Figure 4.9: (a) Example of a circle enclosing a cell track. In the rest of the chapter, we discard all cells whose enclosing circles have a diameter smaller than 30 microns. Axes: position, in microns. (b) Distribution of track lengths.

that this definition implies to calculate  $\bar{v}$ , whose value depends on the time step used. This is the definition used in the recent article by Fuller et al. [34]. Other groups define the chemotactic index as the average cosine of the angle between the cell's direction and the gradient, *i.e.*  $CI = \overline{v_y/v}$ . Up to a numerical factor, this is the definition used by Fisher et al. in [29, 30]. The CI defined in this way does not depend on the time step used, but it also does not take into account the tortuosity of the path followed by the amoeba. We used the first definition of the chemotactic index. The efficiency of cellular chemotaxis is then characterized by comparing the different values of these average quantities, obtained under different experimental conditions. Different experimental conditions may correspond to different mutants lacking or overexpressing given genes, and put in the same gradient of chemoattractant (see for example [44, 36]). Or one might want to characterize, like we do, the chemotaxis of wild-type cells in different profiles of chemoattractant [30, 109]. In this section, we show the evolution of the chemotactic index and of the average speed of all cells as a function of the gradient applied. A quantitative understanding of this evolution is yielded by introducing the signal-to-noise ratio (SNR), which takes into account the noise due to the stochasticity of chemical reactions in the chemotactic pathway, and compares this noise to the average chemotactic signal seen [119].

#### 4.6.1 Stationarity of the velocity histograms with time

We plotted on figure 4.10 a typical histogram of the the velocities  $v_x$ ,  $v_y$  and of the speed  $v$  of cells as a function of time. In this particular case, the histograms were stationary from between 5 and 50 minutes after the gradient was turned on. In a couple of experiments, the histograms were stationary starting from the tenth minute on. For this reason, we will consider only the data taken between 10 and 50 minutes. The non-stationarity during the first five to ten minutes of the experiment may be explained by the fact that the gradient of cAMP takes

time to establish. At the end of the experiment, after 50 minutes, the faster cells have reached the top of the channel, and the slow ones are the only remaining.

### 4.6.2 Cellular velocity as a function of the gradient

We plotted on figure 4.11 the mean velocities  $v_x$ ,  $v_y$  and  $v$  of all cells as a function of the gradient strength. The error bars show the standard error. The results are qualitatively similar to the ones of Fisher et al. [30], and agree quantitatively with Song et al. [109] and Theves [117]. In most of the cases (filled circles), the concentration in the microfluidic channel was 0 on one side and  $c_{\max}$  on the other. For these points, the lower x-axis shows the gradient of cAMP applied (in  $\text{nM}/\mu\text{m}$ ), while the upper x-axis shows the midpoint concentration in the microfluidic channel (in  $\text{nM}$ ). In some cases (empty circles), however, the lower concentration in the channel was set to a non zero value. In these cases, we decided to plot the points at their correct gradient value (lower x-axis), but the midpoint concentration shouldn't be read from the upper x-axis. We will see later how we can build a parameter that takes into account both the amplitude of the gradient and the midpoint concentration seen. For the time being, we can however note that the midpoint concentration plays a role in the ability of a cell to sense a gradient (contrarily to what was concluded in [109] within their experimental precision). For example, for the empty circles at a gradient of  $0.03 \text{ nM}/\mu\text{m}$ , the midpoint concentration is  $105 \text{ nM}$ . The chemotactic index of these cells is clearly different from the chemotactic index of the cells that experience the same absolute gradient but a midpoint concentration of  $5 \text{ nM}$ . However, the average speeds of both these cell populations are similar. The case where no gradient is applied ( $c_{\min} = c_{\max} = 0$ ) has been drawn artificially at a midpoint concentration of  $0.005 \text{ nM}$ .

### 4.6.3 Difference in receptor occupancy

In Song et al. [109], the authors provide a tentative explanation for the observed evolution of the chemotactic velocity  $v_y$  as a function of the gradient. They estimate the difference in receptor occupancy between front and back of the cell, and show that the cells behave chemotactically when this difference is on the order of 10 receptors, but not below. In section 4.4.2 we showed that, in the case of a 2D cell,  $\Delta R$  depended both on the slope  $a$  of the concentration profile and on its midpoint  $ay_m t$ :

$$\Delta R = \frac{K_d R_0 a L}{\pi (ay_m + K_d)^2} \quad (4.22)$$

where  $K_d$  is the binding constant of cAMP to the cAMP receptor on the cell membrane,  $R_0$  is the total number of receptors on the membrane and  $L$  is the length of a cell. On figure 4.12, the evolution of  $\Delta R$  with the gradient and the midpoint concentration is shown, with  $K_d = 230 \text{ nM}$  [25],  $R_0 = 70\,000$  [25] and  $L = 10 \mu\text{m}$  [109]. In our device, when the concentration profile runs from 0 to  $c_{\max}$ , the increase of the absolute gradient is simultaneous to an increase in the midpoint concentration value. Because of this increase in the midpoint concentration, receptors saturate and the difference in receptor occupancy between front and back decreases for steep gradients. We plotted the evolution of the chemotactic index as a function of  $\Delta R$  on figure 4.12c. It appears that the difference in receptor occupancy is not perfectly correlated the observed behavior: at same values of  $\Delta R$ , different chemotactic behaviors can be observed, and different values of  $\Delta R$  lead to the same chemotactic behavior. Note moreover that on

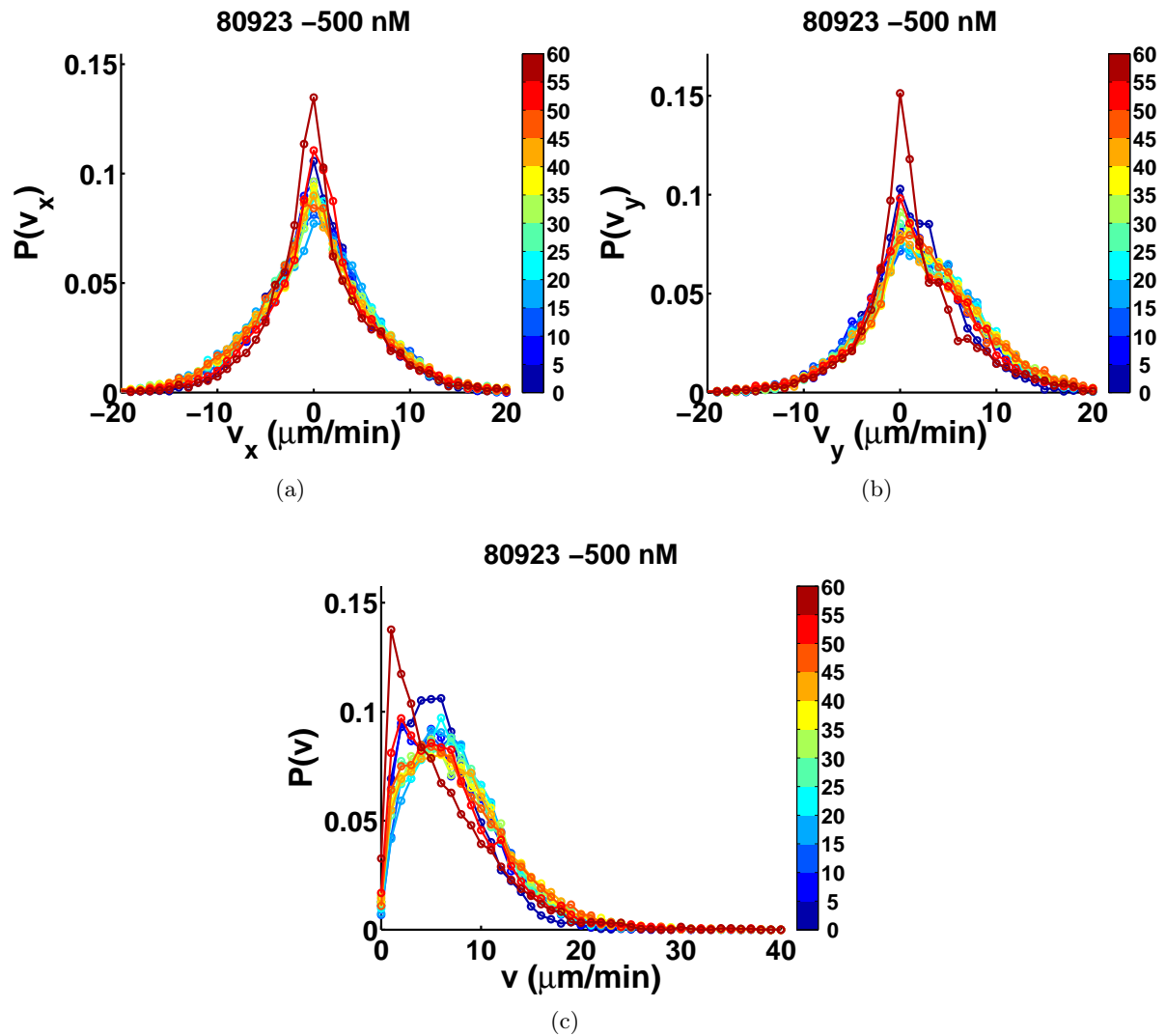


Figure 4.10: Typical evolution of the (a)  $v_x$ , (b)  $v_y$  and (c)  $v$  histograms with time for all cells. The time step used to calculate the velocity is 40 seconds. The histograms are binned by time ranges of 5 minutes, dark blue being the earliest histogram measured (between 0 and 5 minutes after the gradient has been turned on) and red being the latest histogram measured (between 45 and 50 minutes after the gradient has been turned on). The histograms are stationary between 5 and 55 minutes.

#### 4.6. Chemotactic behavior in different gradients

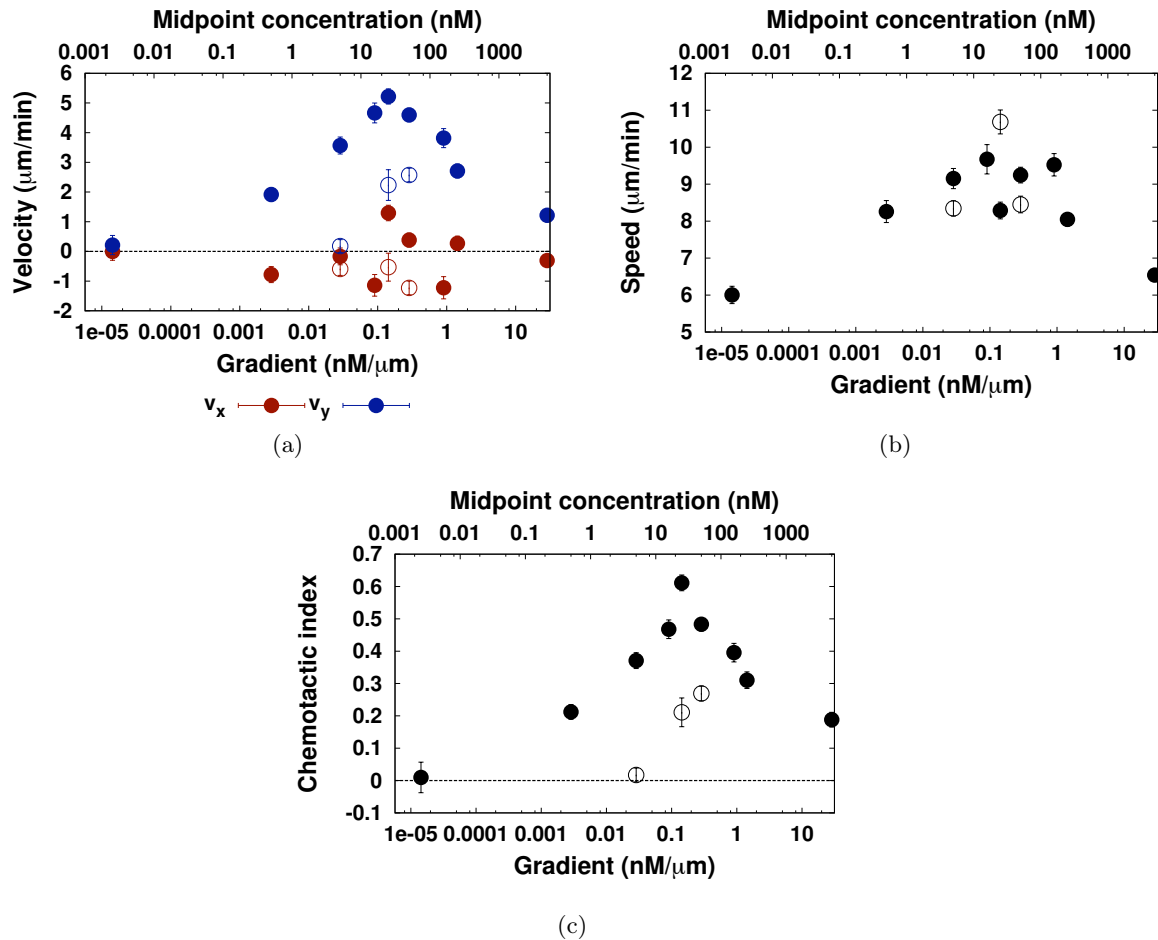


Figure 4.11: Evolution of the velocities (a)  $v_x$ ,  $v_y$ , (b) the speed  $v$ , and (c) the chemotactic index with the gradient for all cells. The first point (plotted at a midpoint of 0.005 nM) had no gradient applied, and was drawn at a non-zero midpoint concentration because of the logarithmic scale. The filled circles show the experiments for which the cAMP concentration in the channel went from 0 to a value  $c_{\text{max}}$ . The empty circles correspond to points where the lower concentration in the channel was set to a nonzero value. For these points, one cannot read the midpoint concentration from the upper x-axis. For the empty circles at a gradient of 0.03 nM/ $\mu\text{m}$ , the midpoint concentration was 105 nM. For the empty circle at 0.14 nM/ $\mu\text{m}$ , the midpoint concentration was 75 nM. For the empty circles at 0.29 nM/ $\mu\text{m}$ , the midpoint concentration was 70 nM.

figure 4.12c, the empty circles are systematically below the filled ones: cells experiencing a given difference in receptor occupancy chemotax less well when the midpoint concentration is raised. This strongly suggests that the data could be quantitatively explained if we had a quantity combining both the effect of the midpoint concentration and the gradient. Moreover, we see on these graphs that the maximal difference in receptor occupancy is of the order of 350 receptors. When this is the case, on average 23 000 receptors are occupied. It is therefore important to take into account the fluctuations in the binding/unbinding process, which is the aim of the next paragraph.

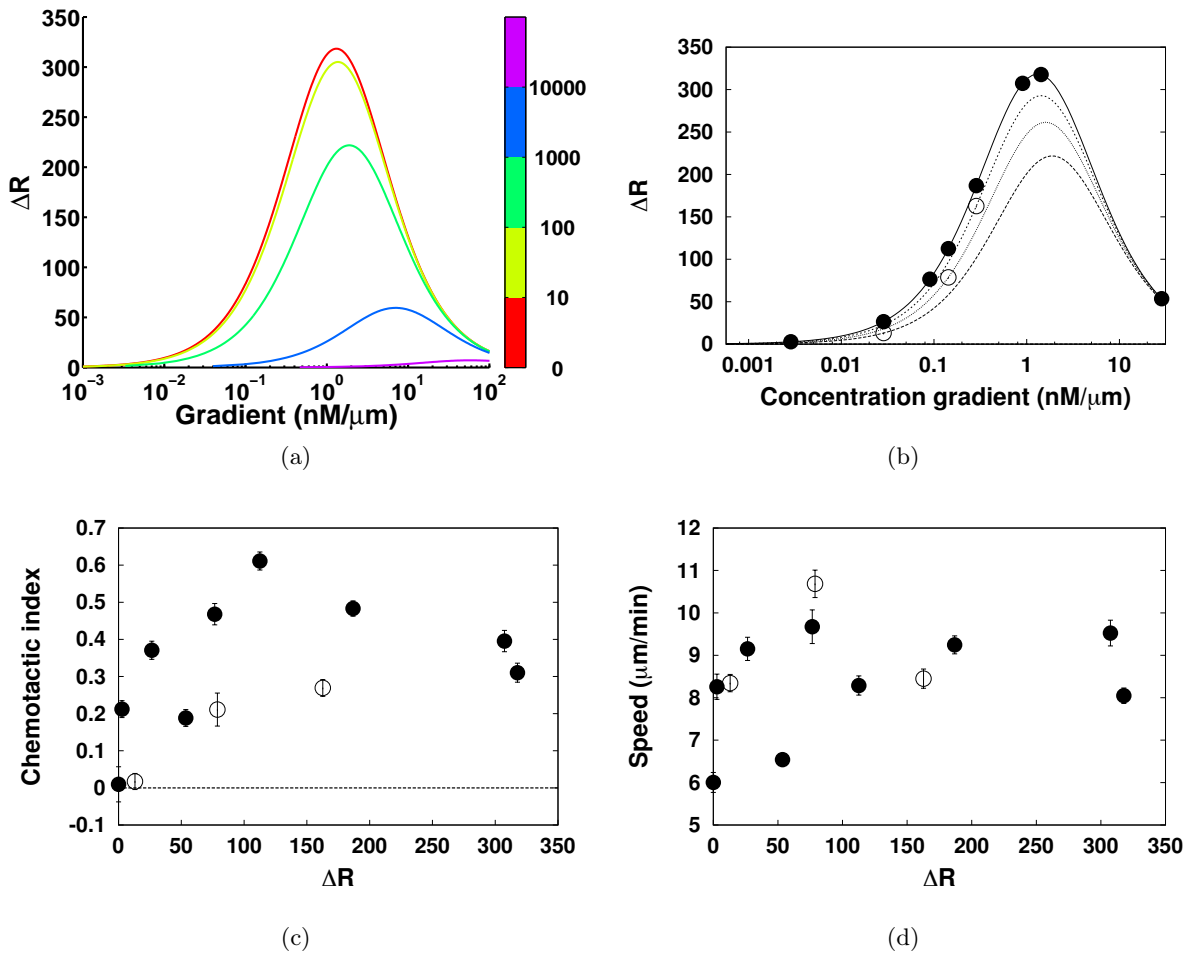


Figure 4.12: (a) Difference in receptor occupancy calculated using equation 4.19, as a function of the gradient. The concentration profiles run from  $c_{\min}$  to  $c_{\max}$ . The value of  $c_{\min}$  is indicated by the colorbar. The gradient spans over  $350 \mu\text{m}$ . (b) Difference in receptor occupancy, with our experimental conditions shown by the dots. Note that the maximal difference in receptor occupancy is of the order of 350 receptors, out of a total of 70 000. (c) Evolution of the chemotactic index with the difference in receptor occupancy  $\Delta R$ . There is no one-to-one relationship between the chemotactic index and the difference in receptor occupancy. (d) Average speed as a function of  $\Delta R$ .



#### 4.6.4 Signal to noise ratio

The stochasticity of receptor binding and its impact on *D. discoideum* chemotaxis has been studied theoretically in recent articles by Rappel and Levine [89, 88]. At the lower limit of detection, the relationship between the chemotactic index of a cell and the fluctuations of the chemoattractant binding on the receptor was experimentally quantified by Van Haastert and Postma [122]. In the following section, we will follow the more general approach of Ueda and Shibata [119] to understand the effect of the fluctuations of cAMP binding on gradient sensing.

It seems reasonable to assume that the number of binding events in two nonoverlapping time intervals are independent, and that moreover the probability distribution of binding events during a time interval depends only on the length of this time interval. If we add to these two properties the fact that the probability to have two binding events in a very small time interval should essentially be zero, we get the result that binding is a Poisson process. This has been confirmed experimentally by Ueda et al. in [118]. In a uniform concentration  $C$  of cAMP, the number of occupied receptors  $R^*$  is :

$$R^* = R_{\text{tot}} \frac{C}{C + K_d} \quad (4.23)$$

where  $K_d$  is the dissociation constant (see section 4.4.2). The stochastic fluctuations  $\delta R^*$  about the steady state  $R^*$  have a variance given by:

$$\langle (\delta R^*)^2 \rangle = \frac{K_d}{C + K_d} R^* \quad (4.24)$$

The proof of this equation is given in Appendix A. The signal to noise ratio is then defined as:

$$\text{SNR} = \frac{R^*}{\sqrt{\langle (\delta R^*)^2 \rangle}} \quad (4.25)$$

This is the SNR describing the fluctuations of receptor occupancy for a cell in a uniform concentration of cAMP. In our case, the cells are in a gradient of cAMP, and what we would like to calculate is the noise in the differences in active receptors between front and back. This was done by Ueda and Shibata in [119], and we will follow their approach in this paragraph. For the details of the calculations, the reader is referred to [119]. If the gradients we are using are shallow (the difference of concentration over the cell  $\Delta C$  is very small compared to the midpoint concentration  $C$ ), the difference in occupied receptors between front and back can be approximated by<sup>2</sup>:

$$\Delta R^* = g_R \frac{\Delta C}{C} \overline{R^*} \quad (4.26)$$

where we have defined the gain  $g_R$  of the binding reaction as

$$g_R = \frac{d \log R^*}{d \log C} = \frac{K_d}{K_d + C}. \quad (4.27)$$

and where  $\overline{R^*}$  is the average number of occupied receptors around the cell. The noise in the differences in active receptors between front and back can then be approximated by:

$$\sigma_{\Delta R^*}^2 = g_R^2 \overline{R^*} \quad (4.28)$$

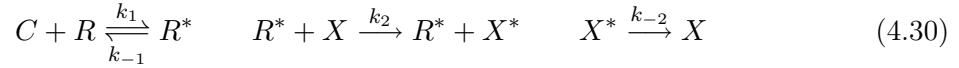
---

<sup>2</sup>In appendix A we give the general formula for the SNR without making any approximation on the strength of the gradient.

so that the SNR is given by:

$$\text{SNR} = \frac{\Delta R^*}{\sigma_{\Delta R^*}} = \frac{\Delta C}{2\sqrt{C}} \frac{\sqrt{K_d R_{\text{tot}}}}{C + K_d} \quad (4.29)$$

The SNR is calculated at the middle of the channel for each experiment. The evolution of the SNR with the gradient is shown on figure 4.13b. Note that the difference in SNR for cells experiencing the same gradient but different midpoint concentrations is more marked than the difference that we had observed in the receptor occupancy (compare figures 4.13b and 4.12b). The chemotactic index of the cells as a function of the SNR is plotted on figure 4.13c. The correlation between chemotactic index and SNR is clearer than it was between chemotactic index and difference in receptor occupancy. However, we have taken into account only the noise at the receptor level. After the binding of cAMP to the cAR1 receptor, a sequence of numerous intracellular reactions are triggered, that lead to chemotactic motion (see chapter 1 for an overview of the biological details). Along this biological pathway, both the signal and the noise are propagated. Imagine that we have the following reactions:



and define the following time constants:

$$\tau_R = (k_1 C + k_{-1})^{-1} \quad \tau_X = (k_2 R^* + k_{-2})^{-1} \quad (4.31)$$

as well as the gains of the two reactions:

$$g_R = K_1 (K_1 + C)^{-1} \quad g_X = K_2 (K_2 + \overline{R^*})^{-1} \quad \text{with} \quad K_i = \frac{k_i}{k_{-i}} \quad (4.32)$$

Then, Shibata and Fujimoto [104] showed that the fluctuations in the second reaction can be written as:

$$\sigma_X^2 = \left[ g_X \overline{X^*} + g_X^2 \frac{\tau_R}{\tau_R + \tau_X} \frac{\sigma_R^2}{\overline{R^*}} (\overline{X^*})^2 \right]. \quad (4.33)$$

The first term of 4.33 corresponds to the intrinsic noise of the second reaction. The second term corresponds to the propagation of the noise of the first reaction to the second reaction, and is termed extrinsic noise. If the time constant of the input noise  $\tau_R$  is much smaller than  $\tau_X$ , the noise is averaged out.

Equation 4.33 can be generalized to a biological pathway with much more than 2 reactions. However, Ueda and Shibata considered in [119] only the first biochemical event of the intracellular pathway after the binding of cAMP to cAR1, which is the dissociation of the G protein. Still, they were able to fit quite well the data of Fisher [30], and related the experimentally observed chemotactic efficiency from [30] to their theoretically estimated SNR after dissociation of the G protein. The basis of the formula is equation 4.33, which has to be slightly adapted for a cell experiencing a gradient, and becomes<sup>3</sup>:

$$\text{SNR} = \left[ \frac{\Delta \overline{X^*}^2}{\sigma_{\Delta X}^2} \right]^{-1/2} = \left[ \frac{1}{g_X \overline{X^*}} \left( \frac{\overline{R^*}}{\Delta \overline{R^*}} \right)^2 + \frac{\tau_R}{\tau_X + \tau_R} \left( \frac{\sigma_{\Delta R}^2}{\Delta \overline{R^*}} \right)^2 \right]^{-1/2} \quad (4.34)$$

<sup>3</sup>As earlier, this equation is valid for shallow gradients, when  $\Delta C \ll C$ . For the general case, the reader is referred to Appendix A.

#### 4.6. Chemotactic behavior in different gradients

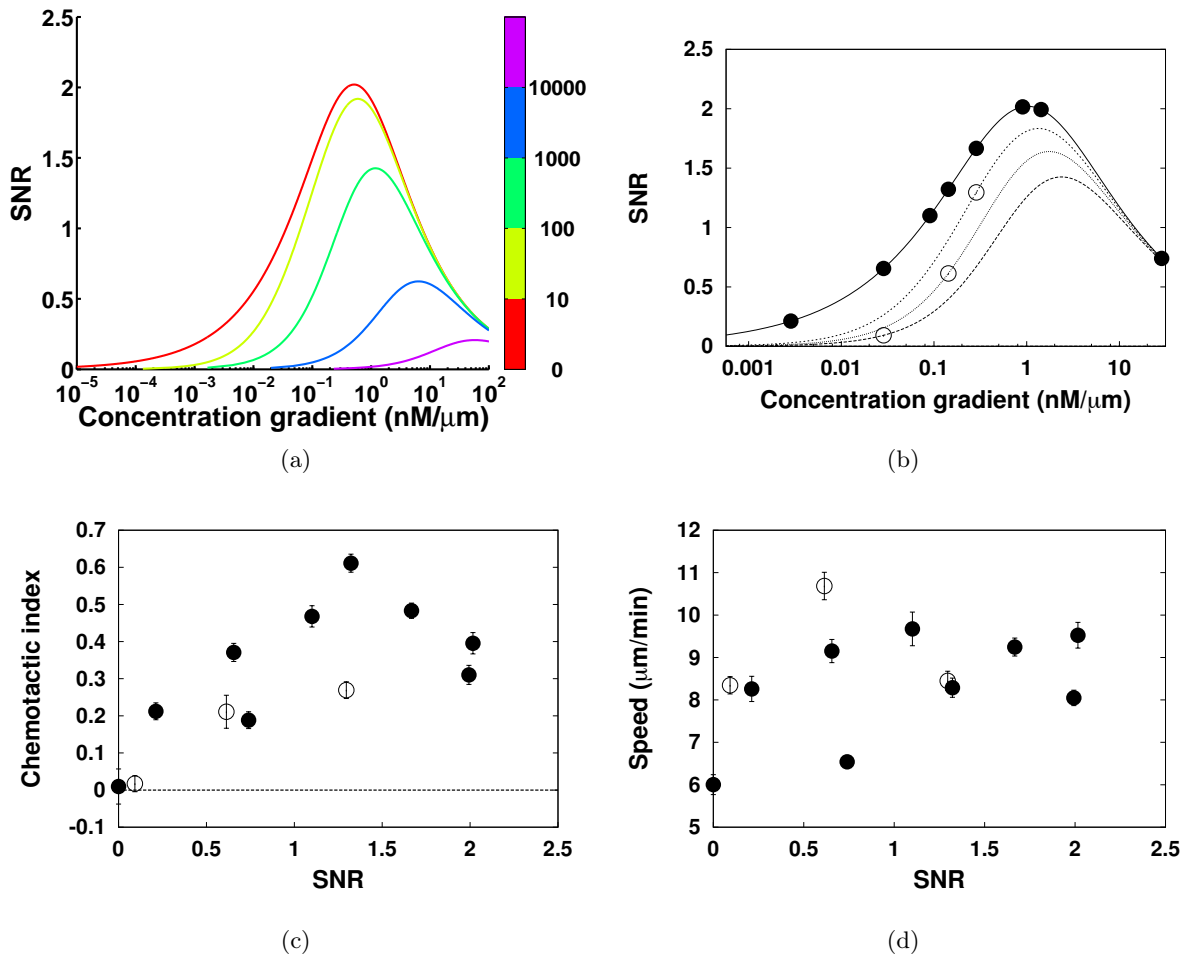


Figure 4.13: (a) SNR at the receptor level calculated using equation 4.29, as a function of the gradient. The concentration profiles run from  $c_{\min}$  to  $c_{\max}$ . The value of  $c_{\min}$  is indicated by the colorbar. The gradient spans over  $350 \mu\text{m}$ . (b) SNR at the receptor level, with the dots indicating where the experimental data was taken. Lines: theoretical curves for the different values of  $c_{\min}$ . (c) Chemotactic index as a function of the SNR. (d) Average speed as a function of the SNR. Empty/filled circles as in figure 4.11.

where  $X$  is the second-messenger, here the G-protein, which gets activated ( $X^*$ ) when a ligand binds to the receptor  $R$ . We have plotted on figure 4.14a the evolution of the SNR as a function of the gradient of cAMP<sup>4</sup>. As for the difference in receptor occupancy and the SNR at the receptor level, the SNR after dissociation of the G protein shows a maximum whose value and position depend on both the gradient and the value of  $c_{\min}$ . At a given value of  $c_{\min}$ , the SNR is small both at low and high gradients. The average chemotactic index is shown as a function of the SNR on figure 4.14b. There is a clear correlation between the SNR and the chemotactic index. This correlation reflects the correlation between the average chemotactic velocity  $v_y$  and the SNR (figure 4.14c). The average speed is shown on figure 4.14d as a function of the SNR. Looking only at the experiments where the concentration profile starts at 0 (filled circles), we see that the speed goes up with the SNR, and reaches a plateau. Because the experiments with an offset concentration (empty circles) do not fit on this graph however, the SNR is likely not the quantity which explains cellular speed.

### Collapsing the data from different sources

In the previous paragraph, we computed the *average* chemotactic index for cells in one experiment. We now test the formula for the SNR further, and estimate the SNR at each position of the cell tracks, for all experiments. The cells' velocity  $v_y$  and speed  $v$  was calculated at each time, enabling us to define the chemotactic index  $CI = v_y/v$ . The data was then binned according to the SNR using a bin size of 0.05. In this case, different experiments contribute to the same bin for the SNR. The results of the binning are showed on figure 4.15. We compared our data with the existing data from the literature [34, 30] (see figure 4.16). The comparison with Fuller et al., where the authors systematically changed the midpoint concentration and the gradient that the cells were experiencing using exponential gradients, is shown on figure 4.16b. Note that in Fuller et al., the data was taken with a time step of 5 seconds, smaller than our time step of 40 seconds, which has an influence on the value of the CI. Note also that we do not know which cells were excluded from the data processing in [34]. Still, the agreement between the datasets is very reasonable. The comparison with the data of Fisher et al. is shown on figure 4.16d. We used the same time step as in [30], as well as the same definition of the CI as in [30]. The data of Fisher's shows a slight discrepancy with ours, which could be explained by three factors. First, the SNR changes across the gradient chamber, and we do not know the distribution of cells in the chamber. Because of this, the average SNR seen by the cell population could be different than the SNR in the middle of the chamber. Second, in the absence of a flow, diffusion increases the gradient around the cells (see section 4.4). The midpoint concentration stays the same however. This would shift the data of Fisher et al. towards higher values of the SNR. Last, the cell lines used in Fisher et al. and in our experiments are different (X22 in [30], AX2 in our experiments).

Also note that the SNR that we use is a combination of the noise at the receptor level and at the intracellular level. By construction of the SNR, the noise at the receptor level dominates at low midpoint concentrations, while the intracellular noise dominates at high midpoint concentrations [119]. This interplay between the two noise contributions and their relative importance was the main conclusion of Fuller et al. [34], who used an information-theoretic framework to characterize chemotactic cell motion.

<sup>4</sup>As above, the SNR has been calculated at the middle of the channel.

#### 4.6. Chemotactic behavior in different gradients

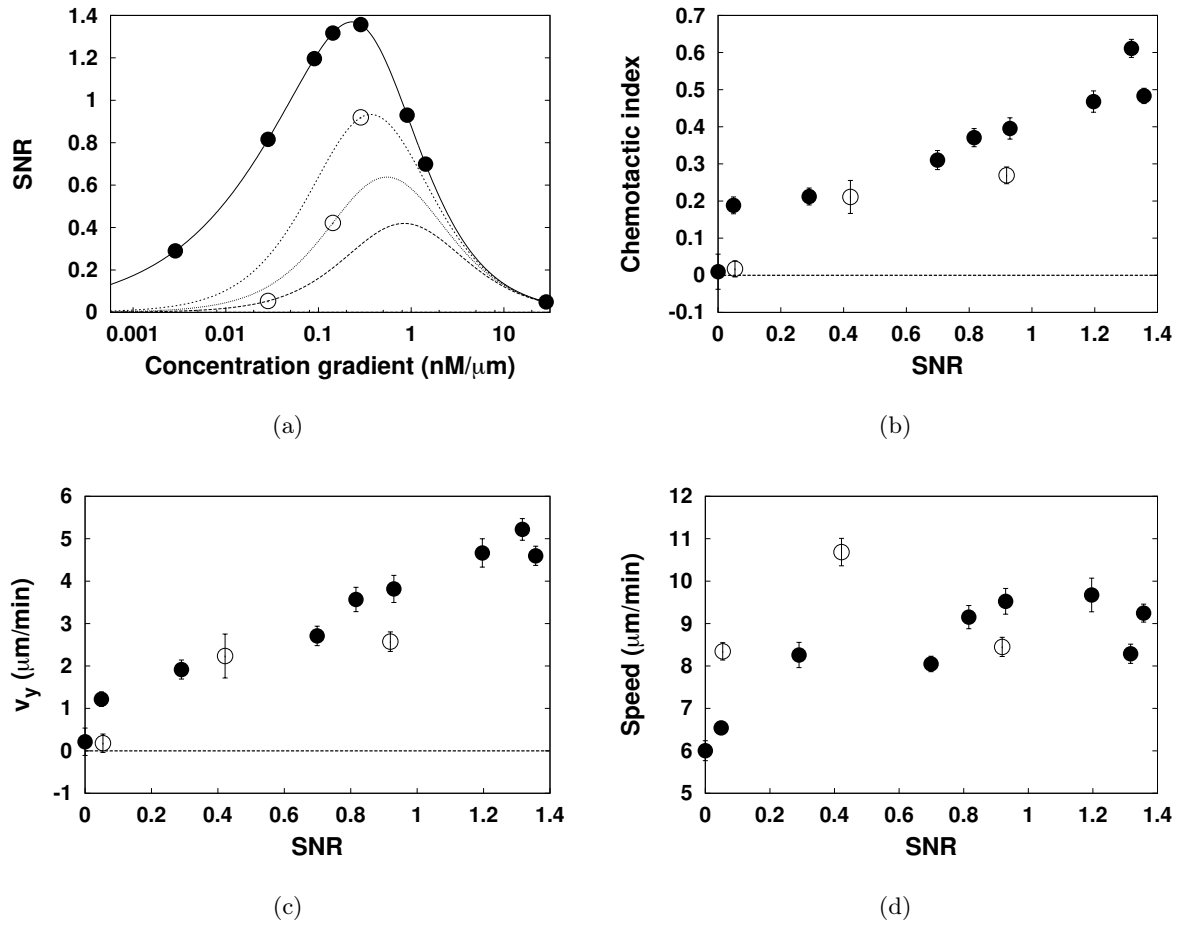


Figure 4.14: (a) SNR after binding of cAMP to cAR1 and dissociation of the G protein, as a function of the gradient. Lines: theoretical curves for the different values of  $c_{\min}$ , with values of the parameters taken from [119]. The dots indicate where the experimental data was taken. (b) Chemotactic index, (c) average chemotactic velocity  $v_y$  and (d) average cell speed as a function of the SNR. Empty/filled circles as in figure 4.11.

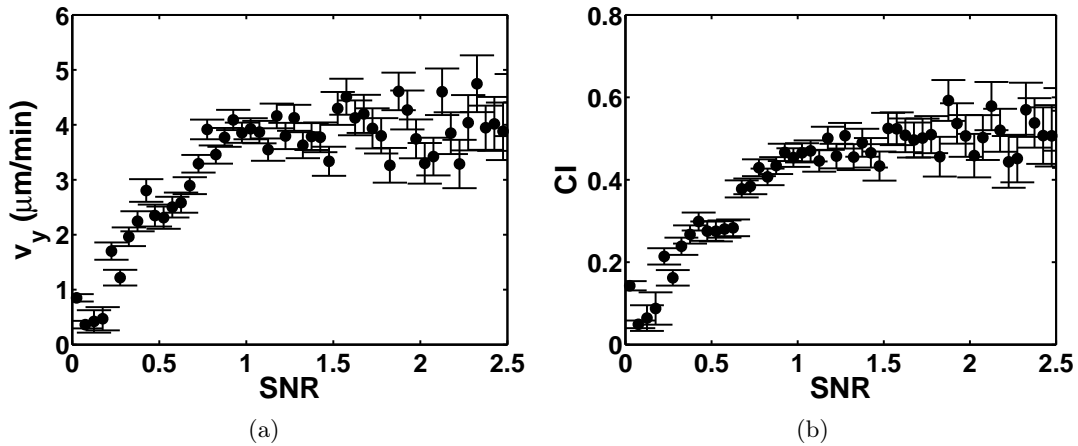


Figure 4.15: The SNR was calculated at each position of the cell track for all experiments, as were the chemotactic velocity  $v_y$  and the chemotactic index. Both quantities  $v_y$  and CI were then binned according to the SNR, with a bin size of 0.05. (a) Average chemotactic velocity  $v_y$  as a function of the SNR. (b) Average CI as a function of the SNR.

#### 4.6.5 Fraction of long tracks

As mentioned earlier, we took into account only the tracks that were longer than 30 microns. The fraction of these tracks also shows a correlation with the SNR, as shown on figure 4.17. Taken together with the previous result, we see that the SNR is both responsible for the number of cells that exhibit a chemotactic behavior (figure 4.17b) and for the average chemotactic index of these cells (figure 4.14b).

#### 4.6.6 Angle histogram, speed as a function of the angle

A cell's trajectory is not a perfect straight line in the gradient direction. Is the cell moving up the gradient because it makes more steps in the correct direction than in the opposite one (as shown on the angle histogram, figure 4.18a), making each step with the same speed, or are the steps in the gradient direction faster than the other ones? We can plot the cell's speed as a function of its angle of propagation. The result is shown on figure 4.18b, where we have averaged the cell speed over bins of range 20 degrees. What we can see on this figure is that the speed in the gradient direction ( $\theta$  between 0 and 180 degrees) is bigger than the speed in the direction opposite the gradient ( $\theta$  between 180 and 360 degrees). This is in agreement with what has been reported by Fisher et al. [30] and by Gruver et al. [42].

### 4.7 Chemotaxis of SCAR/PIR null mutants

#### 4.7.1 Chemotactic index, speed

The same experiments were repeated using SCAR/PIR-null mutants. By activating Arp2/3, SCAR is a key regulator of the actin cytoskeleton, and SCAR/PIR-null mutants show a periodic polymerization and depolymerization of actin filaments [50]. Because amoeboid motion

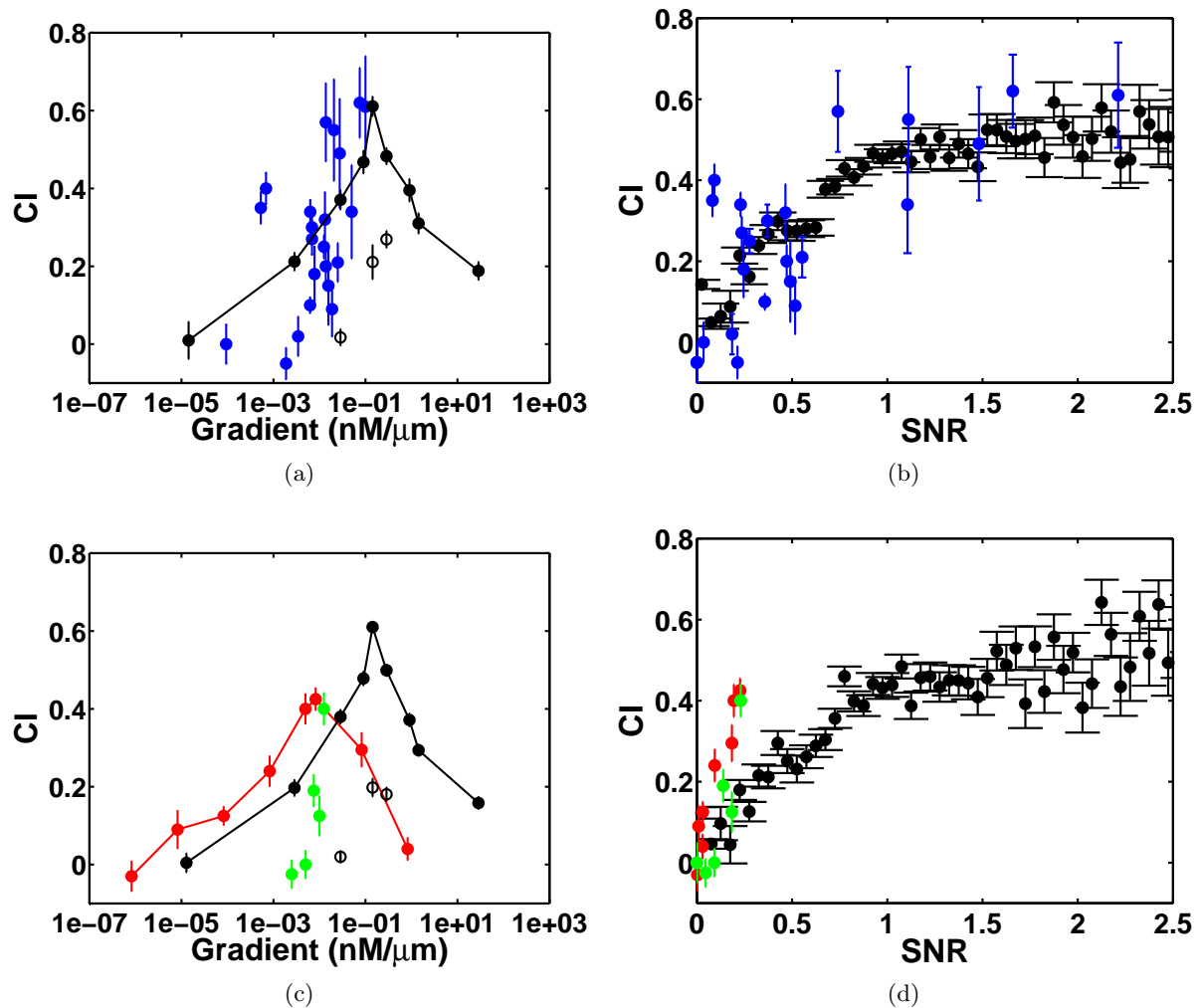


Figure 4.16: (a) Comparison of our data (filled/open black circles as in figure 4.11) with the data from Fuller et al. [34] (blue circles), when the chemotactic index is plotted as a function of the gradient of cAMP. For the data of Fuller et al., the gradient was calculated at the middle of the exponential gradient mixer. (b) Same data, plotted as a function of the SNR. (c) Comparison of our data (filled/open black circles as in figure 4.11) with the data from Fisher et al. [30] (red circles: data from figure 5 in [30], green circles: data from figure 6 in [30]), when the chemotactic index is plotted as a function of the gradient of cAMP. (d) Same data, plotted as a function of the SNR. We used the same time step and the same definition of the chemotactic index as Fisher et al. in these two latter figures.

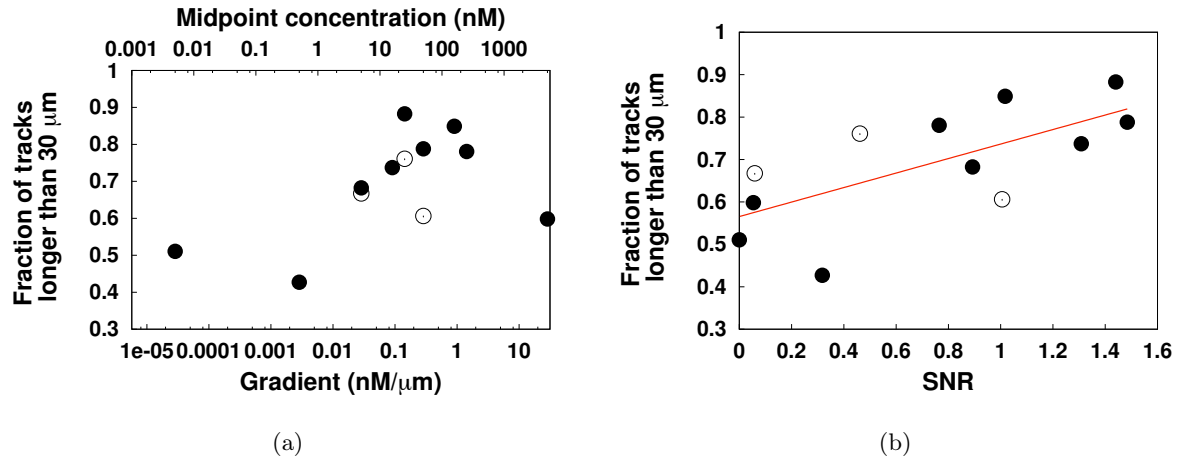


Figure 4.17: Fraction of tracks longer than  $30 \mu\text{m}$  as a function of (a) the gradient and (b) the SNR. Empty/filled circles as in figure 4.11. The red line shows a linear fit of the data.

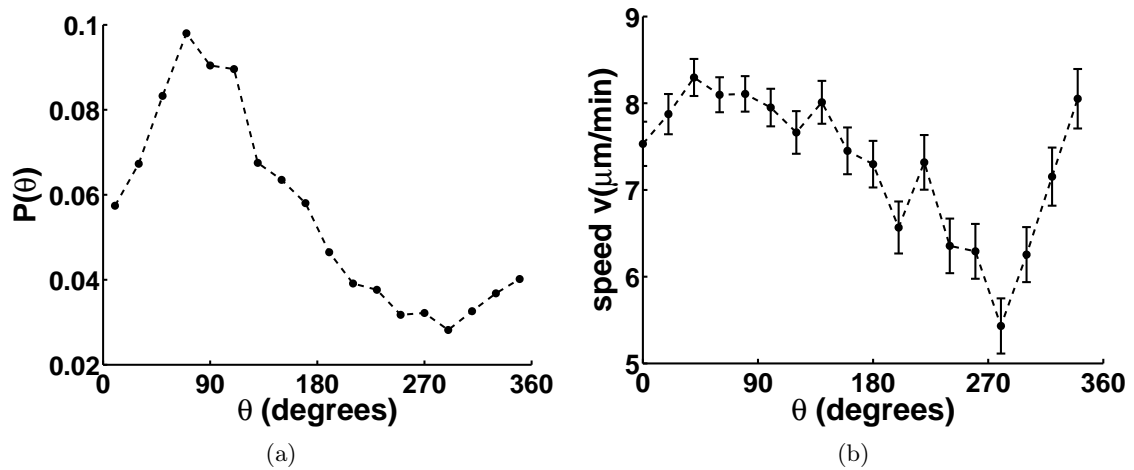


Figure 4.18: (a) The angle histogram is peaked in the direction of the gradient. (b) Average speed of a cell as a function of its angle of propagation. When the cell is going in the gradient direction, its speed is higher than when it goes in the opposite direction. Error bars show the standard error.



#### 4.7. Chemotaxis of SCAR/PIR null mutants

is due to actin polymerization, it was expected that these mutants chemotact poorly to cAMP. The chemotaxis of vegetative cells to folic acid was already reported to be impaired in [11].

Our experimental results are summarized on figure 4.19. Note that there is still a correlation between the chemotactic velocity and the SNR, indicating that the SNR at the G-protein level is still a good quantity to describe chemotactic cell motion, even if the chemotactic pathway has been disrupted. This tends to confirm the claim of Ueda and Shibata that the most important intracellular noise term comes from the G-protein dissociation [119]. We can compare the results from the SCAR/PIR mutants to that of the wild-type (WT) cells (see figure 4.20). Surprisingly, at a given SNR, the chemotactic index of the SCAR/PIR mutants is equal or higher than the chemotactic index of the wild-type cells. This is due to a similar chemotactic velocity  $v_y$  between both cell lines (figure 4.20b), but a smaller speed of the SCAR-PIR mutants compared to the WT cells (figure 4.20c).

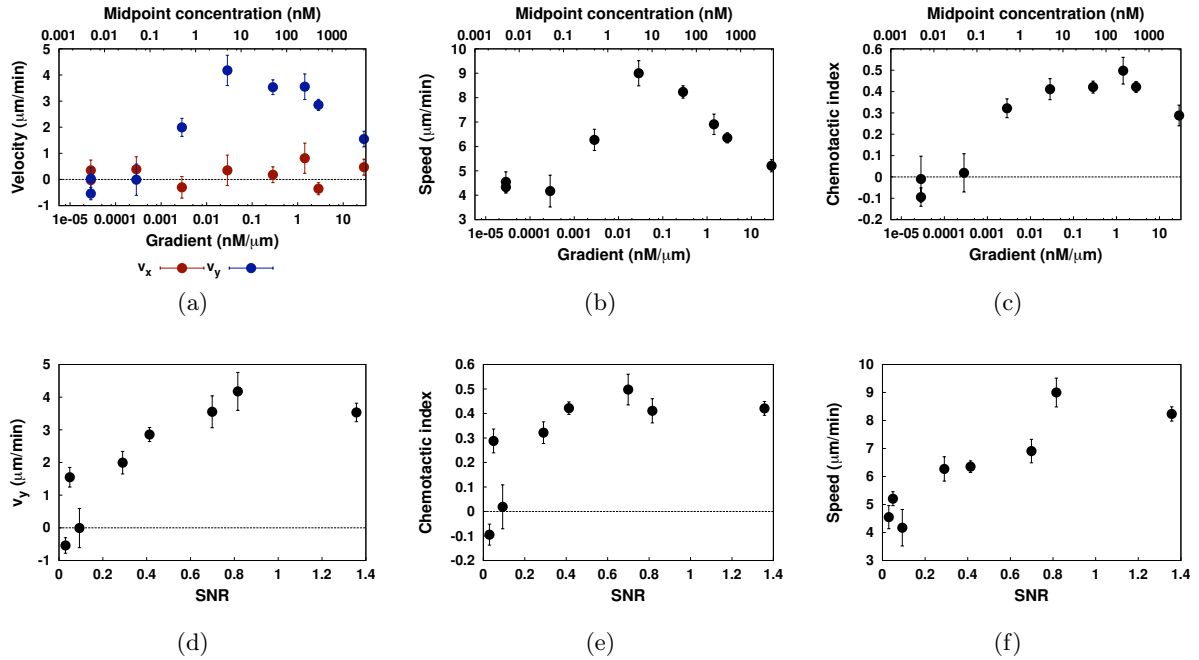


Figure 4.19: Evolution of the velocities (a)  $v_x$ ,  $v_y$ , (b) the speed  $v$ , and (c) the chemotactic index with the gradient for all cells. The first point, drawn at a midpoint of 0.005 nM, corresponds to the case where no gradient is applied, and is drawn artificially at a non-zero midpoint concentration because of the logarithmic scale. In all experiments, the cAMP concentration in the channel goes from 0 to a value  $c_{\text{max}}$ . (d) Evolution of the chemotactic index, (e) of the chemotactic index, and 4.19f of the average cell speed with the SNR.

#### 4.7.2 Fraction of long tracks

In [11], Blagg et al. reported that the SCAR/PIR mutants were twice slower than the WT cells, and less chemotactic. The authors assessed the chemotaxis of vegetative cells to folic acid, but we could have naively expected the same result to hold for the chemotaxis of starved cells to cAMP. From our experiments, we however found the speed of the mutants to be

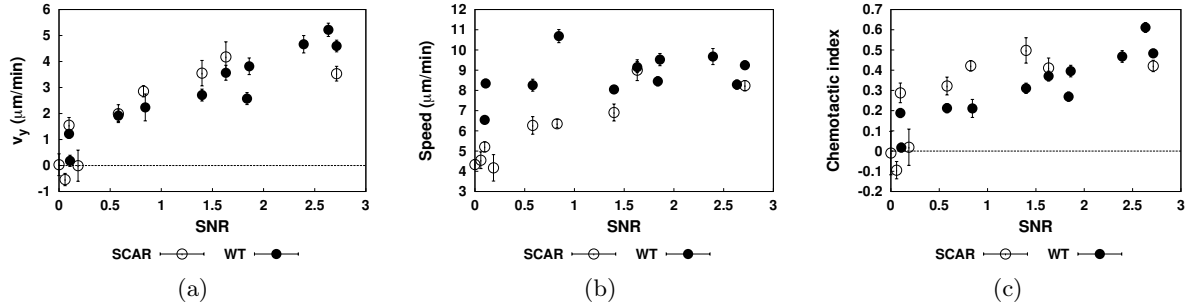


Figure 4.20: Comparison of the WT cells (filled circles) with the SCAR/PIR mutants (empty circles). (a) Chemotactic index, (b) chemotactic velocity  $v_y$  and (c) speed  $v$ , as a function of the SNR. At similar values of the SNR, the speed of the SCAR/PIR mutants is lower than that of the WT cells, but the chemotactic velocity  $v_y$  is comparable for both cell lines, leading to a higher chemotactic index for the SCAR/PIR mutants.

slower by a factor of roughly 80% compared to the WT cells, and their chemotactic index to be higher than the one of the WT cells. This qualitative difference between Blagg’s results and ours could be explained by the fact that Blagg et al. analyzed the cells at the population level and, as far as can be understood from their article, did not make a distinction between immobile and mobile cells. We did this distinction by excluding all tracks smaller than  $30 \mu\text{m}$ , as explained in section 4.5. We plotted the fraction of tracks longer than  $30 \mu\text{m}$  as a function of the SNR on figure 4.21a and compared it to the wild-type cells (figure 4.21b). At a given SNR, the fraction of tracks moving over more than 30 microns is smaller for the SCAR/PIR mutants than for the WT cells. We conclude that the mutants are indeed impaired in their motility: in a buffer solution, 20% of them only move a distance of more than 30 microns, compared to 50% of the wild-type cells. This fraction increases with the SNR, but stays lower than the fraction of WT. In other words, the mutants that chemotact have a similar behavior to the WT cells 4.20, but a smaller fraction of the population acts chemotactically. This could explain the results of Blagg et al. at the population level.

## 4.8 Summary

To summarize this section, we have seen that both the absolute value of the gradient and the midpoint concentration were important for the efficiency of gradient sensing. Because of the very low difference in the receptor occupancy between front and back of the cell (maximally 350 more occupied receptors at the front than at the back, out of a total of 70,000 receptors), stochastic effects become important. A quantity taking into account the slope of the concentration profile, its midpoint concentration and the stochastic fluctuations is the signal to noise ratio (SNR). Considering the noise at the receptor level and its propagation at the level of the G protein, it is possible to observe a rescale our datasets with data taken earlier from the literature. The agreement with data from [34] taken in microfluidic devices is in particular very good, even though the gradients used in [34] are exponential and ours are linear. The number of cells that responds chemotactically is also increasing with the SNR. When a key regulator of the actin cytoskeleton, SCAR, is disrupted, the average cell speed is reduced but

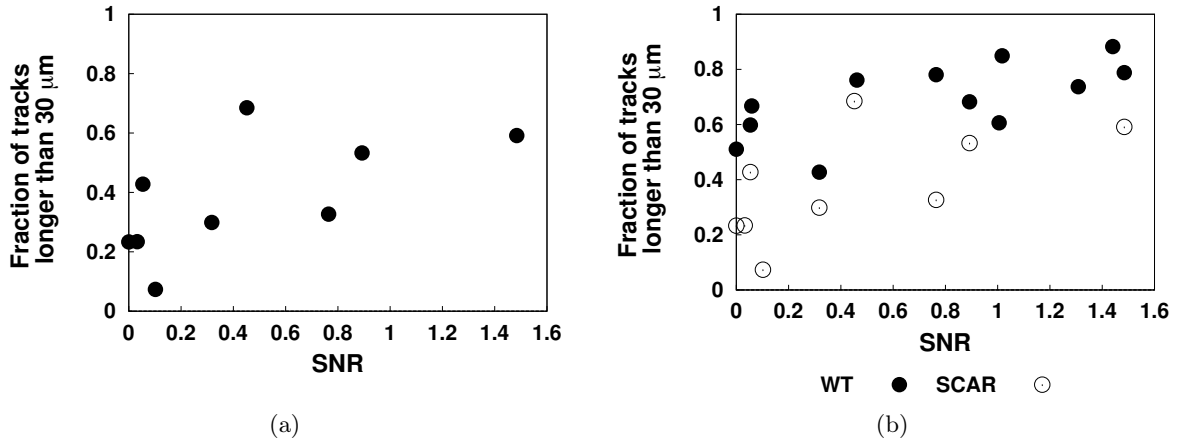


Figure 4.21: (a) Fraction of tracks longer for the SCAR/PIR mutants, as a function of the SNR, and (b) comparison with the WT cells. Under similar SNR conditions, more of the SCAR/PIR mutants are immobile.

the chemotactic velocity stays comparable to the chemotactic velocity of the WT cells. Both for the WT cell and the SCAR mutants (data not shown) the speed of the cells depend on their direction of propagation: steps made in the gradient direction are faster than steps opposite the gradient direction.

Up to now, we have been interested only in average quantities. In the next section, we will describe histograms, and reproduce them using a generalized Langevin equation.

## 4.9 The Langevin equation

In the previous part of this chapter, we assessed the chemotactic performance of a population of cells using average quantities over time, such as the average velocity of cells in the gradient direction, or the chemotactic index. This approach is standard in the literature. However, these average quantities can only convey a limited information about cell motion. By definition, they do not tell anything about the fluctuations inherent in cell motility. Therefore, two different cell lines may exhibit a very different motion under the same external conditions, but time-averaged quantities such as the average speed, average velocity in the gradient direction or chemotactic index might still be the same for both cell types. To fully characterize chemotactic motion, one has to go beyond a description in terms of average quantities, and take into account the temporal fluctuations of cell velocities. In the rest of this chapter, we achieve this aim by modeling the motion of chemotactic cells using a Langevin equation. The shape of the deterministic and stochastic components of the Langevin equation is found directly from the experimental motility data, using a method introduced in [105]. We analyze the motion both wild-type and SCAR/PIR mutants using this analysis. For a given cell type, the evolution of both stochastic and deterministic parts of the Langevin equation as a function of the gradient is discussed. Then, it is shown that, in a gradient, the deterministic components characterizing the motion of both cell lines are similar. However, the stochastic components differ between the wild-type and mutant cells.

### 4.9.1 The early times of a theory of Brownian motion

When he introduced his theory of Brownian motion in 1905 [27], Einstein described the position of a Brownian particle at discrete time intervals making two important assumptions. First, all Brownian particles should move independently from one another (no correlation in space). Second, the time interval considered should be big enough so that the motion of a single Brownian particle at one time step is not correlated with its motion at the previous time step (no correlation in time). Einstein's approach was a probabilistic one: starting from the number of particles that underwent a given displacement in one time step, he was able to derive the diffusion equation for the density of Brownian particles. The average square displacement of a particle after a time  $\tau$  is then given by the usual formula:

$$\langle x^2(\tau) \rangle = 2D\tau \quad (4.35)$$

where  $D$  is the diffusion coefficient of the particle. Three years later, the same result was recovered by Paul Langevin by the means of what he claims to be an "infinitely more simple demonstration" [66]. Langevin describes the motion of a Brownian particle using Newton's equation of motion, where the particle is subject to a viscous drag  $\eta$  and to a random force  $F$ . This random force maintains the thermal agitation of the particle, whose velocity would otherwise go to zero:

$$m \frac{d^2x}{dt^2} = -\eta \frac{dx}{dt} + F \quad (4.36)$$

Integrating the above equation and using equipartition of energy, Langevin then arrived to the result:

$$\langle x^2(\tau) \rangle = \frac{2k_B T}{\eta} \left[ \tau + \frac{m}{\eta} (e^{-\frac{\eta}{m}\tau} - 1) \right] = \frac{2k_B T}{\eta} \left[ \tau + \tau_c (e^{-\tau/\tau_c} - 1) \right] \quad (4.37)$$

where we have introduced  $\tau_c = m/\eta$ . Einstein had shown in [27] that the diffusion coefficient of a species was related to temperature and to the drag coefficient by:

$$D = \frac{k_B T}{\eta} \quad (4.38)$$

At times longer than  $\tau_c = m/\eta$ , we therefore recover Einstein's result. The time  $\tau_c$  represents the characteristic time between two collisions, after which the particle has lost its memory about its previous state. It is a correlation time. At times shorter than  $\tau_c$ , the motion of the particle is not randomized through multiple shocks with other particles and should therefore be ballistic, which is also what we recover from equation 4.37.

In 1913, Karl Przibram observed the motion of *Paramecia* under a microscope [87]. By computing the average squared distance covered by the *Paramecia* at different times, he was able to show that, within the precision of his experiment, the motion of the organism was diffusive.

### 4.9.2 Introducing correlations in Brownian motion

In 1920, Reinhard Fürth [37] complemented Einstein's theory of Brownian motion by adding a correlation in the motion of a Brownian particle. He considered a particle moving on a line. If the particle is moving to the right at time  $t$ , it has a probability  $p$  to go the right at time  $t + \tau$  and a probability  $(1 - p)$  to go the left. In the case of Brownian motion without

correlation,  $p = 0.5$ . In the case where the motion is strongly correlated ( $p \sim 1$ ), Fürth recovers equation 4.37 for the expression of the average quadratic displacement of the particle, only the characteristic time is now given by:

$$\tau_c = \frac{1}{2(1-p)} \quad (4.39)$$

Written as a function of  $\tau_c$ , the dimension  $n$  of the space in which the walk takes place, and the diffusion coefficient  $D$  of the Brownian walker, Fürth's formula for the average squared displacement of a correlated Brownian walker reads:

$$\langle \mathbf{x}^2(\tau) \rangle = 2nD \left[ \tau + \tau_c(e^{-\frac{\tau}{\tau_c}} - 1) \right] \quad (4.40)$$

In the same article [37], Fürth applies his formula to describe the motion of *Paramecium*. The presence of a persistence time makes Fürth's description more precise than Przibram's [87]. Since then, analyzing cell motion by the means of a Langevin equation became the topic of numerous articles (see e.g [38], [98], [97], [103], [100]). One should note that describing cell motion using a Langevin equation has no physical or biological foundation. A Brownian particle has a mass, is subject to friction, and is randomly moving because of the constant shocks that it receives from neighboring molecules. The Langevin equation of a Brownian particle is describing a passive process. On the contrary, cell movement is an active process that has most likely little to do with the cell's mass or with random external forces. In this case, the Langevin equation can be used as an efficient and practical tool that separates the deterministic component of motion from its stochastic contributions.

### 4.9.3 Recent applications of a Langevin equation to cell motion

#### Generic models

In the beginning of the 1990ies, Schienbein and Gruler [98] described the motion of granulocytes using two independent Langevin equations. One of the equations was accounting for the speed of the cells  $v$  while the other one described the evolution of their angle of propagation  $\theta$ . As the authors themselves put it, their description amounts to comparing "the migrating cells [...] with a driven car where the amount of speed, adjusted by the gas pedal, and the moving direction, adjusted by the steering wheel, can be independently altered". The authors also took into account that granulocytes, when subject to an electric field, move towards the positive electrode:

$$\frac{\partial v}{\partial t} = \gamma(v - v_t) + \Gamma_v(t) \quad (4.41)$$

$$\frac{\partial \theta}{\partial t} = -k_P E \sin \theta + \Gamma_\theta(t) \quad (4.42)$$

where  $v_t$  represents the target speed of the cell,  $E$  is the electric field and  $k_P$  quantifies the effect of the electric field on the cell motion. The noise terms  $\Gamma_v(t)$  and  $\Gamma_\theta(t)$  satisfy:

$$\langle \Gamma_i(t) \rangle = 0 \quad \langle \Gamma_i(t) \Gamma_j(t') \rangle = \delta_{ij} q_i \delta(t - t') \quad (4.43)$$

The fit of these equations on their experimental data is good, but not perfect, as can be seen on figure 4.22. In particular, the tails of the experimental speed distribution are larger than the theoretical gaussian fit.

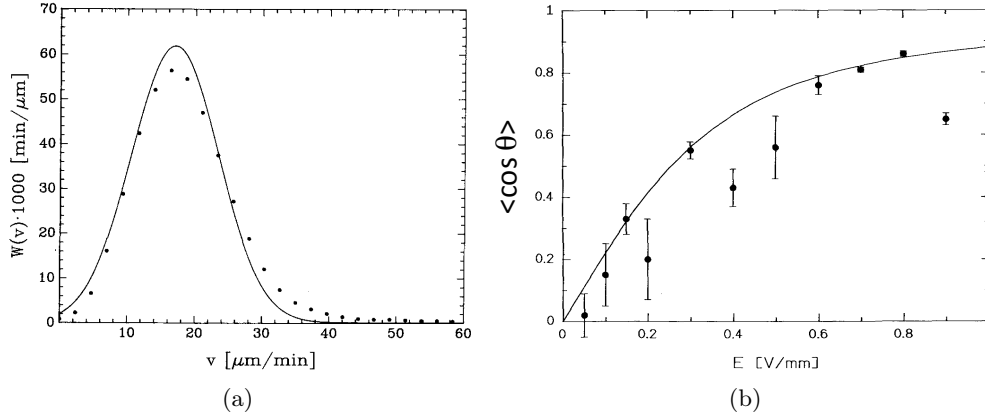


Figure 4.22: (a) Speed distribution  $W(v)$  of granulocytes. The dots are the experimental data and the line is a fit of the model to the data. There is no electrical field applied. (b) Average of  $\cos \theta$  (order parameter) for different values of the electrical field. The dots are the experimental data and the line is the theoretical prediction. Figures taken from [98].

In 1997, Shenderov and Sheetz [103] recorded the random motion of *D. discoideum* for up to 2 hours. They calculated the turning rate of the cells (in rad/s) and saw that there was an anticorrelation between the turning rate and the speed of cells: in a population, the faster cells had a lower turning rate (i.e. had a more directed motion) than slower cells (see 4.23a). This observation contradicts the original assumption of Schienbein and Gruler, according to whom speed and turning are two independent mechanisms. Moreover, Shenderov and Sheetz observed oscillations in the cells' velocity autocorrelation (see 4.23b). Both of these observations were accounted for by introducing a memory term in the Langevin equation describing cell motion:

$$\frac{dv_i(t)}{dt} = -\gamma v_i(t) - \beta \int_{-\infty}^t v_i(\tau) e^{-\alpha(t-\tau)} d\tau + \Gamma_i(t) \quad (4.44)$$

where  $i = \{x, y\}$ ,  $\Gamma_i$  has zero mean and is not correlated in time ( $\langle \Gamma_i \rangle = 0$ ,  $\langle \Gamma_i(t) \Gamma_j(t') \rangle = q \delta_{ij} \delta(t-t')$ ). It can then be shown that the cell motion becomes oscillatory under the condition:

$$\left( \frac{\alpha - \gamma}{2} \right)^2 < \frac{\beta}{\sqrt{2\pi}} \quad (4.45)$$

A toy model describing chemical reactions leading to a memory term was proposed in [103], but the actual mechanism for a memory is still unclear to these days.

The most recent phenomenological Langevin-type model of eukaryotic chemotactic motion was presented by Hu et al. in [45]. There, the authors described the time evolution of the angle of propagation of a cell in a gradient of chemoattractant. The study focused on the impact of stochastic receptor dynamics on the already biased random motion of a cell in a gradient of chemoattractant. One key assumption of the model was however that cell speed is independent of the angle of propagation, which is not what we experimentally found (see section 4.6.6).

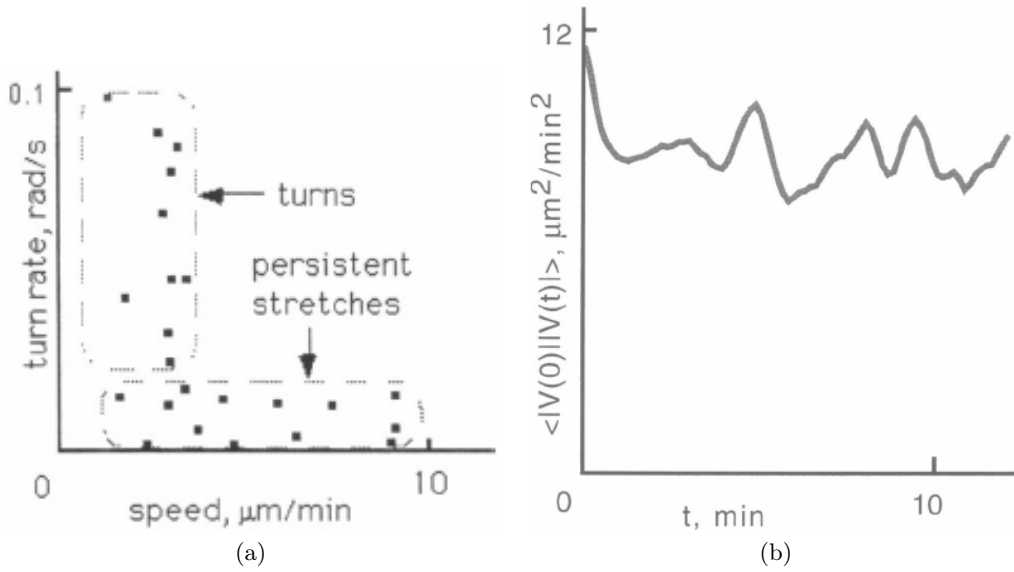


Figure 4.23: (a) Anticorrelation between the turning rate and the speed of cells. (b) Oscillations in the cells' velocity autocorrelation. Figures taken from [103].

### A more quantitative approach

The models used in the previous section can be analyzed analytically and are quite simple. They aim at describing the data qualitatively. With computing power and digital cameras becoming more and more accessible over the years, it became possible to track automatically cells for several hours, and to fit a generalized Langevin equation to their motion. This was first done by Selmeczi et al. [100] in 2005, monitoring the motion of HaCaT cells. The method of Selmeczi et al. to get to the parameters of the Langevin equation will be given in more detail in section 4.10 and is based on a method pioneered by Siegert et al. [105]. The main result of the article is that no model is assumed, rather the form of the Langevin equation comes directly from the data. This is what makes the article interesting: from the data, the authors are able to deduce that the damping is linear with the velocity, that the Langevin equation should have a memory term of a given shape, and that the noise term should be proportional to the velocity. After Selmeczi's paper, three other groups worked on the random locomotion of *D. discoideum*. At Princeton, Li et al. [69] used a Langevin equation to describe the motion of starved *D. discoideum*. The approach was different than that of Selmeczi's because a very general Langevin equation was assumed and its parameters were then fitted to the data. Moreover, whereas Selmeczi et al. found a Langevin equation for the cell's speed, Li et al. did not take into account cellular speed in their analysis and described cell motion by the cell's angle of propagation. A couple of months later, Takagi et al. [114] described the random motion of vegetative and starved *D. discoideum*. They assumed the following Langevin equation to describe the evolution of the cell's speed:

$$\frac{dv}{dt} = \alpha_0 + \alpha_1 v + \alpha_2 v^2 + \beta^2 \int_{-\infty}^t v(t-t') e^{-\gamma t'} dt' + (\sigma_0 + \sigma_1 v) \Gamma(t) \quad (4.46)$$

and fitted the parameters to their experiment. To do so, they had to run simulations of equation 4.46 for different values of all the parameters and find the set of parameters that reproduced the data the most accurately. Even more recently, Boedeker et al. [12] used the same method as Selmeczi et al. to get – from the data – the parameters of a Langevin equation describing the motion of developed and non-developed cells, in different constant backgrounds of cAMP. They found a much simpler equation than 4.46, which contained no memory term and in which the damping term was linear. The noise term was multiplicative. None of the above works considered the motion of starved *D. discoideum* in a gradient of cAMP. In the next part of the chapter, we will use the same method as Boedeker et al. to write a Langevin equation capturing the characteristics of chemotactic cell motion.

## 4.10 Langevin analysis of the cell tracks

### 4.10.1 Principle

Consider a cell moving in the microfluidic channel. We define a fixed reference frame  $(O, \mathbf{e}_x, \mathbf{e}_y)$  with the  $x$ -axis pointing in the flow direction and the  $y$ -axis pointing in the gradient direction. Following Selmeczi [100], we will analyze the cell motion in a reference frame moving with the cell. We therefore define  $\mathbf{e}_\parallel$  to be a unit vector in the direction of the instantaneous velocity  $\mathbf{v}(t)$  of the cell, while  $\mathbf{e}_\perp$  is a unit vector perpendicular to  $\mathbf{e}_\parallel$ . The angle between the cell's instantaneous velocity  $\mathbf{v}(t)$  and the horizontal is called  $\theta$  (see figure 4.24).

The cells' velocities were computed using a time step  $\Delta t = 40$  seconds, as explained in section 4.5. From the velocity vectors  $\vec{v}_j$  calculated at times  $t_j = j\Delta t$  ( $j = 1, 2, 3, \dots$ ), we computed the acceleration vectors  $\vec{a}_j = (\vec{v}_{j+1} - \vec{v}_j)/\Delta t$ . To separate the deterministic part from the stochastic part of motion, we wanted to use a generalized Langevin equation to describe the data:

$$\dot{\mathbf{v}}(t) = \mathbf{F}(\mathbf{v}(t)) + \underline{\mathbf{R}}(\mathbf{v}(t))\mathbf{\Gamma}(t). \quad (4.47)$$

In this equation,  $\mathbf{F}(\mathbf{v})$  is a deterministic force<sup>5</sup>,  $\underline{\mathbf{R}}(\mathbf{v})$  is the noise amplitude, and  $\mathbf{\Gamma}(t)$  is the noise term, that satisfies

$$\langle \Gamma_i(t) \rangle = 0 \quad \text{and} \quad \langle \Gamma_i(t)\Gamma_j(t') \rangle = \delta_{ij}\delta(t - t') \quad (4.48)$$

where  $\Gamma_i$  indicates the  $i$ -th component of  $\mathbf{\Gamma}$ . The aim of our work was to determine the functions  $\mathbf{F}(\mathbf{v})$  and  $\underline{\mathbf{R}}(\mathbf{v})$  from the experimental data. This can be achieved using conditional averaging, as we now explain. Call  $v$  the amplitude of the velocity  $\mathbf{v}$  and  $\theta(t)$  its angle with the horizontal. Then, in order to find  $F_\parallel(\mathbf{v})$ , one should ideally calculate (see e.g [94]):

$$F_\parallel(\mathbf{v}_0) = \lim_{dt \rightarrow 0} \frac{1}{dt} \langle [\mathbf{v}(t + dt) - \mathbf{v}(t)] \cdot \mathbf{e}_\parallel(t) \rangle_{\mathbf{v}(t) = \mathbf{v}_0} \quad (4.49)$$

where  $\mathbf{e}_\parallel(t) = \frac{\mathbf{v}(t)}{v}$ . The perpendicular component  $F_\perp(\mathbf{v}_0)$  is found in a similar way, by replacing  $\mathbf{e}_\parallel$  in the above expression by  $\mathbf{e}_\perp$ . Practically, we approximated this exact expression by:

$$F_\parallel(\mathbf{v}_0) \approx \frac{1}{\Delta t} \langle [\mathbf{v}(t + \Delta t) - \mathbf{v}(t)] \cdot \mathbf{e}_\parallel(t) \rangle_{|v(t) - v_0| \leq \Delta v, |\theta(t) - \theta_0| \leq \Delta \theta} \quad (4.50)$$

<sup>5</sup>In our case, this “force” is of course not a force in the sense of Newton’s law. However, for lack of a better terminology, we will refer to the “forces” that drive cell motion.



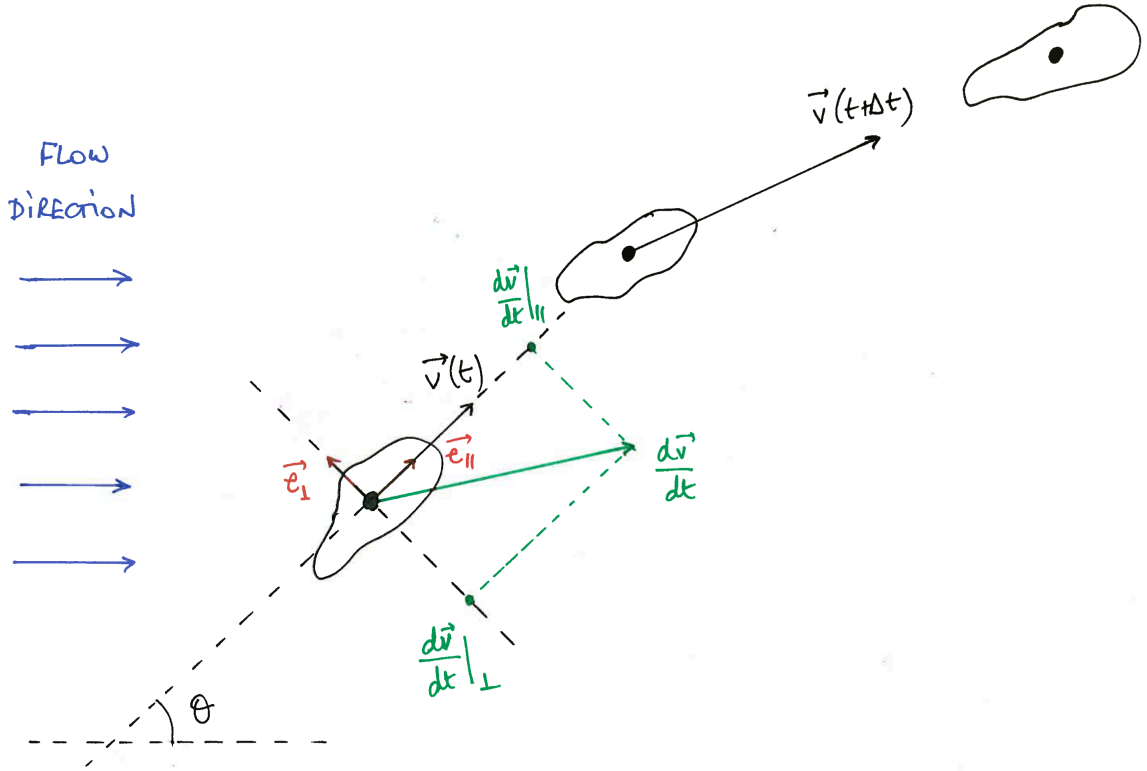


Figure 4.24: Definition of the axis that will be used for the analysis of cell motion:  $\mathbf{e}_{\parallel}$  is a unit vector in the direction of the instantaneous velocity  $\mathbf{v}(t)$  of the cell, and  $\mathbf{e}_{\perp}$  is a unit vector perpendicular to  $\mathbf{e}_{\parallel}$ . The angle between the cell's velocity  $\mathbf{v}(t)$  and the horizontal is  $\theta$ .

where  $\Delta t$  is the (discrete) experimental time interval,  $v(t)$  is within  $\Delta v$  of  $v_0$ , and the angle  $\theta(t)$  is within  $\Delta\theta$  of  $\theta_0$ , the angle that  $\mathbf{v}_0$  makes with the horizontal.

The noise terms are calculated according to:

$$R_{ij}R_{jk}(\mathbf{v}_0) = \frac{1}{\Delta t} \langle [(\mathbf{v}(t + \Delta t) - \mathbf{v}(t)) \cdot \mathbf{e}_i(t) - F_i(\mathbf{v}_0)\Delta t] \times [(\mathbf{v}(t + \Delta t) - \mathbf{v}(t)) \cdot \mathbf{e}_k(t) - F_k(\mathbf{v}_0)\Delta t] \rangle_{|v(t)-v_0| \leq \Delta v, |\theta(t)-\theta_0| \leq \Delta\theta} \quad (4.51)$$

#### 4.10.2 Chapman-Kolmogorov

The method mentioned above to determine the coefficients of a Langevin equation from a stochastic dataset was pioneered by Siegert et al. [105, 33, 60, 61]). As noted in [105], writing that the noise is  $\delta$ -correlated ( $\langle \Gamma_i(t)\Gamma_j(t') \rangle = \delta_{ij}\delta(t-t')$ ) is equivalent to writing that the system has no memory: the dynamics of the system depend only on its current state, not on what has happened before. In other words, the system is Markovian and we can define a probability to go from a velocity  $\mathbf{v}_0$  at time  $t_0$  to a velocity  $\mathbf{v}_1$  at time  $t_1 = t_0 + \Delta t$ . This probability does not depend on the previous states  $\mathbf{v}_{-n}$  that the system was in at previous

times  $t_n = t_0 - n\Delta t$  ( $n \in \mathbb{N}^*$ ). We can then write, considering a time  $t_i$  such that  $t_0 \leq t_i \leq t_1$ :

$$p(\mathbf{v}_1, t_1 | \mathbf{v}_0, t_0) = \sum_{\mathbf{v}_i} p(\mathbf{v}_1, t_1 | \mathbf{v}_i, t_i) p(\mathbf{v}_i, t_i | \mathbf{v}_0, t_0) \quad (4.52)$$

This is the Chapman-Kolmogorov equation, and gives us a condition under which we are allowed to use the analysis presented above. Strictly speaking, having the Chapman-Kolmogorov equation satisfied does not imply that the process we are studying is Markovian. It is a necessary condition, but not a sufficient one [61]. However, it is often (if not always) taken as a sufficient condition in the literature. We checked that the Chapman-Kolmogorov equation was verified for all our data sets. The velocities  $v_x$  and  $v_y$  were each binned into 20 bins and the time step used was 40 seconds ( $t_1 = t_0 + 80$  seconds,  $t_i = t_0 + 40$  seconds). To compare both sides of the equation, one had to compare 2D probabilities:  $\mathbf{v}_0 = (v_{x0}, v_{y0})$  was kept fixed, while one computed  $p(\mathbf{v}_1 = (v_{x1}, v_{y1}), t_1 | \mathbf{v}_0 = (v_{x0}, v_{y0}), t_0)$  for all values of  $\mathbf{v}_1 = (v_{x1}, v_{y1})$ . To ease the visual representation, we did not plot the 2D probability but considered the one-dimensional probability  $p(v_{y1}, t_1 | v_{x1}, t_1, \mathbf{v}_0 = (v_{x0}, v_{y0}), t_0)$  for all values of  $v_{x1}$  at a given  $\mathbf{v}_0$ . Examples of such probabilities are shown on figure 4.25 for different  $\mathbf{v}_0 = (v_{x0}, v_{y0})$  and  $v_{x1}$ , where both sides of the Chapman-Kolmogorov are plotted. It is seen that the Chapman-Kolmogorov condition is verified, which allows us to continue with our Langevin analysis of cell motion.

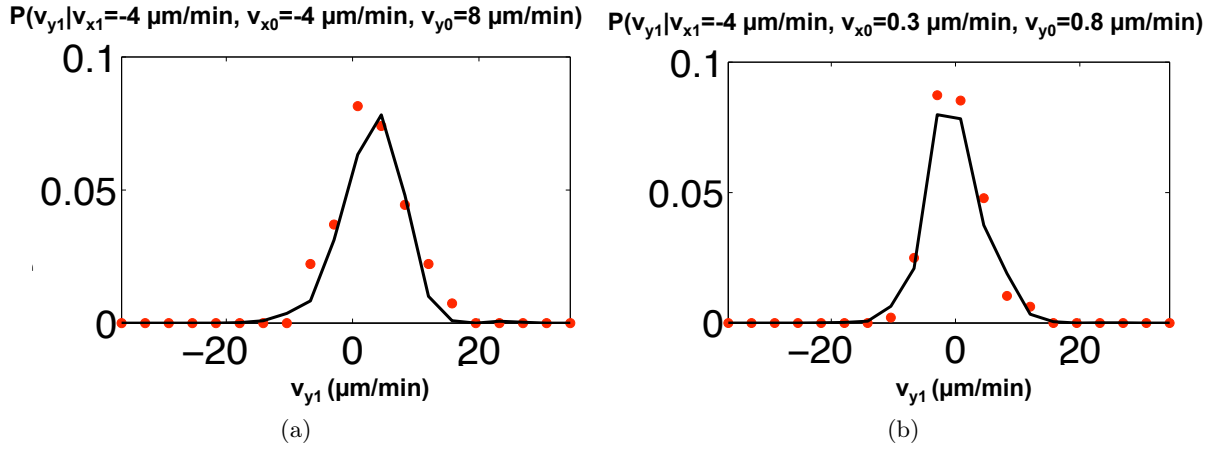


Figure 4.25: Checking the Chapman-Kolmogorov condition. Red dots: lhs of equation 4.52. Black line: rhs of equation 4.52). (a)  $(v_{x0}, v_{y0}) = (-4, 8) \mu\text{m}/\text{min}$ ,  $v_{x1} = -4 \mu\text{m}/\text{min}$  (number of points contributing to the histogram: 39). (b)  $(v_{x0}, v_{y0}) = (0.3, 0.8) \mu\text{m}/\text{min}$ ,  $v_{x1} = -4 \mu\text{m}/\text{min}$  (number of points contributing to the histogram: 127).

### 4.10.3 Conditional averaging - deterministic terms

In the following, we use a typical dataset to describe how we find the functional forms of the deterministic part  $\mathbf{F}(v, \theta)$  and the stochastic part  $\mathbf{R}(v, \theta)$  of equation 4.47. The data used for this example come from an experiment where the concentration profile ran from 0 to 500 nM (gradient:  $1.7 \text{ nM}/\mu\text{m}$ , SNR in the middle of the channel: 0.7). We used a constant binning

size for the angle  $\Delta\theta = 20^\circ$ . For the speed, we divided the range into 20 bins of equal size:

$$\Delta v = \frac{v_{max} - v_{min}}{20} \quad (4.53)$$

For each bin of  $(v, \theta)$ , the acceleration along and perpendicular to the movement direction was calculated, as explained in subsection 4.10.1. All of these quantities are *a priori* functions of the speed of the cell  $v$  and its angle of propagation  $\theta$  ( $\theta = 90^\circ$  being the gradient direction).

#### Deterministic part of the perpendicular acceleration ( $F_\perp(v, \theta)$ )

The deterministic term  $F_\perp(v, \theta)$  is plotted as a function of  $v$  for different angles on figure 4.26. Each point on figure 4.26 is an average over data coming from different tracks. We call  $n_{v,\theta}$  the number of points that contribute to the value of  $F_\perp(v, \theta)$ . At a given angle, the force perpendicular to the cell's motion does not depend significantly on the speed  $v$  of the cell. For each angle  $\theta_0$ , we averaged the values taken by  $F_\perp(v, \theta_0)$ , and defined  $F_\perp(v, \theta_0) = F_\perp(\theta_0)$ . We used a weighted average, where the weight of each point was given by  $n_{v,\theta}$ . In figure 4.27, we plotted  $F_\perp(\theta)$  as a function of  $\theta$ . There is a clear dependence of  $F_\perp(\theta)$  on  $\theta$ , which is cosine-like (see figure 4.27). We write:

$$F_\perp(\theta) = F_1 \cos \theta. \quad (4.54)$$

This shows that the cell tends to align with the gradient. For a cell going in the flow direction ( $\theta = 0^\circ$ ),  $F_\perp(\theta = 0^\circ)$  is positive: the cell has a tendency to go up the gradient. For a cell going opposite the flow direction,  $F_\perp(\theta = 180^\circ)$  is negative, which also means that the cell is pushed in the gradient direction (to see this, recall that the frame of reference is rotating with the cell). A cell going in the gradient direction has  $F_\perp(\theta = 90^\circ) = 0$ , so the only force acting on it is parallel to the cell motion, which is the gradient direction. Similarly if the cell is going opposite the gradient direction, at  $\theta = 270^\circ$ .

#### Deterministic part of the parallel acceleration ( $F_\parallel(v, \theta)$ )

Let us now turn to the deterministic component of the parallel acceleration. Contrary to  $F_\perp(v, \theta)$ , which turned out to be independent on the speed of the cell  $v$ , there is a clear dependence of  $F_\parallel(v, \theta)$  on  $v$ . This is shown on figure 4.28. We fitted a second-order polynomial to these curves:

$$q(v, \theta) = \alpha(\theta) + \gamma(\theta)v^2. \quad (4.55)$$

As above, the fit is weighted by the number of points  $n_{v,\theta}$  that contribute to each value of  $F_\parallel(v, \theta)$ . As  $F_\parallel$  is *a priori* a function of  $\theta$ , the fitting parameters  $\alpha(\theta)$  and  $\gamma(\theta)$  should also depend on  $\theta$ . It turns out that  $\gamma$  is relatively constant for different  $\theta$  (see figure 4.29a), but that  $\alpha$  does depend on the cell's direction. This dependency can be fitted with a sine function with an offset, as shown on figure 4.29b. We write:

$$\alpha(\theta) = \alpha_0 + F_2 \sin \theta. \quad (4.56)$$

On figure 4.29c, we plotted  $\arctan[(\alpha(\theta) - \alpha_0)/F_\perp(\theta)]$  as a function of  $\theta$ . All points collapse on the line  $y = x$ , showing that  $\arctan[(\alpha(\theta) - \alpha_0)/F_\perp(\theta)] = \theta$  and therefore that  $F_1 = F_2$ .

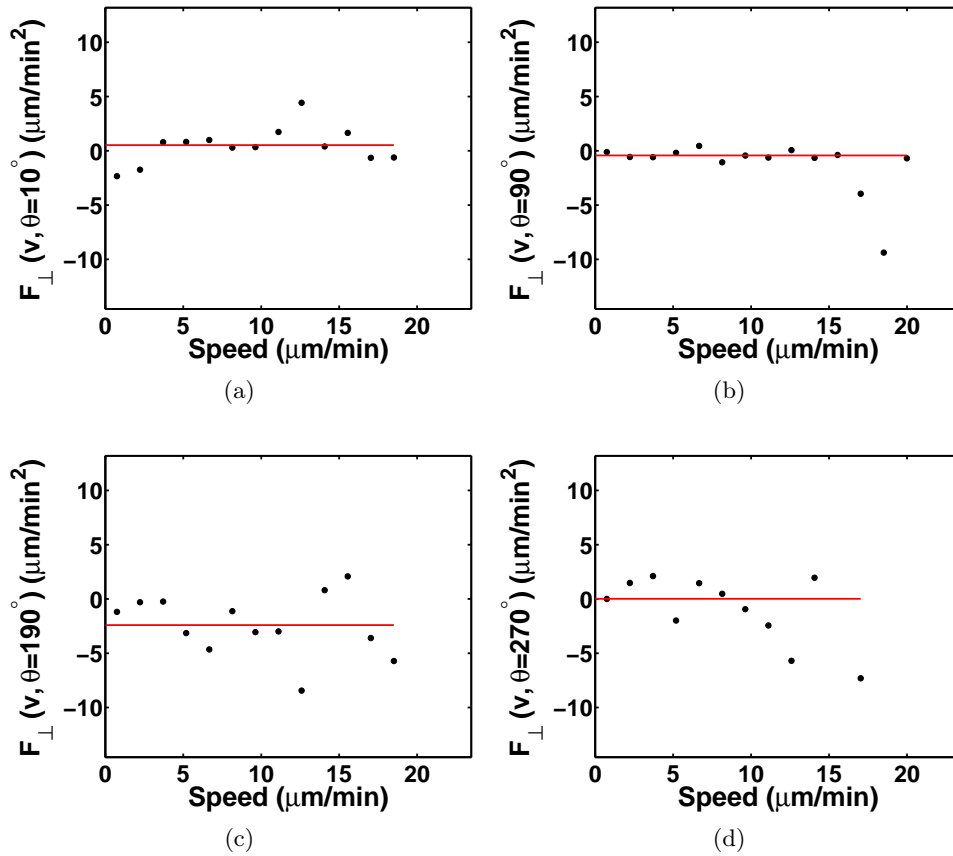


Figure 4.26: Plots showing the deterministic term of the acceleration in the perpendicular direction,  $F_{\perp}(v, \theta)$ , as a function of  $v$  for different values of  $\theta$ . (a)  $\theta = 10^\circ$  (roughly the flow direction), (b)  $\theta = 90^\circ$  (gradient direction), (c)  $\theta = 190^\circ$  (roughly opposite the flow direction), (d)  $\theta = 270^\circ$  (opposite gradient direction). Each point is the average over data coming from different cell tracks, as explained in section 4.10.1. The red line shows the weighted average of the black points, where each point is weighted by  $n_{v,\theta}$  (see main text).

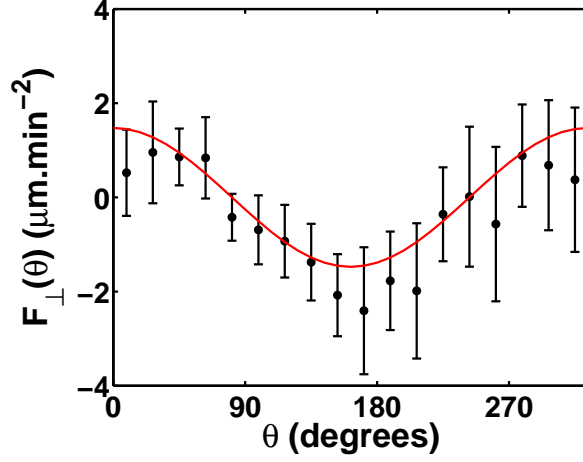


Figure 4.27: Evolution of the average deterministic term  $F_{\perp}(\theta)$  as a function of  $\theta$ . The error bars represent the 95 % confidence intervals.

#### 4.10.4 Conditional averaging - stochastic terms

##### Mixed noise term

The cross-correlation of the perpendicular and the parallel acceleration, as well as the autocorrelations of the parallel and the perpendicular accelerations, are shown on figure 4.30. We see that we can neglect the cross-correlation of the acceleration compared to the autocorrelations, which is why we will consider that there is no mixed noise term. We also calculated the mixed noise term, and we indeed saw that the mixed noise had no dependence on the speed or the angle of propagation of the cell, and that it was averaging to zero.

##### Perpendicular noise

The perpendicular noise was calculated according to the formula:

$$R_{\perp}(\mathbf{v}_0)^2 = \Delta t \left\langle \left( \frac{\mathbf{v}(t + \Delta t) - \mathbf{v}(t)}{\Delta t} \cdot \mathbf{e}_{\perp}(t) - F_{\perp}(\mathbf{v}_0) \right)^2 \right\rangle_{|v(t) - v_0| \leq \Delta v, |\theta(t) - \theta_0| \leq \Delta \theta} \quad (4.57)$$

The evolution of the perpendicular noise term with the angle of propagation  $\theta$  is shown on figure 4.31. At each angle, we fitted the noise in the perpendicular direction by a first-order polynomial  $q(v, \theta) = r_{1,\perp}(\theta) + r_{2,\perp}(\theta)v$ . As for the deterministic part, the fits were weighted by the number of points  $n_{v,\theta}$  contributing to each value of  $R_{\perp}(v, \theta)$ . The evolution of the offset  $r_{1,\perp}(\theta)$  and the slope  $r_{2,\perp}(\theta)$  is shown on figure 4.32a and 4.32b respectively. No dependence on the angle was observed.

##### Parallel noise

The parallel noise is calculated according to the formula:

$$R_{\parallel}(\mathbf{v}_0)^2 = \Delta t \left\langle \left( \frac{\mathbf{v}(t + \Delta t) - \mathbf{v}(t)}{\Delta t} \cdot \mathbf{e}_{\parallel}(t) - F_{\parallel}(\mathbf{v}_0) \right)^2 \right\rangle_{|v(t) - v_0| \leq \Delta v, |\theta(t) - \theta_0| \leq \Delta \theta} \quad (4.58)$$

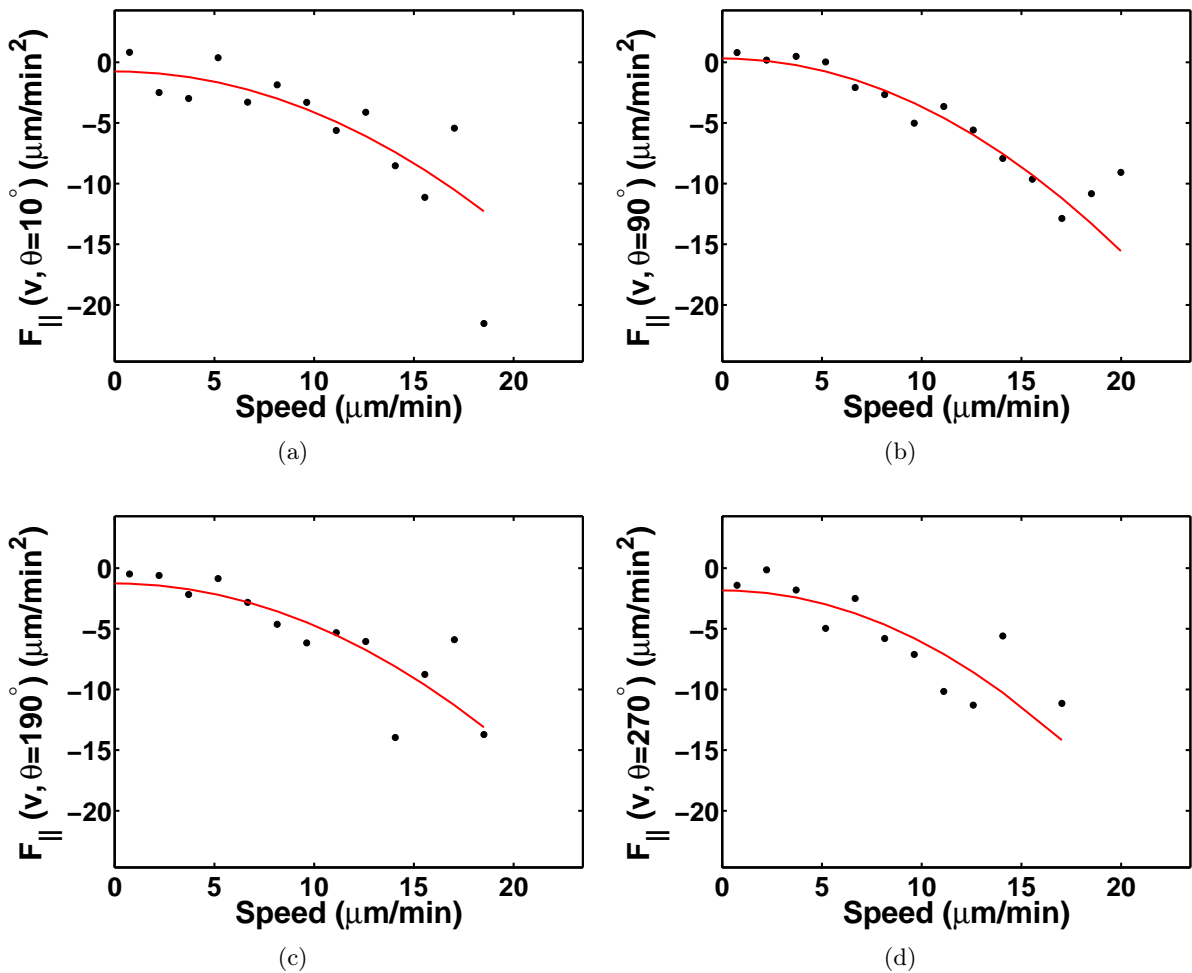


Figure 4.28: Plots showing the deterministic component of the acceleration in the parallel direction,  $F_{\parallel}(v, \theta)$ , for different values of  $\theta$ . (a)  $\theta = 10^\circ$  (roughly the flow direction), (b)  $\theta = 90^\circ$  (gradient direction), (c)  $\theta = 190^\circ$  (roughly opposite the flow direction), (d)  $\theta = 270^\circ$  (opposite gradient direction). Each point is the average over data coming from different cell tracks, as explained in section 4.10.1. The solid lines are fits by a second-order polynomial  $q(v, \theta) = \alpha(\theta) + \gamma(\theta)v^2$ , where each point is weighted by  $n_{v,\theta}$ .

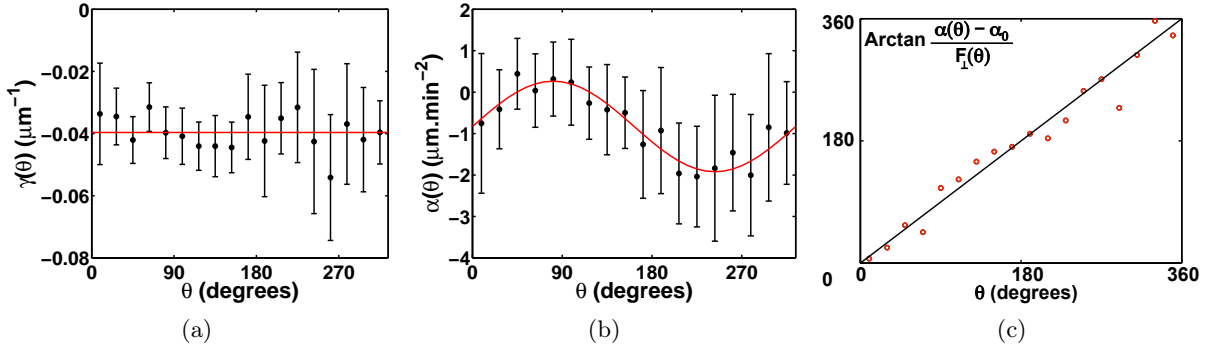


Figure 4.29: Evolution of the fitting parameters  $\alpha$  and  $\gamma$  with  $\theta$ . (a) The damping term  $\gamma$  can be considered as independent of the angle of propagation  $\theta$ . (b) The term  $\alpha$  shows a sine-like dependence with  $\theta$ , with an offset  $\alpha_0$ . Error bars are 95 % confidence intervals on the fit values. (c) Evolution of  $\arctan[(\alpha(\theta) - \alpha_0)/F_{\perp}(\theta)]$  with  $\theta$ . The black line is the curve  $y = x$ , which is plotted to guide the eye.

The evolution of the parallel noise term with the angle of propagation  $\theta$  is shown on figure 4.33. At each angle, we fitted the noise in the parallel direction by a first-order polynomial  $q(v, \theta) = r_{1,\parallel}(\theta) + r_{2,\parallel}(\theta)v$ . The evolution of the offset  $r_{1,\parallel}(\theta)$  and the slope  $r_{2,\parallel}(\theta)$  is shown on figure 4.34a and 4.34b respectively. No dependence on the angle was observed.

### Estimating the noise without binning on the angle

Because none of the noise terms depend on the angle of propagation  $\theta$ , we recalculate them without binning the data on the angle  $\theta$ :

$$R_{\perp}(\mathbf{v}_0)^2 = \Delta t \left\langle \left( \frac{\mathbf{v}(t + \Delta t) - \mathbf{v}(t)}{\Delta t} \cdot \mathbf{e}_{\perp}(t) - F_{\perp}(\mathbf{v}_0) \right)^2 \right\rangle_{|v(t) - v_0| \leq \Delta v} \quad (4.59)$$

The resulting evolution of the perpendicular and parallel noise are shown on figure 4.35, fitted by a first-order polynomial  $q_{\perp,\parallel}(v) = r_{1,\perp,\parallel} + r_{2,\perp,\parallel}v$ .

### Putting the results together

Putting everything together, we can now write the Langevin equation describing chemotactic cell motion:

$$\left. \frac{dv}{dt} \right|_{\parallel} = -\gamma v^2 + \alpha_0 + F \sin \theta + (r_{1,\parallel} + r_{2,\parallel}v)\Gamma_{\parallel}(t) \quad (4.60)$$

$$\left. \frac{dv}{dt} \right|_{\perp} = F \cos \theta + (r_{1,\perp} + r_{2,\perp}v)\Gamma_{\perp}(t). \quad (4.61)$$

For the lack of better names, we will call  $\alpha_0$  a “propelling force” and  $F$  ( $F = F_1 = F_2$ ) a “force in the gradient direction”. In the absence of a gradient ( $F = 0$ ), the quantity  $\alpha_0$  leads to the cells having a target speed  $v_0 = \sqrt{\alpha_0/\gamma}$  if  $\alpha_0 > 0$ , or damps cellular motion if  $\alpha_0 < 0$ . As mentioned earlier, the two quantities  $\alpha_0$  and  $F$  are of course not forces in the classical, Newtonian, sense on the term.

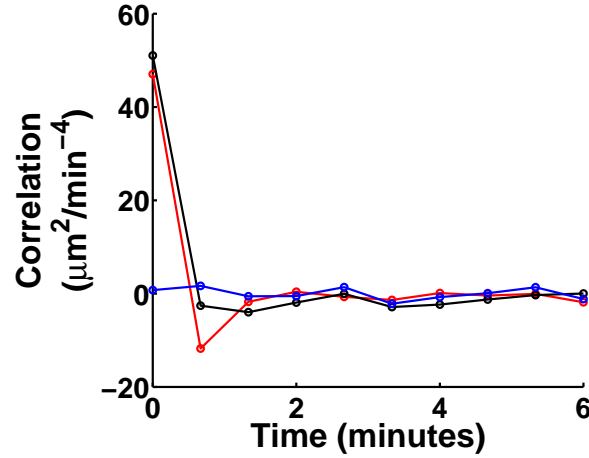


Figure 4.30: Autocorrelation of the parallel acceleration (red), the perpendicular acceleration (black), and cross-correlation (blue).

#### 4.10.5 Evolution of the parameters of the Langevin equation

We have seen in section 4.6.4 that the SNR could explain quantitatively the evolution of the chemotactic velocity  $v_y$ . We however also saw that it was unable to explain quantitatively the evolution of the cellular speed  $v$ . It was shown in [12] that the parameters of the Langevin equation describing the random motion of starved *D. discoideum* depended on the uniform background of cAMP surrounding the cells. In our case, we propose that two quantities might play a role in cellular motion, namely the SNR and the average concentration of cAMP surrounding the cell. In the following, we will discuss the evolution of the parameters of the Langevin equation with the SNR and the midpoint concentration.

##### Friction coefficient

The friction coefficient is plotted as a function of the SNR on figure 4.36a and 4.36b respectively. The plotted quantity is, for each experiment, the average  $\gamma$  over all angles of propagation and the error bars show the standard deviation. As before, filled circles indicate an experiment where the concentration profile goes from 0 to  $c_{\max}$ , and empty circles indicate an experiment where the low concentration  $c_{\min}$  is different from 0. From our data, we cannot see any influence of the SNR or the midpoint concentration on the friction coefficient. For the wild-type cells, the friction coefficient therefore appears to be a constitutive property of the cells, independent of the external conditions.

##### Propelling force

We plotted the propelling force  $\alpha_0$  as a function of the SNR and the midpoint concentration on figure 4.37. No systematic trend appears on these plots. The value of  $\alpha_0$  is in most cases negative, indicating a constant damping of cellular motion.



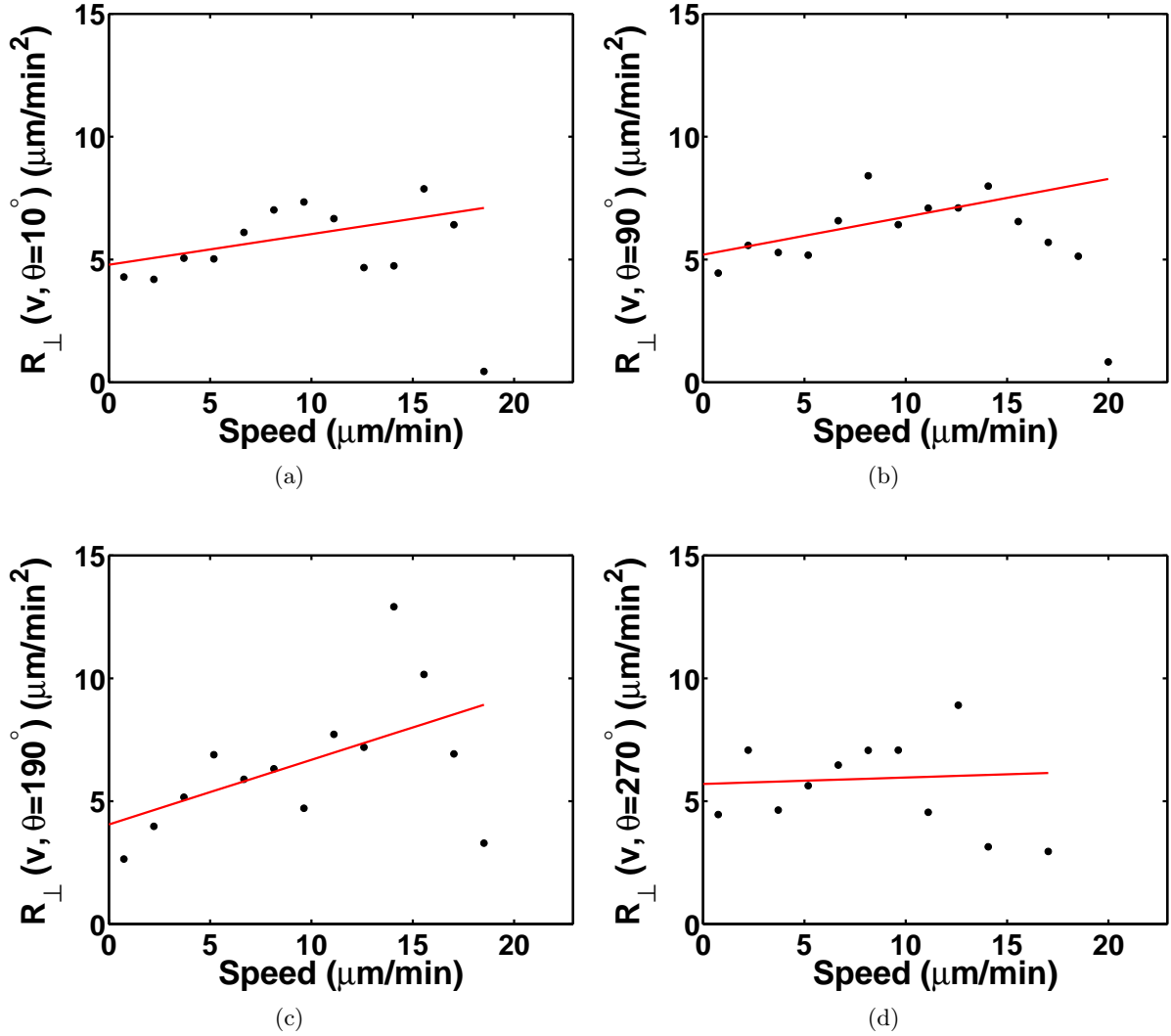


Figure 4.31: Plots showing  $R_{\perp}(v, \theta)$  for different values of  $\theta$ . (a)  $\theta = 10^\circ$  (roughly the flow direction), (b)  $\theta = 90^\circ$  (gradient direction), (c)  $\theta = 190^\circ$  (roughly opposite the flow direction), (d)  $\theta = 270^\circ$  (opposite gradient direction). Each point is the average over data coming from different cell tracks, as explained in section 4.10.1. The solid lines are weighted fits by a first-order polynomial  $q(v, \theta) = r_{1,\perp}(\theta) + r_{2,\perp}(\theta)v$ , where the weight of each point is given by  $n_{v,\theta}$ .

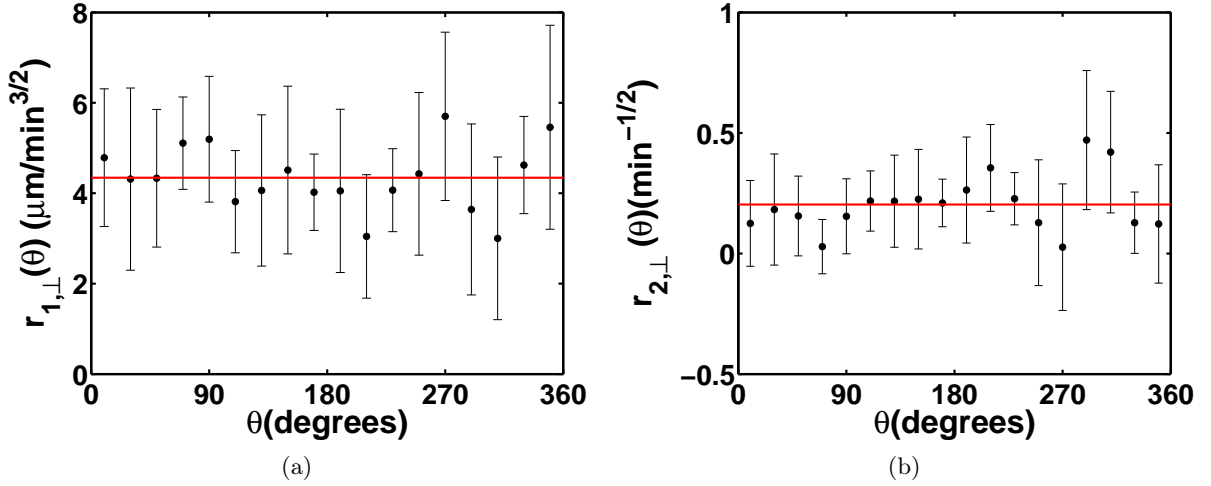


Figure 4.32: Evolution of the fitting parameters (a)  $r_{1,\perp}(\theta)$  and (b)  $r_{2,\perp}(\theta)$  with the angle  $\theta$ . Error bars show the 95% confidence interval on the fit value.

### Force in the gradient direction

The last parameter of the deterministic part is the force in the gradient direction. The amplitude of this force is plotted as a function of the SNR and of the average background concentration on figures 4.38a and 4.38b respectively. The error bars shown on the plots represent the 95% confidence interval on the fit values. There is a clear increase of the force with the SNR, reflecting the increase in the chemotactic velocity  $v_y$  with the SNR. The evolution of the force with the SNR reflects the evolution of the chemotactic velocity  $v_y$  with the SNR, with an onset and a linear increase (compare figures 4.38b and 4.14c).

### Noise offset

The offset of the noise terms are shown on figure 4.39 as a function of the SNR and of the midpoint concentration. We see that the noise in the parallel and the perpendicular direction have similar offset values. It is hard to see a trend on the figures plotted, as a function of the SNR or of the midpoint concentration.

### Noise slope

The slope of the noise terms are shown on figure 4.40 as a function of the SNR and of the midpoint concentration. Here also, there is no clear trend on the plots. The slope of the noise in the perpendicular direction has a value slightly higher than its counterpart in the parallel direction for midpoint concentrations up to 10 nM.

## 4.11 Simulating the data

We used a simple Euler-Maruyama scheme to simulate our Langevin equation [62], using the parameters retrieved from the data. The time step of the simulation was the time step used

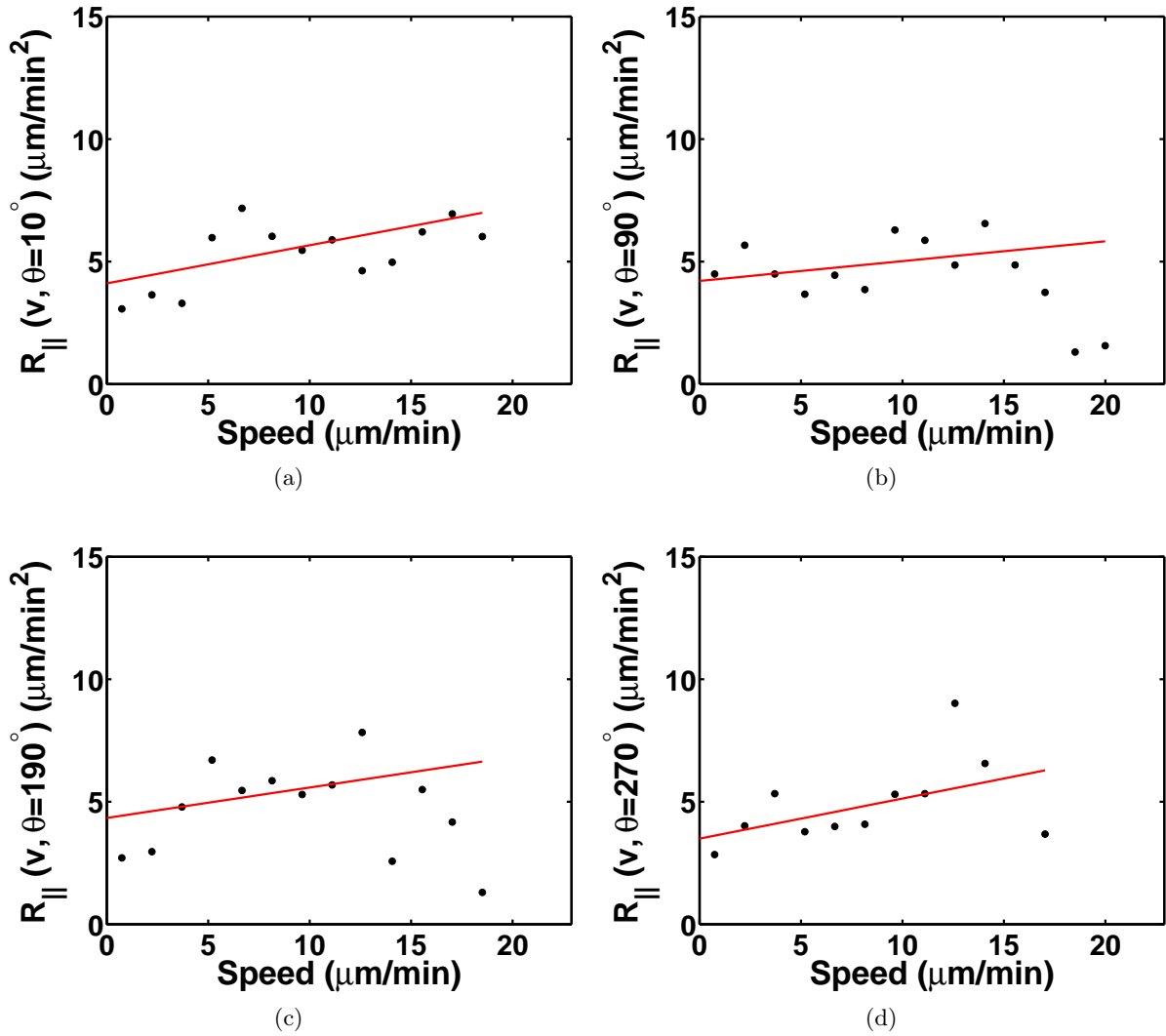


Figure 4.33: Plots showing  $R_{||}(v, \theta)$  for different values of  $\theta$ . (a)  $\theta = 10^\circ$  (roughly the flow direction), (b)  $\theta = 90^\circ$  (gradient direction), (c)  $\theta = 190^\circ$  (roughly opposite the flow direction), (d)  $\theta = 270^\circ$  (opposite gradient direction). Each point is the average over data coming from different cell tracks, as explained in section 4.10.1. The solid lines are fits by a first-order polynomial  $q(v, \theta) = r_{1,||}(\theta) + r_{2,||}(\theta)v$ .

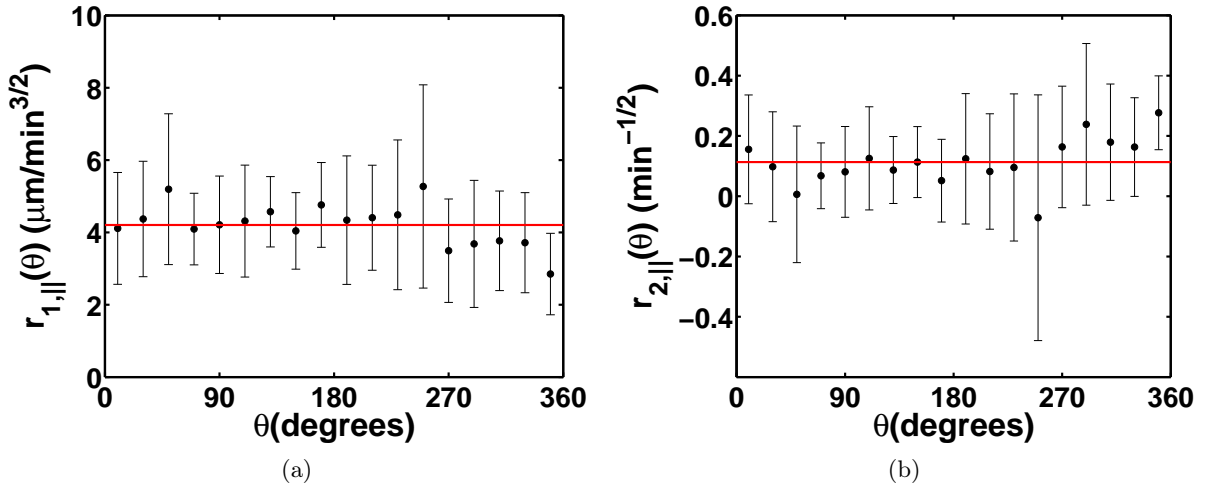


Figure 4.34: Evolution of the fitting parameters (a)  $r_{1,||}(\theta)$  and (b)  $r_{2,||}(\theta)$  with the angle  $\theta$ . Error bars show the 95% confidence interval on the fit value.

for the conditional averaging (40 seconds). We simulated 100 tracks, with each track being 200 points long. This corresponds to a track that lasts for 33 minutes. The data are very well reproduced by the model, as can be seen on figure 4.41. The dependence of the speed on the angle  $\theta$ , reproduced on figure 4.41e, is due to the gradient force  $F$  in the  $y$  direction.

One feature that we do not capture however is the cellular individuality. Indeed, if we plot the cells according to the two usual quantities used to describe their motion, which is their mean speed  $\bar{v}$  and their chemotactic index (CI), we find figure 4.42a for the experiments and figure 4.42b for the simulations. The conditional averaging treats all the cells in the same way, and the result of the conditional averaging is therefore the average behavior of the cellular population. In the next section, we make an attempt to reproduce the biological diversity by dividing the data into 4 regions, as sketched on figure 4.42a. The four regions were delimited by the average speed and the average chemotactic index of the cell population (see figure).

## 4.12 Langevin analysis of four subpopulations

We performed exactly the same analysis as above on the 4 cell subpopulations shown on figure 4.42a. The evolution of the friction coefficient, the propelling force and the force in the gradient direction are shown on figure 4.43. The friction coefficient does not depend on the subpopulation, but the propelling force and the force in the gradient direction do. As might be expected, there is a positive propelling force only in regions 2 and 4, at high values of the mean speed. The value of the force in the gradient direction has an uncertainty of more than 100% in regions 1 and 2. In regions 3 and 4, the force in the gradient direction is positive, a consequence of the high CI of the corresponding cells. The fit parameters for the stochastic terms in the parallel and the perpendicular directions are shown on figure 4.44. The slope of the noise in the parallel direction  $r_{2,||}$  is essentially zero in all regions except region 1. In the perpendicular direction, the slope takes a non-zero value in regions 1 and 3, which are the regions of slow speed. The offset of the noise is higher in regions 2 and 4 than in regions 1

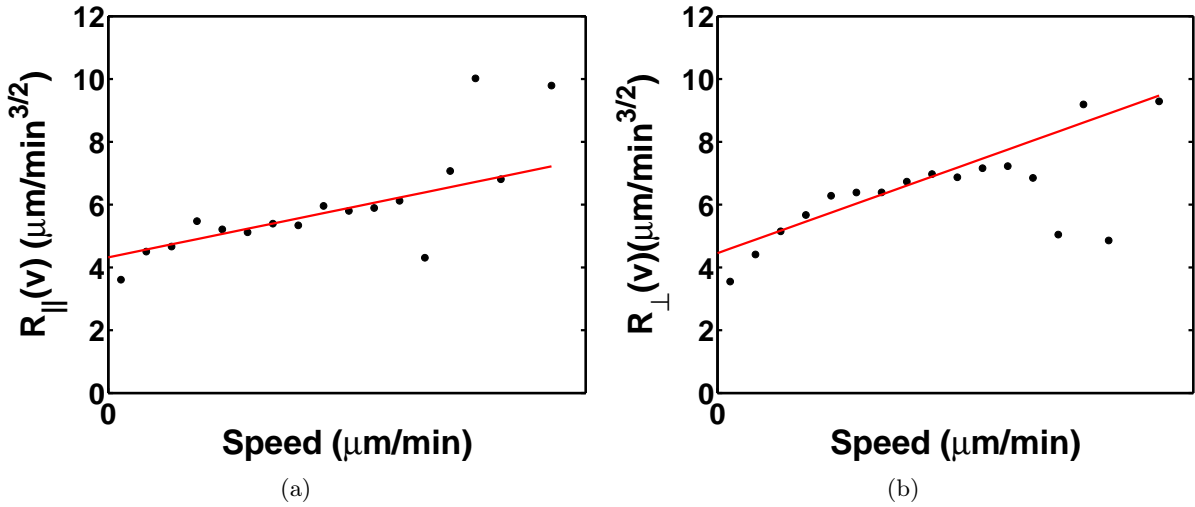


Figure 4.35: (a) Noise in the parallel direction and (b) in the perpendicular direction, calculated without binning on the angle  $\theta$  and fitted by a first order polynomial.

and 3, showing that the basal noise increases when the speed increases. The offset of the noise in region 4 is lower than the offset in region 2, indicating that fast, chemotactic cells (from region 4) exhibit less noise than fast, non-chemotactic cells (from region 2). For the fast cells in regions 2 and 4, the perpendicular noise is bigger than the parallel noise.

However, even if we divide the cell population into these four subpopulations, the experimental spread in the  $(\bar{v}, CI)$  plane is still not reproduced (see figure 4.45). One way to artificially reproduce the spread could be to pick the parameters of the Langevin equation randomly from a distribution, for each simulated track. It would of course be much more satisfactory to get the parameters from the data itself. This would mean to repeat the same procedure of conditional averaging on each individual cell. Is this idea realistic? The track length that we would need would be much longer than what we currently have (we have roughly 25 points per track), in order to get good statistics on the behavior of each cell. If for example we want to keep our bin size for the angle of  $\pi/9$  and assume that we have a cell that always goes up the gradient, we have to consider 9 bins for the angle. If moreover the cell explores roughly speeds varying from 5 to 15  $\mu\text{m}/\text{min}$ , which is not atypical, this would correspond to 10 bins for the speed. Even if not all the bins are full, having 20 points per bin on average (which is what we currently have when we do the analysis for the whole cell population) means that the tracks should be at least 1800 points long. Taking an image every 10 seconds would imply that the data should span over five hours... For a cell that crawls up the gradient with a chemotactic velocity of  $v_y = 4 \mu\text{m}/\text{min}$  on average, this means that the gradient region should be more than 1 mm long. This is a lower estimate since we considered only 90 bins. Apart from the technical difficulties that there are to create a linear, stable profile of concentration over this length scale, we also run into biological problems, as the cells develop and are not reacting in the same way to the same stimulus after 6 hours of starvation or after 11 hours. As this method is clearly not feasible, it would be useful to take more data using our current setup, with the hope to see groups of cells with a similar behavior emerging.

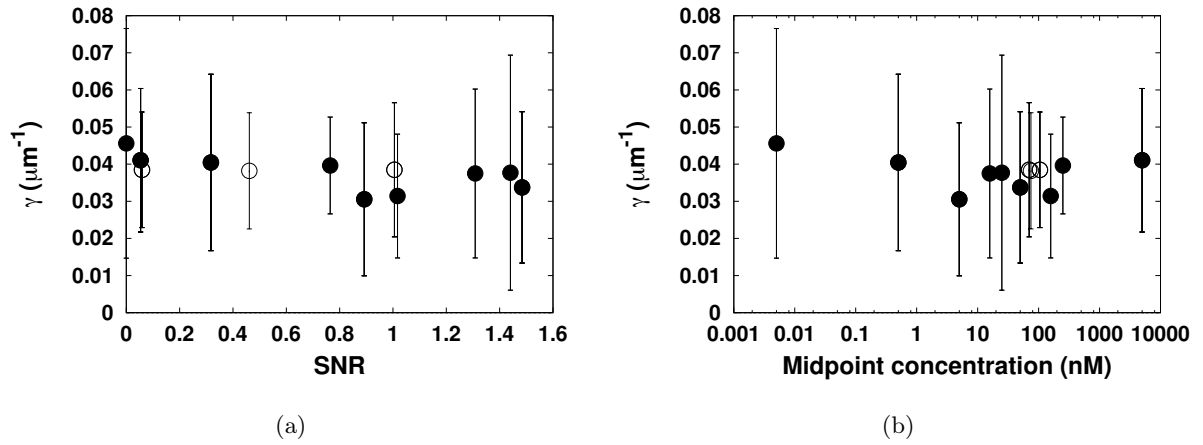


Figure 4.36: Friction coefficient as a function of (a) the SNR and (b) of the cAMP midpoint concentration. Each data point is the average over the different  $\gamma$  evaluated at different angles of propagation, as explained in the main text. The error bars are the standard deviation of these values of  $\gamma$  at different angles. Empty/filled circles as in figure 4.11.

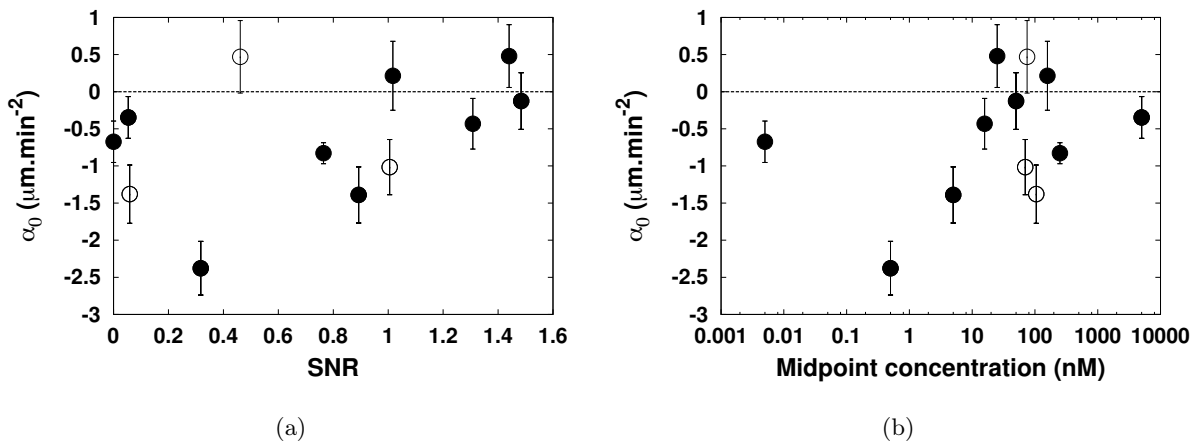


Figure 4.37: Propelling force as a function of (a) the SNR and (b) of the cAMP midpoint concentration. Empty/filled circles as in figure 4.11.

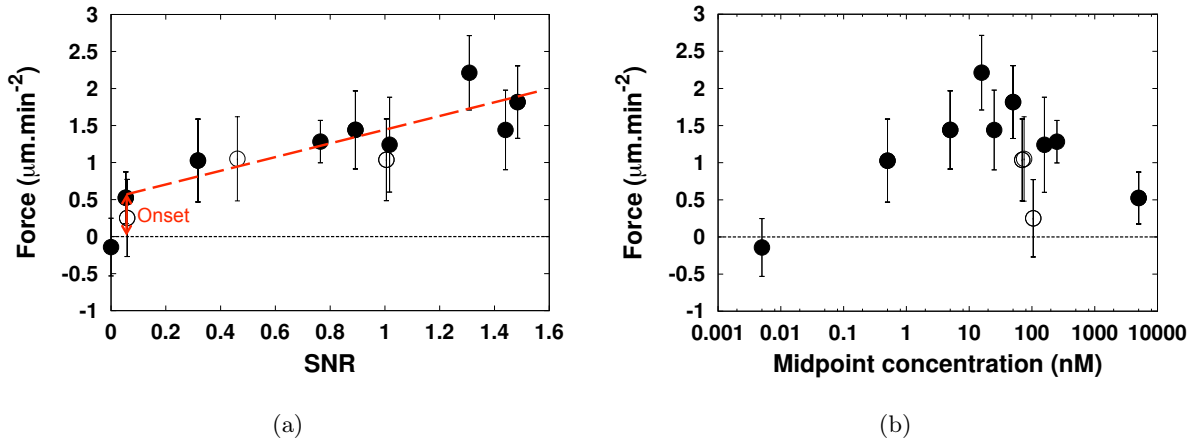


Figure 4.38: Amplitude of the force in the gradient direction as a function of (a) the SNR and (b) the cAMP midpoint concentration. There is a clear correlation between the amplitude of the force and the SNR. The line in (a) is here to guide the eye. Empty/filled circles as in figure 4.11.

### 4.13 Langevin analysis of the SCAR/PIR mutants

We proceeded in the same way for the data taken with the SCAR/PIR mutants. The parameters of the deterministic part of the Langevin equation are summarized on figure 4.46. The parameters describing the stochastic part are shown on figures 4.47 and 4.48. A comparison with the parameters describing the chemotaxis of WT cells is found on figures 4.49 and 4.50.

As for the WT cells, the force increases with increasing SNR. The friction coefficient is higher than the friction coefficient of the WT cells at SNR lower than 0.2, but quickly goes down to similar values than for the WT cells above 0.2. From the plots, we see that the friction goes down both with midpoint concentration and the SNR. We conjecture that the most meaningful quantity to look at is the SNR, and that it is the gradient that rescues the phenotype of the SCAR/PIR null cells, not the midpoint concentration. An experimental verification could be made by tracking SCAR/PIR mutants in uniform backgrounds of concentration of cAMP, and perform the same Langevin analysis on the cells. It would then be possible to see if the friction coefficient depends on the background concentration. The value of  $\alpha_0$  shows the same kind of behavior with the midpoint concentration as for the WT cells. The propelling force is nonzero when the SCAR/PIR cells are in buffer or in a very low background of cAMP (midpoint concentration 0.005 nM, corresponding to  $\sim 30$  of bound receptors only, out of 70 000). It is then goes down to 0 until midpoint concentrations of 5 nM (roughly 3500 bound receptors), and increases for higher concentrations.

Concerning the stochastic part, note that the offset of the noise in the parallel direction increases with the SNR. This increase is simultaneous to a decrease in the slope of the noise in the parallel direction. The parameters describing the noise in the perpendicular direction are essentially independent of the external gradient.

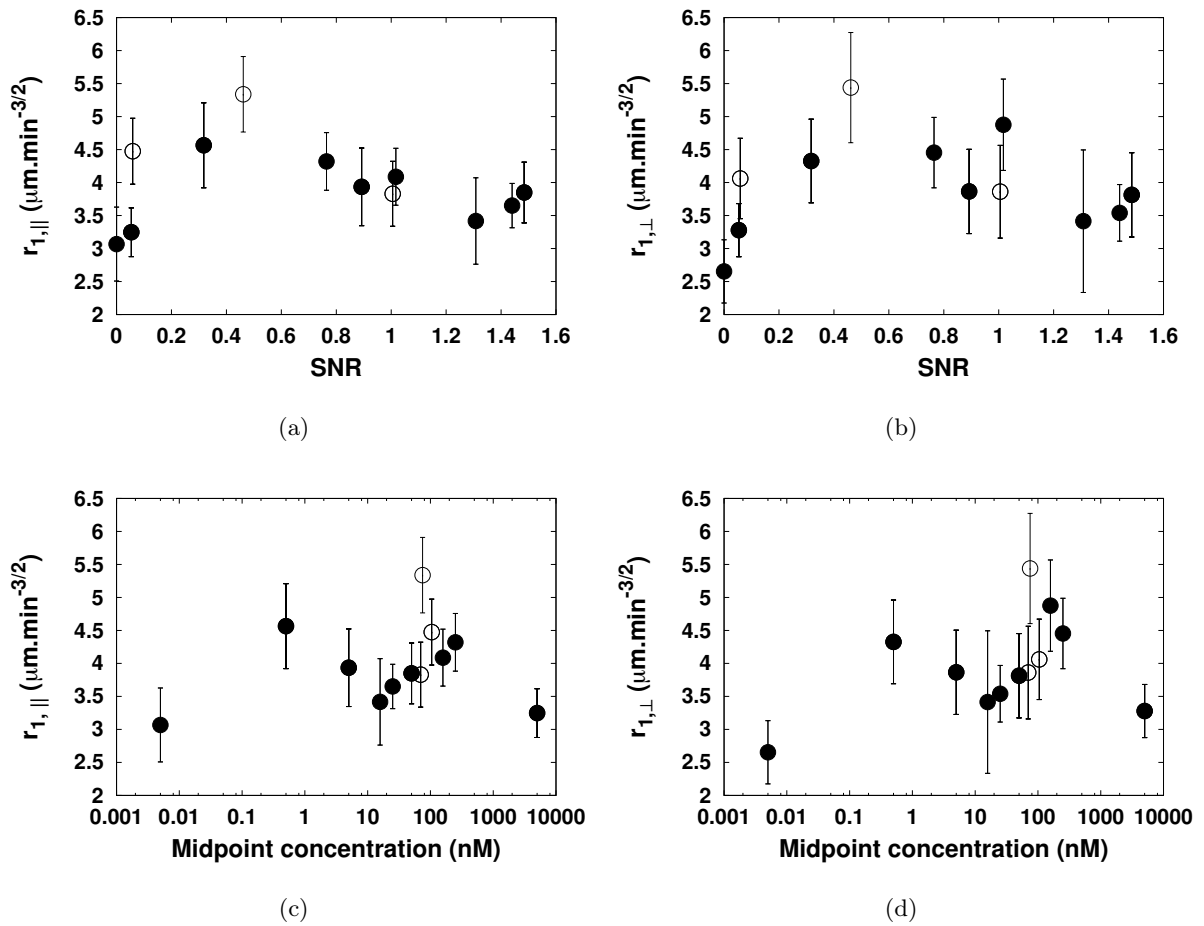


Figure 4.39: Offset of the (a) parallel noise  $r_{1,||}$  and (b) of the perpendicular noise  $r_{1,\perp}$  as a function of the SNR. (c), (d) As a function of the midpoint concentration. Empty/filled circles as in figure 4.11.



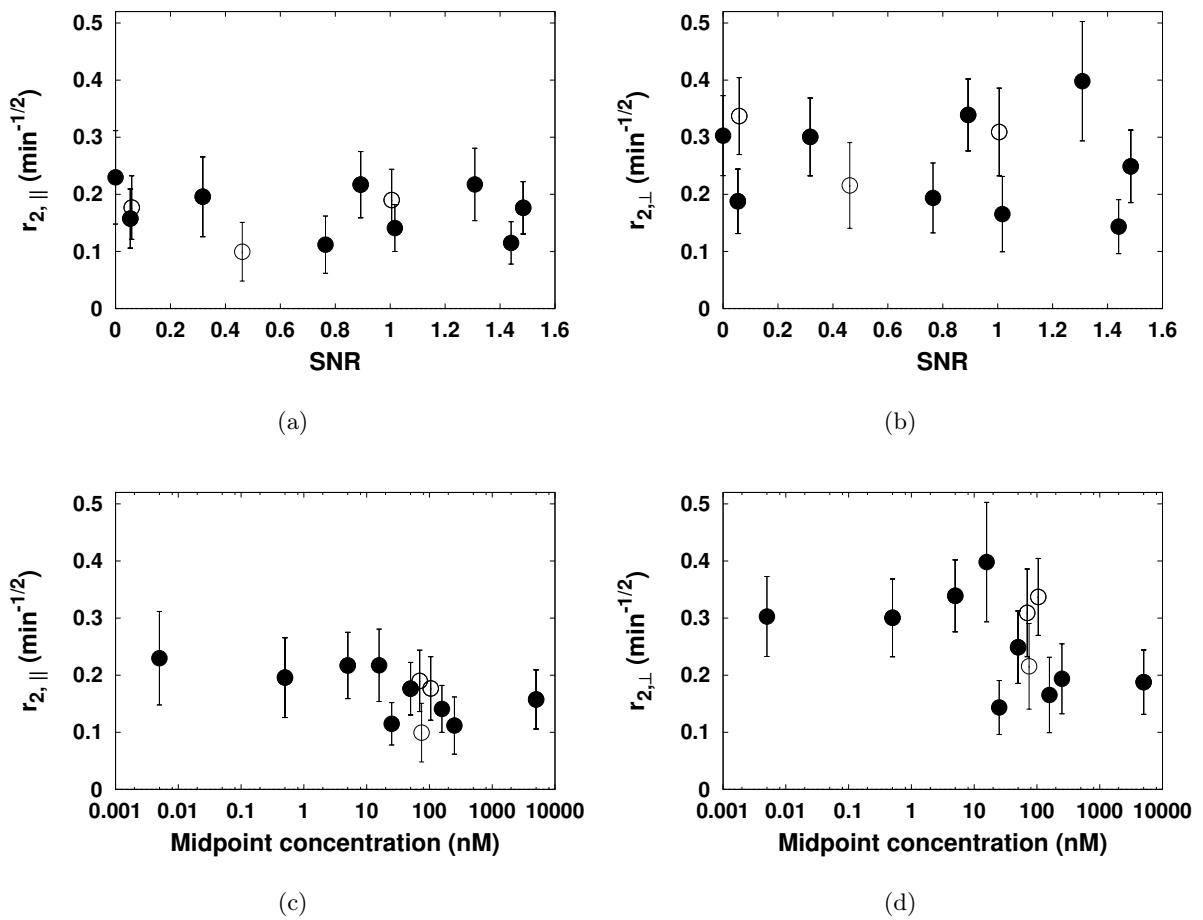


Figure 4.40: Slope of the (a) parallel noise  $r_{2,\parallel}$  and (b) of the perpendicular noise  $r_{2,\perp}$  as a function of the SNR. (c), (d) As a function of the midpoint concentration. Empty/filled circles as in figure 4.11.

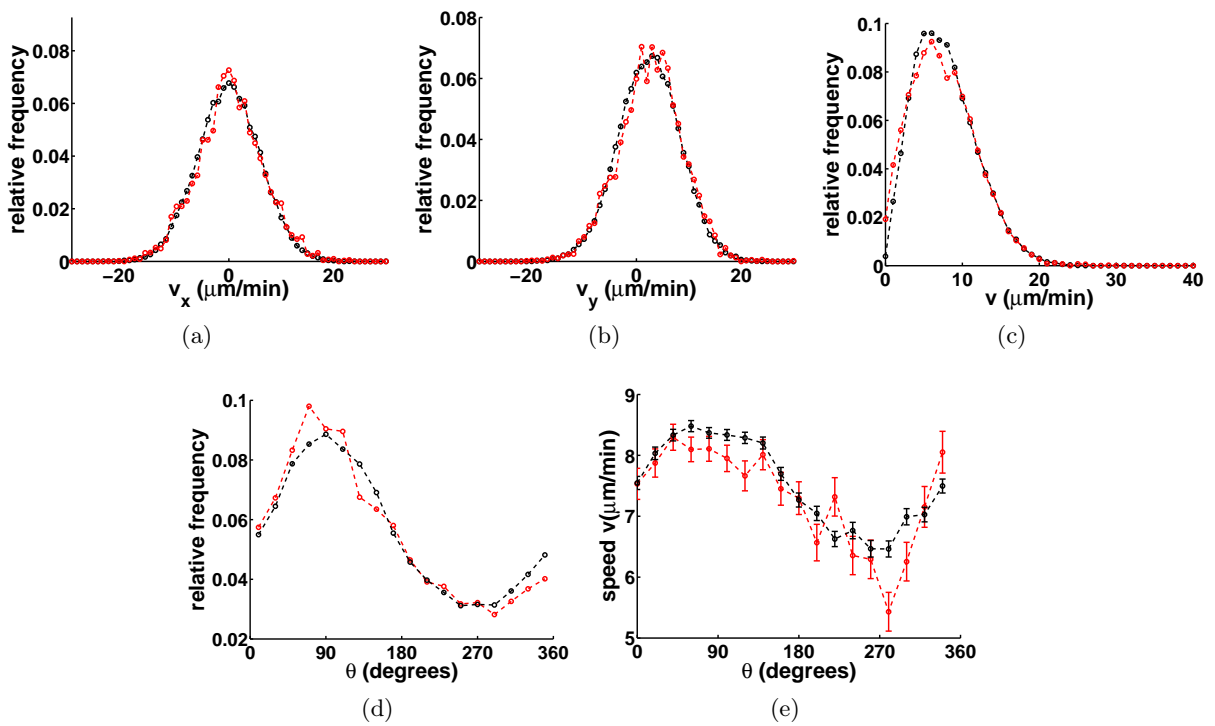


Figure 4.41: Simulated (black) and experimental (red) histograms of (a)  $v_x$ , (b)  $v_y$ , (c)  $v$  and (d) the angle  $\theta$ . (e) Simulated (black) and experimental (red) relationship between the speed  $v$  and the angle of propagation  $\theta$ .

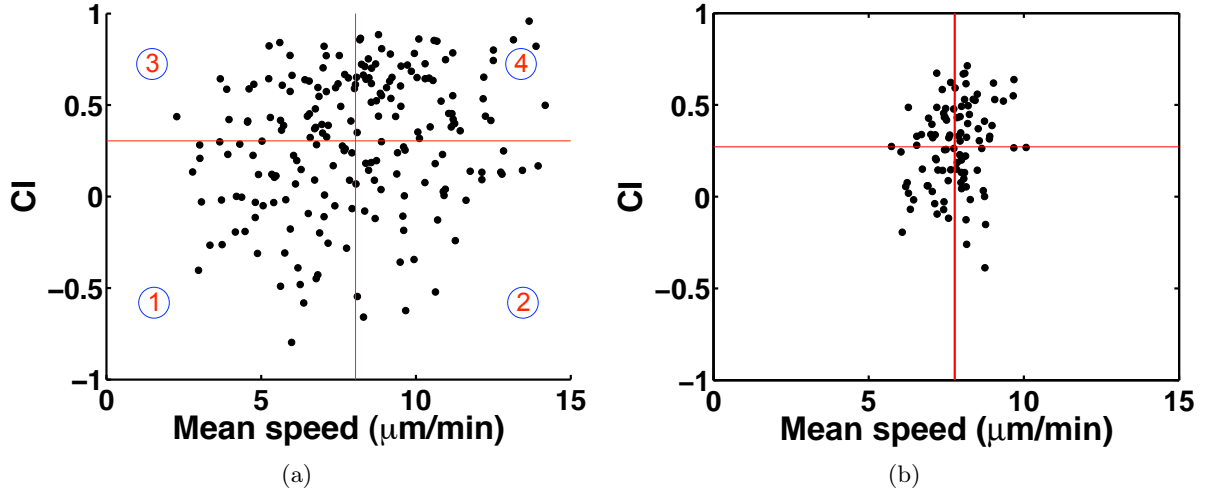


Figure 4.42: Cells in the (Mean speed, Chemotactic index) plane. Each point represent a cell. The vertical red line is the mean speed of the population, the horizontal red line is the mean CI of the cell population. (a) Experimental data. (b) Simulation. The simulation does not reproduce the experimental cellular individuality. The region number, used in the next section, is indicated on figure (a).

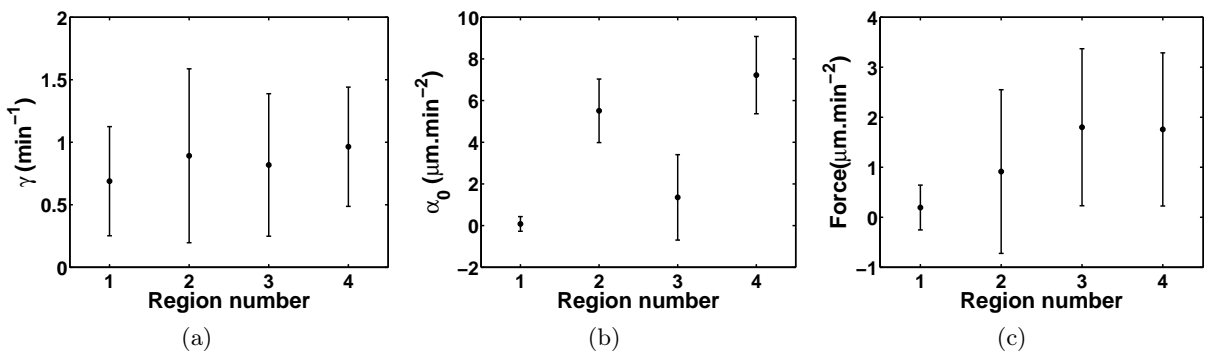


Figure 4.43: (a) Friction coefficient, (b) propelling force and (c) force in the gradient direction for each subpopulation. The friction coefficient does not depend on the subpopulation, but  $\alpha_0$  and  $F$  do.

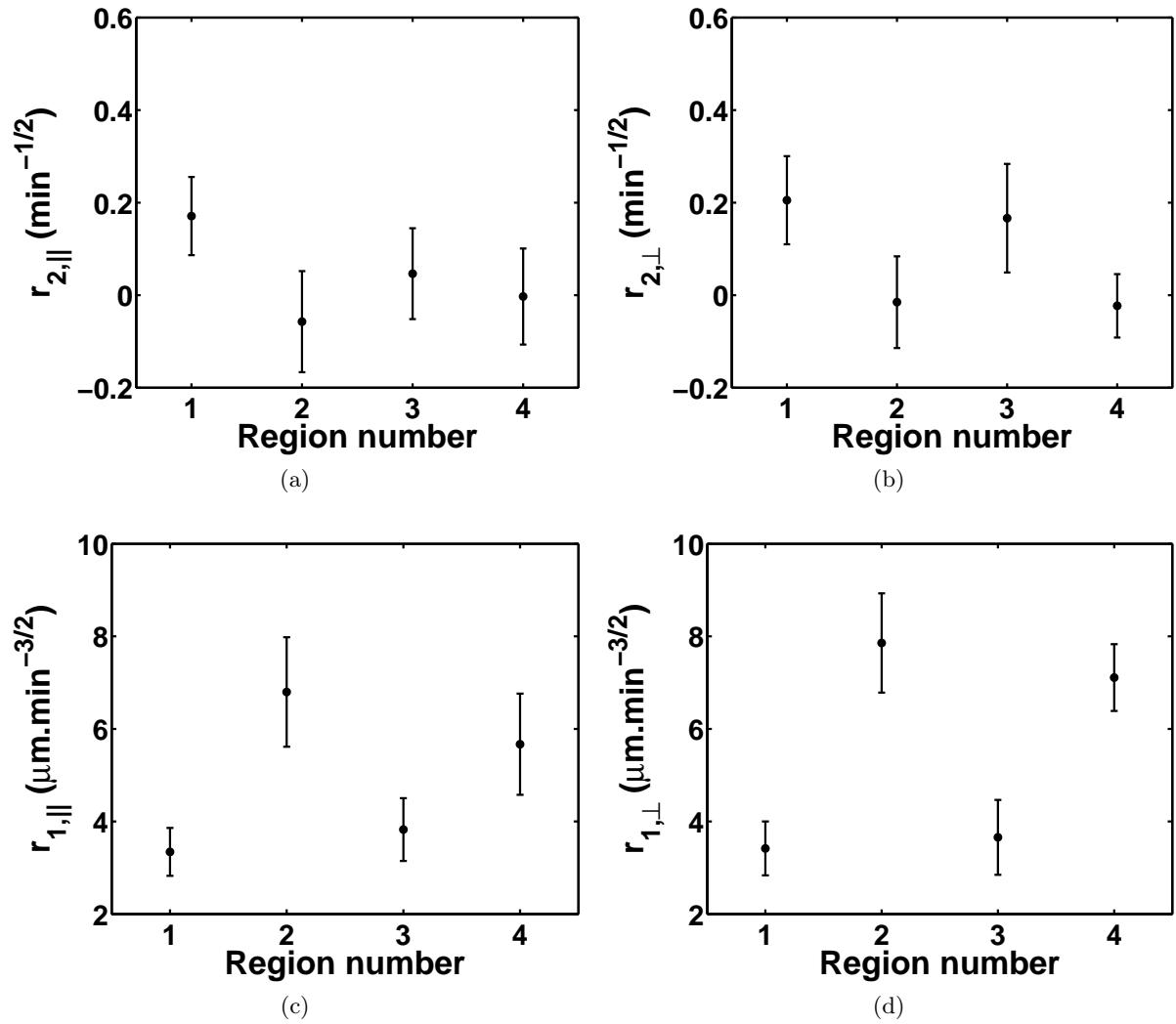


Figure 4.44: Slope of the stochastic term in the (a) parallel and (b) perpendicular directions. Offset of the stochastic terms in the (c) parallel and (d) perpendicular direction.

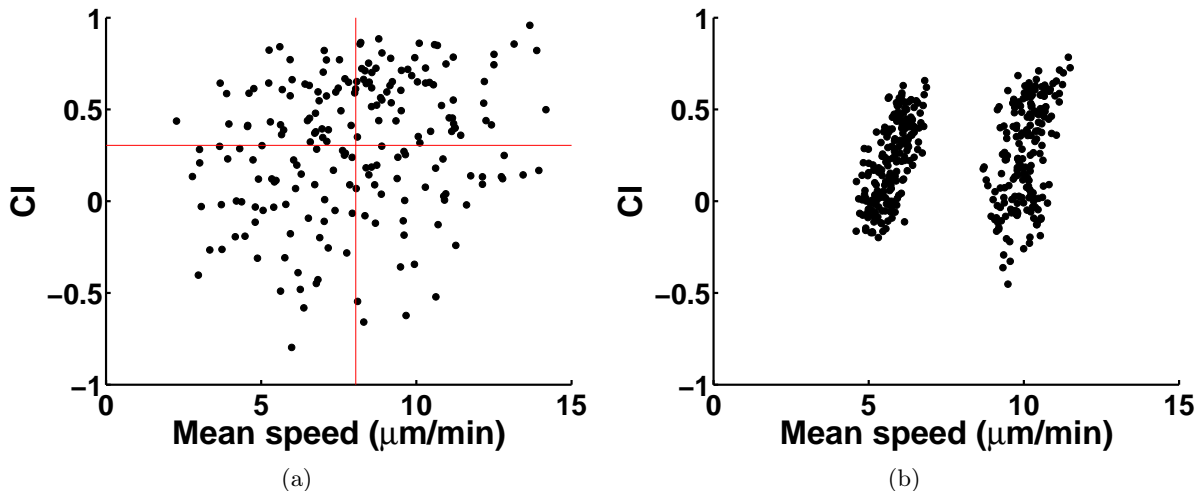


Figure 4.45: Cells in the (Mean speed, Chemotactic index) plane. Each point represent a cell. (a) Experimental data. (b) Results of the simulations for the four regions, combined into one plot. The experimental spread in the speed is not reproduced.

## 4.14 Summary of the stochastic modeling

In this section, we showed that we could describe the *average* chemotactic behavior using a Langevin equation, whose parameters depend on the SNR. This Langevin equation does not take into account the intrinsic cell-to-cell variability. On average, the population of cells acts if it were feeling a force in the gradient direction, and the amplitude of this force increases as the SNR increases. For WT cells, the damping term of the equation is, within its error bars, independent of the gradient. The Langevin equation also contains what we called a propelling force ( $\alpha_0$ ), whose dependence on the midpoint concentration or the SNR is not straightforward. This propelling force is positive for fast cells, and negative or zero for slow ones (figure 4.43b). More experiments would have to be carried out, in uniform backgrounds of concentrations and in gradients whose midpoint concentration would be varied, to help understand the evolution of  $\alpha_0$  with the external stimulus.

The analysis using a Langevin equation proved to be useful in characterizing the motion of mutants. In our work, we used SCAR/PIR null mutants, who were supposedly defective in chemotaxis. In buffer or under weak gradients (SNR smaller than 0.2) the apparent friction coefficient is greater for SCAR/PIR mutants than for WT cells. This shows that the damping coefficient reflects a biological property (it is different in WT and SCAR cells), which can be influenced by the external conditions (the friction coefficient for SCAR/PIR cells decreases with the SNR). The force experienced by the WT and SCAR cells is similar under similar conditions, as is the value of  $\alpha_0$ . The deterministic part of the Langevin equation is therefore the same for both the WT and the SCAR population, as soon as the SNR is bigger than 0.2. What explains the difference in cell motion between WT cells and SCAR/PIR null mutants is the stochastic component of the Langevin equation. In particular, the noise component parallel to cell motion is systematically smaller for the SCAR/PIR mutants than for the WT cells. This can be related to the original observation of Blagg et al. [11] that the SCAR/PIR

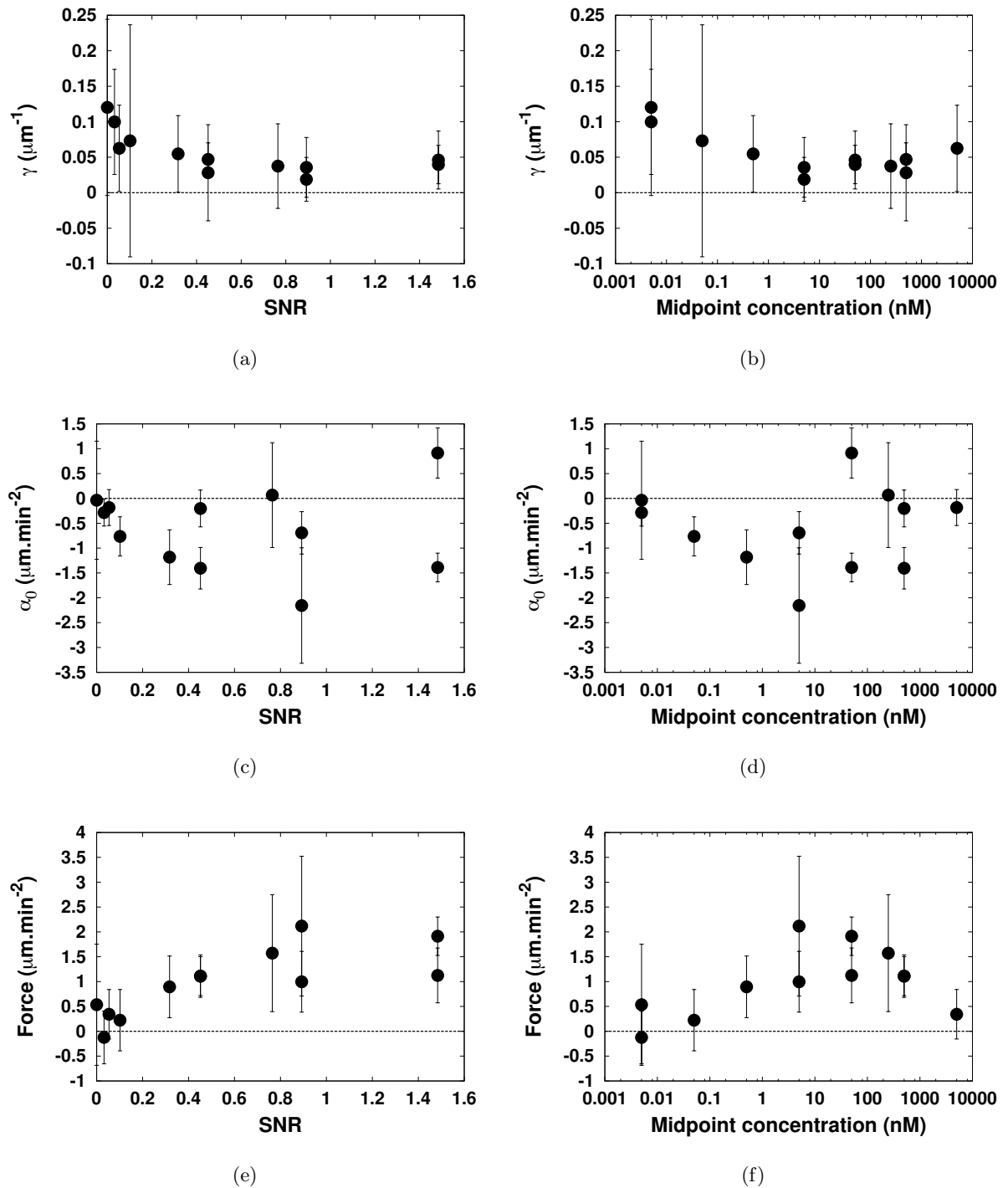


Figure 4.46: Evolution of the deterministic parameters of the Langevin equation for the SCAR/PIR mutants. (a), (b) Evolution of the friction coefficient with the SNR and the midpoint concentration. The friction coefficient decreases with the SNR. This is in contrast with the WT cells, for which the friction coefficient was independent of the external condition. (c), (d) Evolution of  $\alpha_0$ . As for the WT cells,  $\alpha_0$  is negative in most of the experiments. No clear trend can be observed from our data, whether as a function of the SNR or the midpoint concentration. (e), (f) Evolution of the force. As for the WT cells, the force increases with the SNR.

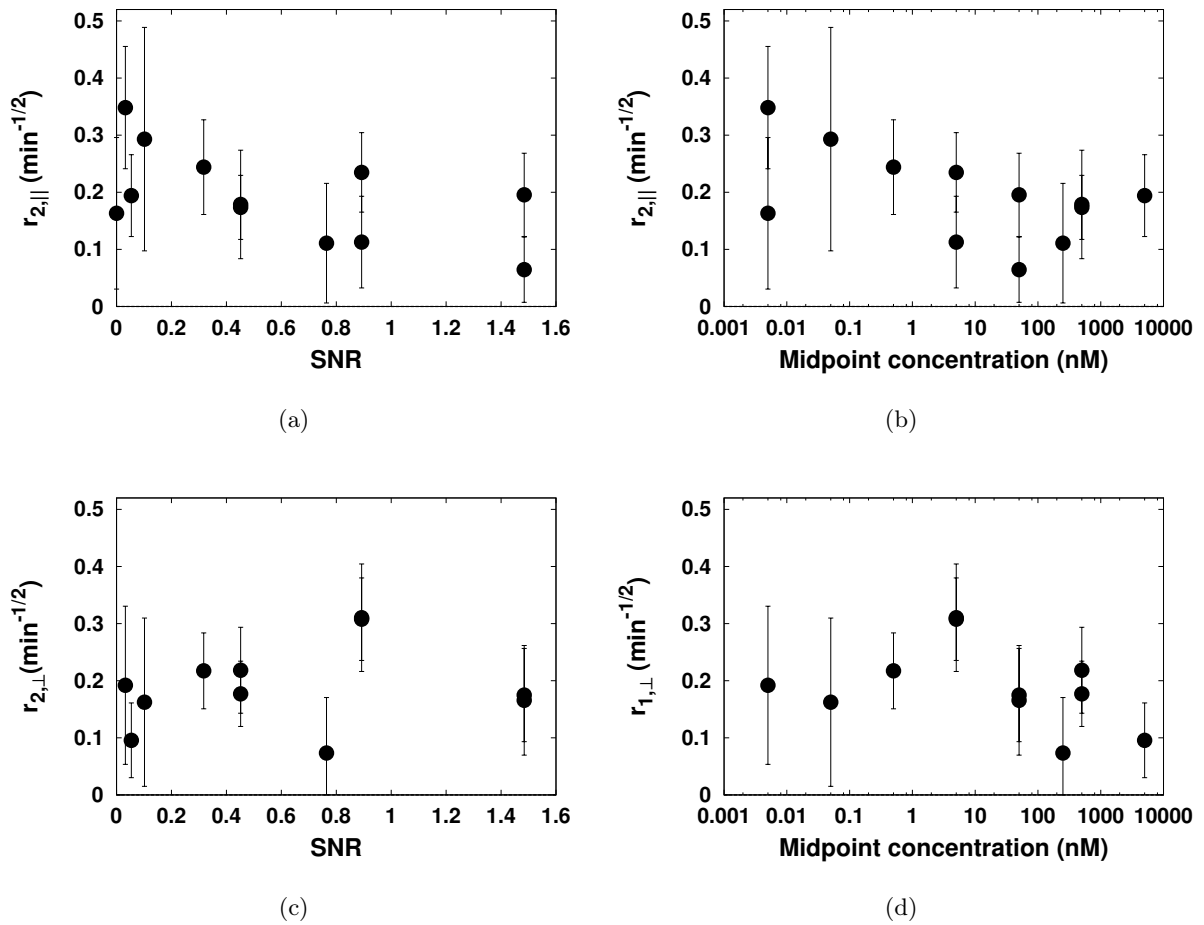


Figure 4.47: Analysis of the SCAR/PIR mutants. Slopes of the stochastic terms in the (a), (b) parallel and (c), (d) perpendicular directions. The slope of the noise in the perpendicular direction  $r_{2,\perp}$  is not significantly influenced by the external conditions. On the contrary, the slope of the noise in the parallel direction  $r_{2,||}$  decreases with the SNR.

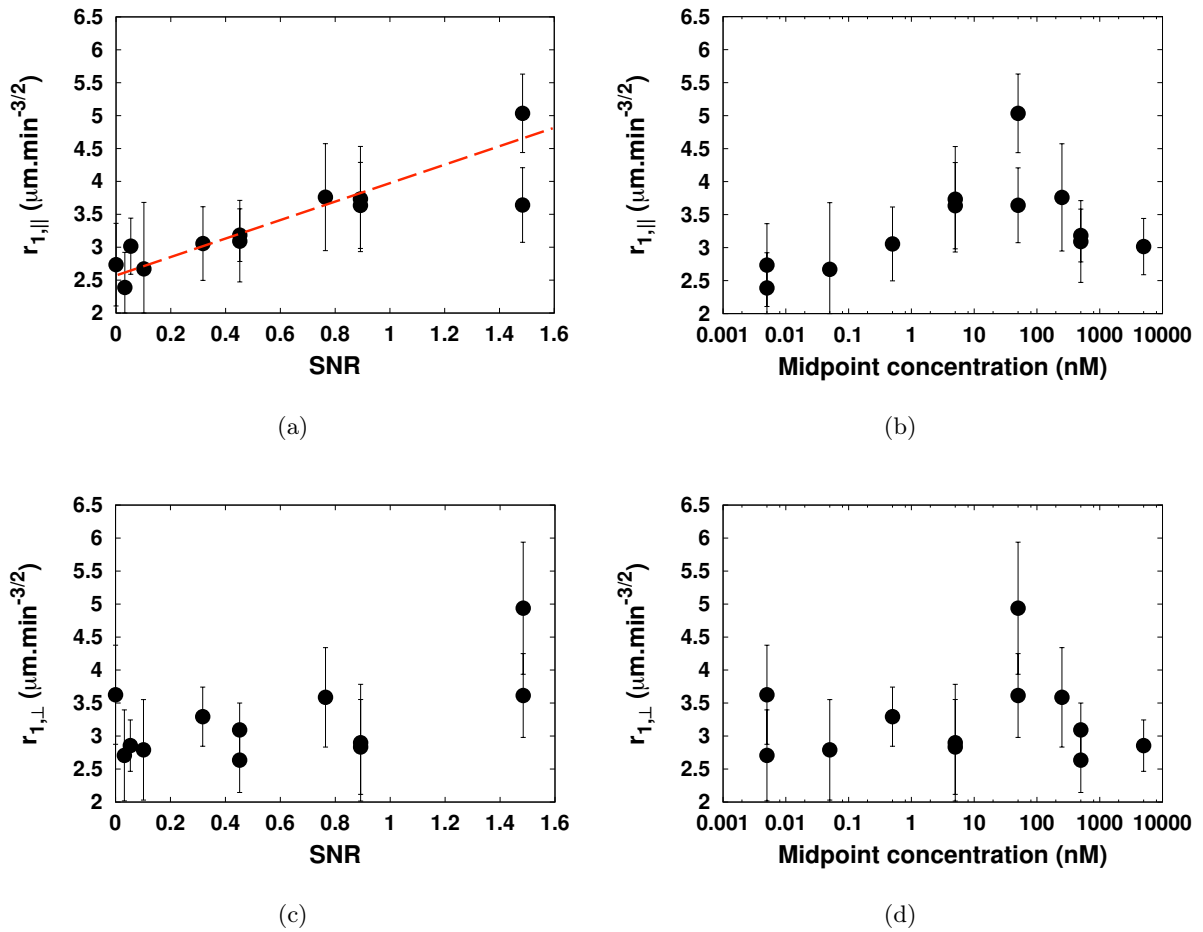


Figure 4.48: Analysis of the SCAR/PIR mutants. Offsets of the stochastic terms in the (a), (b) parallel and (c), (d) perpendicular directions. The SNR has an influence on the offset of the noise in the parallel direction,  $r_{1,\parallel}$ : the value of  $r_{1,\parallel}$  increases with increasing SNR (the line in (a) is there to guide the eye). No definitive conclusion can be drawn for the offset of the noise in the perpendicular direction  $r_{1,\perp}$ .



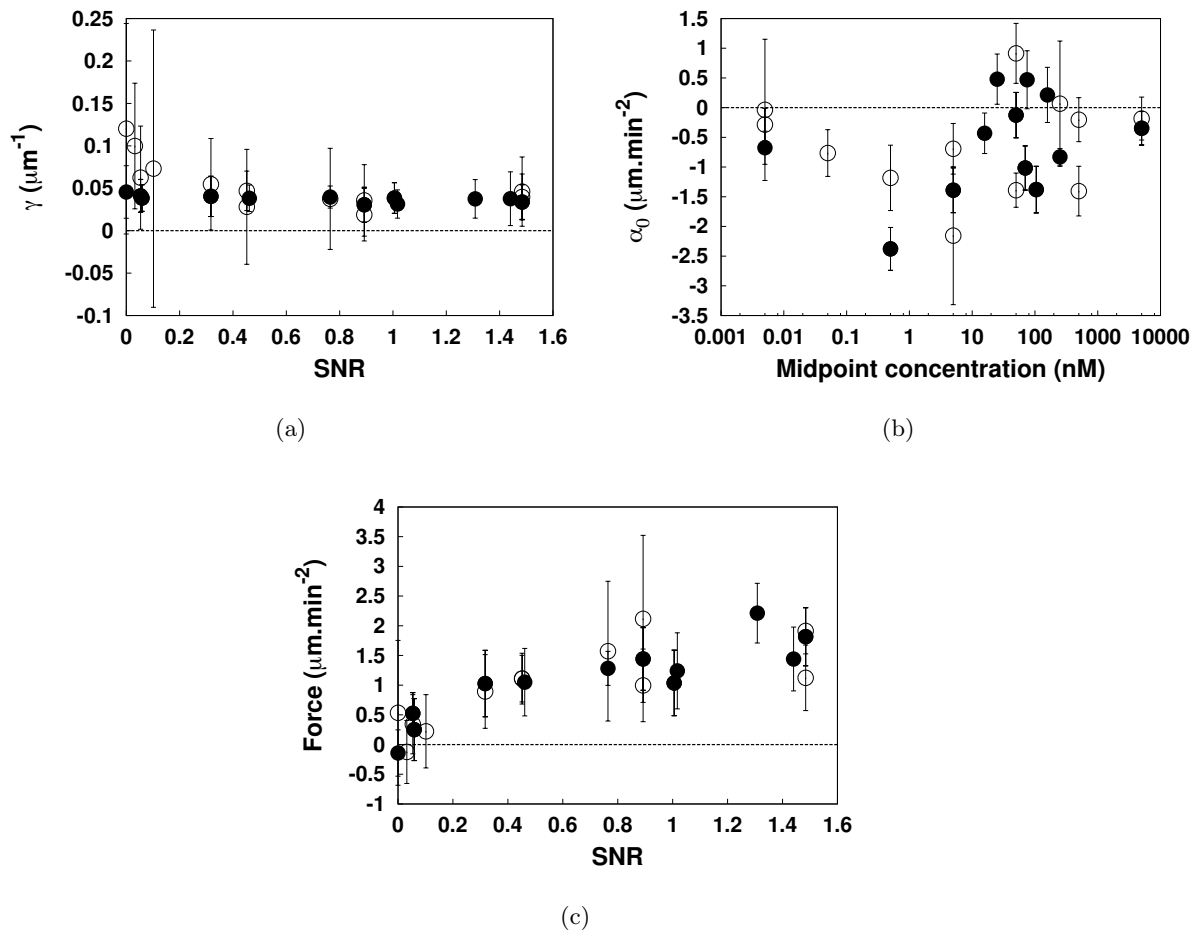


Figure 4.49: In all graphs, the filled circles show the parameters of the Langevin equation for the WT cells, while the empty circles represent the SCAR mutants. The friction coefficient (a) is higher for SCAR mutants than for WT cells at low values of the SNR (<0.2). Above, the wild-type values are recovered. We see on (b) and (c) that  $\alpha_0$  and  $F$  for both cell types fall on the same curve. At high SNR values, the deterministic part of the Langevin equation is therefore similar for both cell types.

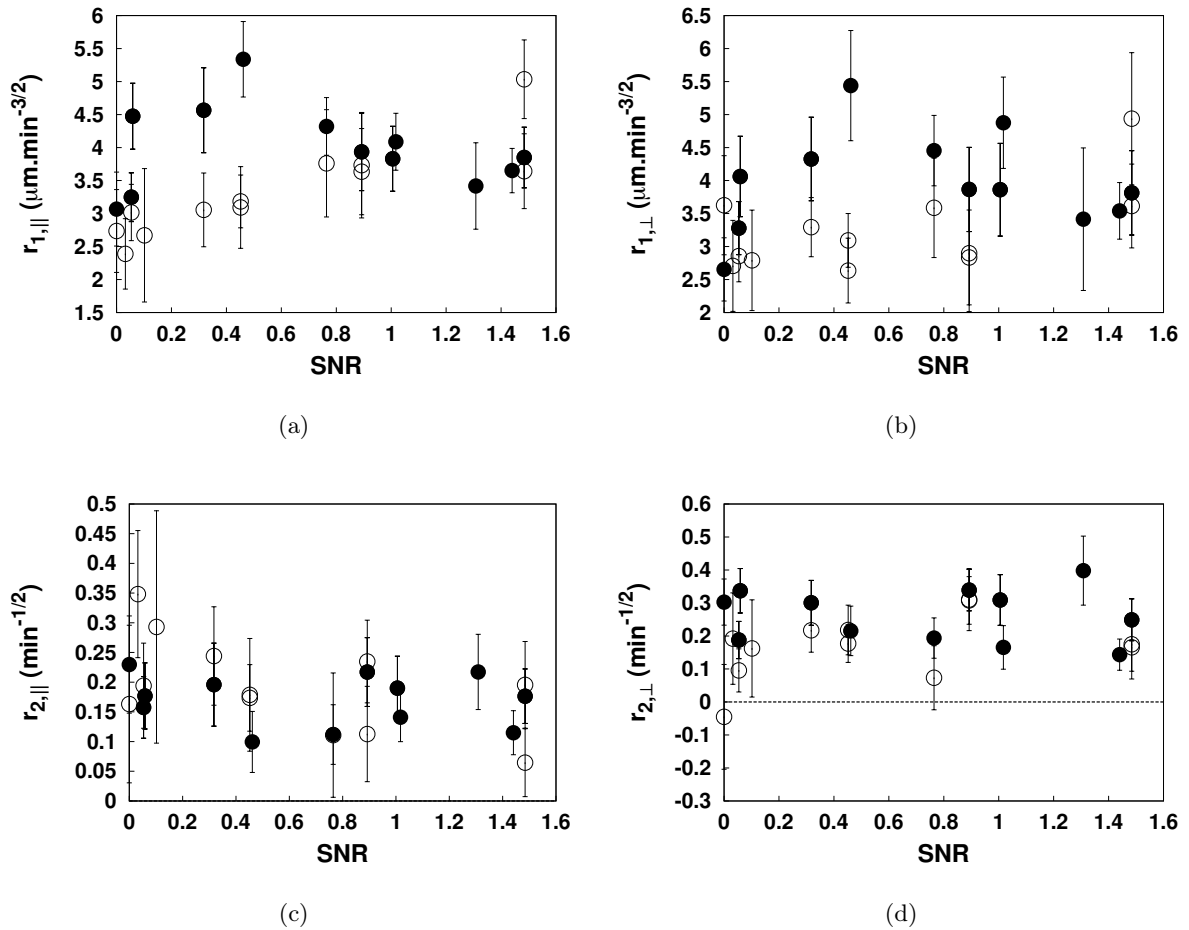


Figure 4.50: In all graphs, the filled circles show the parameters of the Langevin equation for the WT cells, while the empty circles represent the SCAR mutants. All experiments were taken into account. (a), (b) The noise offsets in both the parallel and the perpendicular directions are lower for the SCAR mutants. (c) The slope of the noise in the parallel direction decreases with the SNR for the SCAR mutants and reaches the WT value for a  $\text{SNR} \sim 1$ . (d) The slope of the noise in the perpendicular direction is similar for SCAR and WT cells.

mutants initiate fewer protrusions during chemotaxis than the WT cells.

In the future, it would be interesting to use mutants known to be defective in their basal motility (for example, cells overexpressing PTEN), or in their chemotactic behavior (such as PI3K/PTEN null mutants), and reproduce the Langevin analysis on them. We would then be able to see how the different parameters of the Langevin equation change depending on the mutants. It might very well be that similar phenotypes (*i.e.* similar values of the average speed  $\bar{v}$  and the chemotactic index) are reproduced by different combinations of parameters of the Langevin equation, showing different modes of cell motion.

# Conclusions and outlook

Chemotaxis of *D. discoideum* has been studied for over 60 years [13]. The first stage of chemotaxis, directional sensing, has been attracting considerable experimental and theoretical interest. We performed quantitative experiments at the single-cell level to test the existing models of directional sensing. Our experimental results can only be reconciled with the complex and detailed model of Meier-Schellersheim et al. [72]. It would be worth trying to reduce this model to a simpler one, using for example network analysis tools. Moreover, the model assumes the existence of several biochemical components, which would need to be identified. Our experiments also underlined the importance of cellular individuality, by showing that at a given gradient, not all cells would show a  $\text{PH}_{\text{CRAC}} - \text{GFP}$  translocation. One open question is then related to the sensitization of the gradient sensing process: if a cell does not respond to a given gradient, will it respond if stimulated repeatedly? In other words, is there a memory in the directional sensing process? Single-cell experiments as performed in chapter 3 of this thesis would probably take too long if one would like to do statistics on a large number of cells. One way to apply gradients rapidly and monitor the intracellular dynamics of many cells at the same time would be to use the gradient mixer described in chapter 4, where buffer would be introduced into one inlet and caged cAMP into the other inlet. Uncaging the cAMP would then lead to a rapid stimulation of all cells in the microfluidic channel with different gradients, depending on each cell's position. Alternatively, one could also use simple, straight microfluidic channels as the ones used in chapter 3, through which caged cAMP would be flown. Uncaging on a triangular region as wide as the channel would create a gradient of cAMP, whose amplitude could be changed by varying the shape of the triangle [10]. As stochasticity appears to be an increasingly important aspect of biological processes, performing such quantitative experiments at the limit of detection would be of great interest in unraveling the mechanisms of chemotaxis. These studies could be combined with the use of mutants overexpressing or underexpressing biochemical components of the chemotactic pathway. The component limiting the detection of low concentrations of cAMP could thus be identified.

The chemotactic index of *D. discoideum* in gradients of cAMP has been quantitatively studied by different groups, using various methods to generate gradients, from pipettes to diffusion chambers and microfluidics. We measured the chemotactic index of *D. discoideum* migrating in a microfluidic channel where stable, linear gradients of cAMP were produced. If plotted as a function of the gradient of cAMP, no systematic relation between the different data sets is observed. Based on work by Ueda and Shibata [119], we calculated the signal to noise ratio (SNR) at the level of the G-protein for each cell, at each position in the microfluidic channel. We also measured the chemotactic index of all cells at all positions of their tracks. When plotted as a function of the SNR, the chemotactic index of our experiments as well as experiments published in the literature superpose to one single curve. Several questions can be raised based on this result. First, it would be interesting to test the formula for the SNR

---

further. In particular, the SNR depends on the total number of cAR1 receptors expressed by the cells, and on the total number of G-proteins. By monitoring the chemotaxis of mutants overexpressing (or underexpressing) cAR1 or the G-protein, and plotting their chemotactic index as a function of the SNR, we would have a direct experimental verification of the formula for the SNR. Second, the formula for the SNR takes into account only two reactions, and assumes that the major loss of information occurs at the level of the receptor binding and G-protein dissociation. If this is the case, the asymmetric activation and translocation of intracellular markers of directional sensing should be strongly correlated with the SNR. This could be verified by simultaneously tracking the chemotactic motion of mutants expressing a GFP-tagged marker of directional sensing (PH-domain, Ras-binding domain), and monitoring their intracellular fluorescence intensity. It would also be important to monitor the intracellular fluorescence of cells treated with Latrunculin A, to ensure that the amount of translocation seen is not influenced by actin polymerization. In these latter experiments however, the use of microfluidics to create a gradient would be problematic. Indeed, Latrunculin A treated cells attach less well to surfaces than non-treated cells, and get therefore easily washed away by a flow.

Chemotactic motion has been traditionally quantified using time-averaged quantities, such as the average velocity in the gradient direction or the chemotactic index. Yet, these average quantities can only convey limited information about cell motility – all fluctuations are by definition averaged out. To go beyond this traditional description of cell motion, and describe the fluctuations inherent in cell motility, we quantified cellular chemotactic motion based on a Langevin equation for two different cell lines and in different gradients. One important result of our analysis was to determine which part of the Langevin equation was modified under these different experimental conditions. This analysis would prove particularly useful when the motion of a mutant defective in chemotaxis is monitored, and could be used as a tool to quantify cell motion. Moreover, using mutants would also help relating the parameters of the Langevin equation to biological quantities. For the time being, the analysis based on the Langevin equation has no predictive power, and is purely descriptive. The long-term goal of research on chemotaxis would be to know and understand enough of the chemotactic pathways to be able to predict what the Langevin equation describing cell motion is, based on the cell genotype.

# Appendix A

## Stochastic chemical kinetics equation and signal to noise ratio

In this Appendix, we first consider a cell in a uniform concentration of chemoattractant  $C$ . We show that the number of bound receptors follows a Poisson distribution, as observed experimentally by Ueda et al. [118], and then derive formula 4.24, giving the the signal to noise ratio (SNR) at the receptor level. Then, following Ueda and Shibata [119], we consider a cell exposed to a gradient of chemoattractant and derive the formula of the SNR at the second messenger level.

### A.1 The number of bound receptors follows a Poisson distribution

Receptor binding is described by the chemical equation:



where  $C$  is the ligand,  $R$  is a free receptor,  $R^*$  is an occupied receptor, and  $R + R^* = R_0$ . The evolution of  $R^*$  with time is given by:

$$\frac{dR^*}{dt} = k_1 C R_0 - (k_1 C + k_{-1}) R \quad (\text{A.2})$$

and at equilibrium, the number of occupied receptors is:

$$R^* = R_0 \frac{C}{C + K_d}, \quad (\text{A.3})$$

where we have defined  $K_d = k_{-1}/k_1$ . The above equation is deterministic. Let us now consider reaction binding as a stochastic process, and write down the probability  $P(n, t)$  of having  $n$  bound receptors at time  $t$ . This probability obeys the so-called Master equation (see [123]), which in our case is given by:

$$\frac{\partial P}{\partial t}(n, t) = k_1 C R_0 [P(n-1, t) - P(n, t)] + (k_{-1} + k_1 C) [(n+1)P(n+1, t) - nP(n, t)]. \quad (\text{A.4})$$

To obtain this equation, we write down the probability  $P(n, t + dt)$ . There are three ways of obtaining  $n$  occupied receptors at time  $t + dt$ :

## A.2. Perturbation of the steady state

---

- $n - 1$  receptors are occupied at time  $t$ , and binding of a receptor gives a contribution  $k_1 C R_0 dt$  to  $P(n, t + dt)$ ,
- or there are  $n + 1$  occupied receptors at time  $t$ , and unbinding from one of them gives a contribution  $(k_1 C + k_{-1})(n + 1)dt$ ,
- or there are already  $n$  occupied receptors at time  $t$ , and no reaction occurs in the time interval  $dt$ , which happens with probability  $P(n, t) [1 - k_1 C R_0 dt - (k_1 C + k_{-1})dt]$ . Inside the brackets, we have written the total probability (equal to 1) minus the probability that one of the reactions take place.

Summing all these contributions and taking the limit  $dt \rightarrow 0$ , we obtain the Master equation. At steady state, we have  $P(n, t) = P(n)$  and  $\frac{\partial P}{\partial t}(n, t) = 0$ . The above partial differential equation then reduces to a recurrence relation:

$$P(n + 1) = \frac{n}{n + 1} P(n) + \frac{k_1 C R_0}{(n + 1)(k_{-1} + k_1 C)} [P(n) - P(n - 1)]. \quad (\text{A.5})$$

This recurrence relation leads to the following relationship between  $P(n)$  and  $P(0)$ :

$$P(n) = \frac{1}{n!} \left( \frac{k_1 C R_0}{k_{-1} + k_1 C} \right)^n P(0) \quad (\text{A.6})$$

with  $P(-1) = 0$ . Because the probability should be normalized to 1, we have:

$$\sum_{n=0}^{\infty} \frac{1}{n!} \left( \frac{k_1 C R_0}{k_{-1} + k_1 C} \right)^n P(0) = 1 \quad (\text{A.7})$$

which leads to:

$$P(0) = \exp \left[ -\frac{k_1 C R_0}{k_{-1} + k_1 C} \right] \quad \text{and} \quad P(n) = \exp \left[ -\frac{k_1 C R_0}{k_{-1} + k_1 C} \right] \frac{1}{n!} \left( \frac{k_1 C R_0}{k_{-1} + k_1 C} \right)^n, \quad (\text{A.8})$$

showing that the number of bound receptors follows a Poisson distribution. The average number of bound receptors is  $\frac{k_1 C R_0}{k_{-1} + k_1 C}$ , which is also what was found above when we were considering the deterministic chemical rate equation. As an aside, now that we have the Master equation, we can multiply both of its sides by  $n$ , and sum over all values of  $n$ . We then get an equation for the average value of occupied receptors  $\langle n \rangle$ :

$$\frac{d\langle n \rangle}{dt} = k_1 C R_0 - (k_1 C + k_{-1}) \langle n \rangle. \quad (\text{A.9})$$

This is exactly the rate equation that we wrote at the beginning of the section.

## A.2 Perturbation of the steady state

Receptor binding consists of two reactions, a forward reaction (from  $R$  to  $R^*$ ) and a backward reaction (from  $R^*$  to  $R$ ). Each of these chemical reactions is a Poisson process. Because the two reactions are independent, the variance of the total increment of  $R^*$  is the sum of the variances associated to each of these reactions. For the forward reaction, the associated

variance during time  $\Delta t$  is  $k_1 C R \Delta t$ , and for the backward reaction it is  $k_{-1} C R^* \Delta t$ . At time scales much bigger than the time scale of production of molecules, and when the total number of molecules is large, we can approximate the Poisson process by a Gaussian process (see e.g. Gillespie [40]). The deterministic chemical rate equation can then be transformed into a chemical Langevin equation [23]:

$$\frac{dR^*}{dt} = k_1 C R - k_{-1} C R^* + \eta(t) \quad (\text{A.10})$$

where  $\eta(t)$  is Gaussian white noise with mean  $\langle \eta(t) \rangle = 0$  and autocorrelation

$$\langle \eta(t) \eta(t') \rangle = (k_1 C R + k_{-1} C R^*) \delta(t - t'). \quad (\text{A.11})$$

Substituting the steady-state values of  $R$  and  $R^*$  in this equation, we get:

$$\langle \eta(t) \eta(t') \rangle = \frac{2k_{-1} C}{C + K_d} R_0 \delta(t - t'). \quad (\text{A.12})$$

We now linearize the chemical Langevin equation about the steady state of the concentrations, denoted by  $R_{\text{st}}$  and  $R_{\text{st}}^*$ . We write  $R = R_{\text{st}} + \delta R$  and  $R^* = R_{\text{st}}^* + \delta R^*$ . Because we always have  $R + R^* = R_0$ , we need to have  $\delta R = -\delta R^*$ . The Langevin equation describing the fluctuations  $\delta R^*$  about the steady state  $R_{\text{st}}^*$  is therefore given by:

$$\frac{d\delta R^*}{dt} = -(k_1 C + k_{-1}) \delta R^* + \eta(t). \quad (\text{A.13})$$

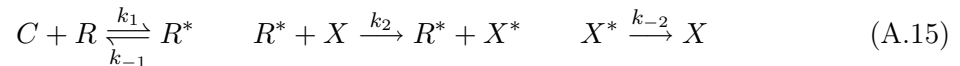
Note that we haven't assumed any fluctuation of the outside concentration of chemoattractant  $C$ . The fluctuations that we write just reflect the stochastic nature of the chemical reaction. The noise intensity  $\langle (\delta R^*)^2 \rangle$  is then given by (see for example [136]):

$$\langle (\delta R^*)^2 \rangle = \frac{\langle \eta(t)^2 \rangle}{2(k_1 C + k_{-1})} = \frac{K_d}{C + K_d} R_{\text{st}}^*, \quad (\text{A.14})$$

which is the result we are using in equation 4.24.

### A.3 Signal to noise ratio in a reaction cascade

Following Ueda and Shibata [119], we consider the binding of cAMP to the cAMP receptor, which leads to the dissociation of the G protein. The chemical reactions at play can be written:



where as before  $C$  is the ligand, in our case cAMP,  $R$  and  $R^*$  represent unbound and bound receptors respectively ( $R + R^* = R_{\text{tot}}$ ), and  $X$  and  $X^*$  represent the G protein in its unactivated (*i.e.* associated) and activated (*i.e.* dissociated) state, respectively ( $X + X^* = X_{\text{tot}}$ ). The gain of a chemical reaction quantifies the change in the output of the reaction as its input is changed. In our two reactions, the gains are given by:

$$g_R = \frac{\partial \log R^*}{\partial \log L} = \frac{K_R}{K_R + C} \quad g_X = \frac{\partial \log X^*}{\partial \log R^*} = \frac{K_X}{K_X + R^*} \quad (\text{A.16})$$



where we have called  $K_R = k_{-1}/k_1$  and  $K_X = k_{-2}/k_2$ . First consider a uniform concentration of cAMP. The average number of occupied receptors  $R^*$  and the average number of dissociated proteins  $X^*$  are then given by

$$R^* = R_{tot} \frac{C}{C + K_R} \quad X^* = X_{tot} \frac{R^*}{R^* + K_X} \quad (\text{A.17})$$

Shibata and Fujimoto showed that the noise in the first reaction could be expressed as:

$$\sigma_R^2 = g_R R^*. \quad (\text{A.18})$$

For the second reaction, there are two contributions to the stochastic fluctuations, one coming from the fluctuations in  $R^*$ , termed the extrinsic noise, and the other coming from the stochasticity of the G protein dissociation reaction. The noise can then be expressed as:

$$\sigma_X^2 = \underbrace{g_X X^*}_{\text{intrinsic noise}} + \underbrace{g_X^2 \frac{\tau_R}{\tau_R + \tau_X} \sigma_R^2 \left( \frac{X^*}{R^*} \right)^2}_{\text{extrinsic noise}} \quad (\text{A.19})$$

In the case where the concentration profile is not uniform, all these quantities can be defined *locally*. At a given position  $y$ , the concentration of chemottractant is  $C(y)$ , and the local *densities* of occupied receptors  $R^*(y)$  and of active second messenger  $X^*(y)$  are given by:

$$R^*(y) = \frac{R_{tot}}{L} \frac{C(y)}{C(y) + K_R} \quad X^*(y) = \frac{X_{tot}}{L} \frac{R^*}{R^* + K_X/L} \quad (\text{A.20})$$

where  $L$  is the length of the cell<sup>1</sup>. The gains of the reactions can be locally expressed as:

$$g_R(y) = \frac{K_R}{K_R + C(y)} \quad g_X(y) = \frac{K_X}{K_X + R^*(y)L} \quad (\text{A.21})$$

and the time constants are:

$$\tau_R(y) = \frac{1}{k_1 C(y) + k_{-1}} \quad \tau_X(y) = \frac{1}{k_2 R^*(y)L + k_{-2}}. \quad (\text{A.22})$$

Locally, the amplitude of the noise of the receptor-binding reaction is then:

$$\sigma_R^2(y) = g_R(y) R^*(y) \quad (\text{A.23})$$

and the amplitude of the noise of the second reaction is:

$$\sigma_X^2(y) = g_X(y) X^*(y) + g_X(y)^2 \frac{\tau_R(y)}{\tau_R(y) + \tau_X(y)} \sigma_R^2(y)^2 \left( \frac{X^*(y)}{R^*(y)} \right)^2 \quad (\text{A.24})$$

We now have all the ingredients needed to define the signal to noise ratio at the G-protein level. We assume, as in [119], that the important signal is the difference  $\Delta X^*$  in number of activated G-protein between front and back of the cell:

$$\Delta X^* = \int_0^{L/2} X^*(y) dy - \int_{-L/2}^0 X^*(y) dy \quad (\text{A.25})$$

---

<sup>1</sup>For simplicity, we consider a 1D cell.

If we assume that there is no correlation between the chemical processes occurring at different locations, the total noise is given by the sum of the contributions of all local noise terms:

$$\sigma_{\Delta X^*}^2 = \int_{-L/2}^{L/2} \sigma_X^2(y) dy \quad (\text{A.26})$$

which can be integrated numerically. The signal to noise ratio is then readily calculated:

$$\text{SNR} = \frac{|\Delta X^*|}{\sigma_{\Delta X^*}} \quad (\text{A.27})$$

# Bibliography

- [1] S. R. Adams and R. Y. Tsien. Controlling cell chemistry with caged compounds. *Annual Review of Physiology*, 55(1), 1993.
- [2] D. Angeli, J. Ferrell, and E. Sontag. Detection of multistability, bifurcations, and hysteresis in a large class of biological positive-feed back systems. *Proceedings of the National Academy of Sciences of the United States of America*, 101(7):1822–1827, 2004.
- [3] R. Aris. On the dispersion of a solute in a fluid flowing through a tube. *Proc R Soc Lon Ser-A*, 235(1200):67–77, 1956.
- [4] A. Bae, private communication.
- [5] A. J. Bae, C. Beta, and E. Bodenschatz. Rapid switching of chemical signals in microfluidic devices. *Lab on a Chip*, 9(21):3059–3065, 2009.
- [6] A. Bagorda and C. A. Parent. Eukaryotic chemotaxis at a glance. *Journal of Cell Science*, 121(16):2621–2624, 2008.
- [7] A.-L. Barabasi and Z. Oltvai. Network biology: understanding the cell’s functional organization. *Nat Rev Genet*, 5(2):101–113, 2004.
- [8] C. Beta, G. Amselem, and E. Bodenschatz. A bistable mechanism for directional sensing. *New Journal of Physics*, 10(8):083015 (20pp), 2008.
- [9] C. Beta, T. Frohlich, H. U. Bodeker, and E. Bodenschatz. Chemotaxis in microfluidic devices—a study of flow effects. *Lab on a Chip*, 8(7):1087–1096, 2008.
- [10] C. Beta, D. Wyatt, W.-J. Rappel, and E. Bodenschatz. Flow photolysis for spatiotemporal stimulation of single cells. *Analytical Chemistry*, 79(10):3940–3944, 2007.
- [11] S. Blagg, M. Stewart, C. Sambles, and R. Insall. PIR121 regulates pseudopod dynamics and SCAR activity in *Dictyostelium*. *Current Biology*, 13(17):1480–1487, 2003.
- [12] H. U. Bödeker, C. Beta, T. Frank, and E. Bodenschatz. Quantitative analysis of random ameboid motion. *EPL (Europhysics Letters)*, 90(2):28005, 2010.
- [13] J. Bonner. Evidence for the formation of cell aggregates by chemotaxis in the development of the slime mold *Dictyostelium discoideum*. *J. exp. Zool*, 1947.
- [14] J. Bonner, A note on the number of cells in a slug of *Dictyostelium discoideum*. 2001, <http://dictybase.org/Bonner%20paper.pdf>.

- [15] L. Bosgraaf, I. Keizer-Gunnink, and P. J. M. V. Haastert. PI3-kinase signaling contributes to orientation in shallow gradients and enhances speed in steep chemoattractant gradients. *Journal of Cell Science*, 121(21):3589–3597, 2008.
- [16] L. Bosgraaf, H. Russcher, J. L. Smith, D. Wessels, D. R. Soll, and P. J. M. Van Haastert. A novel cGMP signalling pathway mediating myosin phosphorylation and chemotaxis in *Dictyostelium*. *EMBO J*, 21(17):4560–4570, 2002.
- [17] M. B. Cannell, P. Kilmartin, M. Jacobs, S. Valiavalappil, J. Travas-Sejdic, C. Soeller, S. K. Hiroshi Masuhara, and F. Tokunaga, *Chapter 14 Nanoscale fluid motion via molecular pores and polymer actuators*, volume 3, 207–224. Elsevier, 2007.
- [18] M. J. Caterina, D. Hereld, and P. N. Devreotes. Occupancy of the *Dictyostelium* cAMP Receptor, cAR1, Induces a Reduction in Affinity Which Depends upon COOH-terminal Serine Residues. *Journal of Biological Chemistry*, 270(9):4418–4423, 1995.
- [19] L. Chen, M. Iijima, M. Tang, M. A. Landree, Y. E. Huang, Y. Xiong, P. A. Iglesias, and P. N. Devreotes. PLA2 and PI3K/PTEN pathways act in parallel to mediate chemotaxis. *Developmental Cell*, 12(4):603–614, 2007.
- [20] L. Chen, C. Janetopoulos, Y. E. Huang, M. Iijima, J. Borleis, and P. N. Devreotes. Two phases of actin polymerization display different dependencies on PI(3,4,5)P3 accumulation and have unique roles during chemotaxis. *Mol. Biol. Cell*, 14(12):5028–5037, 2003.
- [21] J. Condeelis, R. H. Singer, and J. E. Segall. The great escape: When cancer cells hijack the genes for chemotaxis and motility. *Annual Review of Cell and Developmental Biology*, 21(1):695–718, 2005.
- [22] J. Crocker and D. Grier. Methods of digital video microscopy for colloidal studies. *Journal of Colloid and Interface Science*, 179(1):298–310, 1996.
- [23] P. Detwiler, S. Ramanathan, A. Sengupta, and B. Shraiman. Engineering aspects of enzymatic signal transduction: Photoreceptors in the retina. *Biophysical Journal*, 79(6):2801–2817, 2000.
- [24] P. Devreotes and C. Janetopoulos. Eukaryotic chemotaxis: Distinctions between directional sensing and polarization. *J. Biol. Chem.*, 278(23):20445–20448, 2003.
- [25] D. Dormann, J.-Y. Kim, P. N. Devreotes, and C. J. Weijer. cAMP receptor affinity controls wave dynamics, geometry and morphogenesis in *Dictyostelium*. *Journal of Cell Science*, 114(13):2513–2523, 2001.
- [26] M. Dworkin and K. H. Keller. Solubility and diffusion coefficient of adenosine 3':5'-monophosphate. *Journal of Biological Chemistry*, 252(3):864–865, 1977.
- [27] A. Einstein. Über die von der molekularkinetischen Theorie der Wärme geforderte Bewegung von in ruhenden Flüssigkeit suspendierten Teilchen. *Annalen der Physik*, 17(8):549–560, 1905.
- [28] R. A. Firtel and C. Y. Chung. The molecular genetics of chemotaxis: sensing and responding to chemoattractant gradients. *Bioessays*, 22(7):603–615, 2000.

## BIBLIOGRAPHY

---

- [29] P. Fisher, W. Grant, U. Dohrmann, and K. Williams. Spontaneous turning behaviour by *Dictyostelium discoideum* slugs. *J Cell Sci*, 62(1):161–170, 1983.
- [30] P. Fisher, R. Merkl, and G. Gerisch. Quantitative analysis of cell motility and chemotaxis in *Dictyostelium discoideum* by using an image processing system and a novel chemotaxis chamber providing stationary chemical gradients. *Journal of Cell Biology*, 108(3):973–984, 1989.
- [31] T. Förster. Zwischenmolekulare energiewanderung und fluoreszenz. *Ann. Phys*, 1948.
- [32] J. Franca-Koh and P. Devreotes. Moving forward: mechanisms of chemoattractant gradient sensing. *Physiology*, 2004.
- [33] R. Friedrich, S. Siegert, J. Peinke, S. Lück, and M. Siefert. Extracting model equations from experimental data. *Physics Letters A*, 2000.
- [34] D. Fuller, W. Chen, M. Adler, A. Groisman, H. Levine, W.-J. Rappel, and W. F. Loomis. External and internal constraints on eukaryotic chemotaxis. *Proceedings of the National Academy of Sciences*, 107(21):9656–9659, 2010.
- [35] S. Funamoto, R. Meili, S. Lee, L. Parry, and R. Firtel. Spatial and temporal regulation of 3-phosphoinositides by PI3-kinase and PTEN mediates chemotaxis. *Cell*, 109(5):611–623 PB –, 2002.
- [36] S. Funamoto, K. Milan, R. Meili, and R. A. Firtel. Role of phosphatidylinositol 3' kinase and a downstream pleckstrin homology domain-containing protein in controlling chemotaxis in *Dictyostelium*. *J. Cell Biol.*, 153(4):795–810, 2001.
- [37] R. Fürth. Die Brownsche Bewegung bei Berücksichtigung einer Persistenz der Bewegungsrichtung. Mit Anwendungen auf die Bewegung lebender Infusorien. *Zeitschrift für Physik A Hadrons and Nuclei*, 2(3):244–256, 1920.
- [38] M. H. Gail and C. W. Boone. The locomotion of mouse fibroblasts in tissue culture. *Biophys. J.*, 10(10):980–993, 1970.
- [39] A. Gamba, A. de Candia, S. D. Talia, A. Coniglio, F. Bussolino, and G. Serini. Diffusion-limited phase separation in eukaryotic chemotaxis. *Proceedings of the National Academy of Sciences*, 102(47):16927–16932, 2005.
- [40] D. T. Gillespie. The chemical Langevin equation. *The Journal of Chemical Physics*, 113(1):297–306, 2000.
- [41] S. Giovannardi, L. Lando, and A. Peres. Flash photolysis of caged compounds: Casting light on physiological processes. *News in Physiological Sciences*, 13(5):251–255, 1998.
- [42] J. Gruver, J. Wikswo, and C. Chung. 3'-phosphoinositides regulate the coordination of speed and accuracy during chemotaxis. *Biophysical Journal*, 95(8):4057–4067, 2008.
- [43] P. Herzmark, K. Campbell, F. Wang, K. Wong, H. El-Samad, A. Groisman, and H. R. Bourne. Bound attractant at the leading vs. the trailing edge determines chemotactic prowess. *P Natl Acad Sci Usa*, 104(33):13349–13354, 2007.

## BIBLIOGRAPHY

---

- [44] O. Hoeller and R. R. Kay. Chemotaxis in the absence of PIP3 gradients. *Current Biology*, 17(9):813–817, 2007.
- [45] B. Hu, D. Fuller, W. F. Loomis, H. Levine, and W.-J. Rappel. Phenomenological approach to eukaryotic chemotactic efficiency. *Physical Review E*, 81(3), 2010.
- [46] Y. Huang, M. Iijima, C. Parent, S. Funamoto, R. Firtel, and P. Devreotes. Receptor-mediated regulation of pi3ks confines pi(3,4,5)p3 to the leading edge of chemotaxing cells. *Mol. Biol. Cell*, 14(5):1913–1922, 2003.
- [47] P. Iglesias and A. Levchenko. Modeling the cell’s guidance system. *Sci. STKE*, 2002(148):re12, 2002.
- [48] M. Iijima and P. Devreotes. Tumor suppressor PTEN mediates sensing of chemoattractant gradients. *Cell*, 109(5):599–610, 2002.
- [49] M. Iijima, Y. E. Huang, H. R. Luo, F. Vazquez, and P. N. Devreotes. Novel mechanism of PTEN regulation by its phosphatidylinositol 4,5-bisphosphate binding motif is critical for chemotaxis. *Journal of Biological Chemistry*, 279(16):16606–16613, 2004.
- [50] H. Ishikawa-Ankerhold. *Functional organization of the actin system in Dictyostelium*. Ph.D. thesis, Technische Universität München and Max Planck Institute of Biochemistry, 2009.
- [51] C. Janetopoulos, T. Jin, and P. Devreotes. Receptor-mediated activation of heterotrimeric g-proteins in living cells. *Science*, 291(5512):2408–2411, 2001.
- [52] C. Janetopoulos, L. Ma, P. N. Devreotes, and P. A. Iglesias. Chemoattractant-induced phosphatidylinositol 3,4,5-trisphosphate accumulation is spatially amplified and adapts, independent of the actin cytoskeleton. *Proceedings of the National Academy of Sciences*, 101(24):8951–8956, 2004.
- [53] E. Jares-Erijman and T. Jovin. FRET imaging. *Nature biotechnology*, 2003.
- [54] N. L. Jeon, S. K. W. Dertinger, D. T. Chiu, I. S. Choi, A. D. Stroock, and G. M. Whitesides. Generation of solution and surface gradients using microfluidic systems. *Langmuir*, 16(22):8311–8316, 2000.
- [55] R. L. Johnson, C. L. Saxe, R. Gollop, A. R. Kimmel, and P. N. Devreotes. Identification and targeted gene disruption of cAR3, a cAMP receptor subtype expressed during multicellular stages of *Dictyostelium* development. *Genes & Development*, 7(2):273–282, 1993.
- [56] Z. Kam. Microscopic differential interference contrast image processing by line microscopic integration (LID) and deconvolution. *Bioimaging*, 6(4):166–176, 1998.
- [57] I. Keizer-Gunnink, A. Kortholt, and P. J. M. V. Haastert. Chemoattractants and chemorepellents act by inducing opposite polarity in phospholipase C and PI3-kinase signaling. *Journal of Cell Biology*, 177(4):579–585, 2007.
- [58] R. H. Kessin, *Dictyostelium - Evolution, Cell Biology and the Development of Multicellularity*. Developmental and Cell Biology Series, Cambridge University Press, 2001.

## BIBLIOGRAPHY

---

- [59] J. S. King and R. H. Insall. Chemotaxis: finding the way forward with *Dictyostelium*. *Trends Cell Biol*, 19(10):523–30, 2009.
- [60] D. Kleinhans, R. Friedrich, A. Nawroth, and J. Peinke. An iterative procedure for the estimation of drift and diffusion coefficients of Langevin processes. *Physics Letters A*, 346(1-3):42–46, 2005.
- [61] D. Kleinhans, R. Friedrich, M. Waechter, and J. Peinke. Markov properties in presence of measurement noise. *Physical Review E*, 76(4):041109, 2007.
- [62] P. E. Kloeden and E. Platen, *Numerical solution of stochastic differential equations*, volume 23. Springer-Verlag, Berlin ;New York, 1992.
- [63] V. Kölsch, P. G. Charest, and R. A. Firtel. The regulation of cell motility and chemotaxis by phospholipid signaling. *Journal of Cell Science*, 121(5):551–559, 2008.
- [64] A. Kortholt, J. S. King, I. Keizer-Gunnink, A. J. Harwood, and P. J. M. V. Haastert. Phospholipase C regulation of phosphatidylinositol 3,4,5-trisphosphate-mediated chemotaxis. *Molecular Biology of the Cell*, 18(12):4772–4779, 2007.
- [65] A. Kortholt and P. J. van Haastert. Highlighting the role of Ras and Rap during dictyostelium chemotaxis. *Cellular Signalling*, 20(8):1415 – 1422, 2008.
- [66] P. Langevin. Sur la théorie du mouvement brownien. *Comptes Rendus Hebdomadaires des Séances de l’Académie des Sciences*, 146:508–533, 1908.
- [67] A. Levchenko and P. A. Iglesias. Models of eukaryotic gradient sensing: Application to chemotaxis of amoebae and neutrophils. *Biophysical Journal*, 82(1):50–63, 2002.
- [68] H. Levine, D. A. Kessler, and W.-J. Rappel. Directional sensing in eukaryotic chemotaxis: A balanced inactivation model. *PNAS*, 103(26):9761–9766, 2006.
- [69] L. Li, S. F. Nørrelykke, and E. C. Cox. Persistent cell motion in the absence of external signals: A search strategy for eukaryotic cells. *PLoS ONE*, 3(5):e2093, 2008.
- [70] L. Ma, C. Janetopoulos, L. Yang, P. N. Devreotes, and P. A. Iglesias. Two complementary, local excitation, global inhibition mechanisms acting in parallel can explain the chemoattractant-induced regulation of PI(3,4,5)P3 response in *Dictyostelium* cells. *Biophysical Journal*, 87(6):3764–3774, 2004.
- [71] P. Martin and S. M. Parkhurst. Parallels between tissue repair and embryo morphogenesis. *Development*, 131(13):3021–3034, 2004.
- [72] M. Meier-Schellersheim, X. Xu, B. Angermann, E. J. Kunkel, T. Jin, and R. N. Germain. Key role of local regulation in chemosensing revealed by a new molecular interaction-based modeling method. *PLoS Computational Biology*, 2(7):e82–, 2006.
- [73] H. Meinhardt. Orientation of chemotactic cells and growth cones: models and mechanisms. *J Cell Sci*, 112(17):2867–2874, 1999.
- [74] A. Mikhailov. Foundations of synergetics i. distributed active systems. *Springer Series in Synergetics*, 1994.

- [75] Y. Mori, A. Jilkine, and L. Edelstein-Keshet. Wave-pinning and cell polarity from a bistable reaction-diffusion system. *Biophys. J.*, biophysj.107.120824, 2008.
- [76] S. Nadkarni. Protocols for fabrication of microfluidic devices. Technical report, Cornell University, 2004, [http://www.lfpn.ds.mpg.de/biophysics/documents/Nadkarni\\_microfluidics\\_protocol.pdf](http://www.lfpn.ds.mpg.de/biophysics/documents/Nadkarni_microfluidics_protocol.pdf).
- [77] A. Narang, K. Subramanian, and D. Lauffenburger. A mathematical model for chemoattractant gradient sensing based on receptor-regulated membrane phospholipid signaling dynamics. *Annals of Biomedical Engineering*, 29(8):677–691, 2001.
- [78] J. M. Nerbonne, S. Richard, J. Nargeot, and H. A. Lester. New photoactivatable cyclic nucleotides produce intracellular jumps in cyclic AMP and cyclic GMP concentrations. *Nature*, 310(5972):74–76, 1984.
- [79] C. A. Parent. Making all the right moves: chemotaxis in neutrophils and dictyostelium. *Current Opinion in Cell Biology*, 16(1):4–13, 2004.
- [80] C. A. Parent, B. J. Blacklock, W. M. Froehlich, D. B. Murphy, and P. N. Devreotes. G protein signaling events are activated at the leading edge of chemotactic cells. *Cell*, 95(1):81–91, 1998.
- [81] C. A. Parent and P. N. Devreotes. Molecular genetics of signal transduction in dictyostelium. *Annual Review of Biochemistry*, 65(1), 1996.
- [82] C. A. Parent and P. N. Devreotes. A cell’s sense of direction. *Science*, 284(5415):765–770, 1999.
- [83] M. Pluta. Nomarski’s DIC microscopy: a review. *Phase Contrast and Differential Interference Contrast Imaging Techniques and Applications*, 1846(1):10–25, 1994.
- [84] M. Postma and P. J. Haastert. Mathematics of experimentally generated chemoattractant gradients. 571, 2009.
- [85] M. Postma and P. J. M. V. Haastert. A diffusion-translocation model for gradient sensing by chemotactic cells. *Biophys. J.*, 81(3):1314–1323, 2001.
- [86] M. Postma, J. Roelofs, J. Goedhart, T. W. Gadella, A. J. Visser, and P. J. V. Haastert. Uniform camp stimulation of dictyostelium cells induces localized patches of signal transduction and pseudopodia. *Mol. Biol. Cell*, 14(12):5019–5027, 2003.
- [87] K. Przibram. Über die ungeordnete Bewegung niederer Tiere. *Pflügers Archiv European Journal of Physiology*, 153(8):401–405, 1913.
- [88] W.-J. Rappel and H. Levine. Receptor noise and directional sensing in eukaryotic chemotaxis. *Physical Review Letters*, 100(22):228101, 2008.
- [89] W.-J. Rappel and H. Levine. Receptor noise limitations on chemotactic sensing. *Proceedings of the National Academy of Sciences*, 105(49):19270–19275, 2008.
- [90] W.-J. Rappel and W. F. Loomis. Eukaryotic chemotaxis. *Wiley Interdisciplinary Reviews: Systems Biology and Medicine*, 1(1):141–149, 2009.



- [91] W.-J. Rappel, P. J. Thomas, H. Levine, and W. F. Loomis. Establishing direction during chemotaxis in eukaryotic cells. *Biophysical Journal*, 83(3):1361–1367, 2002.
- [92] D. S. Rhoads, S. M. Nadkarni, L. Song, C. Voeltz, E. Bodenschatz, and J.-L. Guan. Using microfluidic channel networks to generate gradients for studying cell migration. in *Cell Migration, Methods in Molecular Biology*, volume 294 (J.-L. Guan, ed.), 347–357, Humana Press, 2005, 10.1385/1-59259-860-9:347.
- [93] T. W. Ridler and S. Calvard. Picture thresholding using an iterative selection method. *Systems, Man and Cybernetics, IEEE Transactions on*, 8(8):630–632, 1978.
- [94] H. Risken. The Fokker-Planck equation: Methods of solution and applications. *Springer Series in Synergetics, Vol. 18*, 1989.
- [95] A. T. Sasaki, C. Chun, K. Takeda, and R. A. Firtel. Localized Ras signaling at the leading edge regulates P13K, cell polarity, and directional cell movement. *Journal of Cell Biology*, 167(3):505–518, 2004.
- [96] A. T. Sasaki, C. Janetopoulos, S. Lee, P. G. Charest, K. Takeda, L. W. Sundheimer, R. Meili, P. N. Devreotes, and R. A. Firtel. G protein-independent Ras/PI3K/F-actin circuit regulates basic cell motility. *The Journal of Cell Biology*, 178(2):185–191, 2007.
- [97] M. Schienbein, K. Franke, and H. Gruler. Random walk and directed movement: Comparison between inert particles and self-organized molecular machines. *Physical Review E*, 49(6), 1994.
- [98] M. Schienbein and H. Gruler. Langevin equation, Fokker-Planck equation and cell migration. *Bulletin of Mathematical Biology*, 55(3):585–608, 1993.
- [99] R. Sekar and A. Periasamy. Fluorescence resonance energy transfer (FRET) microscopy imaging of live cell protein localizations. *Journal of Cell Biology*, 160(5):629–633, 2003.
- [100] D. Selmecki, S. Mosler, P. H. Hagedorn, N. B. Larsen, and H. Flyvbjerg. Cell motility as persistent random motion: Theories from experiments. *Biophys. J.*, 89(2):912–931, 2005.
- [101] B. Shaffer. Secretion of cyclic amp induced by cyclic amp in the cellular slime mould dictyostelium discoideum. *Nature*, 255(5509):549–552, 1975.
- [102] T. J. Shaw and P. Martin. Wound repair at a glance. *Journal of Cell Science*, 122(18):3209–3213, 2009.
- [103] A. D. Shenderov and M. P. Sheetz. Inversely correlated cycles in speed and turning in an ameba: an oscillatory model of cell locomotion. *Biophys. J.*, 72(5):2382–2389, 1997.
- [104] T. Shibata and K. Fujimoto. Noisy signal amplification in ultrasensitive signal transduction. *Proceedings of the National Academy of Sciences of the United States of America*, 102(2):331–336, 2005.
- [105] S. Siegert, R. Friedrich, and J. Peinke. Analysis of data sets of stochastic systems. *Physics Letters A*, 243(5–6):275–280, 1998.

## BIBLIOGRAPHY

---

- [106] R. Skupsky, W. Losert, and R. J. Nossal. Distinguishing modes of eukaryotic gradient sensing. *Biophysical Journal*, 89(4):2806–2823, 2005.
- [107] R. Skupsky, C. McCann, R. Nossal, and W. Losert. Bias in the gradient-sensing response of chemotactic cells. *Journal of Theoretical Biology*, 247(2):242–258, 2007.
- [108] M. Sohrmann and M. Peter. Polarizing without a c(1)ue. *Trends in Cell Biology*, 13(10):526–533, 2003.
- [109] L. Song, S. M. Nadkarni, H. U. Bodeker, C. Beta, A. Bae, C. Franck, W.-J. Rappel, W. F. Loomis, and E. Bodenschatz. *Dictyostelium discoideum* chemotaxis: Threshold for directed motion. *European Journal of Cell Biology*, 85(9-10):981–989, 2006.
- [110] T. M. Squires and S. R. Quake. Microfluidics: Fluid physics at the nanoliter scale. *Reviews of Modern Physics*, 77(3), 2005.
- [111] L. Stephens, L. Milne, and P. Hawkins. Moving towards a better understanding of chemotaxis. *Current Biology*, 18(11):R485–R494, 2008.
- [112] K. Subramanian and A. Narang. A mechanistic model for eukaryotic gradient sensing: Spontaneous and induced phosphoinositide polarization. *Journal of Theoretical Biology*, 231(1):49–67, 2004.
- [113] K. F. Swaney, C.-H. Huang, and P. N. Devreotes. Eukaryotic chemotaxis: A network of signaling pathways controls motility, directional sensing, and polarity. *Annual Review of Biophysics*, 39(1):265–289, 2010.
- [114] H. Takagi, M. J. Sato, T. Yanagida, and M. Ueda. Functional analysis of spontaneous cell movement under different physiological conditions. *PLoS ONE*, 3(7):e2648, 2008.
- [115] G. Taylor. Dispersion of soluble matter in solvent flowing slowly through a tube. *Proceedings of the Royal Society of London. Series A, Mathematical and Physical Sciences*, 219(1137):186–203, 1953.
- [116] R. Thar and M. Kühl. Bacteria are not too small for spatial sensing of chemical gradients: An experimental evidence. *Proceedings of the National Academy of Sciences of the United States of America*, 100(10):5748–5753, 2003.
- [117] M. Theves. *Quantitative studies of Dictyostelium discoideum chemotaxis*. Master’s thesis, Universität Göttingen and Max-Planck Institut für Dynamik und Selbstorganisation, 2009.
- [118] M. Ueda, Y. Sako, T. Tanaka, P. Devreotes, and T. Yanagida. Single-molecule analysis of chemotactic signaling in dictyostelium cells. *Science*, 294(5543):864–867, 2001.
- [119] M. Ueda and T. Shibata. Stochastic signal processing and transduction in chemotactic response of eukaryotic cells. *Biophysical Journal*, 93(1):11–20, 2007.
- [120] P. J. M. Van Haastert and P. N. Devreotes. Chemotaxis: signalling the way forward. *Nat Rev Mol Cell Biol*, 5(8):626–634, 2004.

## BIBLIOGRAPHY

---

- [121] P. J. M. Van Haastert, I. Keizer-Gunnink, and A. Kortholt. Essential role of PI3-kinase and phospholipase A2 in *Dictyostelium discoideum* chemotaxis. *The Journal of Cell Biology*, 177(5):809–816, 2007.
- [122] P. J. M. van Haastert and M. Postma. Biased random walk by stochastic fluctuations of chemoattractant-receptor interactions at the lower limit of detection. *Biophysical Journal*, 93(5):1787–1796, 2007.
- [123] N. Van Kampen, *Stochastic processes in physics and chemistry*. North-Holland Personal Library, Elsevier, 2007.
- [124] B. Varnum and D. Soll. Effects of camp on single cell motility in dictyostelium. *The Journal of Cell Biology*, 99(3):1151–1155, 1984.
- [125] R. A. Vaughan and P. N. Devreotes. Ligand-induced phosphorylation of the cAMP receptor from *Dictyostelium discoideum*. *Journal of Biological Chemistry*, 263(28):14538–14543, 1988.
- [126] D. M. Veltman, I. Keizer-Gunnik, and P. J. M. Van Haastert. Four key signaling pathways mediating chemotaxis in *Dictyostelium discoideum*. *Journal of Cell Biology*, 180(4):747–753, 2008.
- [127] M. Vicker. The regulation of chemotaxis and chemokinesis in *Dictyostelium* amoebae by temporal signals and spatial gradients of cyclic AMP. *J Cell Sci*, 107(2):659–667, 1994.
- [128] G. H. Wadhams and J. P. Armitage. Making sense of it all: bacterial chemotaxis. *Nat Rev Mol Cell Biol*, 5(12):1024–1037, 2004.
- [129] G. M. Whitesides, E. Ostuni, S. Takayama, X. Jiang, and D. E. Ingber. Soft lithography in biology and biochemistry. *Annual Review of Biomedical Engineering*, 3(1):335–373, 2001.
- [130] D. Wyatt. *Chemotaxis in microfluidic channels*. Ph.D. thesis, Cornell University, 2007.
- [131] Z. Xiao, N. Zhang, D. B. Murphy, and P. N. Devreotes. Dynamic Distribution of Chemoattractant Receptors in Living Cells During Chemotaxis and Persistent Stimulation. *The Journal of Cell Biology*, 139(2):365–374, 1997.
- [132] X. Xu, M. Meier-Schellersheim, X. Jiao, L. E. Nelson, and T. Jin. Quantitative imaging of single live cells reveals spatiotemporal dynamics of multistep signaling events of chemoattractant gradient sensing in dictyostelium. *Mol. Biol. Cell*, 16(2):676–688, 2005.
- [133] X. Xu, M. Meier-Schellersheim, J. Yan, and T. Jin. Locally controlled inhibitory mechanisms are involved in eukaryotic GPCR-mediated chemosensing. *The Journal of Cell Biology*, 178(1):141–153, 2007.
- [134] E. G. Yarmola, T. Somasundaram, T. A. Boring, I. Spector, and M. R. Bubb. Actin-latrunculin A structure and function. differential modulation of actin-binding protein function by latrunculin A. *Journal of Biological Chemistry*, 275(36):28120–28127, 2000.
- [135] S. H. Zigmond. Ability of polymorphonuclear leukocytes to orient in gradients of chemotactic factors. *The Journal of Cell Biology*, 75(2):606–616, 1977.

## BIBLIOGRAPHY

---

- [136] R. Zwanzig, *Nonequilibrium statistical mechanics*. Oxford University Press, 2001.

# Acknowledgements

First and foremost, my acknowledgments go to Eberhard Bodenschatz for accepting me as an intern in his group, making me discover the exciting world of biophysics, and then allowing me to continue my work as his Ph.D. student. Eberhard's door was always open for enthusiastic scientific discussions, during which he would constantly push me to know any work I would present in each and every detail. Eberhard's endless energy is contagious, which encouraged me to take initiatives and to use as best as possible the freedom I was given. I am also very grateful for the many opportunities I have had to "be proud of my work" by presenting my results at various conferences and summer schools.

I wholeheartedly thank Carsten Beta for his constant support throughout my stay in Göttingen, from the first days of my arrival, where he introduced me to the experimental setups, to his last corrections on the draft of my thesis. Carsten was always ready to help me clarify details of my work, whether he was in Göttingen or, as became the case later, in Berlin. Our many exchanges helped me considerably in obtaining the results presented in this thesis.

Thanks go to Reiner Kree, for accepting to be referee of this work, and for giving me very useful advices and insights on my work with the Langevin equation. I would also like to thank Jürgen Vollmer, Ulrich Parlitz, Marc Timme and Stefan Luther for accepting to be part of my Ph.D. committee.

It is with great pleasure that I acknowledge the help and the cheerful atmosphere of the Dicty group. My first thanks go to Albert Bae, without whom most of this work would never have been possible. Albert's knowledge of physics, his constant rigor and his depth of analysis when confronted to a new problem of whatever complexity keep amazing me every day. Moreover, it was always a pleasure to chat about non-work related topics, to play music together, or just to hang out in Göttingen or in Portland, where he and his parents generously hosted four of us during one week. My fellow GAUSS-Doktorand Christian Westendorf had a hard time introducing me to biology, punctuality and traditions. It was a delight to be in his company both at work and outside work, and I will always remember the parties we went to together. I will dearly miss his dry sense of humor. I have also had the pleasure to be closely working with Matthias Theves, and even more pleasure to have had countless and thrilling arguments with him on topics ranging from science to religion, via international politics and French cinema. Azam Gholami and Noriko Oikawa brought their experience to the group, and I have learnt much by talking with them. I was moreover lucky enough to be able to play music with Noriko and to taste many of her delicious dishes. I would like to thank Marco Tarantola for reading most of this thesis and giving me his comments during his first week in the lab. Eva Pfannes, Rabea Sandmann and Weixing Li were in the group for a short time, and contributed to the pleasant working atmosphere. None of this work could have been done without the constant assistance of Katharina Schneider (and at one point, of Jan-Sebastian Wittwer) in the lab and the organisation planned by Barbara Kasemann. Special thanks go

to Katharina for the many early mornings that she drove me to work, for our discussions in the car, and the fun and enjoyable moments we had together.

I highly appreciated the efficiency and kindness of Angela Meister, who made sure that all administrative details would be taken care of immediately, helped me with the bureaucracy, and facilitated my life in this Institute greatly. Thanks go to Gerhard Nolte, Artur Kubitzek, Andreas Renner and Andreas Kopp for helping with technical problems, and to Olaf Truemper for driving me countlessly from Faßberg to the Bunsenstrasse or the University and back. Many thanks to Barbara Kutz for her warmth, her joyful and optimistic character and her support during this thesis.

Special thanks go to Denis Funfschilling, who pitied my fate in Germany and kept bringing me cheese and other delicacies from Nancy each time he would visit Göttingen. It was a pleasure to know, work, talk, eat, party and more with Mathieu Gibert, Mireia Torralba, Kelken Chang (and our unforgettable rides in the car), Greg Bewley, Stephan Weiss, Fabio Di Lorenzo, Ewe-Wei Saw, Walter Pauls, Gabriel Seiden, Haitao Xu, Hengdong Xi, Sebastian Lambertz, Robert Zimmermann, Claudia Richter, Holger Nobach, Toni Frohlich, and Nick and Lisa Ouellette. I also acknowledge wise advices from Valentin Krinsky.

During my first year in Göttingen, I shared flats with Amgad Squires and Dario Vincenzi. They both know how much I have appreciated this time together. Thanks to Dario for making me discover many operas and for sharing his insights on countless topics. Thanks to Amgad for our many discussions over the past four years in Göttingen, where we shared our happiness and frustrations, and for the motivation that he gave me at the very end to finish this thesis. Many thanks also go to my other flatmates, Angelika, Petra and Gudrun, and of course to Sebastian and Aurélie for the time that we spent together, be it in Germany, France or Italy.

Out of work, several people supported me throughout the thesis. Thanks go to my once-neighbors Audrey, Taha and Marie-Charlotte. Thanks to Emma for the energetic support from New York, to Naomi for the music, to Thomas for some very pleasant evenings, and to Larissa for introducing me to the parties in the physiology building. Rehearsals with the orchestra was one of the highlights of the week thanks to Lorenz. I have had many nice lunches, brunches and dinners with Martin, Martin, Jakob and Raoul. It was a pleasure to get to know Minou, Hannah and Catarina.

I cannot thank Britta enough for helping me keep my balance even while literally standing on my head, for some too rare outings in the countryside, and for bearing with me during the final months of this thesis.

My family has been a constant source of support during all my studies, and the thesis time was no exception. It is a particular pleasure to thank my parents for their continuous encouragement.

Ласт бут нот лист, Алиса, нукодем, спасибо за всё...

# Curriculum Vitae

Name	Gabriel Amselem
Born	September 6, 1983 in Paris, France
Nationality	French
Since 03/2007	PhD student with Prof. E. Bodenschatz, Max Planck Institute for Dynamics and Self-Organization, Göttingen
07/2006 – 01/2007	Intern with Prof. E. Bodenschatz, Max Planck Institute for Dynamics and Self-Organization, Göttingen
09/2005 – 06/2006	MSc in Theoretical Physics of Complex Systems, Paris 7 University, France
07/2004 – 12/2004	Intern with Dr. J. Bahren and Dr. V. Protopopescu, Oak Ridge National Laboratory, Oak Ridge, TN
09/2002 – 06/2006	Ecole Supérieure de Physique et de Chimie Industrielles (ESPCI), Paris, France
09/2000 – 06/2002 06/2000	Preparatory classes in Physics and Chemistry, Paris, France Baccalauréat